



***In silico* and *in vitro* modelling of chronic wounds to improve  
our understanding of wound biomechanics and to test novel  
medical devices.**

being a thesis submitted in fulfilment of the  
requirements for the degree of  
Doctor of  
Philosophy

in the University of Hull

by

Alexandra Claire Hendon, MEng

July 2023

# Dedication

*To my younger self, who's determination and resilience carried me through every challenge  
faced on this journey.*

*You did it kid!*

## Acknowledgements

This thesis would not have been possible without my supervisor, Michael Fagan, who I'm sure didn't expect to retire and still be supervising a PhD student! Thank you for always being on hand with advice and help, even when I haven't made supervising me easy. I will forever be grateful to you for supporting me and not judging me through the many highs and lows of not only the past 6 years of my PhD, but the 4 years before that during my undergraduate degree as well.

I'd also like to thank Smith and Nephew for funding this project.

Behind every PhD student there's a community who rides the rollercoaster with them. I have been so lucky to have so many people who've held my hand every step of the way. I've been so lucky to have such a large gang around me throughout this – way too many people to acknowledge individually.

Sabrina and James (and Rosie and Jim!). You've been by my side since I stepped foot in Hull for the first time and have done more for me than I could ever write! I'm forever grateful for you both – thank you so so so so so much. You've shaped the semi-competent adult I've turned into and, whilst I no longer live nearby, you're never getting rid of me - sorry!

Ron and Clarissa, my rabbits. Thank you for making me laugh and not eating *all* of my journal articles, only the most important!

My family. Thank you for being by my side through my entire education journey, from my first day of playschool to my final day of university. I had to do something to make it so there weren't 3 Miss A Hendon's...

Tiffany. Thank you for always cheering me on, even if you didn't quite understand what I was doing or why I'd decided to do it.

Hannah. We met halfway through my PhD in rather unique circumstances, but you've been by my side ever since. You're my biggest cheerleader and the most skilful person I know.

Holly. Thank you for always listening to me, encouraging me, and never judging me. I don't think I'd have gotten through the last few months without you.

Gina, Kate and the Advice Centre team - thank you for teaching me the life skills I need to survive in the world. Thank you for always being on hand when I've needed help.

The team at UHBW, particularly Brett. Thank you for supporting me with trying to complete my PhD whilst also starting another Masters. Thank you for being flexible and understanding.

My scouting and guiding family. I'm so grateful for the fun I've had and the friendships I've developed. Scouting and Guiding has been such a welcome break on my evenings and weekends throughout my PhD and has given me friends and family across the world. I can't wait for more adventures!

And to the writing group gang, Cathy, Kodi, Claire and Janine – I can't believe we're actually finishing! We've gone through this together and I appreciate you all!

## Abstract

Negative pressure wound therapy (NPWT) is a widely used system that aids the healing of chronic wounds through the application of sub-atmospheric pressure. The effectiveness of this method is widely recognised, however the mechanisms behind this are not well understood. In particular, it is widely believed that NPWT has a strong biomechanical influence on the wound healing process, however the precise mechanisms involved are unknown.

This project aimed to fill some of the gaps in our understanding of the biomechanics of the wound healing process by creating validated *in silico* and *in vitro* wound models. The overall goal was to provide tools that enable the investigation of how biomechanical forces dissipate through wounds and the surrounding tissues and provide physiologically representative physical wound models to allow novel medical devices and procedures to be tested *in vitro* and *in silico*.

A multiphase approach was taken to the investigation of the mechanical strain throughout the surrounding biological tissue. The first stage was the development of a biomechanically similar *in vitro* wound model through the mechanical testing of elastomeric materials followed by the development of an equivalent *in silico* model. Macroscopic and microscopic *in silico* models with biological material properties were then created to investigate the strain distribution and displacement induced by NPWT with different wound filler materials.

It was found that the strains induced through the model during NPWT were comparable to those known to induce the expression of hormones and proteins known to promote granulation tissue growth and wound healing. These strains were experienced around the wound in addition to throughout the surrounding tissue. The models developed in this project are adaptable and able to be utilised in the future testing of novel medical devices.

# Contents

Dedication.....	i
Acknowledgements.....	ii
Abstract.....	iv
Contents.....	v
List of Figures.....	ix
List of Tables.....	xvii
List of Equations.....	xviii
Chapter 1 Introduction.....	19
Chapter 2 Literature Review.....	23
2.1 Pathophysiology of Wound Healing.....	23
2.1.1 Chronic Wounds.....	25
2.1.2 Negative Pressure Wound Therapy.....	30
2.2 Biomechanical Behaviour of Biological Tissues.....	31
2.2.1 Skin.....	32
2.2.2 Subcutaneous Adipose Tissue.....	35
2.2.3 Muscle.....	35
2.2.4 Biomechanical Testing.....	36
2.2.5 Mechanical Properties of Biological Materials.....	38
2.3 Wound Modelling – <i>in vivo</i> , <i>in vitro</i> and <i>in silico</i> approaches.....	48
2.3.1 In Vivo Modelling.....	48
2.3.2 In Vitro Modelling.....	54
2.3.3 <i>In Silico</i> Modelling.....	58
Chapter 3 Experimental Preliminary Testing.....	65
3.1 Preliminary Testing.....	65
3.1.1 Mould Design.....	65
3.1.2 Silicone Mixing.....	66
3.1.3 Tensile Testing.....	69
3.2 Silicone Sample Results.....	71

3.2.1	S30.....	71
3.2.2	GP 3481 F .....	72
3.2.3	T4.....	73
3.2.4	Food Grade.....	74
3.2.5	Silskin 10 (1:1) .....	75
3.2.6	Silskin 10 (1:2) .....	76
3.2.7	T15.....	78
3.3	Discussion.....	79
Chapter 4 <i>In Silico</i> Modelling .....		82
4.1	Building the model .....	83
4.2	Testing the model .....	84
4.3	Basic Model Analysis .....	88
4.3.1	Effect of Model Dimensions.....	88
4.3.2	Varying Film Surface Shell Element Thickness .....	92
4.3.3	Varying Wound Surface Shell Elements (for Pressure Application).....	93
4.3.4	Linear vs Non-Linear Material Properties .....	94
4.3.5	Initial Model Testing – Varying Dimensions.....	98
4.3.6	Varying Pressure .....	115
4.3.7	Varying Wound Shape.....	117
4.4	Discussion.....	121
Chapter 5 Design of a Physical Model.....		122
5.1	Introduction .....	122
5.2	Model Requirements .....	122
5.3	Mould Development .....	123
5.4	Final Design .....	123
5.5	Testing the Model .....	124
5.5.1	Results .....	126
Chapter 6 Biologically Representative Wound Model.....		129
6.1	Introduction .....	129

6.2	Selection of Material Properties .....	129
6.2.1	Skin .....	130
6.2.2	Subcutaneous Fatty Tissue.....	131
6.2.3	Muscle .....	132
6.3	Finite Element Analysis .....	133
6.3.1	Results .....	133
6.4	Discussion.....	138
Chapter 7 – Microscopic Computational Comparison of Wound Filler Materials.....		139
7.1	Methodology.....	140
7.1.1	Design of the model .....	140
7.2	Preliminary Testing – Mesh Convergence .....	141
7.2.1	Foam Strut Model .....	142
7.3	Preliminary Testing – Loading the Model .....	143
7.4	Varying Foam Density .....	145
7.5	Gauze Model.....	149
7.5.1	Mechanical Properties of Gauze .....	149
7.5.2	Development of Gauze Model .....	150
7.5.3	Mesh Convergence Study – Square Gauze Model .....	152
7.5.4	Mesh Convergence Study – Cylindrical Gauze Model .....	158
7.6	Discussion.....	172
7.6.1	Impact of Foam .....	172
7.6.2	Influence of Gauze as a Wound Filler .....	173
Chapter 8 Discussion.....		174
8.1	Project Summary.....	174
8.2	Macroscopic Impact of NPWT.....	176
8.3	Microscopic Impact of NPWT.....	179
8.3.1	Foam Model .....	180
8.3.2	Gauze Model .....	181
Chapter 9 Conclusions .....		184

9.1 Future Work .....	184
Reference list .....	186
Appendix 1 – Engineering Drawing of ASTM D412 Moulds .....	I
Appendix 2 – Engineering Drawings of <i>In Vitro</i> Model Mould .....	II
Appendix 3 – Surface Shell Element Thickness Variation Graph .....	V
Appendix 4 – Macroscopic <i>In Silico</i> Model Log File .....	VI
Appendix 5 – Macroscopic <i>In Silico</i> Model Post Processing File .....	XVII
Appendix 6 – Microscopic <i>In Silico</i> Foam Model Log File .....	XXIII
Appendix 7 – Microscopic <i>In Silico</i> Foam Model Post Processing Log File .....	XXIX
Appendix 8 – Microscopic <i>In Silico</i> Gauze Model Log File .....	XXXV
Appendix 9 – Microscopic <i>In Silico</i> Gauze Model Post Processing Log File .....	XLI

## List of Figures

<b>Figure 1</b> A cartoon depiction of the key processes in the healing of an acute skin wound. Within the wound, a fibrin clot, pervaded by a combination of fibroblasts, granulation tissue and inflammatory cells is shown in more detail (Martin, 1997).....	24
<b>Figure 2</b> A cartoon diagram showing the direction of flow of blood through the deep and superficial venous systems of the lower leg. It can be seen that a one way system is observed with the separate venous systems being connected by perforator veins (Anderson, 2006).....	27
<b>Figure 3</b> A photograph of two legs. The patient’s right leg is clearly affected by lipodermatosclerosis with the classic inverted champagne bottle appearance being observed (Etufugh & Phillips, 2007). .....	29
<b>Figure 4</b> A schematic illustration demonstrating some of the hypothesised mechanisms of action for negative pressure wound therapy including oedema reduction and remodelling (Hasan et al., 2015). .....	30
<b>Figure 5</b> A detailed diagram of the various structures of the skin (Benítez & Montáns, 2017).	33
<b>Figure 6</b> A detailed diagram of the structures of skeletal muscle (Marieb & Keller, 2021). .....	36
<b>Figure 7</b> An illustration of the experimental tensile testing set up used by Griffin et al. (2016). A sample of a synthetic biomaterial can be seen between the clamps.....	37
<b>Figure 8</b> A graph showing the stress-strain relationship for skin using values found in literature. A large variation in results can be seen. ....	42
<b>Figure 9</b> A graph presenting the stress-stretch relationship of Calvo et al. (2010)’s experimental data. This data was gained from the tensile testing of rat <i>tibialis anterior</i> muscle. ....	44
<b>Figure 10</b> Schematic illustration showing the position of two full thickness wounds on a murine model of wound healing. Silicone splints (the red doughnuts) can be seen preventing healing by wound contraction (Dunn et al., 2013).....	50
<b>Figure 11</b> (a) A schematic showing the distribution of wounds on the back of a porcine wound model. (b) A photograph showing a porcine wound 3 days after wound creation (Hadad et al., 2010). .....	52
<b>Figure 12</b> (Left) a schematic of negative pressure wound therapy applied to a wound. Including wound filler and vacuum connection. (Right) Finite element model showing the variation in pressures and micro stresses (Saxena et al., 2004). .....	60
<b>Figure 13</b> Finite element models designed by Wilkes et al. (2009b) to investigate the impact of foam and gauze on tissue during negative pressure wound therapy.....	61
<b>Figure 14</b> Photograph of an ASTM D412 compliant sample of Food Grade silicone. This is the size of sample used for all tensile testing. ....	66

<b>Figure 15</b> The mean stress $\pm$ 1 S.D. for silicones subjected to 2.5% - 30% strain 1,7,and 28 days post removal from mould. It was found that the mean stress is significantly different on day 1 and day 28 for strains 5% and greater. ....	72
<b>Figure 16</b> Variation of mean stress with strain for samples of GP 3481 F at 1, 7 and 28 days post removal from moulds. It can be seen that there is no significant variation between the mean values of stress.....	73
<b>Figure 17</b> Stress-Strain graph achieved through tensile testing of T4 silicone samples 1, 7 and 28 days post removal from moulds. ....	74
<b>Figure 18</b> Variation of stress with strain for samples of Food Grade silicone subjected to tensile testing at 1, 7 and 28 days post removal from moulds. It can be seen that the samples have significantly different values for stress at 30% strain. ....	75
<b>Figure 19</b> Variation of stress for strain values between 2.5 and 30% for samples of Silskin 10 (1:1) silicone tested at 1, 7 and 28 days post removal from moulds. It was seen that the stress was significantly different at strains of 5% and greater. ....	76
<b>Figure 20</b> Silskin 1:2 ratio had a Young's modulus of $2.63 \times 10^{-3}$ MPa (3 s.f.) at $\epsilon = 0.3$ . The data was gained from tensile testing in accordance to ASTM D412 over a period of 28 days to ensure repeatability. The data had a range of approximately 50%.....	77
<b>Figure 21</b> The variation of stress with strain experienced by samples of T15 silicone during tensile testing at 1, 7 and 28 days post removal from moulds. It was found that at lower strains, the difference in mean stress between the datasets was not significantly different, but at strains of 7.5% and greater, a significant difference was found. ....	78
<b>Figure 22</b> Cross sectional view of the macroscopic <i>in silico</i> wound model. Each colour denotes a different material: pink = wound filler; turquoise = skin; purple = subcutaneous fatty tissue; red = muscle; blue = bone. (Coarse mesh presented to demonstrate model structure. Finer mesh used to produce results). ....	83
<b>Figure 23</b> Convergence of 1 <sup>st</sup> and 3 <sup>rd</sup> principal strain along a central path with varying line edge size for the macroscopic model .....	85
<b>Figure 24</b> Convergence of displacement along a central path with varying line edge size for the macroscopic model .....	86
<b>Figure 25</b> The effect of variation in model dimensions on the 1 <sup>st</sup> and 3 <sup>rd</sup> principal strains down the central vertical path of the models. (The location of the path in this figure and subsequent figures is highlighted in red in the small schematic).....	88
<b>Figure 26</b> The variation in vertical displacement along the central axis with variation in model size. A similar pattern is followed for all model variations with minimal dissimilitude in the data sets. ....	89

<b>Figure 27</b> The distribution of 1st and 3rd principal strain around the wound circumference with varying model dimensions. ....	90
<b>Figure 28</b> The horizontal displacement around the wound circumference with varying model dimensions, showing that the wound is enlarging in a transverse direction. ....	91
<b>Figure 29</b> The distribution of 1st and 3rd principal strain along a centrally plotted path when the surface shell thickness is varied.....	92
<b>Figure 30</b> The distribution of 1st and 3rd principal strain along a central vertical path with varying wound shell thickness. ....	93
<b>Figure 31</b> 1st and 3rd principal strain plotted along a vertical path from the wound base shows that linear and non-linear material properties produce the same strain profile, but the non-linear stress values are less than those of the linear model.....	94
<b>Figure 32</b> Vertical displacement along a centrally plotted path in the y-direction shows that the non-linear model experiences greater displacement than the model with linear material properties.....	95
<b>Figure 33</b> The distribution of 1 <sup>st</sup> and 3 <sup>rd</sup> principal strains down the wound face follows a similar pattern for both the linear and non-linear model. The key difference is the magnitude of the 1 <sup>st</sup> principal strain through the skin layer where the linear value is larger than that of the non-linear model. ....	96
<b>Figure 34</b> The horizontal displacement down the wound face models with both linear and non-linear material properties. Both models follow the same pattern with a greater displacement being experienced by the non-linear model through the skin and fat layers, and the linear model through the muscle layer.....	97
<b>Figure 35</b> 1 <sup>st</sup> and 3 <sup>rd</sup> principal strains along a centrally plotted path for different skin thicknesses. It can be seen that the results follow the same pattern, but with the magnitude of the tensile strains decreasing and compressive strains increasing as thickness decreases.....	98
<b>Figure 36</b> A graph showing the vertical displacement along the central y-axis. The greater the thickness of the skin layer, the lower the magnitude of deformation. ....	99
<b>Figure 37</b> Plot of the 1 <sup>st</sup> and 3 <sup>rd</sup> principal strains down the wound face when the skin thickness is varied. A similar pattern is followed throughout the graphs with the main differences being a higher value of 1 <sup>st</sup> principal strain for the 1.5mm skin thickness model at the skin-fat interface. ....	100
<b>Figure 38</b> Variation of the horizontal displacement around the wound circumference when skin thickness is varied. Prior to reaching the muscle layer, the pattern of the greater the skin thickness, the smaller the magnitude is observed. From this point, the models run concurrently.....	101

<b>Figure 39</b> 1 <sup>st</sup> and 3 <sup>rd</sup> principal strain along a central path, with varying subcutaneous fatty tissue thickness. There is minimal variation in the stresses along the majority of the plots. Where variation occurs, the thinner fatty tissue models have higher 1 <sup>st</sup> principal strain than the models with thicker layers of subcutaneous fat.....	102
<b>Figure 40</b> A graph showing the vertical displacement along the central y-axis when the thickness of subcutaneous fatty tissue is varied. The plots for the 10mm and 15mm fat thickness run almost simultaneously, with little variation. In comparison, the 5mm fat model has a much smaller magnitude throughout.....	103
<b>Figure 41</b> The variation in 1 <sup>st</sup> and 3 <sup>rd</sup> principal strain around the wound circumference when the thickness of subcutaneous fatty tissue is changed. It can be seen that the thinner the fatty tissue layer, the greater the magnitude of tensile strain. ....	104
<b>Figure 42</b> The distribution of horizontal displacement around the circumference of the wound when the thickness of subcutaneous fatty tissue is varied. The greater the fat thickness, the greater the displacement.....	105
<b>Figure 43</b> A graph of 1 <sup>st</sup> and 3 <sup>rd</sup> principal strains throughout the model when the muscle thickness is varied. Prior to reaching the muscle layer, all models have the same strain. Following this, the smaller muscle thicknesses have a greater magnitude of compressive strain. ....	106
<b>Figure 44</b> The vertical displacement along the central y-axis for models with varying muscle thickness. The greater the muscle thickness, the greater the displacement in the y-direction. ....	107
<b>Figure 45</b> 1 <sup>st</sup> and 3 <sup>rd</sup> principal strain around the wound circumference when the muscle thickness is varied. Prior to the muscle layer, there is no variation in the strain values. The variation throughout is minimal. No clear pattern of variation is visible, however all models run closely. ....	108
<b>Figure 46</b> The distribution of 1 <sup>st</sup> and 3 <sup>rd</sup> principal strain through the central Y-axis when the diameter of bone is varied. There is no variation through the soft tissue layers. The only obvious variation is the depth of the bone-muscle interface.....	109
<b>Figure 47</b> The distribution of vertical displacement through the central y-axis. There is minimal variation throughout, although the smallest bone diameter has a slightly higher displacement than the larger bone diameters.....	110
<b>Figure 48</b> 1 <sup>st</sup> and 3 <sup>rd</sup> principal strain around the wound circumference. There is no noticeable variation between the models.....	111
<b>Figure 49</b> The 1 <sup>st</sup> and 3 <sup>rd</sup> principal strains with varying wound diameters.....	112
<b>Figure 50</b> The vertical displacement through the centre of the model when the wound diameter is varied. In general, the larger the wound, the greater the displacement. ....	113

<b>Figure 51</b> 1 <sup>st</sup> and 3 <sup>rd</sup> principal strains around the wound for models with varying wound diameters. The wounds with larger diameters have a higher magnitude of stress than those with smaller diameters. ....	113
<b>Figure 52</b> A graph of horizontal displacement around the wound circumference. There is approximately 0.4mm difference between each model. The greater the wound diameter, the greater the displacement.....	114
<b>Figure 53</b> 1 <sup>st</sup> and 3 <sup>rd</sup> principal stress from along a central path through the model. By changing the pressure, the stresses are scaled up or down. More pressure results in greater stress....	115
<b>Figure 54</b> The vertical displacement through the central axis when the pressure is varied. There is a scalar relationship with the higher pressure creating a greater displacement.....	116
<b>Figure 55</b> The 1 <sup>st</sup> and 3 <sup>rd</sup> principal strain around the wound circumference. There is a direct relationship between the amount of applied pressure, and the quantity of strain produced. The greater the pressure, the greater the strain experienced by the surrounding tissue.....	117
<b>Figure 56</b> Distribution of 1 <sup>st</sup> and 3 <sup>rd</sup> principal strains when varying the shape of the wound.	118
<b>Figure 57</b> Variation of vertical displacement through the central path of two models with hemispherical and cylindrical wounds.....	118
<b>Figure 58</b> 1st and 3rd principal strain around the wound face of a filleted cylindrical wound and a hemispherical wound.....	119
<b>Figure 59</b> Displacement around the wound experienced by the hemispherical and cylindrical wound models. ....	120
<b>Figure 60</b> Cross sectional isometric view of the mould used to cast the <i>in vitro</i> model. It can be seen that an interlocking modular design was used to allow adjustment for further model development.....	124
<b>Figure 61</b> Attachment of NPWT device to the surface of the <i>in vitro</i> model. ....	126
<b>Figure 62</b> Segmentation of wound from a microCT scan of the <i>in vitro</i> wound model without loading.....	127
<b>Figure 63</b> Segmented hole from a microCT scan of the <i>in vitro</i> wound model whilst subjected to NPWT at a pressure of 200mmhg.....	127
<b>Figure 64</b> Stress-strain plots for skin from a review of literature, showing a large range of Young's modulus values.....	130
<b>Figure 65</b> A stress-strain analysis of the biomechanical properties of subcutaneous adipose tissue gained from reviewing literature.....	131
<b>Figure 66</b> A stress-strain analysis of skeletal muscle tissue with values gained from a review of literature. ....	132
<b>Figure 67</b> A graph showing the displacement of the 1st and 3rd principal strain around the wound. There is an initial tensile peak at approximately 5mm below the wound base. ....	134

<b>Figure 68</b> Displacement through a central path for a macroscopic model with biomechanically similar properties to biological tissues .....	135
<b>Figure 69</b> A graph showing the distribution of tensile and compressive strain around a hemispherical wound face for a model with biomechanically similar properties.....	136
<b>Figure 70</b> Horizontal displacement (UX) experienced around the wound face of a model with biomechanically similar material properties. ....	137
<b>Figure 71</b> Vertical displacement (UY) around the wound face for a biomechanically similar model. ....	137
<b>Figure 72</b> Convergence study for foam strut model showing displacement through a central path.....	142
<b>Figure 73</b> Convergence study for foam strut model showing displacement along a horizontal path.....	143
<b>Figure 74</b> The variation of displacement during incremental loading of a finite element model. ....	144
<b>Figure 75</b> A graph showing the variation of displacement with different porosities of polyurethane foam. The greater the porosity, the greater the deformation surrounding the foam strut. ....	146
<b>Figure 76</b> The variation of tensile and compressive strain with foam porosity on a strut model during negative pressure wound therapy. It can be seen that there is greater strain, both compressive and tensile, around the immediate edge of the foam struts, with more strain being experienced by the more porous foams.....	147
<b>Figure 77</b> Compressive and tensile strains experienced along a central vertical axis underneath the strut-wound interface for varying pores per inch foams. ....	148
<b>Figure 78</b> Displacement experienced along a central vertical axis underneath the strut-wound interface for foams with varying porosities.....	149
<b>Figure 79</b> Image of gauze model with arbitrary dimensions .....	150
<b>Figure 80</b> Gauze model with arbitrary dimensions showing the applied loading conditions. .	151
<b>Figure 81</b> Convergence study for square gauze model showing displacement through the model. ....	152
<b>Figure 82</b> Convergence study for a square gauze model showing displacement along a horizontal path.....	152
<b>Figure 83</b> Vertical displacement experienced along the horizontal axis throughout the gradual loading of a square threaded gauze model. ....	153
<b>Figure 84</b> 1st and 3rd principal strain variation along a horizontal path for a square threaded gauze model with gradual loading during model development.....	154

<b>Figure 85</b> Vertical displacement experienced by a square threaded gauze model during the gradual loading process. ....	155
<b>Figure 86</b> 1st and 3rd principal strain through a central path for a square threaded gauze model with gradual loading .....	156
<b>Figure 87</b> Figure showing the construction of the cylindrical gauze model.....	157
<b>Figure 88</b> Convergence study for the cylindrical gauze model showing displacement through a central path.....	158
<b>Figure 89</b> Convergence study for the cylindrical gauze model showing displacement through a horizontal path.....	159
<b>Figure 90</b> Variation in displacement experienced a cylindrical thread gauze model during the gradual loading process. ....	160
<b>Figure 91</b> Compressive and tensile strains through a central path during the gradual loading of a cylindrical thread model. ....	161
<b>Figure 92</b> 1st and 3rd principal strains through the vertical (Y-axis) path underneath the cylindrical gauze during gradual loading.....	163
<b>Figure 93</b> 1st and 3rd principal strains through a vertical central path for the gradual loading of a gauze model with cylindrical threads. ....	164
<b>Figure 94</b> Variation in displacement for a cylindrical gauze model with polyurethane thread material properties in comparison with cotton thread material properties through a horizontal path.....	165
<b>Figure 95</b> Variation in 1st and 3rd principal strains for a cylindrical gauze model with polyurethane thread material properties vs cotton thread material properties. ....	166
<b>Figure 96</b> Variation of vertical displacement through a central vertical path for cylindrical thread models with polyurethane and cotton material properties .....	166
<b>Figure 97</b> Comparison of the displacement experienced by microscopic models simulating gauze and foam with polyurethane material properties and equal loading. ....	167
<b>Figure 98</b> Variation of 1st and 3rd principal strain through a horizontal path for models simulating gauze and foam with polyurethane material properties and equal loading. ....	168
<b>Figure 99</b> Displacement through a central vertical axis for models simulating polyurethane foam and gauze with varying thread shapes. ....	169
<b>Figure 100</b> 1st and 3rd principal strains through a central path for varying polyurethane gauze thread and foam strut shapes with equivalent loading.....	169
<b>Figure 101</b> Vertical displacement through a horizontal path for cotton gauze thread and polyurethane foam on a microscopic level.....	170
<b>Figure 102</b> Variation of tensile and compressive strain along a horizontal path for models of polyurethane foam and cotton gauze on a microscopic level.....	171

<b>Figure 103</b> Variation of vertical displacement through a central path for microscopic models of cotton gauze and polyurethane foam. ....	171
<b>Figure 104</b> Variation of 1st and 3rd principal strain for models of gauze and foam through a central path on a microscopic level .....	172
<b>Figure 105</b> Engineering drawing of ASTM D412 compliant "dog-bone" moulds used in the tensile testing of silicones.....	I
<b>Figure 106</b> Engineering drawing of the base of the <i>in vitro</i> model mould.....	II
<b>Figure 107</b> Engineering drawing of the muscle layer of the <i>in vitro</i> model mould.....	III
<b>Figure 108</b> Engineering drawing of the muscle layer of the <i>in vitro</i> model mould.....	IV
<b>Figure 109</b> Variation of strain around the wound face when the surface shell element thickness is varied. It can be seen that there is no variation in strains experienced. ....	V

## List of Tables

<b>Table 1</b> Sample tissue thicknesses and Young's modulus values for the different tissues. ....	46
<b>Table 2</b> A table containing the types of silicones tested in this project, alongside the manufacturers recommended ratios, mixing, working, and curing times. ....	67
<b>Table 3</b> The silicones selected to represent the biological tissues and the appropriate layer depth.....	81
<b>Table 4</b> The variables the model was tested under during the development of the <i>in silico</i> model. The wound shape for these variables is hemispherical.....	87
<b>Table 5</b> Young's moduli of biological materials used in the biomechanically similar <i>in silico</i> model. ....	133

## List of Equations

(1).....	32
(2).....	40
(3).....	40
(4).....	62
(5).....	63
(6).....	63
(7).....	70
(8).....	70
(9).....	70

## Chapter 1 Introduction

The wound healing process is complex and consists of a series of overlapping phases: inflammation, proliferation, and maturation. In a chronic wound, the healing process is unable to progress 'naturally' beyond the inflammation stage (Guo & DiPietro, 2010). This causes painful breaks in the skin that are at high risk of infection, leading to the need for long term specialist treatment. This, in part, contributes to the large expense chronic wounds impose on health services.

Chronic wounds are an ongoing issue for both healthcare professionals and patients. Not only do these hard-to-heal wounds cause long term pain and discomfort for the patient, but they also require complex and intense care to prevent infection and to encourage the healing process to progress. They are one of the larger burdens on the budget of healthcare providers worldwide, including the UK's National Health Service (NHS) and local Clinical Commissioning Groups (CCGs), costing each CCG approximately £15 million annually in 2017 (Guest et al., 2017). When it is considered that there were 106 CCGs in England alone at that time, this is an enormous expenditure for the country as a whole (NHS Confederation, 2021). CCGs were replaced with Integrated Care Systems in July 2022. Chronic wounds are the most expensive of all wound types due, in part, to their longevity and the need for consistent specialist care (Guest et al., 2017).

Affecting 1-2% of over 65-year-olds across the world, ulceration creates a significant burden on the population (Marola et al., 2016). It is estimated that at any one time, between 1.5 and 3 in 1000 of the general population have an open or active ulcer; when focussing on those over 80 years, this figure rises to 20 in 1000 (Alavi et al., 2016). Clearly, understanding exactly how such ulcers develop and subsequently what assists in their healing is of great importance. The sequence of biological events involved in the healing process for both acute and chronic wounds is generally well understood, despite there being disagreements in the approximate timescales of the stages involved. However, the influence of biomechanical processes in wound healing is less well understood.

One of the most effective treatments for chronic wounds, particularly ulceration, is negative pressure wound therapy (NPWT). This is a non-invasive wound treatment that uses a vacuum pump (negative pressure) in a closed system to promote wound healing (Thompson, 2008). Whilst there are many ideas as to how NPWT works, there isn't a single theory accepted by the majority of researchers. In particular, it is

widely believed that there is a strong biomechanical influence in the healing process of wounds treated with NPWT, however the precise mechanisms involved are unknown. If these were better understood, NPWT could presumably be improved and optimized further, and possibly tailored to different wound types and/or locations, and individual patients.

In order to increase understanding, wounds have been examined and investigated in a variety of ways. Historically, animal models have been used to replicate chronic human wounds due to the ability to replicate almost all aspects of a wound, both the biomechanical and biological processes, relatively accurately. However, in addition to substantial ethical concerns, there is no ideal animal model of human wound healing (Fang & Mustoe, 2008; Trøstrup et al., 2016; Ud-Din & Bayat, 2017). This is partially due to the difficulty in finding an animal with a similar skin structure and immune response to that of humans, which can be easily housed and cared for (Perez & Davis, 2008).

Russell & Burch (1960) published “The Principles of Humane Experimental Technique”, a book detailing the importance of ensuring the welfare of animals used in scientific research. In this book, the “3Rs”, i.e., ‘replacement, reduction and refinement’ were first outlined, although they were only applied to vertebrate species. Since this publication, it has been applied to all species, not just those with vertebrae, and widely adopted by governments around the world. The passing of the Animals (Scientific Procedures) Act (1986) was the first time the 3Rs became implicit in UK law, however Directive 2010/63/EU made explicit that it is compulsory for researchers to demonstrate the use of the 3Rs in research. Due to this, and an increased move towards a more ethical use of animals in science, *in silico* and *in vitro* models are needed. Whilst this does not pose a significant issue for researchers investigating biological processes, for example the formulation of granulation tissue in the proliferation stage of wound healing, there is a distinct paucity of available models for researchers investigating the biomechanical effects of wound healing. Current physical models that focus on biomechanics at a macroscopic level have a tendency to focus on a single layer of biological tissue, generally the skin, and allow researchers to investigate the deformational and frictional behaviour of that specific tissue (Nachman & Franklin, 2016). Whilst single layer physical models are useful for some applications, to truly represent the biomechanics of tissue, a multilayer model is needed. This is because

wounds often affect more than one tissue layer and the interaction between the layers also influence the dissipation of stresses and strains through the tissue during different treatments.

Furthermore, whilst physical wound models demonstrate the overall deformation of tissue when forces or treatments are applied, *in silico* wound models can show not only the deformation, but the distribution of forces, and resultant stresses and strains, through the model. This not only allows the identification of areas where those forces may be more concentrated but makes it possible to actually estimate the magnitude of the local resultant stresses and strains. This is beneficial as it allows a detailed understanding of exactly what the wounds and surrounding tissue experience during different treatments. Currently, there is a distinct lack of *in silico* models that consider the bulk deformation of the tissues that surround a wound. Saxena et al. (2004) and Wilkes et al. (2009b) both created finite element models of tissue undergoing NPWT but focussed on the stresses and strains at the wound bed. Neither investigated how NPWT impacts the overall wound geometry, nor were multilayer models considered to investigate how the layers of biological tissue interact, or how wound size affects the stress and strain in the wound.

This project aims to fill some of these gaps in our understanding of the biomechanics of the wound healing process by creating validated *in silico* and *in vitro* wound models. The overall goal is to provide tools that enable the investigation of how biomechanical forces dissipate through wounds and the surrounding tissues and provide physiologically representative physical wound models to allow novel medical devices and procedures to be tested *in vitro* and *in silico*. In addition, this project will study the changes in shape of wounds during biomechanical treatments such as NPWT.

The project will begin with a thorough review of literature before investigating the mechanical properties of silicones through tensile testing, outlined in Chapter 3. Statistical analysis will then be carried out to investigate how the mechanical properties of silicone change over time, and the materials which were the most mechanically similar to biological materials are selected to be used in an *in vitro* wound model, developed in Chapter 5. Whilst the *in vitro* model is being developed, an *in silico* equivalent will be created using Ansys (Ansys Inc, 2019). The *in vitro* model will be scanned using a MicroCT scanner to validate the *in silico* equivalent. The *in silico* model will then have the mechanical properties of biological tissues applied to provide a

macroscopic model of negative pressure wound healing. Further *in silico* models will be developed to investigate the impact of wound filler materials on a microscopic level.

The coronavirus pandemic caused challenges for this project as it prevented further development of the *in vitro* model due to the inability for this activity to be carried out remotely. The first lockdown occurred prior to the validation of the initial *in silico* model, leading to *in silico* model development being taken forward without validation as this could progress remotely.

## Chapter 2 Literature Review

This chapter introduces the general topic of wound care and reviews the previous research that is most relevant to the current project. It begins with an overview of the pathophysiology of the wound healing process then investigates the biomechanical properties of biological tissues. Following this, past and current developments in *in vivo*, *in vitro*, and *in silico* research of wound care and wound care devices are considered. This reveals where there are gaps in our knowledge and where there are needs and opportunities to expand understanding of this important subject.

### 2.1 Pathophysiology of Wound Healing

Wound healing is an essential response to injury and crucial for survival (Fang & Mustoe, 2008; Machado et al., 2011). Due to the complex functions and properties of the human skin, wound healing is a conglomerate of processes (Dąbrowska et al., 2016). It is generally accepted that there are three overlapping stages in the wound healing process; inflammation, proliferation, and maturation, although some literature identifies haemostasis, the formation of a clot and subsequent stopping of blood flow to an area, as a standalone process in its own right (Geris et al., 2009).

The first stage of wound healing, inflammation, occurs the moment trauma happens and, in an acute wound, lasts 1-2 days (Geris et al., 2009). Inflammation begins with the occurrence of haemostasis, when a fibrin clot is formed, stopping blood loss and providing a scaffold for subsequent stages of wound healing (Trøstrup et al., 2016). In a healthy human, this stage should only last a few hours (Geris et al., 2010). Whilst haemostasis is occurring, macrophages accumulate at the site, removing foreign bodies by phagocytosis and fighting infection (Trøstrup et al., 2016). This removal of foreign bodies also assists with the removal of bacteria from the wound and the overall prevention of infection (Geris et al., 2010). Assisting with the degradation of necrotic tissue are neutrophils and monocytes, which differentiate into phagocytes. Whilst this is occurring, growth factors and cytokines are released, triggering individual processes in each stage of wound healing. These hormones act as catalysts for the further stages of wound healing (Trøstrup et al., 2016).

Once inflammation is nearly complete, the proliferation stage of wound healing begins. There is a debate as to the length of this stage and when it begins, with some authors stating that it occurs on days 3-24 post-trauma, whereas others suggest that it occurs during

days 4-14 (Seaton et al., 2015; Trøstrup et al., 2016). What is agreed upon, however, is that during the proliferation stage, growth factors continue to be released and angiogenesis, the return of blood supply to the wound, occurs (Geris et al., 2010). New blood vessels form from existing vasculature, allowing granulation tissue to grow (Machado et al., 2011; Trøstrup et al., 2016). This granulation tissue formation and angiogenesis begins the creation of a provisional wound matrix and reepithelialisation of the wound bed (Fang & Mustoe, 2008). This is the result of fibroblasts, keratinocytes and endothelial cells working in conjunction with each other (Geris et al., 2010). The keratinocytes proliferate to form an endothelial layer, protecting the wound site from infection and further damage, whilst the fibroblasts begin the creation of collagen, the basis of the extracellular matrix. Although the reepithelialisation process can take a variable amount of time, it is of immense importance as it protects the wound site and re-establishes a protective outer shell (Fang & Mustoe, 2008). Figure 1 below shows the formation of granulation tissue in the wound bed.

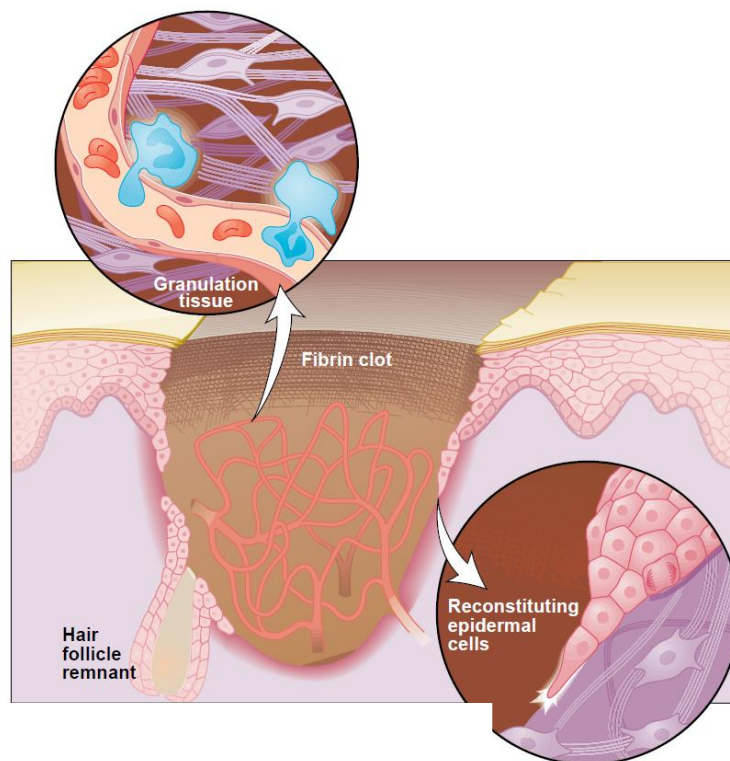


**Figure 1** A cartoon depiction of the key processes in the healing of an acute skin wound. Within the wound, a fibrin clot, pervaded by a combination of fibroblasts, granulation tissue and inflammatory cells is shown in more detail (Martin, 1997).

Also during proliferation, wound contraction begins. Fang & Mustoe (2008) define wound contraction as “the recruitment of surrounding unwounded tissue to decrease the size of an open wound”. Although there are several fields of thought as to the exact

mechanism of this process, Yang et al. (2013) suggest that “polarised coordinating fibroblast migration”, pulls the skin’s edges together, thus closing the wound.

The third and final phase of the wound healing process is the maturation phase. As with the inflammation stage, there is debate as to when it occurs with the majority of authors agreeing it takes place between 21 days and 2 years post trauma (Trøstrup et al., 2016). It is during this phase that tissue remodelling occurs. The main contributors during maturation are the fibroblasts. These fibroblasts differentiate into myofibroblasts, releasing  $\alpha$ -smooth muscle actin ( $\alpha$ -SMA) in the process (Seaton et al., 2015). In addition to this, fibroblasts improve the mechanical strength of the new tissue by rearranging the extracellular matrix (Geris et al., 2010).

### 2.1.1 Chronic Wounds

One of the largest wound-related issues currently facing healthcare services is the management of chronic wounds. These hard-to-heal wounds affect approximately 6.5 million people in the US alone, with a combined annual cost of \$28 billion (Seaton et al., 2015; Nussbaum et al., 2018). Wounds are classified as chronic if they remain in a prolonged inflammatory state, are slow- or non-healing, and last for weeks, months or years, even with appropriate care (Cukjati et al., 2000; Geris et al., 2010). Examples of chronic wounds include leg ulcers, pressure ulcers, diabetes-related ulceration, and surgical site infections (Frykberg & Banks, 2015). One of the main characteristics of chronic wounds is that they remain in a prolonged inflammatory state, thought to be, in part, due to the presence of a bacterial biofilm layer (Geris et al., 2010). Causative factors include diabetes, ischemia, prolonged external pressure and foreign bodies, amongst others. Although on their own these factors can cause chronic wounds, multiple factors working together can predispose a patient to getting a non-healing wound (Fang & Mustoe, 2008; Seaton et al., 2015).

The presence of hypoxia or ischemia, or a combination of the two, is a pre-requisite to the formation of chronic wounds (Geris et al., 2010). Hypoxia, reduced oxygen, stimulates an angiogenic response, however cells cannot function without oxygen, and this leads to fibroblasts, inflammatory cells and bacteria competing for oxygen in the wound. Unsurprisingly, ischemia, the transient impairment of blood flow, can also occur in chronic wounds. Ischemic wounds can be modelled using skin flap models (Trøstrup et al., 2016). Seaton et al. (2015) found that in porcine tests using this model, ischemic wounds had delayed macrophage response and impaired epithelialisation, evidence of both a non-healing wound and an impaired inflammatory response. In addition to this, impaired

angiogenesis was confirmed by the immunolocalisation of the von Willenbrand glycoprotein. It is similarly clear that ischemia impairs human wound healing (Lindblad, 2008).

One of the most common categories of chronic wounds is the pressure ulcer. In 2015, it was estimated that these affected 2.5 million patients per year in the United States (Seaton et al., 2015). It is believed that pressure exerted over a bony prominence is the primary cause, however many other factors contribute. Certain populations, such as the elderly or those who are bed bound, have higher susceptibility to pressure sores. Fang & Mustoe (2008) suggest that this may be due to a lower resistance to cutaneous ischemia-reperfusion.

Being the underlying cause of approximately 80% of non-traumatic lower-extremity amputations, diabetes-related wounds are also a significant problem for healthcare providers (Seaton et al., 2015). The lifetime risk of patients with *diabetes mellitus* developing a foot ulcer is approximately 15%, which, considering 7% of the UK population suffers from the condition, is a considerable burden on the budget and time of healthcare services (Diabetes UK, 2019). It is thought, in individuals with diabetes, angiogenesis deficiencies within the wound are a causative factor to the formation of diabetes-related chronic wounds (Fang & Mustoe, 2008).

#### **2.1.1.1 Venous Leg Ulcers**

One of the largest burdens on healthcare budgets in the developed world are leg ulcers, costing the NHS approximately £7706 per patient per annum (Phillips et al., 2020). When it is considered that ulcers have a duration of over one year for more than half of patients, and over 5 years for 34% of patients, the costs of treating one ulcer can amount to nearly £40,000. At any one time, between 1.5 and 3.0 in 1000 of the general population have an active or open ulcer, increasing to approximately 20 in 1000 of those over 80 years (Nelson & Adderley, 2016). Studies have shown that approximately 70% of leg ulcers are of venous origin, and recurrent in up to 70% of those at risk (Alavi et al., 2016). The treatment of this type of ulcer costs almost \$2.5 billion (£1.6 billion) in the US and accounts for 1% of the total annual healthcare budget in European countries (van Gent et al., 2010). But it is not only the costs of treatment that cause venous leg ulcers to have a large financial impact – in 2010, it was estimated that two million workdays were lost each year due to venous leg ulcers (van Gent et al., 2010).

The lower leg has a complex venous system, as shown in Figure 2, comprising of three components: the superficial, perforator and deep veins (Etufugh & Phillips, 2007). The

deep veins are high pressure systems, encased within the muscles of the lower leg. Overlapping these is a low-pressure system of superficial veins, lying overlying the fascia that covers the muscles. The superficial and deep venous systems are connected by perforator veins; allowing the blood to pass between them. Each venous system contains one-way valves, allowing blood to pass only towards the deep veins, preventing the backflow or reflux of blood, as seen in Figure 2. The deep venous system is compressed when the muscles of the lower leg contract during ambulation, forcing the blood to move toward the heart (Etufugh & Phillips, 2007). This action is referred to as the calf muscle pump.

An ulcer is defined as “a circumscribed inflamed lesion with complete loss of the epidermis and possible loss of part of the dermis and subcutaneous fat” (van Gent et al., 2010). Specifically, a venous ulcer is “an area of epidermal discontinuity that persists for four weeks or more as a result of venous hypertension and calf muscle pump insufficiency” (van Gent et al., 2010). They typically occur in the gaiter area of the lower leg, over the medial malleolus however, they can be found at more proximal points (Etufugh & Phillips, 2007; van Gent et al., 2010). The aetiology of an ulcer presenting outside of the gaiter area is unlikely to be venous in origin (Etufugh & Phillips, 2007).

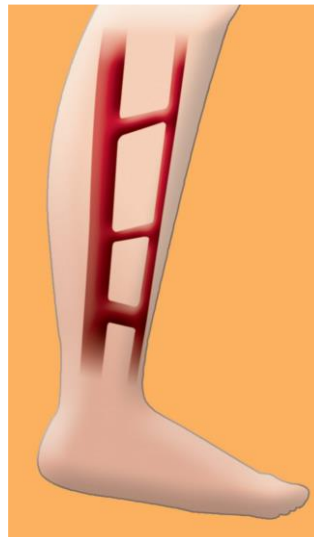


**Figure 2** A cartoon diagram showing the direction of flow of blood through the deep and superficial venous systems of the lower leg. It can be seen that a one way system is observed with the separate venous systems being connected by perforator veins (Anderson, 2006).

There are several conditions that may predispose a person to develop a venous leg ulcer, the most common being venous disease (van Gent et al., 2010). As the calf muscle pump is only active when contracting the muscles of the lower leg, a sedentary lifestyle is a risk factor for ulcer development. Other risk factors include being male, phlebitis, trauma to

the legs, congestive heart failure, obesity, and a family history of leg ulcers (Etufugh & Phillips, 2007). When the calf muscle pump is unable to force all the blood proximal to the heart, or the valves within the leg become damaged and unable to prevent the backflow of blood, the residual blood pools in the lower leg veins (Anderson, 2006). This pooling, in turn, stretches the walls of the veins, allowing fluid, red blood cells, and proteins to leak into the surrounding tissues, which subsequently become swollen with fluid and leak. A lymphoedema forms as the lymphatic system becomes unable to cope with the excess fluid, resulting in venous congestion and hypertension which starves the skin of nutrients. This puts the lower leg at increased risk of cellulitis and trauma which can result in the formation of a leg ulcer (Anderson, 2006).

During the development of the ulcer, before the skin becomes broken, a pitting oedema often develops (Grey et al., 2006). An open ulcer bed is often covered in a combination of granulation tissue and fibrinous exudate, however it is rare in venous ulcers for the tissue to turn necrotic (Etufugh & Phillips, 2007). Lipodermatosclerosis may also be present. This is related to venous insufficiency which causes the tissue surrounding the ulcer to become fibrous resulting in firm skin due to the loss of subcutaneous fatty tissue. This presents difficulties when modelling an ulcer as the biomechanical properties of lipodermatosclerotic tissue differ to that of unaffected tissue and the specific biomechanical properties of this are largely undocumented. Figure 3 shows the difference between a leg affected by lipodermatosclerosis (left) compared to an unaffected leg. The inverted champagne bottle shape can be clearly observed.



**Figure 3** A photograph of two legs. The patient's right leg is clearly affected by lipodermatosclerosis with the classic inverted champagne bottle appearance being observed (Etofugh & Phillips, 2007).

Although there are several ways to manage leg ulcers, the most common treatment is compression therapy which has been shown to aid healing (Etofugh & Phillips, 2007). The mechanism behind this is thought to be the compression facilitates venous return to the heart which improves lymphatic drainage and venous pump function whilst subsequently reducing venous hypertension. As the local hydrostatic pressure is increased and the superficial venous pressure is reduced, the oedema improves. An alternative method of reducing oedema is leg elevation. However, this method is often not practical as it requires the patient to spend long periods of time with their legs elevated, negatively impacting on their quality of life.

Graded compression can be used to increase the hydrostatic pressure in the limb and to reduce the pressure in the superficial venous system. The greatest pressure, approximately 40 mmHg, is applied at the ankle. This gradually reduces to a pressure of 18mmHg approximately just below the knee (Grey et al., 2006). It is thought that compression systems which are multi-component are more effective than single component systems (van Gent et al., 2010). There are a multitude of different types of wound dressings available to those with venous leg ulcers including hydrocolloids, foams, alginates, hydrogels, antimicrobials, gauze, and films; however no single wound dressing has been shown to be superior to another.

### 2.1.2 Negative Pressure Wound Therapy

The mechanism of action for negative pressure wound therapy is not yet fully understood, but there are a number of theories as to why it is effective, some of which are included in Figure 4. There are two principal ideas. The first is the removal of exudate from the wound (Webb & Pape, 2008). When NPWT is applied, the negative pressure removes any exudate from the wound base via suction, subsequently significantly reducing the likelihood of infection (Hasan et al., 2015). This removal also increases the blood flow to the area which subsequently increases angiogenesis, encouraging wound repair.

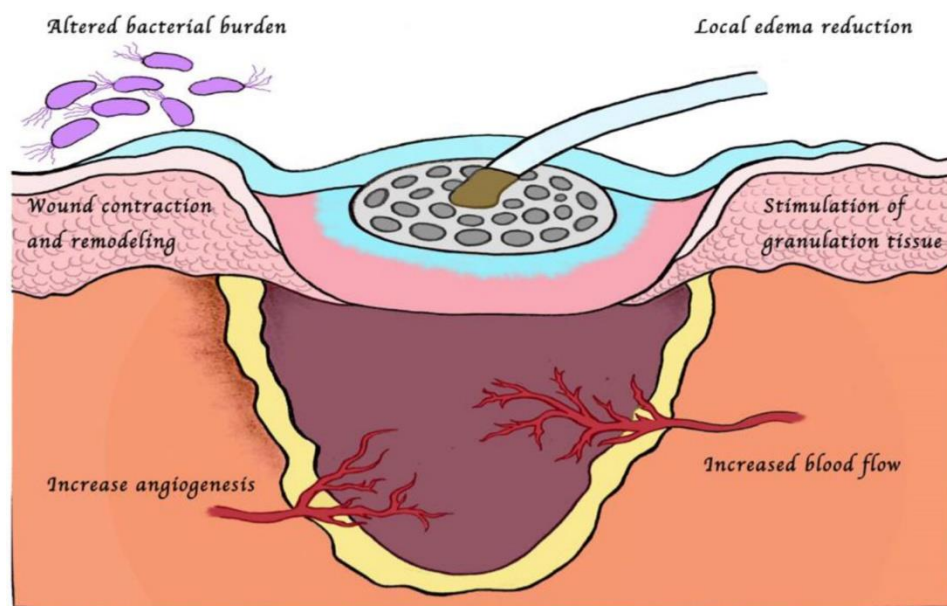


**Figure 4** A schematic illustration demonstrating some of the hypothesised mechanisms of action for negative pressure wound therapy including oedema reduction and remodelling (Hasan et al., 2015).

The second mechanism that researchers suggest increases wound healing is the induction of macrodeformation, caused by the collapse of pores and the compressive forces exerted on the wound surface by the foam. The NPWT causes wound shrinkage, pulling the edges of the wound closer together so that the overall wound size reduces (Huang et al., 2014; Hasan et al., 2015).

NPWT traditionally utilises open cell polyurethane foam or a gauze as a wound filler during treatment. Applying negative pressure compresses this filler and leads to the development of contact stresses and microdeformations on the base of the wound. The term microdeformation describes the imprinting of the wound bed with the contours of the NPWT foam (Lalezari et al., 2017). Whilst this current project does not consider cellular-level activities in detail, it is important to note that this microdeformation is associated with the

expression of multiple proteins related to wound healing, including growth factors and collagen (Nie & Yue, 2016).

In addition to the release of these proteins, the cell deformation that occurs during NPWT is associated with a number of other key wound repair mechanisms. The negative pressure applied has been shown to upregulate extracellular matrix production in human fibroblasts, an important factor in wound repair (Nie & Yue, 2016). This, in addition to the negative pressure induced migration and proliferation of endothelial cells, results in the acceleration of the wound healing process. Mesenchymal stem cells (MSCs), a key part of bone repair and regeneration, have also been shown to be positively affected by NPWT (Zhang et al., 2010). Used intermittently, NPWT has been shown to induce the differentiation of MSCs to bone cells. This may be due to the inhibition of MSC proliferation and stress-associated cellular apoptosis likely caused by the molecular mechanisms associated with NPWT (Zhu et al., 2014). This initiates the differentiation of the MSCs into osteoblasts, thus increasing bone synthesis and subsequently osteogenesis (Nie & Yue, 2016). Short term NPWT treatment at a pressure of 125mmhg has been shown to have a positive effect on periosteum-derived MSCs and their differentiation to an osteogenic phenotype (Zhu et al., 2014).

Whilst it is generally accepted that the micro- and macro-deformations discussed in the previous paragraphs have a positive influence on granulation tissue growth, the stresses and strains across the tissue have not been commonly quantified. However, it has been observed that a negative pressure of 125mmhg is effective at increasing cell proliferation, with a study by Takei et al. (1997) finding keratinocytes exhibited a  $49.2 \pm 15.8\%$  increase in cell proliferation when subjected to cyclic strain of 150mmhg at a rate of 10 cycles/min.

## 2.2 Biomechanical Behaviour of Biological Tissues

Understanding the biomechanical behaviour of biological tissues is immensely important when investigating treatments for clinical conditions, and for the topic of this research. Palpation has been used as a diagnostic tool by medical professionals for centuries as pathologic changes resulting from medical conditions can alter the stiffness of the affected tissues (Glozman & Azhari, 2010). The complexity of biological materials makes it difficult to determine their biomechanical properties. In particular, the elastic modulus of soft tissue can vary by four orders of magnitude.

The ‘stiffness’ of tissue is generally assessed using Young’s modulus or shear modulus. The Young’s modulus, a simple measure of a material’s response to tensile or compressive stress, is of importance as a stiffer tissue will experiences less strain than a more flexible one. Whilst this convenient property is widely used to characterise, model and predict the mechanical response of tissues such as skin, cartilage, bones, and ligaments, they are not as useful when it comes to measuring tissues which do not have a simple response such as muscle and fat (Glozman & Azhari, 2010). For these tissues without a simple mechanical nature, there is no single parameter which can describe fully their elastic behaviour, and for these materials, the bulk modulus – defined as ‘material resistance to uniform compression’ – can provide a more meaningful single-parameter measure of behaviour.

When modelling biological tissues, material incompressibility is often assumed, i.e. the material’s Poisson’s ratio,  $\nu$ , approaches 0.5 (Glozman & Azhari, 2010). In this case, the shear modulus, defined in equation (1) approaches  $\frac{E}{3}$ .

$$G = \frac{E}{2(1 + \nu)}$$

(1)

### 2.2.1 Skin

The skin is the largest organ in the human body, accounting for approximately 15% of overall bodyweight with an average surface area of 1.8 m<sup>2</sup>. The main functions of this organ are to maintain homeostasis by acting as a protective barrier to the internal systems of the body and providing a method of temperature regulation by controlling sweating and perfusion rates (Dąbrowska et al., 2016; Benítez & Montáns, 2017). It is also responsible for the synthesis of vitamin D from the sun, improving bone strength, and the excretion of water and urea, amongst other substances.

There are three main types of human skin, glabrous, hairy and mucocutaneous (Benítez & Montáns, 2017). The thickest skin layer, glabrous, is found on the palms and soles with a thickness close to 4mm. Hairy skin covers the majority of the human body and typically varies between 1-2mm (Gould, 2018). The thinnest skin, with a thickness of approximately

1.5mm, is found around the natural orifices of the human body. This type of skin is known as mucocutaneous.

All three skin types consist of three layers: the epidermis, dermis and hypodermis, which is sometimes referred to as subcutaneous fatty tissue (Trøstrup et al., 2016). Although the exact structure of the skin varies depending on biological age, gender, race and physical health of the individual in addition to the type and location of the skin, all layers of the skin consist of an extracellular proteinic matrix (Held et al., 2015). This extracellular matrix is responsible for approximately 75% of the total weight of the skin and consists of three types of biomolecules structural proteins, specialised proteins and proteoglycans, as shown in Figure 5 (Benítez & Montáns, 2017).

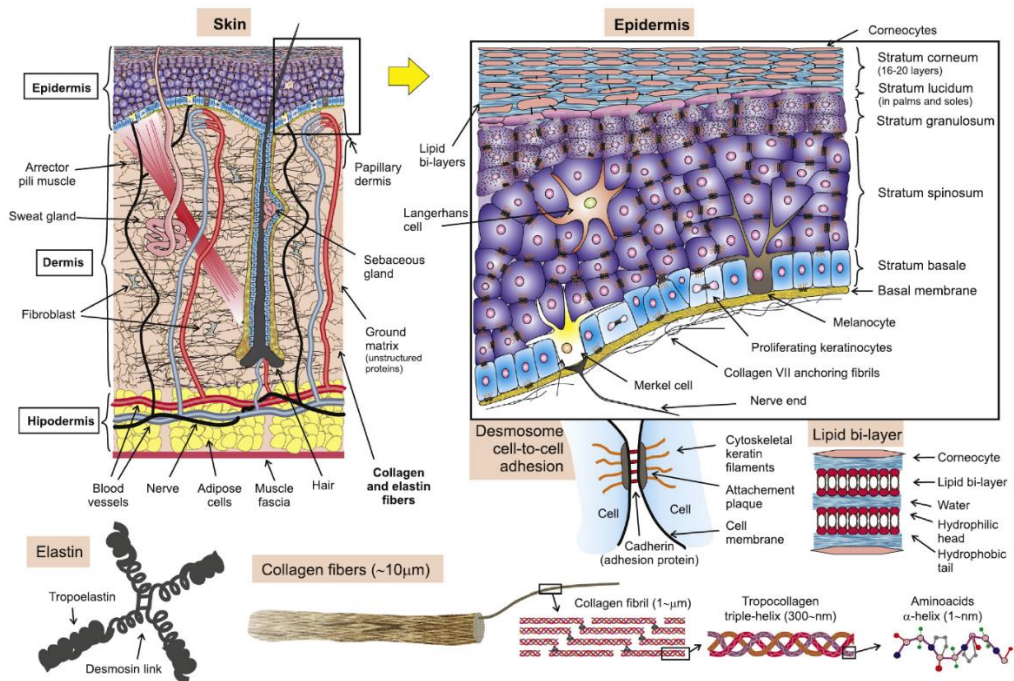


**Figure 5** A detailed diagram of the various structures of the skin (Benítez & Montáns, 2017).

The epidermis is a protective outer layer consisting of keratinocytes, with a typical thickness of 20-150µm (Buganza Tepole et al., 2012; Dąbrowska et al., 2016). These keratinocytes differentiate into corneocytes in the stratum basale, before migrating to the outer layer of the epidermis to form the stratum corneum which is approximately 14µm thick (Dąbrowska et al., 2016). The second layer of the skin, with a thickness of between 1mm and 4mm, is the dermis. This dermal layer consists of a complex web of collagen and keratin fibres to provide structural support and elasticity, giving the skin its mechanical strength and elastic

properties to the skin (Buganza Tepole et al., 2012; Corr & Hart, 2013). The third and final layer of skin is the hypodermis, also referred to as the subcutaneous fatty tissue and superficial fascia (Trøstrup et al., 2016). This tissue acts as a layer of insulation from heat and cold, whilst also protecting the vital organs and skeleton from mechanical shocks (Dąbrowska et al., 2016). By working in coalition, these layers of the skin provide protection, repair and adaptation, sensation and temperature regulation to the body.

Skin consists of inhomogeneous and anisotropic composite materials (Dąbrowska et al., 2016). This makes biomechanical testing key to understanding how the skin reacts under different conditions and for the development of wound treatment methods. Corr & Hart (2013) state that the skin's biomechanical properties are usually characterised by tensile failure, and while this is ideal for understanding the resistance to rupture of the skin, it does not provide detail as to the biomechanical response to normal daily function.

It has been shown that the material behaviour of skin is anisotropic, viscoelastic and time dependent (Corr & Hart, 2013). Dąbrowska et al. (2016) found that the position of the skin on the body, temperature, and the method used for measurement all influence the overall material properties. In addition, the biomechanical properties of skin are influenced and modified by many external factors. These factors include: ultraviolet light, trauma, mechanical and chemical strain, age, genetic predispositions, and diseases, in addition to lifestyle choices such as smoking and alcohol consumption (Held et al., 2015). When testing the biomechanical properties of skin, it is important to remember that the rate of strain application, and the time under strain, influence the properties recorded (Edwards & Marks, 1995). The properties of skin of particular interest are the strain and tensile properties, as these are experienced *in vivo* however, the deformation and flow are of immense importance when understanding how wound care modalities influence the wound healing process. Other properties that are of interest are the Young's modulus and breaking strength of tissue. The Young's modulus is of particular importance when modelling the biomechanical behaviour of wounds under treatment as it allows for the material properties of skin to be replicated.

The stress-strain relationship of skin needs to be expressed mathematically to enable researchers to calculate the Young's modulus. Lapeer et al. (2010) used *in vitro* experimentation to calculate how stress varies with strain in different skin samples, in order to enable the creation of a real-time haptic model for the simulation of plastic surgery.

### 2.2.2 Subcutaneous Adipose Tissue

Adipose tissue consists of a variety of cytotypes. The most common type of cell present are mature adipocytes, constituting one third of adipose tissue (Avram et al., 2005). The remaining two thirds consists of preadipocytes, nerve tissue, small blood vessels, and fibroblasts. Subcutaneous adipose tissue, of which there are two types, exists to some extent in all mammals. White adipose tissue consists of white adipocytes and has the primary function of storing excess energy as a lipid. This is then converted back into accessible energy at times of metabolic need and transferred to the tissues in need. On the other hand, brown adipose tissue accumulates lipids from food and converts it into heat energy (Avram et al., 2005).

Subcutaneous adipose tissue acts as a protective and insulating layer in the body. Its biomechanical properties provide shock absorption, protecting the internal organs and skeleton from impact damage. In addition to this, the subcutaneous fatty tissue insulates the body, assisting with homeostasis, and the maintenance of a constant body temperature.

### 2.2.3 Muscle

Skeletal muscle is attached to bones by tendons and facilitates the movement of the body. There has been significant research into the understanding of the biomechanical and neuromuscular properties of muscle as it has important applications in tissue engineering (Calvo et al., 2010; Hinds et al., 2011). Previous research has mostly focussed on the hyper-elastic material properties, however there have been studies looking at the time dependent response of muscular tissues (Wheatley et al., 2016). As with other biological tissues, skeletal muscle is a challenging material to define the mechanical properties of; however it can be characterised as highly non-linear, anisotropic, viscoelastic, and constant in volume (Böl et al., 2012).

The physiology of skeletal muscle is complex, consisting of approximately 70-80% water, 10% collagen and 3% fat (Vignos & Lefkowitz, 1959). Muscle displays anisotropic properties due, in part, to its fibrous networks of collagen, muscle fibres, and elastin embedded in an isotropic matrix (Calvo et al., 2010). The physiology of muscle tissue is shown in Figure 6. It can be seen that each muscle consists of fascicles containing individual bundles of fibres (Takaza et al., 2013). Morrow et al. (2010) hypothesised that skeletal muscle could be considered transversely isotropic with the plane of symmetry defined by the longitudinal axis.

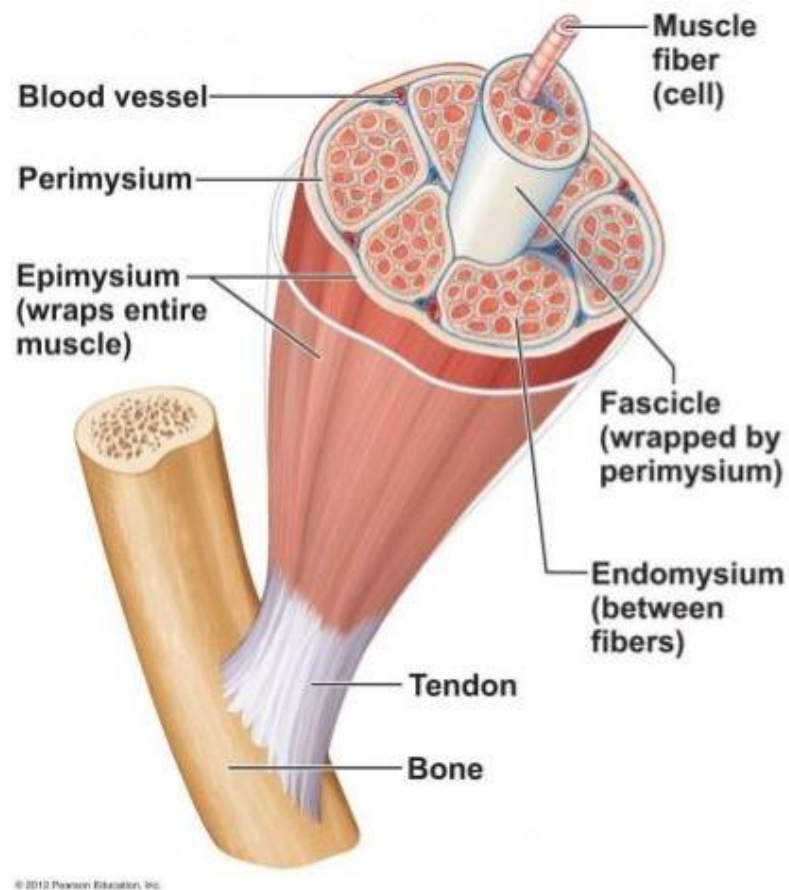


**Figure 6** A detailed diagram of the structures of skeletal muscle (Marieb & Keller, 2021).

There have been a variety of models of skeletal muscle tissue developed starting with the first mathematical model designed by Hill (1938). Some models focus on the microstructure of the muscle whereas others are phenomenological. For all models, the primary purpose of these models has been to characterise muscle contraction, with the muscle's material properties being central to all the models' success (Calvo et al., 2010; Morrow et al., 2010).

#### 2.2.4 Biomechanical Testing

Many testing methods and techniques can be used to measure the biomechanical properties of biological tissues. The most common are tensile testing, suction, traction and torsion testing, in addition to elastic wave propagation and optical coherence elastography (Zahouani et al., 2009; Annaidh et al., 2012).

One of the most common tests undertaken when characterising the mechanical properties of any material is the tensile test. This allows the Young's modulus, ultimate

tensile strength, strain energy and failure strain to be calculated. Tensile tests are performed by clamping, or gluing, two ends of a sample to a testing machine, and applying a tensile force to stretch the sample, thus subjecting it to tension. Edwards & Marks (1995) described two methods for carrying out this test. The first method involves applying strain to the sample in one large increment and with a minimal amount of time between zero and maximum strain. This allows researchers to investigate the stress relaxation of the sample. However, as biological tissues have non-linear properties, if a load is applied at too high a rate, the sample may rupture sooner than expected. An alternative to this method is the application of load in small increments or the slow loading of the skin. It has been demonstrated that using a strain rate of 5cm/min produces consistent and reproducible results (Edwards & Marks, 1995).



**Figure 7** An illustration of the experimental tensile testing set up used by Griffin et al. (2016). A sample of a synthetic biomaterial can be seen between the clamps.

As there are no international standards relating to the uniaxial stretching of skin, there is variation in the way researchers may carry out this testing. This, and the nature of sample creation for tensile testing, creates some challenges when comparing values gained. The skin is a composite material consisting of networks of fibrous proteins (Annaihd et al., 2012). This means that cutting the structures cause disruption and values gained by tensile testing are sample dependent. Soft tissues are soft in nature and therefore unable to provide a study structure. This leads to challenges defining the zero point as to where extension stretches the tissue rather than straightens it. This subsequently impacts the repeatability of skin tensile testing.

To combat these challenges, there are some basic principles that are used when carrying out the tensile testing of skin and other biological tissues. These are the use of an optical extensometer rather than using the movement of the clamps to measure movement. There are two main reasons for this. The first is that there is likely to be slippage at the clamps due to the nature of skin being soft and malleable. The second is that machine compliance influences the displacement of the specimen, leading to inaccuracies. To counteract this, soft grips are required in order to not compress the sample, however this can result in slippage.

On their own, uniaxial tensile tests do not provide enough information about the biomechanical properties of the skin for multidimensional material models (Annaihd et al., 2012). Non-linear regression analysis can be used to determine constitutive parameters; however, this can cause poorly conditioned equations, slow convergence rates, and non-unique solutions. One way of minimising this is to test the skin using planar biaxial tests and through-thickness shear tests. Tensile testing is often destructive, however it is thought of as the gold standard of mechanical characterisation (Wang & Larin, 2015). Particularly in the assessment of the biological tissues, the structural and functional properties of soft tissues are difficult to maintain. In addition to this, *in situ* and *in vivo* testing of the biomechanical properties is near impossible using a tensile testing method, both physically and due to ethical concerns.

A testing method which is becoming more prominent in the definition of the biomechanical properties of soft tissues is elastography. Developed in 1980, elastography is the non-invasive assessment of the biomechanical and rheological properties of human tissue using ultrasound (Wang & Larin, 2015). One of the benefits of using elastography is that, unlike traditional tensile testing, it is a non-destructive method. There are different types of elastography, one of the more recent developments is magnetic resonance elastography (MRE). This uses phase-constant magnetic resonance imaging (MRI) to measure mechanically induced acoustic waves in tissue. A more traditional method of elastography is ultrasound elastography. This method is used clinically in the detection of cancer and uses ultrasound to measure the dispersion of ultrasonic waves in the tissue (Wang & Larin, 2015).

### 2.2.5 Mechanical Properties of Biological Materials

Biological tissues are highly individual and their mechanical properties are influenced by a number of external factors including: biological age, race, physical health, and some lifestyle choices (Held et al., 2015). The high variability in values presents difficulty when it

comes to providing definitive values, as a result of which ranges of values are normally presented. In addition, a wide range of models and testing methods for biological tissues, specifically skin, means the values measured for Young's modulus can vary by a factor of up to 3000 (Diridollou et al., 2000). Many biological tissues have anisotropic hyper elastic properties, with the values dependent on the direction of testing.

The literature reports on how biological tissues have been tested both *in vivo* and *ex vivo*. As a result, multiple testing methods, including tensile testing, indentation and elastography have been used to investigate the mechanical properties of tissues. However, this project focuses on the lower leg, and unfortunately there is a sparsity of data for this area of the body, with the majority of literature focusing on abdominal data.

The skin provides a protective barrier to the internal organs and contributes to homeostasis by controlling sweating and perfusion rates (Dąbrowska et al., 2016). The skin's biomechanical properties are typically tested to tensile failure, and it has been shown that the anisotropy of skin is linked to the sample orientation in relation to the topological lines of skin tension; the most commonly used map of these contour lines of tension was devised by Karl Langer in 1861, referred to as Langer lines (Gallagher et al., 2012; Corr & Hart, 2013).

The thickness of skin tissue is highly variable across the body and dependent on skin type. Glabrous skin, the thickest type of skin is primarily found on the soles of the feet and palms of the hand and has a thickness of approximately 4mm. In comparison, mucocutaneous skin is the thinnest skin type, with an average thickness of 1.5mm and is found surrounding the natural orifices of the human body (Benítez & Montáns, 2017). The third type of skin, hairy skin, is found covering the majority of the body. This type of skin has a thickness between that of mucocutaneous and glabrous skin. A study by Annaidh et al. (2012) used 56 excised human skin samples from the back of seven corpses (3 male and 4 female; average age  $89 \pm 6$  years) and carried out uniaxial tensile testing. In addition, the thickness of the skin samples was measured using Vernier callipers following the careful removal of adipose tissue. It was found that the hairy skin on the back of the corpses had a mean thickness of  $2.56 \pm 0.39$  mm. Annaidh et al. (2012) continued by cutting the samples into a 'dog-bone' shaped specimen in accordance with ASTM D412 and using uniaxial tensile testing to determine the Young's modulus, which they found to be  $83.3 \pm 34.9$  MPa.

Gallagher et al. (2012) also used uniaxial tensile testing of samples from the backs of three elderly human cadavers, aged 77, 82 and 85 years. 11 samples, cut in accordance to

ASTM D412, were taken from each subject and grouped into categories with relation to the location and the orientation with respect to the Langer lines. These samples were tested at three speeds,  $1 \text{ ms}^{-1}$ ,  $1.5 \text{ ms}^{-1}$ , and  $2 \text{ ms}^{-1}$ . The first set of samples were tested to compare the influence of different testing speeds, with samples from the left side of the back being tested at  $1 \text{ ms}^{-1}$ , and samples from the right side of the back were tested at  $2 \text{ ms}^{-1}$ . The final set of samples were then all tested at  $1.5 \text{ ms}^{-1}$ . From this testing, the mean Young's modulus was found to be  $98.91 \pm 97 \text{ MPa}$ , the large range due to the variability in samples.

A study by Ottenio et al. (2015) used a similar methodology. Thirty-three samples were excised from a fresh cadaver before being tested at three strain rates:  $0.06 \text{ s}^{-1}$ ,  $53 \text{ s}^{-1}$ , and  $167 \text{ s}^{-1}$ . It was found that the orientation of the samples in relation to Langer lines had a strong influence on the ultimate tensile stress and Young's modulus, with a value of  $160 \pm 53.2 \text{ MPa}$  parallel to Langer lines, and  $70.6 \pm 59.5 \text{ MPa}$  with perpendicular.

Whilst tensile testing of biological tissues allows for easy comparison between their biomechanical values and those of other testing methods, excised samples taken post mortem are often affected by *rigor mortis* meaning results are often inevitably stiffer, dependent on storage techniques, than *in vivo* testing (Van Ee et al., 2000). One method of testing *in vivo* is suction. This involves the use of a suction chamber and ultrasound device to measure the vertical displacement of the skin's surface, and its thickness (Diridollou et al., 2000). Using this method, Diridollou et al. (2000) tested the skin of the forearm of 10 males aged between 20 and 30 years. It was found that the mean value for Young's modulus of the skin is  $129 \pm 88 \text{ kPa}$  – significantly lower than those values found *ex vivo*.

Another *in vivo* study was conducted by Hendriks et al. (2003). This was also conducted using a suction method on the forearm of male young adults. A model using a Mooney-Rivlin hyper elastic formula was then created, where the standard Mooney-Rivlin material behaviour equation is:

$$W = C_{10}(I_1 - 3) + C_{11}(I_1 - 3)(I_2 - 3) \tag{2}$$

From this,  $C_{10}$  can be converted into Young's modulus using the formula

$$E = 6C_{10} \tag{3}$$

which was found to be  $56.4 \pm 21.6$  kPa, and within the range given by (Diridollou et al., 2000).

Khatyr et al. (2004) also studied the viscoelastic behaviour of skin *in vivo*, focussing on the anisotropy of the tissue. A single-axis extension test was used, applying forces in four directions across the skin with a maximum force of 4N. The tests were carried out on the forearm of 63 participants of different ages. It was found that the average Young's modulus found in a direction close to the longitudinal axis of the forearm was 657 kPa, with a value of 130 kPa perpendicular to the axis of the arm.

A study by Agache et al. (1980) used torsion applied to *in vivo* dermis tissue to study the mechanical properties of the skin in 138 individuals between 3 and 89 years of age. A reduced elasticity was found in the skin of participants over 30 years old, however the viscoelasticity of the skin increased. This study did not specify the region of the body the samples were taken from, but it was found that the Young's modulus of participants aged between 3 and 30 years was 420 kPa whereas the participants aged between 31 and 89 years had a Young's modulus of 850 kPa. As chronic wounds are more likely to develop in elder patients, the value of Young's modulus between 31 and 89 years has the potential to be more useful for this project.

Oltulu et al. (2018) used 180 skin samples from six major body regions to measure the thickness of the epidermis, dermis and total skin thickness. These samples came from 90 male and 90 female subjects aged between 30 and 40 years from a pathology archive. The samples were examined using a light microscope, with microphotographs of the samples then taken. The computer software, Pixera, was then used to digitally calculate the thicknesses of the epidermal and dermal layers of skin. It was found that the total skin thickness ranged between  $2.284 \pm 1.407$  mm to  $6.0524 \pm 2.4354$  mm.

A study by Alkhoul et al. (2013) used a custom built one dimensional tensile testing apparatus to find the initial and final elastic moduli of samples of subcutaneous adipose tissue to be  $1.6 \pm 0.8$  kPa and  $11.7 \pm 6.4$  kPa respectively. In this investigation, hydrated specimens had their dimensions measured using a micrometer screw gauge before being attached to tensile testing apparatus using a small quantity of high-viscosity superglue gel. Following this, the initial sample length was measured, and the tensile testing could begin.

Glozman & Azhari (2010) measured the elastic, shear and bulk moduli of porcine fat, in addition to recording the Poisson's ratio using combined ultrasound computed

tomography with elastography. It was found that porcine adipose tissue has a Young's modulus of  $140 \pm 86.2$  kPa, a shear modulus of  $46.7 \pm 28.7$  kPa, a bulk modulus of  $2.25 \pm 0.01$  GPa and a Poisson's ratio of  $0.49 \pm 5 \times 10^{-6}$ . In addition to this, Nachman & Franklin (2016) gave values of the elastic modulus for subcutaneous adipose tissue as 2.0 kPa with the thickness of the layer being 0.8 mm. As the Young's modulus has been shown to vary drastically with the thickness of the fatty tissue, it is important to ensure the model depth is comparable with that of the tissue being modelled.

Figure 8 illustrates the complexities in the stresses and strains of skin samples obtained from the abdomen of healthy adult volunteers. The non-linear and variable nature of these relationships present challenges in determining the Young's modulus of such materials, as the value fluctuates with stress levels. It is important to highlight that within the expected range of strains experienced by wounds during Negative Pressure Wound Therapy (NPWT), biological tissues exhibit near-linear behaviour. While Figure 8 exhibits non-linear trends at higher strain values, there is significant variation in Young's modulus within the NPWT range. The characterization of skin is complicated by the significant influence of strain rates on calculated Young's modulus. Due to the absence of a standard strain rate, different studies employ diverse approaches in conducting tensile tests on skin samples.

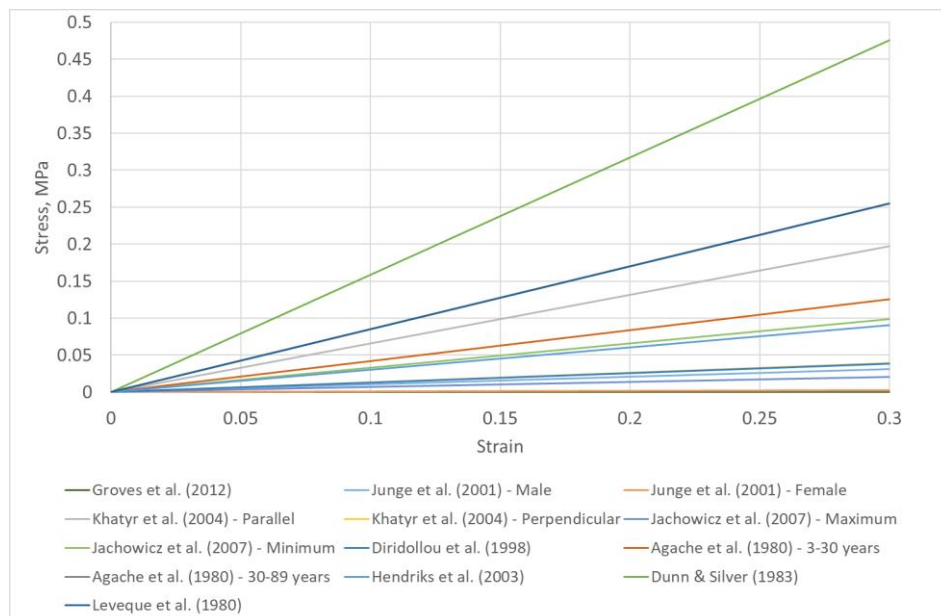


**Figure 8** A graph showing the stress-strain relationship for skin using values found in literature. A large variation in results can be seen.

The structure of subcutaneous adipose tissue is similar to that of a fluid filled foam, with the viscosity of the lipid low enough for it to behave like an incompressible inviscid fluid (Comley & Fleck, 2010). This causes some difficulties when investigating the biomechanical properties of this type of tissue, leading to a distinct paucity in data. Alkhouli et al. (2013) conducted tensile testing of subcutaneous adipose tissue using non-linear microscopy and a one-dimensional custom built tensile testing apparatus. Hydrated tissue samples were superglued to paddles at each end and tested to 30% strain at a strain rate of  $5\mu\text{ms}^{-1}$ . From this, it was found that the Young's modulus of fatty tissue at a strain of 30% was  $11.7 \pm 6.4$  kPa, significantly lower than the values found for skin.

The main purposes of subcutaneous adipose tissue are to store energy, to provide insulation and to protect vital organs. Due to its primary role as an energy store, people who lead a largely sedentary lifestyle often have larger energy stores and therefore a thicker subcutaneous fatty tissue than those who follow a healthy diet and an active lifestyle. Therefore the thickness of this layer is highly variable and unique to each individual. Ishida et al. (1997) studied 80 moderately active Caucasian female participants (36 aged 18-29 years; 44 aged 45-64 years). Using a brightness-mode ultrasound apparatus, the study determined the subcutaneous fat thickness for 13 sites across the body. The study also investigated the muscle thickness at 9 sites. Sites of particular interest for the modelling of chronic ulceration are the medial and posterior calf in middle-aged participants. It was found that the mean thickness of subcutaneous fatty tissue in the medial calf was found to be  $9.91 \pm 3.58$  mm. The posterior calf had a layer of fatty tissue that was less thick than that found in the medial calf at  $6.77 \pm 2.52$  mm.

In addition to the investigation into subcutaneous adipose tissue thickness, Ishida et al. (1997) also investigated the thickness of muscle tissue. Of particular interest for the development of a biomechanically similar chronic wound model is the thickness of muscle tissue on the posterior calf. Ishida et al. (1997) found this value to be  $57.61 \pm 5.72$  mm in women aged 45-64 years.

Muscle is an anisotropic biological material consisting of fibres that run along its length. Morrow et al. (2010) investigated the mechanical properties of muscle using 18 extensor digitorum longus muscles from 9 New Zealand white rabbits. These muscle samples were tested under both longitudinal extension and transverse extension. From this, a linearised Young's modulus was calculated and found to be  $447 \pm 97.7$  kPa along the length of the muscle, and  $22.4 \pm 14.7$  kPa in the transverse direction.

Ultrasound shear-wave imaging was used by Shinohara et al. (2010) to visualise the muscle stiffness distribution during muscle contraction. This study used one healthy subject (male, 42 years) in varying positions. The stiffness of the muscle varied with the position of the participant. The study focused on the effect of these positions on the medial gastrocnemius muscle specifically. During quiet standing, it was found that the Young's modulus of this muscle was  $111.2 \pm 5.0$  kPa, whereas when the muscle was at rest, the medial gastrocnemius had a Young's modulus of  $16.5 \pm 1.0$  kPa.

There have been many previous studies looking at defining the biomechanical properties of muscular tissue, primarily utilising rodent models and tensile testing. Calvo et al. (2010) removed the *tibialis anterior* muscle from 10 female Wistar rats before using an INSTRON 5548 micro tester to perform uniaxial tensile tests with a 5N load cell. The testing velocity used was  $0.2L/100 \text{ mm min}^{-1}$  where 0.2 was the deformation rate and L is the initial sample length. In addition, a displacement test was performed at  $5 \text{ mm min}^{-1}$ . The results gained in this experiment can be seen in Figure 9. It was found that the muscle demonstrates non-linear stress-stretch properties, and that the experimental data differed slightly from the parameterised calculations.

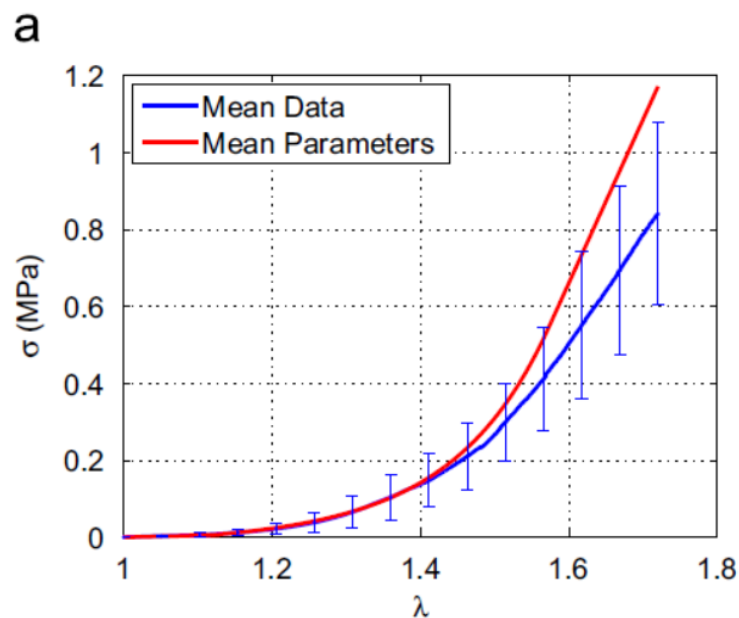


**Figure 9** A graph presenting the stress-stretch relationship of Calvo et al. (2010)'s experimental data. This data was gained from the tensile testing of rat *tibialis anterior* muscle.

Takaza et al. (2013) investigated the Poisson's ratio of porcine *Longissimus Dorsi* skeletal muscle; harvesting samples from 5 3 month old female pigs. These samples were measured to be approximately 10 mm thick and 10 mm wide, as required for ASTM E8/E8M tensile testing. Exact dimensional specifications were not possible due to the mobile nature of freshly harvested biological tissue. The variability in the sample length was considered by adjusting the testing speed to maintain a constant strain rate of  $0.05\% \text{ s}^{-1}$ . Takaza et al. (2013) also investigated the effect of the fibre orientation on the mechanical properties of the tissue samples, taking samples at: the fibre direction, perpendicular to the muscle fibres (cross-fibre),  $45^\circ$  to the fibre direction,  $60^\circ$  to the fibre direction, and  $30^\circ$  to the fibre orientation. It was found that the cross-fibre orientation demonstrated primarily linear mechanical properties and was the stiffest with failure occurring at a low stretch value, approximately  $\lambda = 1.15$ . In the longitudinal direction, the stress-stretch relationship was non-linear and significantly less stiff than that in the cross-fibre orientation. Failure for this orientation occurred at approximately  $\lambda = 1.65$ . In the cross-fibre direction, the Poisson's ratio of muscle tissue was calculated by Takaza et al. (2013) as being 0.28.

As muscle tissue has anisotropic mechanical properties, it is important to consider it as a three dimensional material when modelling it. Morrow et al. (2010) used *extensor digitorum longus* muscles from New Zealand White rabbits to test under three conditions: longitudinal shear, transverse extension, and longitudinal extension. From these results, the ultimate stress, failure strain, and linear modulus were calculated. It was found that the linear modulus of muscle was  $447 \pm 97.7$  kPa when subjected to longitudinal extension,  $22.4 \pm 14.7$  kPa under transverse extension, and  $3.87 \pm 3.39$  kPa for longitudinal shear forces. This demonstrates the anisotropy of skeletal muscle and highlights the need for muscle models to have anisotropic material properties.

This preliminary research on soft tissue properties provides a basis to guide the selection of silicones with properties akin to those of skin, subcutaneous fat and muscle, from which a silicone-based physical wound model for the testing of novel wound care devices can be developed.

Table 1 summarises the material properties of biological tissues found during a review of literature.

**Table 1** Sample tissue thicknesses and Young's modulus values for the different tissues.

Reference	Area of the Body <sup>1</sup>	Skin		Subcutaneous Fatty Tissue		Muscle	
		Thickness	Young's Modulus	Thickness	Young's Modulus	Thickness	Young's Modulus
<b>Agache et al. (1980)</b>			420 kPa (Age 3-30 yrs) 850 kPa (Age 30-89 yrs)				
<b>Alkhouli et al. (2013)</b>	Abdomen ( <i>ex vivo</i> )				11.7 ± 6.4 kPa		
<b>Diridollou et al. (2000)</b>	Forearm ( <i>in vivo</i> )		129 ± 88 kPa				
<b>Gallagher et al. (2012)</b>	Back ( <i>ex vivo</i> )		98.97 ± 97 MPa				
<b>Hendriks et al. (2003)</b>	Forearm ( <i>in vivo</i> )		56.4 ± 21.6 kPa				
<b>Jachowicz et al. (2007)</b>	Forearm Face ( <i>in vivo</i> )		70 – 330 kPa				
<b>Khatyr et al. (2004)</b>	Forearm ( <i>in vivo</i> )		E <sub>parallel</sub> = 657 kPa E <sub>perpendicular</sub> = 130 kPa				
<b>Lacourpaille et al. (2012)</b>	Gastrocnemius ( <i>in vivo</i> )						7.774 ± 1.82 kPa <sup>2</sup>
<b>Linder-Ganz et al. (2007)</b>	Buttock ( <i>in vivo</i> )			13 ± 8 mm		20 ± 7 mm	

<b>Morrow et al. (2010)</b>	Rabbit – <i>Extensor Digitorum Longus</i> ( <i>ex vivo</i> )				$E_{\text{Parallel}} = 44.7 \pm 97.7 \text{ kPa}$ $E_{\text{Transverse}} = 22.4 \pm 14.7 \text{ kPa}$
<b>Annaidh et al. (2012)</b>	Back ( <i>ex vivo</i> )	$2.56 \pm 0.3^9 \text{ mm}$	$83.3 \pm 34.9 \text{ MPa}$		
<b>Oltulu et al. (2018)</b>	( <i>ex vivo</i> )	$2.284 \pm 1.407 \text{ mm}$ $- 6.0524 \pm 2.435 \text{ mm}$			
<b>Ottenio et al. (2015)</b>	Back ( <i>ex vivo</i> )		$E_{\text{Parallel}} = 160 \pm 53.2 \text{ MPa}$ $E_{\text{Perpendicular}} = 70.6 \pm 59.5 \text{ MPa}$		
<b>Shinohara et al. (2010)</b>	Gastrocnemius ( <i>in vivo</i> )				$E_{\text{Relaxed}} = 40.6 \text{ kPa}$ $E_{\text{Contraction}} = 258 \text{ kPa}$
<b>Wu et al. (2007)</b>	Pig paw ( <i>ex vivo</i> )	$2.5 \pm 0.6 \text{ mm}$		$2.46 \pm 1.4 \text{ mm}$	
<b>Zahouani et al. (2009)</b>	Forearm ( <i>in vivo</i> )		$8.3 \pm 2.1 \text{ kPa}$		

<sup>1</sup> human samples unless specified otherwise

<sup>2</sup> converted from Shear Modulus with the assumption  $\nu = 0.3$

## 2.3 Wound Modelling – *in vivo*, *in vitro* and *in silico* approaches

At present, the key method for furthering our understanding of the wound healing process and developing wound treatment devices, is *in vivo* modelling. It is critical as it allows medical device developers and healthcare professionals to gain a greater understanding of how devices or treatments interact with the body, but clearly it is essential that *in vivo* models have a similar immunological response and tissue characteristics to humans (Seaton et al., 2015).

Thus, whilst the perfect *in vivo* model would always be human, there is currently great difficulty in getting a phenotypically similar human population large enough to produce reliable results. In wound care in particular, suitable human models for chronic wounds are difficult to obtain, therefore acute wounds currently provide the most insight into the wound healing process (Ud-Din & Bayat, 2017). However, research into wound healing using human models is problematic. The ethics surrounding the removal of numerous biopsies of a human wound during the healing process are complicated as it is painful for the subject and may cause scarring (Seaton et al., 2015).

### 2.3.1 In Vivo Modelling

Due to the difficulties in using human volunteers for *in vivo* modelling of chronic and acute wounds, alternatives are required. Animal models have been widely utilised as a tool for investigating the *in vivo* reactions of medical products in the body and have become indispensable when furthering understanding of the wound healing process. However, it is widely accepted that there is currently no ideal animal model of human wound healing (Fang & Mustoe, 2008; Trøstrup et al., 2016; Ud-Din & Bayat, 2017). This is in large part due to the difficulty in finding an animal with a similar skin structure and immune response to that of humans and which can be easily housed and cared for (Perez & Davis, 2008). Many animals, particularly rodents, have their skin attached to the *panniculus carnosus*, a muscle humans do not have (Seaton et al., 2015). This changes the wound healing mechanism to be one where wound healing is primarily by muscular contraction, different to the wound healing process for humans (Lindblad, 2008).

One limitation of using animal models to replicate chronic wounds is that some animal models are only able to display partial thickness wounds (i.e. where the wound is superficial and only involves the top two skin layers, the epidermis and dermis), whereas most human chronic wounds are full thickness (Trøstrup et al., 2016). In addition, there are many potential issues associated with the use of animal models. These include ethical and

moral difficulties in addition to the associated costs of keeping larger animals (Ud-Din & Bayat, 2017). The use of animal specimens for *in vivo* modelling is highly regulated by governing bodies, with many governments publishing guidelines on how to ensure good practice. In an ideal world, there would be alternatives to *in vivo* modelling that allow all testing to be done *in vitro* or *in silico* with minimal *in vivo* participation. However, this is not currently possible. In order to improve the welfare of animals being used for such experiments, the “three Rs” of animal testing have been developed (Fenwick et al., 2009). These are a set of ethical guidelines adopted by many governments worldwide, aimed at *reducing, refining and replacing* the use of animals in science (Ansell et al., 2012). When the use of animal models is unavoidable, minimising animal discomfort must be a priority and, where possible, reagents should be tested *in vitro* first (Seaton et al., 2015).

### **2.3.1.1 Rodent Models**

By far the most common *in vivo* model for understanding the wound healing process is the rodent model. Their rapidly healing wounds and relatively easy care make them the model of choice for many researchers (Lindblad, 2008; Perez & Davis, 2008; Seaton et al., 2015). Skin contraction due to the *panniculus carnosus* muscle (attached to the skin) leads to the rapid healing of excisional wounds and minimises complications such as infections, meaning experimentation lasts for days rather than weeks or months as it would in human subjects (Lindblad, 2008; Perez & Davis, 2008). Although some wound contraction occurs in humans, it is not the primary method of wound healing and occurs on a much smaller scale (Fang & Mustoe, 2008). This is particularly true in the lower extremities where the majority of chronic wounds occur. The popularity of the rodent model means that there are already many experimental reagents available to the researcher (Seaton et al., 2015). In addition to this, the ease of genetic modification in small rodents means that knock out and transgenic breeds are readily available for use (Perez & Davis, 2008; Seaton et al., 2015).

Since rodents are small, their care is relatively inexpensive and they do not require a large space to be housed (Perez & Davis, 2008; Seaton et al., 2015). In addition, small mammals often have multiple offspring and short gestation periods, allowing experiments to use several generations (Perez & Davis, 2008). This is particularly important when genetic modification is required, providing models capable of exhibiting conditions such as diabetes and obesity. However, due to their size, the number of wounds that can be investigated when using rodent models is limited, as seen in Figure 10. Thus their small size means that a greater number of animals are required to study the same number of wounds

when compared to a larger model. This, in combination with their ability to participate in experiments where the end result is death, raises several ethical issues (Perez & Davis, 2008).

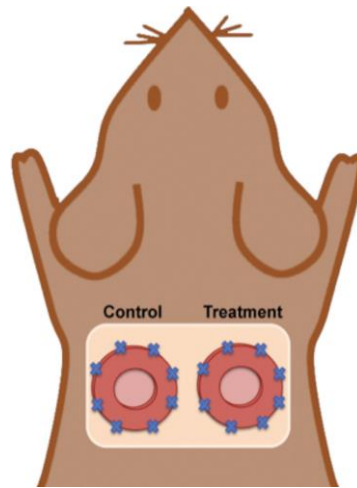


**Figure 10** Schematic illustration showing the position of two full thickness wounds on a murine model of wound healing. Silicone splints (the red doughnuts) can be seen preventing healing by wound contraction (Dunn et al., 2013).

Overall, whilst there are many similarities between the wound healing processes when comparing the physiology of rodent skin to that of humans, there are also several key differences. The main criticism of rodent models of wound healing is the thin dermal and epidermal layer, consisting of only a few layers of cells with empty hair follicles (Fang & Mustoe, 2008; Perez & Davis, 2008). In addition, small mammals have a tendency to be covered in loose, dense fur meaning their hair growth cycle is different to that of humans, and the hair follicles and epidermal appendage density differ from that of humans (Perez & Davis, 2008). Their fur and 'loose' skin can also create difficulties when attaching treatments to the model.

There are many rodent models available to the researcher, the most common being the rat (*Rattus Norvegicus*). As with the majority of rodent models, the rat is cost effective and easy to keep. Many transgenic strains are available due to the rat model being extensively used for wound healing studies (Lindblad, 2008). The rat's close physiology to humans often makes it the model of choice for researchers, however there are few immunological evaluation tools available (Trøstrup et al., 2016).

Another common rodent used for modelling wound healing is the mouse (*Mus Musculus*). Incisional, excisional and diabetic wounds are able to be modelled on mice. They

are also frequently used in burn models, but they are only able to tolerate approximately 30% burns (Seaton et al., 2015), and the immunological response to burns in mice is not the same as in humans; the hypermetabolic response seen after human burns is not observed in mice (Pereira & Herndon, 2005; Abdullahi et al., 2014). Thus the use of mice as models for wound healing has many limitations when compared to humans, the first being the notable difference in adaptive and innate immune systems (Seaton et al., 2015). This, in addition to the difference in the primary wound healing mechanism and their small size, creates limitations associated with wound healing studies in this species (Fang & Mustoe, 2008). There is also difficulty in creating partial thickness wounds in mice as their epidermis is just 50µm thick (Seaton et al., 2015). However, as mice are widely used, the mouse genome is fully sequenced and whole genome microarrays are available, increasing the potential for the mouse as an animal model. Fang & Mustoe (2008) describe the mouse as a 'well-balanced animal model for studying wound healing' dependent on the wound model and experimental design being optimised.

Rats and mice are not the only rodent models available to wound researchers – rabbits (*Oryctolagus*) and guinea pigs (*Cavia Porcellus*) are also used. These animals have a closer physiology to humans when studying different types of wounds. In particular, the hairless guinea pig has skin physiologically close to that of humans, and meets limitations in terms of immunological response (Trøstrup et al., 2016). Rabbit ear models are also commonly used to investigate vascularisation and angiogenesis (Perez & Davis, 2008). Unlike other rodent models, the skin of the rabbit's ear is attached to cartilage, allowing it to act as a splint and subsequently minimising contraction in excisional wounds (Fang & Mustoe, 2008). The dermal ulcer model of the rabbit ear is a strong model for studying reepithelialisation and granulation tissue formation in excisional wounds. The close physiology of the rabbit to humans is a major positive when choosing a model for wound healing, however as a less popular model, there are fewer immunological evaluation tools at the researcher's disposal (Trøstrup et al., 2016).

### **2.3.1.2 Porcine Models**

An alternative to using rodent wound models is the porcine model, which is used extensively for wound healing studies due to the similar physiology of pig skin when compared to that of humans (Lindblad, 2008). As with human wounds, porcine models show wound healing primarily by granulation tissue growth with a degree of wound contraction (Fang & Mustoe, 2008; Lindblad, 2008). The larger size of the pig in comparison to rodent models means that

fewer animals are required to produce statistically significant data (Lindblad, 2008). This allows multiple wounds to be placed on one animal; enabling a single pig to have a large number of identical wounds. Figure 11 shows the number of wounds possible on a standard porcine model.

Whilst porcine models are physiologically similar to humans, they are not widely used for modelling wounds (Seaton et al., 2015). They are substantially more difficult to house and feed, requiring much more space than a rodent model (Trøstrup et al., 2016). In addition, unlike rodent models, porcine models require specialist expertise, including a skilled vet to administer anaesthetic (Seaton et al., 2015). A specific surgical operating facility

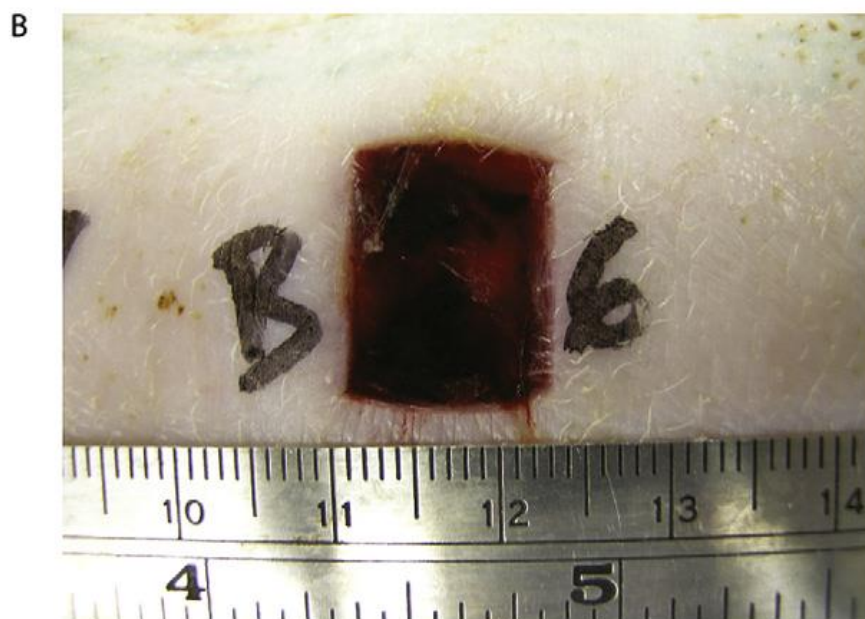
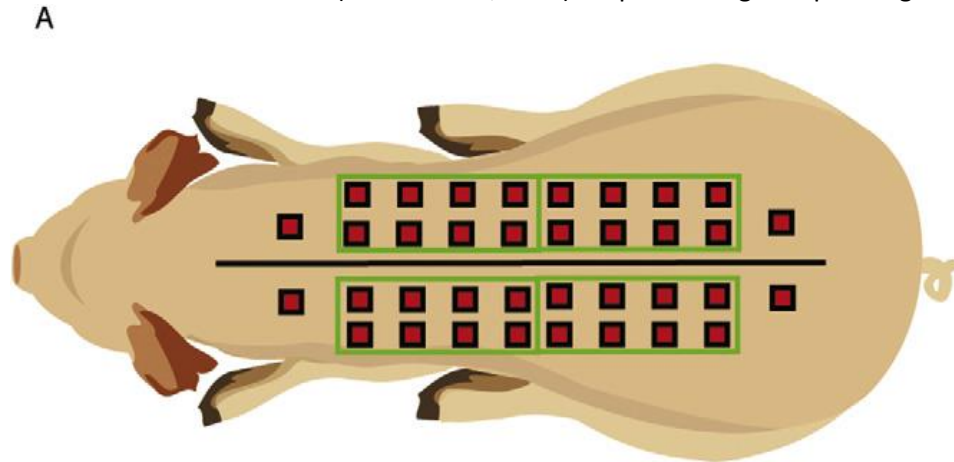


**Figure 11** (a) A schematic showing the distribution of wounds on the back of a porcine wound model. (b) A photograph showing a porcine wound 3 days after wound creation (Hadad et al., 2010).

is also needed, with sterile conditions due to their size (Lindblad, 2008). Despite of these complications, expertise and facilities for the appropriate care and handling exist in a number of research centres.

The physiology of porcine skin has many similar qualities to that of humans (Perez & Davis, 2008; Trøstrup et al., 2016). Seaton et al. (2015) found that the results found in porcine models are similar to those in human studies. Porcine skin has similar attachment to underlying structures to that of human skin and, unlike rodent models, pig skin does not have fur, instead having individual coarse hairs (Trøstrup et al., 2016). A similar epidermal and dermal thickness is also found when comparing porcine skin to that of humans, however, Fang & Mustoe (2008) found that pig skin has an overall thickness greater than that of human skin, likely to be due to differences in the subcutaneous adipose tissue thickness. Another advantage of using a porcine model is that the dermal collagen and elastic content is more similar to that of humans than other commonly used mammals, and the biochemical structure of porcine collagen is similar to that of humans. Porcine epidermis also has similar patterns of blood vessels and hair follicles to humans and a 'turnover time', the time taken for the top layer of skin to fully regenerate, of approximately 30 days, the same as that of humans (Seaton et al., 2015). In addition to the many similarities in the physical properties of porcine models to human models, there are also many immunological similarities because porcine immune cells are very similar to those in human skin. There are also similarities in the responses to growth factors, both physical and molecular (Perez & Davis, 2008).

Despite the many similarities between human and porcine models, there are several key differences. The first of these is that the dermis is less vascular in porcine models than it is in humans (Trøstrup et al., 2016). In addition, the cutaneous blood vessel's endothelium does not produce alkaline phosphatase (ALP) as it does in humans. Alpaslan et al. (1997) found, in a preliminary study, localisation of ALP activity in regions of granulation tissue formation suggesting that ALP is a marker of this process. Pig skin also has apocrine sweat glands rather than the eccrine sweat glands that humans have, meaning that porcine models secrete sweat into the hair follicle rather than directly onto the skin's surface as human models do (Seaton et al., 2015). It is unclear how this effects the wound healing model.

There is sparse literature using porcine models for the study of wound healing. Their unpopularity in comparison to the use of rodent models may be due to there being less tools available for the evaluation of the host response (Seaton et al., 2015; Trøstrup et al., 2016). Traditionally, porcine models come from domestic farm breeds, such as the Yorkshire pig

(Seaton et al., 2015). Transgenic porcine models are less common than transgenic rodent models, due to the difficulty in their production. However, over the past 30 years, progress has been made in producing transgenic pig models for several human conditions.

Despite their current short-comings, in terms of dermal wound healing, the pig is currently the best animal model in terms of dermal structure and immune response (Ud-Din & Bayat, 2017). The versatility of the model and the ability to produce numerous aetiologies of wound healing make the pig an excellent wound healing evaluation tool (Perez & Davis, 2008; Seaton et al., 2015).

### 2.3.2 In Vitro Modelling

Traditionally, *in vitro* modelling has involved the use of assays and cell culture to allow studies into individual components of the skin (Ud-Din & Bayat, 2017). These methods allow the direct quantitative study of specific cell types without the other tissue-matrix components influencing the result. Whilst assays allow fast results and are relatively inexpensive for the researcher, they are of course incapable of reproducing the exact biological conditions found in a wound and do not allow for the study of the biomechanical effects of treatments on wound healing (Perez & Davis, 2008).

In more recent years, the biomechanical processes involved in wound healing have become increasingly of interest. This has led to the development of artificial skin models, also referred to as 'skin phantoms', 'skin replicas' and 'skin model substrates' (Dąbrowska et al., 2016). Such physical (biomechanical) models are typically used to investigate the deformational and frictional behaviour of biological tissues, focussing on the biomechanics on a macroscopic level rather than the movement of individual cells on a microscopic level (Nachman & Franklin, 2016). The understanding of these biomechanics is often important in the development of medical devices.

Prior to the development of artificial wound models, the most common methods of understanding the biomechanics of wound healing involved the use of *ex vivo* models using either animal or human tissue. Thus there is a strong argument for carrying out physical *in vitro* modelling, because, unlike their *in vivo* counterparts, these models do not use animal or human material, eliminating ethical concerns (Perez & Davis, 2008). In addition, experiments using biological tissues are inherently variable due to the variability across tissue samples (Dąbrowska et al., 2016). Not only are the physical models devoid of ethical issues, but they also allow better control over the physical properties due to increased

reproducibility. In addition to this, they are able to be stored between uses because of their long term stability and the requirement for less storage space. The ability of a physical model to potentially be used multiple times, depending on the type of model and testing methods, usually leads to lower overall costs than their *in vivo* counterparts.

When developing a physical model, especially for the skin, there are a variety of material groups that are available to the researcher, each with particular strengths. There are skin models developed using elastomers, resins, metals, liquid suspensions, gelatinous substances and textiles incorporating micro- and nano-fillers, for example those based on albumen (Dąbrowska et al., 2016).

### **2.3.2.1 Elastomer Based Models**

An elastomer is a polymer which demonstrates rubber-like viscoelastic properties and are either thermoplastic or thermoset with a glass transition temperature significantly below that of room temperature (Dąbrowska et al., 2016). There is a broad spectrum of natural and synthetic elastomers available to the researcher including: silicones, polyurethanes, polyether block amides, polybutadiene and polyisoproprene, with silicones and polyurethanes being the most commonly used.

Silicones are inorganic-organic polymers containing silicon, oxygen, carbon and hydrogen with added fillers to strengthen and tune their properties (Dąbrowska et al., 2017). There are a number of advantages to using silicone-based models including: long term stability, easy manipulation, non-toxicity and the broad range of properties that can be simulated. Silicone based models have been used to simulate skin in a variety of settings, the main being clinical training, allowing the simulation of needle penetration and drug delivery (Nachman & Franklin, 2016). In addition to this, silicones are used for modelling biomechanics, including tactile assessment, indentation and friction (Dąbrowska et al., 2017).

Another popular elastomer are polyurethane-based materials. These are addition polymers, of which the majority are thermosetting, however some are thermoplastic (Dąbrowska et al., 2017). Polyurethane elastomer models can have their properties modified by incorporating reinforcing particles, polyurethane sponges or elastomers with different soft-to-hard phase ratios. As with silicone-based physical tissue models, polyurethane models have long term stability and therefore a long shelf life. Polyurethane sponges in particular have been shown to simulate the biomechanical properties of the human dermis

in non-ballistic wound modelling. In addition to this, polyurethanes are also useful for modelling the frictional behaviour of the skin (Dąbrowska et al., 2017).

### **2.3.2.2 Gelatinous Substances**

A less common method of modelling the biomechanics of skin is the use of gelatinous substances. These models have the ability to interact with water, leading to the creation of reversible gels (Dąbrowska et al., 2017). The mechanical behaviour of these models can be influenced by pH, temperature and pressure, allowing for the control and modification of a variety of physical, mechanical, and chemical properties e.g., hardness, optical or surface properties, and elastic modulus.

Gelatine, the substance that gives gelatinous substances their name, is a protein produced by the partial hydrolysis of collagen, abundant in skin, bone and connective tissue (Dąbrowska et al., 2017). The matrix of gelatine provides density, absorption, light scattering, stiffness, and sound speed similar to that of human skin, making it an ideal material from which to develop a model to demonstrate those properties. In addition to this, dry gelatine is a relatively stable substance and can be stored for a long time without change in its qualities.

Another type of gelatinous substance used for skin models is agar. Made from seaweed polysaccharides, the applications of agar based skin models are diverse but limited to testing using light or non-contact methods (Dąbrowska et al., 2017). Typical examples are optical and thermal imaging, photoacoustic and ultrasound imaging, dosimetry and body centric applications. One drawback of the use of agar in modelling is the instability of the substance, giving any models created with it a limited lifetime. However, the versatility and reproducibility of agar, in addition to the similarities between its density, and acoustic velocity and impedance to skin, make it a material of choice for many researchers (Dąbrowska et al., 2017).

Polyvinyl alcohol (PVA) is a synthetic gelatinous polymer, often used for medical applications (Dąbrowska et al., 2017). These cryogels, in comparison to agar, are relatively stable and easy to store, as well as being able to be produced with similar properties of human skin. This type of model is particularly useful when simulating tissue for magnetic resonance studies. PVA cryogels have mechanical properties that can be modified to be within the range of those of the soft tissues to be modelled (Dąbrowska et al., 2017).

### **2.3.2.3 Other Materials**

There are a variety of other, useful but less common, materials used for the creation of physical tissue models. For example, epoxy resins can be used to produce cross-linked or thermoset plastics with a variety of properties (Dąbrowska et al., 2017). These are used particularly for the observation of temperature profiles inside or on the surface during cryogen spray cooling and can be used for the validation of optical tomography and the calibration of instrumentation.

One type of model that is perhaps less useful for looking at the biomechanical properties of biological tissue are metal based skin models. These have their main uses in the study of thermophysiological response and the thermal properties of clothing, simulating skin temperature, sweating rate and heat transport (Dąbrowska et al., 2016). These models are mainly influenced by the design of the entire testing system, and therefore the specific choice of material is not of critical importance, as it would be in elastomer models. The main advantages of using metal-based physical models are their stable properties, robustness, high thermal responsiveness and the ease of production. As metal is widely used in other areas of engineering and product development, equipment for the manufacture of the model often does not require purchasing specially.

Finally, another type of model, the textile model, is used primarily in the simulation of sweat distribution across the skin (Dąbrowska et al., 2016). These models use synthetic and natural leather, for example lorica, and chamois, to simulate the mechanical and frictional behaviour of skin. This type of model can incorporate micro- and nano-fillers to alter the material properties of the textiles used. These fillers can be a range of materials including: metallic gold, polystyrene, titanium dioxide, aluminium oxide, carbon black, graphite, lipids, and silicone dioxide, and can be incorporated into solid and liquid matrices (Dąbrowska et al., 2016).

### **2.3.2.4 Development Process of *In Vitro* Models**

The development of an *in vitro* model begins with the specification of the properties to be modelled, and under what conditions these properties will be tested (Dąbrowska et al., 2016). Once these have been established, material selection occurs, which can take months of rigorous testing to ensure the selection of the materials with the most appropriate properties to those selected (Dąbrowska et al., 2016). Whilst material selection is ongoing, the design of the model can occur, whether that is the design of a mould, for gelatinous and

elastomeric materials, or the design of the model itself for textile and metal models. Once these steps have been completed, model manufacture and testing can occur. As with any *in vitro* experimentation, the results must be validated. In the case of the modelling of biological tissue, this may be done using either *in vivo* or *in silico* techniques, ensuring the model accurately represents *in vivo* conditions.

### 2.3.3 *In Silico* Modelling

Understanding the mechanical behaviour of biological tissues *in vivo* is of great importance for both clinical and cosmetic purposes (Hendriks et al., 2003). There is, however, great controversy around the use of *in vivo* models, and *in vitro* models inevitably lack the complexity required to fully understand the processes occurring. A theoretical alternative to both *in vivo* and *in vitro* modelling is the use of *in silico* modelling. This can be used as a screening tool to predict the effect of a treatment, drug or stimulus and can assist in the planning of experimental research and clinical trials, allowing a faster insight into the likely effectiveness of treatments (Vermolen & Javierre, 2010; Ud-Din & Bayat, 2017). It provides an alternative to *in vivo* modelling with very few ethical issues (Vermolen & Javierre, 2010). However, mathematical modelling does not completely eliminate the need for *in vivo* modelling because all results gained *in silico* remain theoretical until validated by physical experimentation which may be in the form of an *in vitro* or *in vivo* model (Ud-Din & Bayat, 2017). Mathematical models can however reduce overall costs by allowing more targeted experimentation, minimising the quantity of unnecessary trials (Geris et al., 2010).

Mathematical models have a tendency to focus on only one area of the wound healing process, either investigating the cellular interactions or the biomechanical properties (van Gent et al., 2010). Wound models developed during the 1990s can be categorised depending on the area of wound healing process they focus upon: wound contraction, wound angiogenesis, epidermal healing or the repair of the extracellular dermal matrix (Geris et al., 2010). Prior to 2009, all *in silico* studies modelled only one partial process of wound healing, which can be problematic since the phases of wound healing overlap and influence each other (Vermolen & Javierre, 2010). In more recent years, *in silico* studies have no longer focussed on the individual wound healing phases, but instead the impaired healing of chronic wounds and the design of treatment strategies (Geris et al., 2010). Recently, mathematical models have been developed to study the biomechanical effects of wound healing treatments, for example negative pressure wound therapy, hyperbaric oxygen, and commercially engineered skin substitutes (Geris et al., 2010; Ud-Din & Bayat, 2017). By

studying the micromechanical forces involved in wound healing, biomechanical *in silico* models can be used to evaluate different treatment methods to investigate their effects on cell proliferation, wound angiogenesis and growth factor proliferation (Ud-Din & Bayat, 2017). These biomechanical models are generally developed using finite element analysis (Geris et al., 2010).

Finite element analysis (FEA) is widely used in engineering to examine the mechanical interactions of complex systems. However, in more recent years, this technique has found many applications in the medical field, particularly in plastic surgery for the analysis of skin deformation, burn heat transfer, and craniofacial stress. In the investigation of wound treatments specifically, FEA has been used primarily used in the investigation of negative pressure wound therapy. However, despite a large quantity of clinical studies into the effects of NPWT on wound healing, there has been little specific research into the effects of mechanical signals, including tensile, shear and compressive deformation resulting from NPWT using a computational model (Wilkes et al., 2009a).

Although creation of *in silico* model of wound healing has few associated ethical concerns, there are some model specific limitations. Arguably the biggest limitation is the simplification of the biological phenomena under investigation (Geris et al., 2010). This is, in part, due to the difficulty associated with assigning exact numerical values for the properties, as is standard practice when modelling non-biological materials (Dąbrowska et al., 2016). The difficulty in the parameterisation of *in silico* models is contributed to by the sparseness of experimental data and the great variability in the anisotropy, non-linearity, mechanical properties of biological tissues (Geris et al., 2010; Glozman & Azhari, 2010). This can lead to the omission of certain biological and mechanical factors. These simplifications can mean that there are parameters that are unable to be validated entirely (Geris et al., 2010).

The variability and non-linearity of biological tissues leads to their properties being difficult to define and, subsequently, models displaying Hookean (linear) properties are often used to find the Young's modulus,  $E$  (Hendriks et al., 2003). This leads to a large variability in the values of Young's modulus used for models. In addition, the mechanical properties of biological tissue are highly variable; affected by many factors including: hydration, the amount of deformation applied to the tissue, and tissue thickness. The variability in testing procedure and experimental techniques also affects the mechanical properties of biological tissue, meaning that the same values are rarely used for more than one model.

The wound healing process itself contributes to the difficulty in its modelling. The wound tissues become increasingly fibrotic, increasing the Young's modulus, and subsequently decreasing the average strain across the surface of the wound when NPWT is applied (Saxena et al., 2004). Challenges in computational modelling also arise when studying wounds on a cellular level as cell movement is dominated by chemotactic responses to signals such as growth factors (Geris et al., 2010). In addition, in literature published prior to 2007, neo-vascularisation, also known as angiogenesis was considered to be sequential with wound contraction as they were modelled individually, however in medical literature, it is found that these processes overlap partially (Vermolen & Adam, 2007).

Shown in Figure 12, Saxena et al. (2004) created a two-dimensional *in silico* finite element model to investigate the effect of negative pressure wound therapy on the wound bed. In this study, it was found that the surface strains across the wound are more sensitive to changes in the Young's modulus than to changes in the Poisson's ratio when NPWT was simulated. Saxena et al. (2004) also found that when negative pressure was applied to the wound, the surface strain varies with negative strains located directly beneath the struts, indicating this tissue is under compression. This agreed with research carried out by (Wilkes et al., 2009b) who also found a repeating pattern to be present in their computational analysis of negative pressure wound therapy. The study by Wilkes et al. (2009b) differed from that of Saxena et al. (2004) as it used a three-dimensional model for the investigation of strain measurements in soft tissue, focussing on a tissue phantom exposed to negative pressure wound therapy and observed using microcomputed tomography (microCT). An image of Wilkes et al. (2009b)'s model can be seen in Figure 13 below.

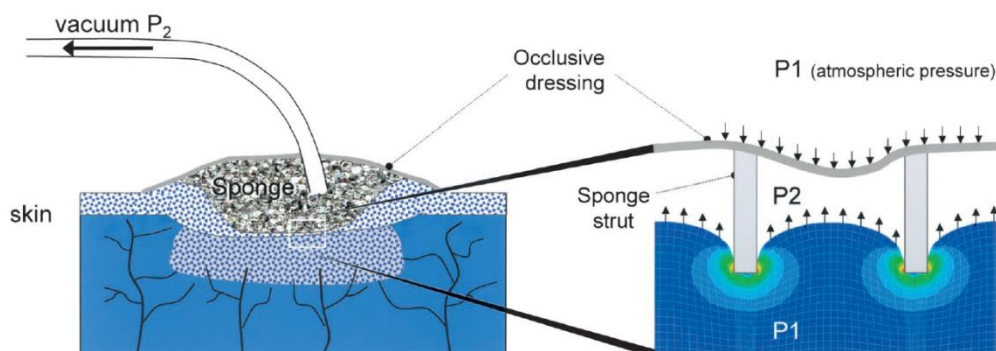


**Figure 12** (Left) a schematic of negative pressure wound therapy applied to a wound. Including wound filler and vacuum connection. (Right) Finite element model showing the variation in pressures and micro stresses (Saxena et al., 2004).

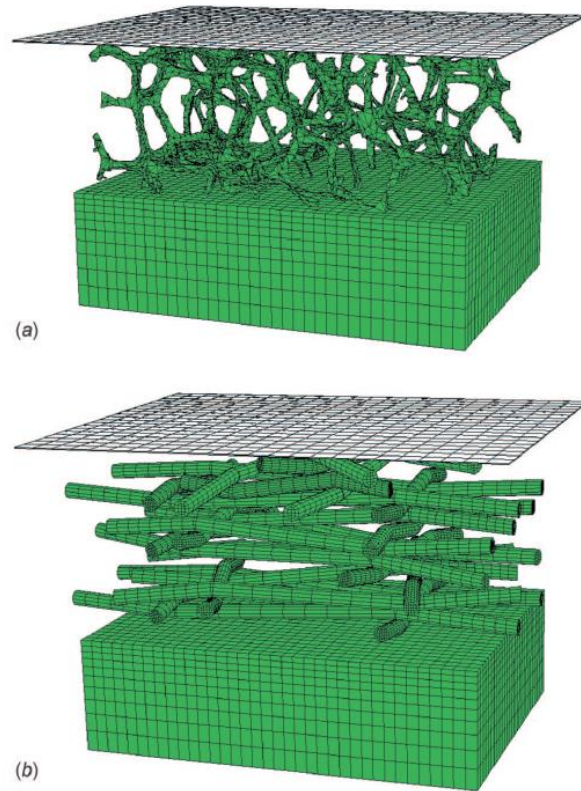


**Figure 13** Finite element models designed by Wilkes et al. (2009b) to investigate the impact of foam and gauze on tissue during negative pressure wound therapy.

It is generally accepted that the optimal *in silico* model should have measurable variables, a minimum number of parameters, and should have a biophysical basis (Cukjati et al., 2000). In addition to this, the model should be representative of the current experimental data, irrespective of wound location, aetiology and treatment methodology. When this is the case, the model should be capable of making reliable predictions of wound healing with reasonable accuracy, allowing the model to be used to improve understanding of the wound healing process.

One of the earlier wound deformation models created using finite element analysis was that created by Larrabee (1986). This model was developed to close the gap that was observed at the time between simple mechanical ‘skin flap’ models and the advanced equations developed by biomechanists to describe tissue properties. It was crude and highly simplified when compared to its present-day counterparts, however, this was due to the lack

of availability of the sophisticated software for finite element modelling that is available to present-day researchers.

Larrabee's model was subject to a variety of key simplifications and generalisations. During the parameterisation of their model, it was decided to only model the stress-strain relationship that is observed in a clinical setting. This led to the model being defined with linear biomechanical properties and deformation. Additionally, the viscoelastic mechanical properties were ignored, and the skin was considered to be an isotropic material with no tension present in its resting state, however, in later developments, it was possible to incorporate the directional and underlying stresses. The model was only developed as a two-dimensional model, because a three-dimensional model was considered to be 'very complex and probably impractical' (Larrabee, 1986). Whilst this model was very simplified model in comparison to what is available today, it paved the way for later models to be developed using finite element modelling and was, in a way, an ancestor of the models' researchers use today.

Hendriks et al. (2003) investigated the deformation of skin under suction in both *in vivo* and *in silico* experiments. An iterative analytical process was then used to compare the numerical and experimental fields until convergence was reached. The thickness of the dermal layer was obtained using ultrasonic imagery for each subject and subsequently a unique finite element mesh was developed from these ultrasound images for each subject. Hendriks et al. (2003) made a number of key assumptions in the development of their model. This includes the assumption that skin is incompressible with a Poisson's ratio of 0.499999 and isotropic, allowing a 2D axisymmetric model to be utilised. In addition, time dependent behaviour is ignored. The finite element model was produced using an extended Mooney material behaviour equation to account for the non-linearity of the stress-strain relationship of the skin.

Hendriks et al. (2003) used a strain energy function to mathematically define the mechanical properties of skin, where:

$$W = C_{10}(I_1 - 3) + C_{11}(I_1 - 3)(I_2 - 3) \tag{4}$$

and  $I_1$  and  $I_2$  are the invariants of the finger strain tensor  $\mathbf{B}$  (Hendriks et al., 2003). When the strains experienced by the skin are small, the second term:

$$C_{11}(I_1 - 3)(I_2 - 3)$$

(5)

is negligible and the Young's modulus of the material can be calculated from:

$$E = 6C_{10}$$

(6)

Hendriks et al. (2003) found that  $C_{10, \text{dermis}}$  was equal to  $9.4 \pm 3.6$  kPa and  $C_{11, \text{dermis}}$  was equal to  $82 \pm 60$  kPa. This gives the Young's modulus to be 56 kPa for the dermal layer. This value is in the same order of magnitude as Diridollou et al. (2000). Hendriks et al. (2003) also considered the Young's modulus of subcutaneous fatty tissue; an estimate gave  $C_{10, \text{fat}}$  as 0.2 kPa, giving the Young's modulus of subcutaneous fatty tissue to be approximately 1.2 kPa. However, the significant difference in Young's modulus of subcutaneous fatty tissue when compared to that of the dermal layer meant that the experimental set up used by Hendriks et al. (2003) was not an appropriate choice if the intention was to measure the biomechanical properties of subcutaneous fatty tissue.

*In silico* modelling is more frequently used in the development of wound treatments such as negative pressure wound therapy. This is due to the influence of micromechanical forces on the formation of granulation tissue. Saxena et al. (2004) investigated the effect of NPWT, and in particular the properties of the foam used in NPWT (see Chapter 7), on wounds using finite element analysis. These models focussed on a homogeneous, single layer wound with the biomechanical properties of skin. The material properties were assumed to be linear, isotropic and elastic, which appears to be a limitation because non-linear stress-strain relationships are generally observed when investigating the mechanical properties of biological tissues. However, in the observed strain ranges, the skin does demonstrate a stress-strain relationship with reasonable linearity.

These models were developed to investigate the effect of changing the wound's parameters on the deformation of the wound bed, in particular Poisson's ratio ( $\nu$ ), Young's modulus ( $E$ ), pore diameter of the foam (used to fill the wound), pore volume fraction of the sponge and the pressure applied to the wound (Saxena et al., 2004). These were varied sequentially, ensuring that all parameters apart from the one being observed were kept at a standard value. These standard foam values were as follows:  $E = 70$  kPa,  $\nu = 0.49$ , pore diameter = 1.2 mm,  $P = 110$  mmHg, and pore volume fraction = 0.889.

The study by Saxena et al. (2004) found that no matter what parameters were used, surface strain varies in a repeating pattern along the wound's surface. When subjected to 15 kPa pressure (approximately 110 mmHg), the tissue directly below the struts was subjected to a peak strain of 125% under standardised conditions. This is a particularly important observation as it shows the tissue experiences micromechanical forces, a phenomenon known to increase granulation tissue growth and wound regeneration, even in chronic or hard-to-heal wounds.

From the literature discussed in this chapter, it can be seen that wound healing is a complex process and therefore modelling this is difficult for many reasons. It was seen that *in vitro* and *in silico* modelling offers great potential for further development and replication of the mechanical properties of biological tissue. Previous work has focussed on producing simplified single material models *in silico* models of the deformation of wounds during mechanical wound treatments such as negative pressure wound therapy and a biomechanically similar *in vitro* model has not yet been developed for this purpose. This project aims to fill the gaps in understanding surrounding how negative pressure wound therapy influences the strains experienced throughout the layers of biological tissue surrounding a wound and provide a model for the testing of novel medical devices. Fully parameterised multilayer models representing the skin, subcutaneous adipose tissue, and muscle, will be created *in silico* and *in vitro* to provide an understanding of how strains dissipate through tissue. Further models will be developed looking at negative pressure wound therapy on a microscopic scale, allowing the impact of wound filler material to be studied.

## Chapter 3 Experimental Preliminary Testing

This chapter describes the various methods used to create both *in vitro* and *in silico* wound models in the current research. The process began with a thorough review of current literature to find target properties for each layer of the wound models, before preliminary experimentation took place to find the polymers with values most comparable to those *in vivo*. Due to the non-linear nature and uniqueness of human tissues, literature has a large variation in the range of values given for the elastic modulus. This paucity of definitive values means there is no single biomechanical definition of many biological materials, increasing the challenge for scientists and engineers working to move away from *in vivo* testing by replicating tissues with polymers *in vitro*.

### 3.1 Preliminary Testing

In order to ensure accurate and replicable results, a variety of preliminary tests were carried out. The final methodologies are outlined below.

#### 3.1.1 Mould Design

The first step in establishing the properties of different silicone materials was to design a mould in accordance to the most relevant silicone testing standards. An engineering drawing of the mould used is contained in Appendix 1. The design and dimensions of the moulds aimed to produce samples that are 'Type D' in accordance with ASTM D412, the American standard for the testing of vulcanised rubber and thermoplastic elastomers under tension. This standard was chosen, in part, due to the lack of accessible EU standards for testing relating specifically to hyperelastic material properties of polymers. **Figure 14** shows a sample of Food Grade silicone, used for tensile testing. This has the same dimensions and shape as the samples for other silicones.



**Figure 14** Photograph of an ASTM D412 compliant sample of Food Grade silicone. This is the size of sample used for all tensile testing.

After the mould design was completed, the moulds were 3D printed out of polylactic acid (PLA) using UltiMaker 2+ 3D printer (UltiMaker, 2015). Each mould allowed simultaneous casting of 6 samples with five moulds manufactured so that 30 samples were able to be cast for each silicone. This allowed 3 sets of 10 samples to be tested, ensuring the reliability of the results. Following a check for defects, the moulds were able to be used to cast test samples.

### 3.1.2 Silicone Mixing

The mechanical properties of two-part silicones vary depending on the ratios and mixing methods used. The appropriate mixing ratios are dependent on the silicone, with some silicone types requiring a 1:1 ratio, and others requiring a 10:1 ratio. Therefore, it is important that the manufacturer's instructions are followed, and the silicone mixtures used in this project were measured by weight (rather than volume) as per the manufacturer's instructions. Setting times also vary depending on the type of silicone and therefore the length of time allowed for mixing varies by type to allow transfer to moulds in a timely fashion. These constraints are outlined in Table 2 below.

**Table 2** A table containing the types of silicones tested in this project, alongside the manufacturers recommended ratios, mixing, working, and curing times.

Silicone Type	Catalyst	Ratio	Mixing Time (s)	Working Time (mins)	Curing Time (hrs)
Polycraft Silskin 10 Special Effects Addition Cure Silicone	-	1:1	60	15	50 – 60 mins
Polycraft T-15 Clear RTV Addition Cure Silicone Rubber	-	1:1	-	20	48
Polycraft T-20 Clear RTV Addition Cure Silicone Rubber	-	1:1	-	3	35 mins
Polycraft Silastic T4 Translucent Addition Cure Silicone Shore A40	-	1:10	-	90	24
Polycraft GP3481-F General Purpose RTV Condensation Cure Mould Making Silicone Rubber	Red Fast Set	1:10	-	40 – 60	12 – 24
Polycraft Food Grade Addition Cure Silicone Mould Making Rubber	-	1:10	-	60	16
Polycraft S30 RTV Addition Cure Silicone Rubber Shore A30	-	1:10	-	60	24

The silicones used can be grouped into two main categories, those that require a 1:1 ratio, and those that set from a 1:10 ratio. The method used for each silicone type is outlined below.

### 3.1.2.1 1:1 Ratio Silicone Rubbers

1. Place a mixing bowl on *Traveler TA1501* scales (S/N: B338803679) and tare the balance.
2. Using a syringe from an approximate height of 30cm, transfer 150g of base into the mixing bowl.

3. After taring the balance, transfer 150g of catalyst into the mixing bowl using a syringe from a height of approximately 30cm.
4. Mix silicone for the time specified by the manufacturer, found in Table 2, or 90 seconds if not specified, being careful to ensure the minimal amount of air is added to the mixture.
5. Once mixed, transfer the silicone from the mixing bowl to the mould using a 5ml syringe to ensure the silicone is accurately loaded into the moulds.
6. Remove excess silicone from the surface of the moulds with a scraping tool, flattening the tops of the samples.
7. Allow the sample to sit for 30 seconds before using a needle to burst any large bubbles on the surface of the samples.
8. Once again, remove any excess silicone using a scraping tool and leave to cure for the manufacturer recommended curing times, found in Table 2 before removing from the moulds.
9. On removal, label the samples 1 – 30 using a permanent marker and place 10 in each of three appropriately labelled Petri dishes.

#### 3.1.2.2 10:1 Ratio Silicone Rubbers

1. Place a mixing bowl on *Traveler TA1501* scales and tare the balance.
2. Using a syringe from an approximate height of 30cm, transfer 300g of base into the mixing bowl.
3. After taring the balance, transfer 30g of catalyst into the mixing bowl using a syringe from a height of approximately 30cm.
4. Mix silicone for the time specified by the manufacturer, found in Table 2, or 90 seconds if not specified, being careful to ensure the minimal amount of air is added to the mixture.
5. Once mixed, transfer the silicone from the mixing bowl to the mould, using a 5ml syringe to ensure the silicone is accurately loaded into the moulds.
6. Remove excess silicone from the surface of the moulds with a scraping tool, flattening the tops of the samples.
7. Allow the sample to sit for 30 seconds before using a needle to burst any large bubbles on the surface of the samples.
8. Once again, remove any excess silicone using a scraping tool and leave to cure for the manufacturer recommended curing times, found in Table 2, before removing from the moulds.

9. On removal, label the samples 1 – 30 using a permanent marker and place 10 in each of three appropriately labelled Petri dishes.

### 3.1.3 Tensile Testing

Following the production of the samples, mechanical testing was carried out to determine the Young's modulus of each type of silicone rubber. A Lloyds Machine LS1 (S/N: 201474) was used to perform the testing; labelled samples were tested at 1, 7, and 28 days post removal from moulds. Prior to the testing of materials, the machine was set up to allow repetitive testing. The method for this is outlined below.

1. Using a Vernier calliper, measure the dimensions of the face of the TG34 'Vice Action Grip for Thin Film' clamps with the rubber coating removed (S/N: S1093) and draw 4 rectangles the same size on the reverse of a sheet of P100 self-adhesive sandpaper.
2. Cut the rectangles out of the sandpaper and remove the backing before attaching to the faces of the clamps.
3. Attach the 100N Load Cell to the machine following the manufacturer's instructions prior attaching the clamps using a pin.
4. Adjust the clamps to ensure they line up.

Once the machine was set appropriately, testing began by loading the first sample into the machine. The exact methods used for testing follow.

1. Using the vice grip, attach the shoulders of the sample to the clamps and tighten.
2. The handheld remote was then used to set the sample so that it was straightened but not under tension. The machine was then zeroed.
3. Using a Vernier calliper, measure the gauge length of the sample and calculate 30% of this value.
4. Open NEXYGEN PLUS 3 software and select 'Create new batch of tests' and when asked for the test type, select "tension and compression test".
5. Once this has been done, the parameters of the test can be defined. For the preliminary testing, a preload of 0.1N was used, applied at a speed of 0.1 mm s<sup>-1</sup>. Ensure the equipment is set to automatically zero both load and extension at the start of the test, and that the machine is set to return to zero at the end of the test. Ensure the test speed is set to 0.1 mm s<sup>-1</sup>.
6. Select the 'limits' tab and input the result of the calculation made in *step 3*, 30% of the gauge length into the 'max extension' box.

7. Select the green start button and wait for the test to finish before removing the sample and repeating these steps for the next sample.

#### 3.1.3.1 Numerical and Statistical Analysis

The data collected through the NEXYGEN PLUS 3 (Ametek, 2017) software was exported as a .txt file for input into Excel (Microsoft, 2019). The raw data is produced in the form of a Load-Extension graph and was subsequently converted into mechanical stress and strain using the following equations:

$$\frac{\text{Machine Extension (N)}}{\text{Gauge Length (m)}} = \text{Strain } (\varepsilon) \quad (7)$$

$$\frac{\text{Load (N)}}{\text{Area (m}^2\text{)}} = \text{Stress } (\sigma) \quad (8)$$

Following the calculation of stress and strain for each sample point, the LINEST function was utilised to calculate a second order regression which produced the curve fitting coefficients for each sample. These coefficients were then used to calculate the stress for strain values between 2.5% and 30% for each sample. From here the Young's modulus was calculated using the formula:

$$\frac{\text{Stress } (\sigma)}{\text{Strain } (\varepsilon)} = \text{Young's Modulus (E)} \quad (9)$$

and compared to the values of Young's modulus for biological materials found in literature to select the most biomechanically similar silicones for the development of an *in vitro* model for the testing of novel medical devices.

In addition to the selection of materials, it was hypothesized that the Young's modulus of silicone changes with time. To investigate this, 10 measurements were taken at 1, 7 and 28 days post removal from the mould. Each set of 10 datasets were then grouped to allow the mean and standard deviation to be calculated for each time point. These values were then plotted, producing graphs with the mean and  $\pm 1$  standard deviation between 2.5% and 30% strain for each silicone at 1, 7, and 28 days post removal from the moulds. These

graphs were combined to provide a visualisation of the variation of stress with strain over time.

To determine whether the mean stress for each silicone varied significantly over time, a 2-tailed t-test was carried out for each strain percentage. It was assumed that the means had similar variances. The null hypothesis was that the stress for each silicone did not vary significantly over time. As is standard in statistics, a p-value less than 0.05 was considered to be significant and thus there is strong evidence against the null hypothesis.

## 3.2 Silicone Sample Results

This section will outline the results gained by tensile testing silicone samples in order to calculate the mechanical properties. In the raw data, the coefficient of determination ( $R^2$ ) is greater than 0.95 for all datasets. The majority of silicones had  $R^2$  values greater than 0.99.

### 3.2.1 S30

Figure 15 shows the mean and standard deviation for the variation of stress with strain for S30 silicone rubber under tension at 1, 7 and 28 days post removal from the moulds. It can be seen that, the mean stress experienced at lower strain levels is similar for all samples, however as the strain increases, the stress experienced becomes more different. This is supported by carrying out a t-test which finds the difference between the mean stress on day 1 and day 28 different for values of strain 5% and greater. Through differentiation of the trendlines, it was found that S30 silicone has a Young's modulus of  $1.645 \pm 0.045$  MPa.

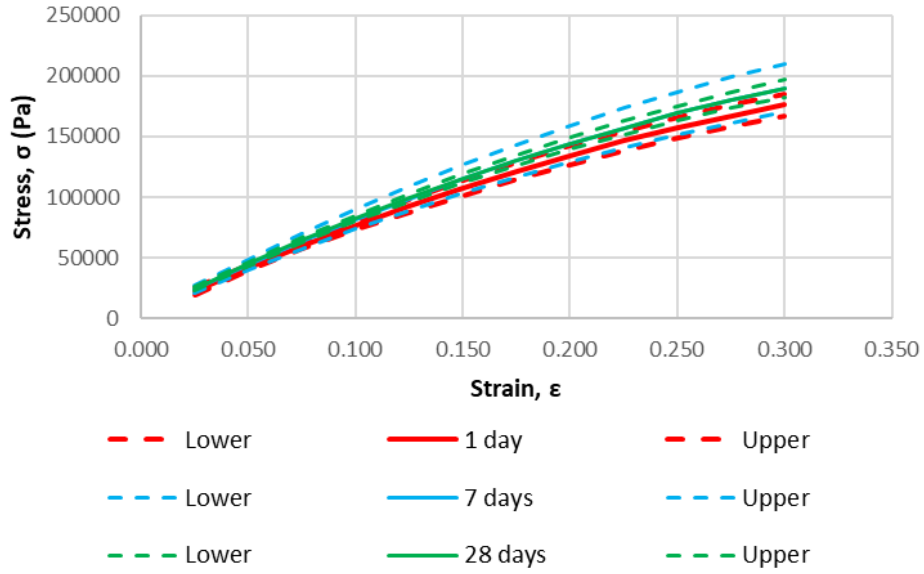


**Figure 15** The mean stress  $\pm$  1 S.D. for silicones subjected to 2.5% - 30% strain 1,7,and 28 days post removal from mould. It was found that the mean stress is significantly different on day 1 and day 28 for strains 5% and greater.

### 3.2.2 GP 3481 F

The stress-strain variation over time for GP 3481 F silicone can be seen in Figure 16. It can be seen that the mean and standard deviation of the stress for samples tested at 1, 7 and 28 days post removal from the mould are similar at all values of strain. This is confirmed by a t-test where it is seen that there is no significant statistical difference between the stress experienced by the samples at 1 and 28 days. It was found that GP 3481F silicone had a Young's modulus of  $387.25 \pm 33.43$  kPa when differentiating the stress-strain graphs.

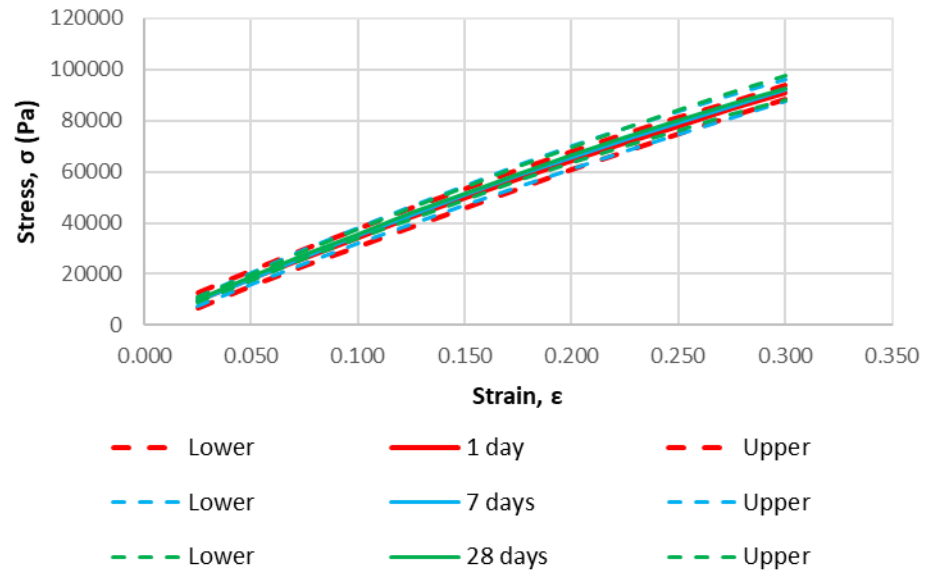


**Figure 16** Variation of mean stress with strain for samples of GP 3481 F at 1, 7 and 28 days post removal from moulds. It can be seen that there is no significant variation between the mean values of stress.

### 3.2.3 T4

Figure 17 shows the variation of mean stress with strain for T4 silicone samples tested at 1, 7, and 28 days post removal from moulds. It can be seen that there is a large variation in mean stress for the samples over time, with this increasing significantly at 28 days post removal from the moulds. A t-test confirms that for strains between 2.5% and 30%, the stress experienced during tensile testing 1 day after removal from moulds is significantly different to that at 28 days post removal from moulds. The Young's modulus of this silicone was found to be approximately  $1.61 \pm 0.34$  MPa through the differentiation of the polynomial trendlines on the stress-strain graph.

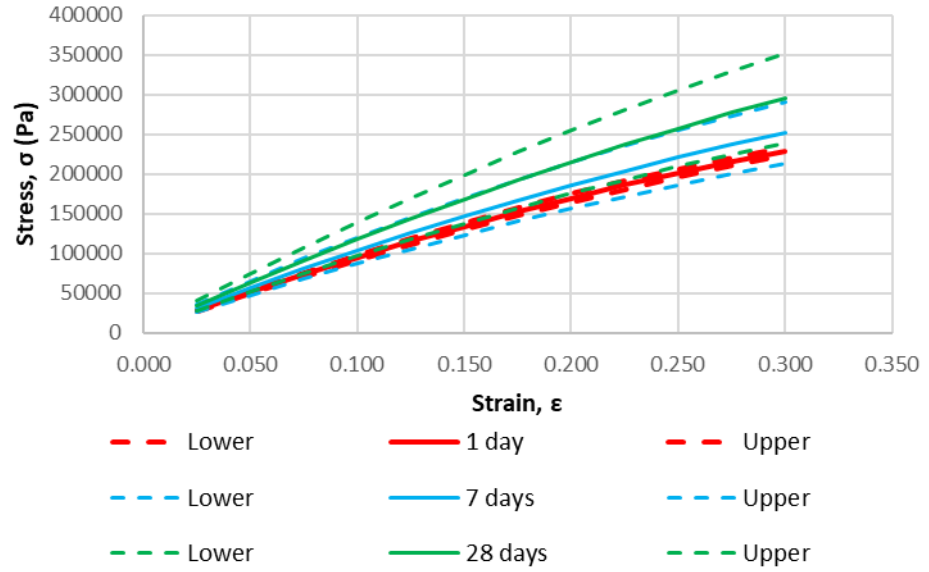


**Figure 17** Stress-Strain graph achieved through tensile testing of T4 silicone samples 1, 7 and 28 days post removal from moulds.

### 3.2.4 Food Grade

In comparison to the previous silicones tested, the range in stress for samples tested at 1, 7 and 28 days was much greater at 30% strain. Whilst it is clearly visible on the graph in Figure 18 that there is a difference in these samples, a two-tailed t-test confirmed that this is a statistically significant difference. It was found that the Young's modulus of Food Grade silicone was approximately  $2.289 \pm 1.56$  MPa, making it the stiffest silicone tested.

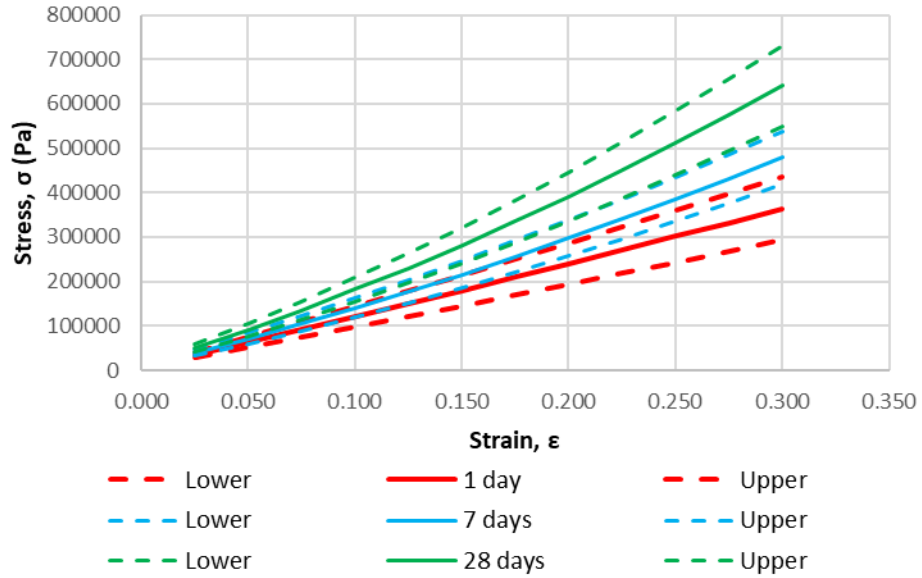


**Figure 18** Variation of stress with strain for samples of Food Grade silicone subjected to tensile testing at 1, 7 and 28 days post removal from moulds. It can be seen that the samples have significantly different values for stress at 30% strain.

### 3.2.5 Silskin 10 (1:1)

Figure 19 shows the variation of stress with strain for Silskin 10 silicone with a 1:1 base to catalyst ratio. It can be seen that there is a variation between stress values over time for strain values within the range of 2.5% - 30%. This was confirmed by a two-tailed t-test that was carried out. The stress values experienced by the samples are significantly different at strains of 5% and greater. The Young's modulus of this silicone was found to be  $407.57 \pm 36.55$  kPa.

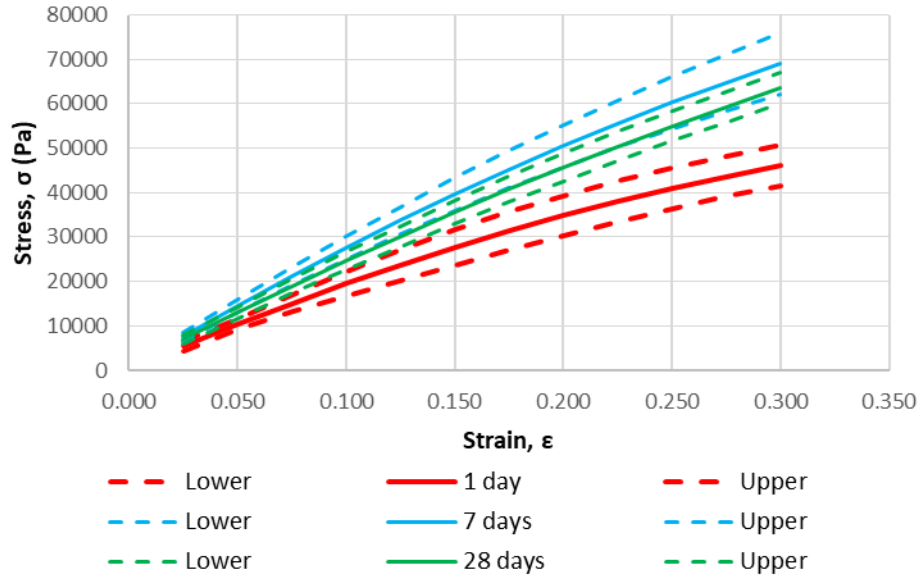


**Figure 19** Variation of stress for strain values between 2.5 and 30% for samples of Silskin 10 (1:1) silicone tested at 1, 7 and 28 days post removal from moulds. It was seen that the stress was significantly different at strains of 5% and greater.

### 3.2.6 Silskin 10 (1:2)

A smaller sample size of 6 was used to investigate the effect of altering the base:catalyst ratio of Silskin 10 on the Young's modulus of samples. The samples had a wide distribution between the upper and lower boundaries (mean  $\pm$  1 standard deviation) at  $\epsilon = 0.3$  however there were no obvious outliers attributing to this, as seen in Figure 20. The averaged relationship between stress and strain for this type of silicone rubber is defined by the equation:  $\sigma = -2.48 \times 10^{-3} \epsilon^2 + 4.12 \times 10^{-3} \epsilon$  (3 s.f.). From this, the Young's modulus was found, by differentiation, to be:  $E = -4.97 \times 10^{-3} \epsilon + 4.12 \times 10^{-3}$  (3 s.f.). This gives a Young's modulus of  $E = 26.3 \times 10^3$  kPa (3 s.f.) at  $\epsilon = 0.3$ , much lower than any other silicones studied.

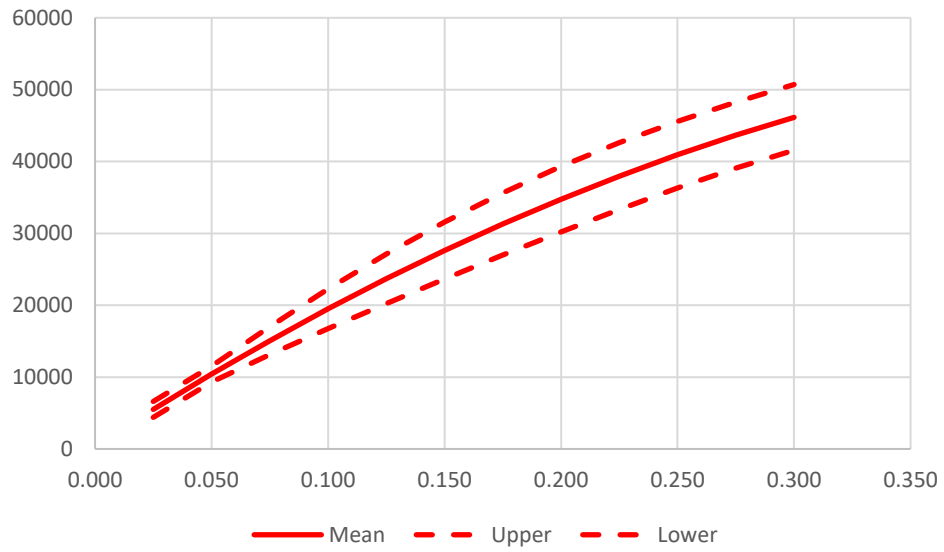


**Figure 20** Silskin 1:2 ratio had a Young's modulus of  $2.63 \times 10^{-3}$  MPa (3 s.f.) at  $\epsilon = 0.3$ . The data was gained from tensile testing in accordance to ASTM D412 over a period of 28 days to ensure repeatability. The data had a range of approximately 50%.

### 3.2.7 T15

The final silicone studied in this preliminary work is T15 silicone rubber. It can be seen in Figure 21 that the mean stress values for all three sets of samples tested are similar at lower strain values, but as the strain increases, so does the difference in the mean stress experienced between the samples at 1, 7 and 28 days. A two-tailed t-test was carried out and it was found that for strains of 7.5% and above, there is a significant difference between the mean stress of samples tested at 1 and 28 days. Tensile testing allowed a value of  $346.39 \pm 62.17$  kPa to be calculated as the Young's modulus of this material.

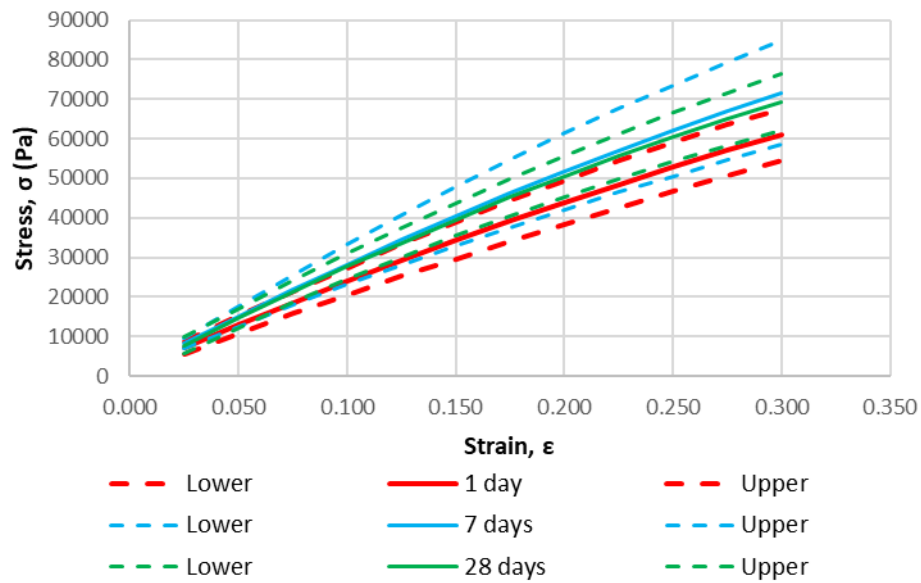


**Figure 21** The variation of stress with strain experienced by samples of T15 silicone during tensile testing at 1, 7 and 28 days post removal from moulds. It was found that at lower strains, the difference in mean stress between the datasets was not significantly different, but at strains of 7.5% and greater, a significant difference was found.

### 3.3 Discussion

Biological soft tissues have a non-linear response to mechanical loading and are sometimes assumed to be incompressible during finite element modelling. The non-linearity increases the difficulty in providing definite values for Young's modulus and other mechanical properties of these tissues, in addition to the individuality and uniqueness of each sample. Therefore, these values are often presented as a range and frequently linearised. A summary of values of Young's modulus for skin, subcutaneous fatty tissue and muscle found in literature can be seen in Table 1. In this section, the biomechanical properties of tissues as found in literature will be compared to the mechanical properties of the silicone samples tested in the laboratory.

Forming a protective barrier for the body, skin has the highest Young's modulus of the biological tissues researched. In Table 1, it can be seen that there is range of values of the factor of 10 kPa. This is a huge variation in values which creates difficulty when selecting a silicone to be used to represent this layer of tissue. As can be seen in Table 1, Agache et al. (1980) found the Young's modulus of skin in participants between 30 and 89 years of age to be 850 kPa using torsion. Khatyr et al. (2004) developed a method of mechanically testing skin by tension and compression *in vivo*. It was found that the Young's modulus taken parallel to the longitudinal axis of the arm was 657 kPa. This is a similar value to that from Agache et al. (1980). Food Grade silicone has the closest Young's modulus of elasticity to that of skin with a value of 1600 kPa at  $\epsilon = 0.3$ . Whilst this is larger than the values given in literature for skin, the non-linear pattern of the stress-strain relationship means that getting an exact value is impossible due to the biological processes that occur in the skin.

Referring to the values of skin thickness in Table 1, it can be seen that, on the posterior side, the skin thickness is approximately 2.5 mm (Annaidh et al., 2012). Whilst this is not the lower leg, as being modelled in this project, there is as distinct paucity of data for the thickness of skin in the lower leg region. The skin type on both the leg and the back is hairy skin, meaning its thickness and structure is similar. This allows the data for the thickness of skin in the back to be used as reference for hairy skin across the body, including in the lower leg.

Subcutaneous fatty tissue has the lowest Young's modulus of all tissue layers studied, with a value of  $11.7 \pm 6.4$  kPa. The standard mixes of silicone did not produce a low enough Young's modulus for this, with the closest being Silskin 10 (1:1) ratio. This was then adjusted

and tested with a 1:2 ratio and the Young's modulus reduced significantly to  $39.6 \pm 6.2$  kPa. Whilst this is still not identical to subcutaneous adipose tissue, it is the closest of the silicones tested, and therefore is the most suitable material to be used.

A study in 1997 by Ishida et al. (1997) used ultrasound to measure the thickness of subcutaneous fatty tissue and muscle throughout the body. Measurements of the thickness of subcutaneous fat at the medial calf were taken from both middle aged and Young female participants. The majority of people suffering from chronic wounds are middle aged and above. The thickness of subcutaneous adipose tissue in the medial calf is  $9.91 \pm 3.58$  mm, meaning the wound model was developed to have a thickness of 10mm.

Ishida et al. (1997) also investigated the thickness of the muscle layer in the posterior calf. A value of  $57.61 \pm 5.72$  mm was found. This is significantly thicker than that of both the skin and subcutaneous fat which fits the known structure of the lower leg. There is a paucity of data for the thickness of the *gastrocnemius* muscle, the data available suggests a sensible value to use for the muscle layer would be between 60 and 70mm.

Muscle is highly anisotropic due to its composition of fibres and striation. The Young's modulus perpendicular to the orientation of the fibres is significantly lower than the Young's modulus along the fibres. This anisotropy is impossible to replicate with silicones alone. Along the fibres, the Young's modulus has a value between 20 and 40 kPa (Morrow et al., 2010; Wang & Larin, 2015). When standing quietly, with little movement, the *gastrocnemius medialis* is slightly contracted, increasing the Young's modulus of the muscle. This gave Shinohara et al. (2010) a Young's modulus of  $111.2 \pm 5.0$  kPa for this muscle. This value is close to the range of both Silskin 10 (1:1 Ratio) and T15 (1:1 Ratio). From the data presented by Shinohara et al. (2010), it can be seen that as the Gastrocnemius muscle is contracted, and thus the strain it is subjected to is increased, the Young's modulus of the muscle also increases. This is the opposite of the mechanical reaction of Silskin 10 under strain, but similar to that of Food Grade silicone.

There are many limitations to using silicones to create a physical model of biological tissues. Silicones are inherently isotropic due to their liquid composition during the casting process. Due to this, the anisotropy of biological materials is impossible to model using silicone alone. One potential way of adjusting this is to add fabric fibres to the silicone to reduce the isotropy. This is something that would need to be further investigated should the physical model be developed beyond an initial model. A further limitation is the impact of

the mechanical properties of silicone changing with time. Whilst this can present issues if the model is being used for exact values, the physical model is used as a representation to visualise the impact of the displacement experienced during novel wound treatments and therefore exact values are less important than gaining an initial idea of the biomechanical treatment impact. In addition, for the majority of silicones the difference in Young's modulus over time is not significant week to week and would only be significant if comparing the models over a month. Humans are also highly unique, meaning there is a large range in values for Young's modulus. This causes difficulties as the silicone will never have the exact Young's modulus of the tissue it is modelling.

Biological tissues are highly complex meaning that no silicone will be able to exactly replicate the properties of the tissue it is modelling. The silicones selected to represent biological tissues in the physical wound model, whilst not perfect, are the most suitable for the purpose out of the samples tested and are seen in Table 3 below.

**Table 3** The silicones selected to represent the biological tissues and the appropriate layer depth.

<b>Biological Tissue</b>	<b>Silicone Selected</b>	<b>Layer Depth</b>
Skin	Food Grade	2.5 mm
Subcutaneous Fatty Tissue	Silskin 10 (2:1 Ratio)	10 mm
Muscle	Silksin 10 (1:1 Ratio)	70 mm

## Chapter 4 *In Silico* Modelling

Finite element modelling allows an insight into the stresses and strains experienced by an object when subjected to external loading. In this project, finite element modelling is used to investigate what occurs in a wound model when wound care devices are applied. In addition to the *in silico* model developed in this chapter, an *in vitro* equivalent model was developed for the validation of the *in silico* model. The development of the *in vitro* model was also used to confirm that the deformations experienced in the physical model are reasonable and relevant if the *in vitro* model was to be used for examining wound care devices and to demonstrate that the *in silico* model was able to reveal the strains experienced by the *in vitro model* during testing. The models developed in this chapter utilised the material properties of the silicones selected in Chapter 3. The development of the model is discussed in section 4.1. This model was developed to investigate model sensitivity and to give a basic understanding of the impact of wound geometry changes and anatomical changes on the strain and displacements experienced by the wound.

The strain around the wound face was investigated to understand the influence of negative pressure on the wound bed itself. A further path was plotted through the depth of the model to determine the effects of negative pressure through the surrounding model.

An equivalent *in vitro* model was designed in Chapter 5. Further development of this *in vitro* model was planned and therefore the testing of the *in silico* model in this chapter was developed further that strictly necessary for the development of a biomechanically similar model. The further development of the *in vitro* model was halted by the coronavirus pandemic in 2020.

Fully parameterised model (applied in the form of a log file in the ANSYS software) was created for this project. The model is multi-layered, with each colour representing a different layer of biological tissue. This can be seen in Figure 22. The layers modelled from top to bottom are skin, subcutaneous fatty tissue, muscle, and bone, where the bone is simplified into a simple horizontal cylindrical segment that runs through the model. The material properties were also parameterised allowing for the application of both linear and non-linear models.

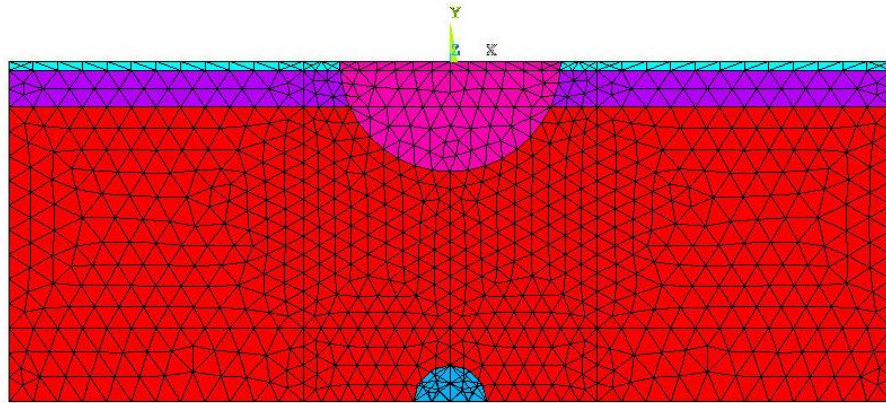


**Figure 22** Cross sectional view of the macroscopic *in silico* wound model. Each colour denotes a different material: pink = wound filler; turquoise = skin; purple = subcutaneous fatty tissue; red = muscle; blue = bone. (Coarse mesh presented to demonstrate model structure. Finer mesh used to produce results).

#### 4.1 Building the model

In ANSYS there are two main ways of building a model: either creating the model in the programme using solid-modelling primitives (such as blocks and cylinders) via the graphical user interface or writing a LOG file in the form of a \*.txt document which includes the commands to create and process those primitives in a completely automatic way. In this project, a LOG file approach is used because it allows the model to be easily parameterised and different geometries, material properties or boundary conditions to be examined, and for post-processing to be carried out automatically following the model's solution.

The model used in this project was constructed using a top-down approach, defining a top layer of key points before copying them to the depth of the skin-fat and fat-muscle interfaces to create the lower layers. The volumes were then defined and, following this, the wound was defined and subtracted from the volumes. A hemicylindrical volume on the base of the model was created to represent bone. Following this, the material properties were defined, and the model was subsequently loaded and constrained.

Multiple options were created in the log file, including one for non-linear material properties (and a non-linear solution) and one for linear properties. During the development of the model, a linear model was primarily used allowing for a single-step solution and faster analysis. The effects of assuming such a linear solution were tested. In this chapter, the mechanical properties of the model used the properties of the silicones selected during the mechanical testing in the preliminary experimentation (see previous chapter). This, combined with a physical model produced using those silicones, allowed the model to be

validated, as outlined in 4.2 'Testing the Model'. A model with biologically representative properties is discussed in Chapter 6.

The model was used to investigate the effects of varying the many parameters of the wound model, as described below, but its main features were as follows:

- a. Material properties. The model used material properties that corresponded with the material properties of the silicones selected in Chapter 3 to be most mechanically similar to skin, subcutaneous adipose tissue, and muscle Young's modulus values found in literature.
- b. Size. The size of the model was varied to ensure the size does not influence the strain experienced by the model. In addition, it ensured the model size was not excessive and thus taking longer than necessary to solve.
- c. Boundary conditions. The model represents a small section of tissue, and to reflect the fact that ensure rather than a stand-alone block, constraining the model correctly to reflect that is important. By adding symmetry to the base and sides of the model, the material properties are reflected meaning that the model behaves as if there is tissue surrounding it, like in the body. This allowed the model to become more biomechanically accurate during the simulation of the dissipation of applied loads.
- d. Loading. The model was loaded in a gradual fashion to ensure it behaved as expected. The negative pressure was also varied as NPWT can be applied with different magnitudes and therefore it was of interest to understand this impact on the wound and surrounding tissue.

## 4.2 Testing the model

Following the creation of the model, testing and model validation occurred. During building, the LOG file was regularly loaded into the ANSYS software, and the displacement was animated to ensure the model was deforming as expected. An additional LOG file was produced to automate the postprocessing. This provided continuity of results and ensured comparability between model iterations.

Prior to carrying out modelling, a convergence study was required to ensure that the results being provided by the model were accurate and correct and demonstrated mesh independence. As the area of most interest was located directly underneath the wound and the surrounding edges, a finer mesh was used in the centre of the model adjacent to the wound, and at the model edges the mesh was more coarse as strain gradients were reduced.

This improved efficiency when meshing and solving the model. To alter the size of the mesh, the line edge size was varied. Line edge size influences the number of divisions along a line. This subsequently influences the number of nodes along the line and therefore the size of the mesh. The smaller the line edge size value, the finer the mesh produced.

Figure 23 presents the convergence of 1<sup>st</sup> and 3<sup>rd</sup> principal strains along the same central path. Several line edge sizes were tested. These are labelled with the central line edge size first, and the outer line edge size second e.g. “10mm,15mm” has a central line edge size of 10mm and an outer line edge size of 15mm. It can be seen that the model with the line edge size of “5mm,9mm” has converged with the model with the line edge size of “6mm,11mm”. This is supported by the displacement convergence shown in Figure 24. It can be seen that the model with a line edge size of 6mm,11mm has converged to the model with a line edge size of 5mm,9mm.

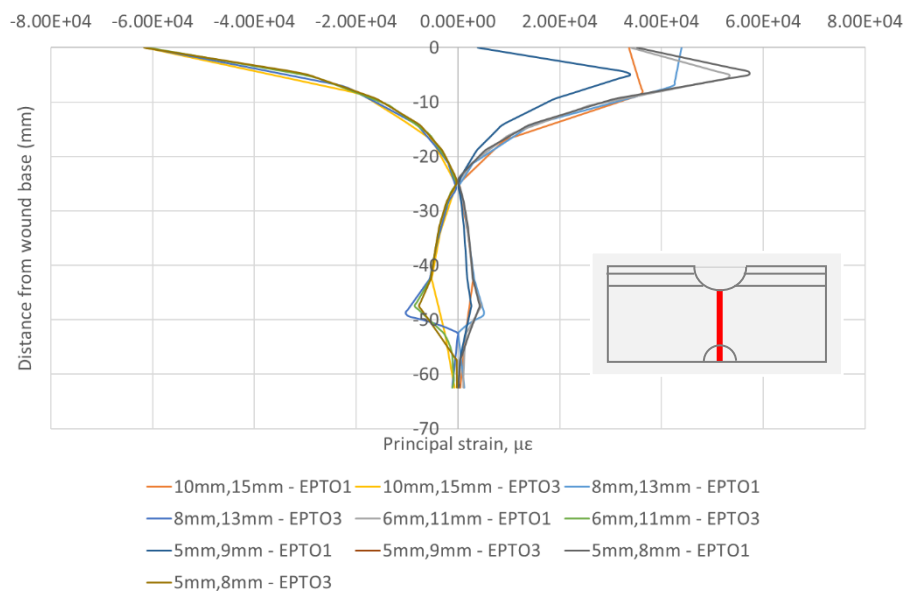


**Figure 23** Convergence of 1<sup>st</sup> and 3<sup>rd</sup> principal strain along a central path with varying line edge size for the macroscopic model

Many different configurations of the model were used and to avoid repeated mesh convergence testing for each configuration (as summarised in TABLE 4), a significantly finer mesh than this mesh convergence study suggested was acceptable was used. Therefore, whilst the convergence testing proved that a central line edge size of 5mm would be acceptable, a mesh size of 0.25mm was used. This is 20 times finer and therefore the convergence of all following models is guaranteed. This is shown in Figure 24 by the convergence between the “5mm,9mm” model and the “0.25mm,0.5mm” model. The mesh

was proportionately fine through the skin layer which was 2.5mm thick. Due to the large number of elements used by the model, a final mesh plot was unable to be included as it would have appeared as a solid black colour due to the element edges being close together.

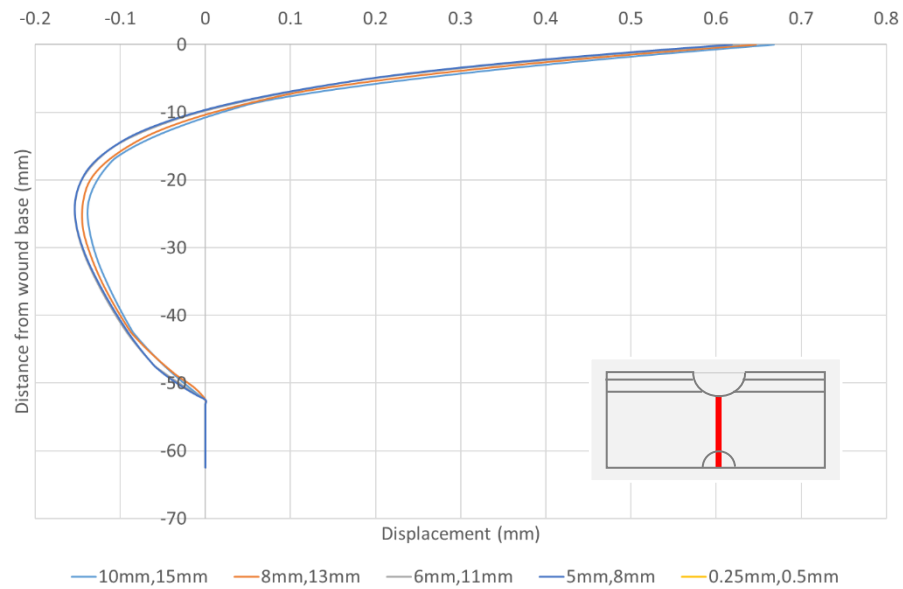


**Figure 24** Convergence of displacement along a central path with varying line edge size for the macroscopic model

To ensure the model size and boundaries did not impact the results produced, initial testing was carried out varying the size of the model and the thickness of layer of shell elements, looking at the principal stresses and strains, and Von Mises stress and strain. Paths were plotted across the surface of the model and along the Y-axis. The principal stresses and strains were then mapped onto these paths and plotted as a graph. This allowed an insight into to see whether the model was behaving as expected in a symmetrical manner. The testing also ensured the boundary conditions were not stopping the stress/strains in the model from decreasing. A horizontal cross section was also taken to investigate how the stress/strain dissipated vertically through the layers of the model.

Once this initial testing had been carried out, the many variables of the model could be adjusted to investigate the impact these have on the results being produced. The variables are shown in Table 4 below.

**Table 4** The variables the model was tested under during the development of the *in silico* model. The wound shape for these variables is hemispherical.

Wound Shape: 	Model dimensions (mm)	Layer (mm)				Diameter (mm)	Pressure (mmhg)
		Skin	Fat	Muscle	Bone		
Varying Transverse Model Dimensions (x and z)	300 240 180	2.5	10	60	20	60	200
Varying Skin Thickness	300	1.5 2.5 3.5	10	60	20	60	200
Varying Fatty Tissue Thickness	300	2.5	5 10 15	60	20	60	200
Varying Muscle Thickness	300	2.5	10	40 60 80	20	60	200
Varying Bone Thickness	300	2.5	10	60	10 20 30	60	200
Varying Wound Diameter	300	2.5	10	60	0	25 42.5 60	200
Varying Pressure	300	2.5	10	60	20	60	100 150 200

## 4.3 Basic Model Analysis

### 4.3.1 Effect of Model Dimensions

To ensure the model dimensions and boundary conditions did not influence the results, initial tests examined the effects of model size. With an assumed wound diameter of 60mm, the overall model dimensions were varied between 300mm (1:5 ratio), 240mm (1:4 ratio), and 180mm (1:3 ratio), assuming linear material properties and a pressure of 200 mmHg (0.0266645 MPa). Figure 25 presents the resultant variation in 1st and 3rd principal strains along a path down the centre of the model (i.e., through the 'muscle' and 'bone' materials) for these three different model sizes. The location of the path in this figure and paths in subsequent figures is highlighted in red in the small schematic (not to scale).

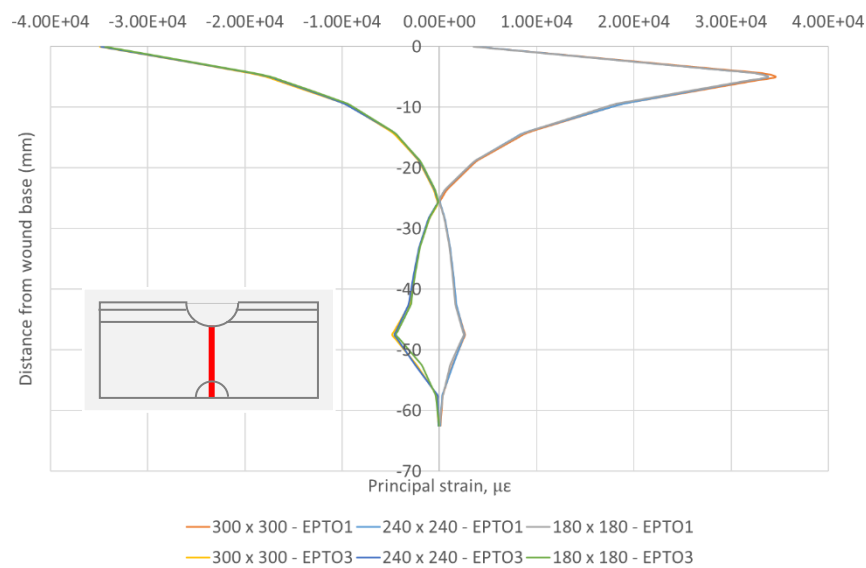


**Figure 25** The effect of variation in model dimensions on the 1<sup>st</sup> and 3<sup>rd</sup> principal strains down the central vertical path of the models. (The location of the path in this figure and subsequent figures is highlighted in red in the small schematic).

Clearly the results are very close to each other, and the 300x300 and 240x240 models in particular frequently overlap each other, confirming that there is no advantage in modelling a larger volume. Considering the 1<sup>st</sup> principal strain in more detail, it is evident that the peak tensile strain is approximately equal for all model dimensions. The tensile zone ends at approximately 25mm below the wound base for all models when equiaxial strain is achieved. 1<sup>st</sup> principal strain then increases to reach a second peak at approximately 47mm below the wound surface. The strain then reduces once more, reaching negligible strain at approximately 62mm below the wound surface.

Upon studying the 3<sup>rd</sup> principal strain in Figure 25, it can be seen that the models run synchronously throughout, with minor variations occurring between 50 and 55mm below the wound surface.

Figure 26 shows the variation in displacement along the same central path, again through the 'muscle' and 'bone' materials.

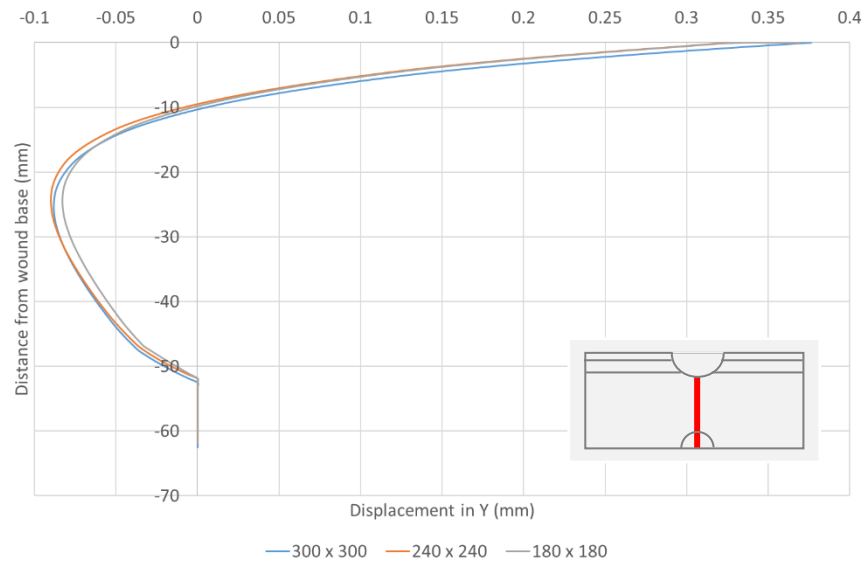


**Figure 26** The variation in vertical displacement along the central axis with variation in model size. A similar pattern is followed for all model variations with minimal dissimilitude in the data sets.

Figure 26 demonstrates, that while all the models follow a similar pattern, there is some variation in the values. It is of note that until approximately 10mm below the wound base, the wound is being lifted, presumably by the negative pressure. Over this 10mm range, the 240mm and 280mm models run concurrently, with the 300mm model having a slightly greater value of displacement. Below -10mm, the models experience compression. The compression is approximately equal for the 300mm and 240mm. The 180mm has approximately 0.01mm less displacement in the area of compression. The models then reach the muscle-bone interface and the path travels through the bone. At this point, the displacement is neutral, because of the relative stiffness of the bone.

The distribution of the 1<sup>st</sup> and 3<sup>rd</sup> principal stresses along a path down the wound face, starting from the upper surface are presented in Figure 27.

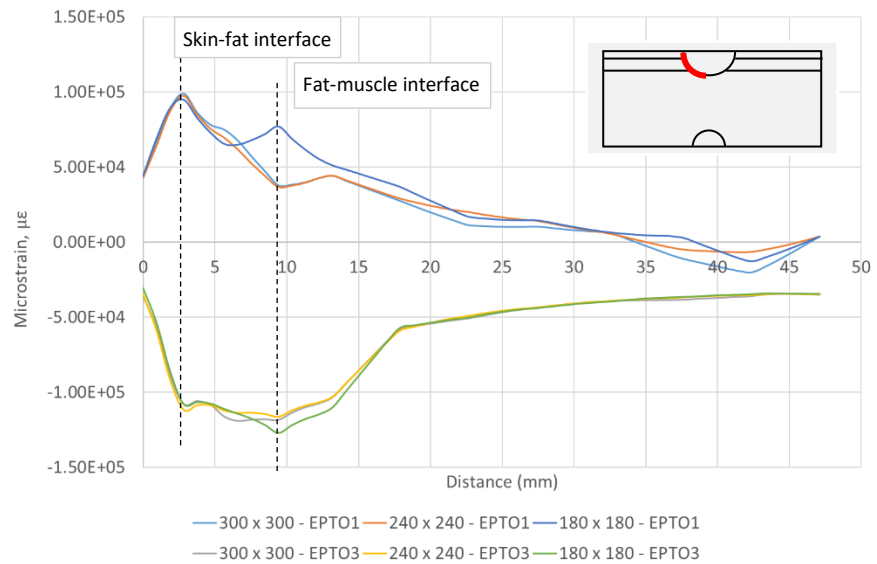


**Figure 27** The distribution of 1st and 3rd principal strain around the wound circumference with varying model dimensions.

In both the 1<sup>st</sup> and 3<sup>rd</sup> principal strains, the results of the 300mm and 240mm models run almost synchronously. The peak tensile strain that occurs at the skin-fat interface, as indicated on the graph, is approximately equal for all models, with a value of  $0.9 \times 10^5 \mu\epsilon$ . From here, the tensile strain for the 300mm model and 240mm model are similar with a maximum difference of approximately  $0.1 \times 10^4 \mu\epsilon$  where the strain experienced by the 300mm model is less than that of the 240mm model. The 180mm model has a significant difference in peak tensile strain at the fat-muscle interface, with the tensile strain for this model being approximately  $7.5 \times 10^4 \mu\epsilon$  in comparison to approximately  $4.5 \times 10^4 \mu\epsilon$  for the 300mm and 240mm models.

The 3<sup>rd</sup> principal strain demonstrates a similar relationship between the models with the 300mm and 240mm models experiencing very similar strain levels throughout, whereas the 180mm model generally experiences increased compressive strain which is particularly apparent at the fat-muscle interface.

In Figure 28, the horizontal displacement (UX) around the wound circumference is shown, where a negative value indicates that wound is enlarging. Whilst all three models run approximately concurrently throughout, the local peak at approximately 2.5mm around the wound is greater for the 180mm model with a value of approximately -0.7mm displacement in comparison to approximately -0.78mm for the 240mm and 300mm. From this point onwards, the models run synchronously in terms of displacement around the wound circumference. The maximum wound enlargement occurs in the centre of the fat layer, beyond the edge of this layer, it decreases linearly to zero (at the vertical axis of the model).

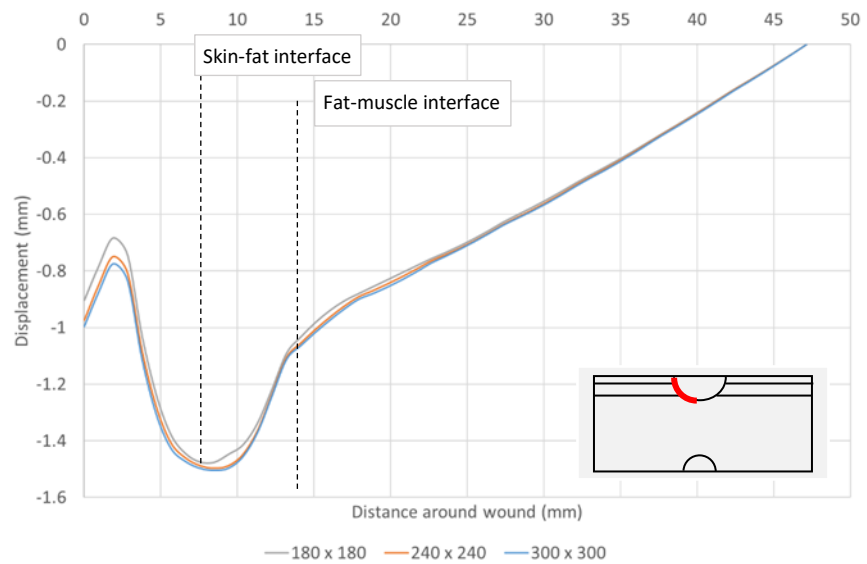


**Figure 28** The horizontal displacement around the wound circumference with varying model dimensions, showing that the wound is enlarging in a transverse direction.

Already these models are showing some interesting information on the behaviour of the wound when subjected to a negative pressure. The results clearly show that there is negligible difference between the results of the 300x300 and 240x240 models, and hence the later size was used in all modelling going forward.

### 4.3.2 Varying Film Surface Shell Element Thickness

In order to simulate a film over the surface of the model, a layer of shell elements was added to the top of the model. This section examines the sensitivity of the model's performance to the thickness of those shell elements. The thickness and type of film used in practice can vary, hence in this analysis the thickness of the layer varies by two orders of magnitude from 0.01 to 1mm.

Figure 29 shows the variation in the 1<sup>st</sup> and 3<sup>rd</sup> principal strains with the variation in surface shell thickness. The plots in this figure are superimposed on each other, confirming negligible variation in the central results when the surface shell layer thickness is varied. From this, it can be deduced that this variation has no impact on the results gained along the central path from the wound base.

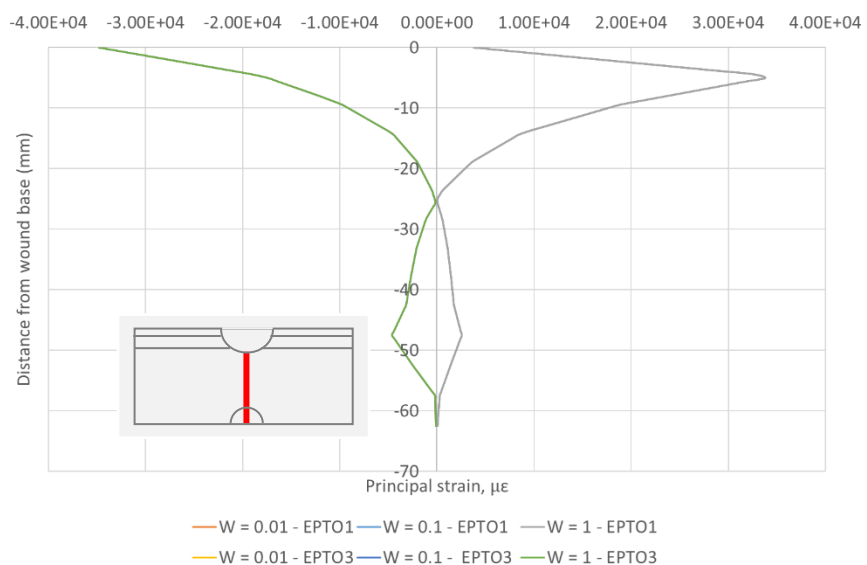


**Figure 29** The distribution of 1st and 3rd principal strain along a centrally plotted path when the surface shell thickness is varied.

As with the principal strains displayed in Figure 29, the vertical displacement along the central axis from the wound base also showed a minimal variation between models. This pattern repeats for the path plots around the circumference of the wound, as can be seen in Figure 109 found in Appendix 2.

It can, therefore, be concluded that varying the thickness of the shell elements on the surface has little, if any, impact on the results produced. Although the thickness of these shell elements has little influence over the results gained, the shell elements themselves are representing the plaster that covers a wound. Therefore, a realistic thickness should be applied to the model. In this case, future models will have a surface shell thickness of 0.1mm.

### 4.3.3 Varying Wound Surface Shell Elements (for Pressure Application)

To simulate the application of negative pressure on the wound, a negative pressure needs to be applied over the surface of the wound itself. To enable the easy application of that pressure and facilitate the extraction of in-plane surface wound stresses and strains, a lining of thin shell elements was applied over the wound surface. This lining needed to be as thin as possible so that it did not impact the results produced by the model, to confirm this was the case a number of different lining thicknesses were applied in the model. Figure 30 shows the influence of varying the thickness of the wound lining on the 1<sup>st</sup> and 3<sup>rd</sup> principal strains.

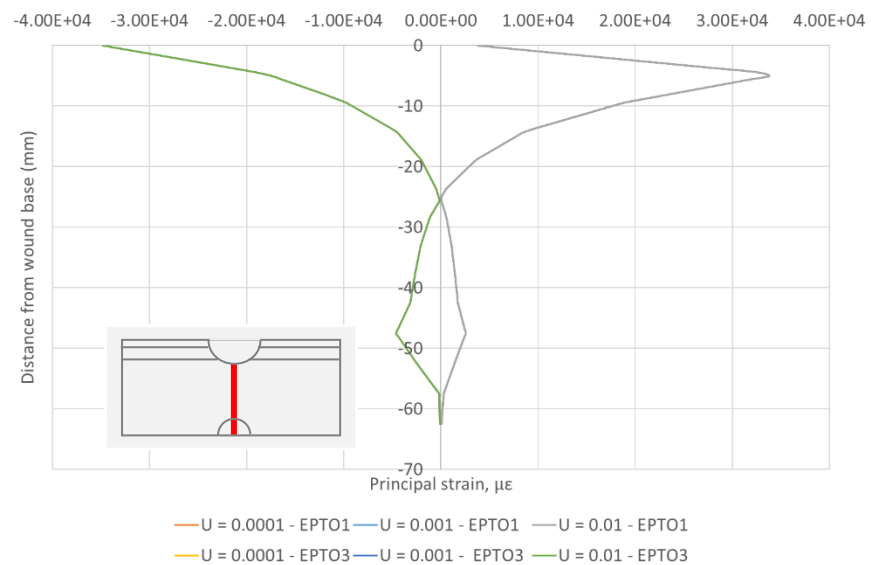


**Figure 30** The distribution of 1st and 3rd principal strain along a central vertical path with varying wound shell thickness.

Again, it can be seen that there is no visible variation between the data plotted on the graph, implying that, once again, the thickness of the shell elements has no impact on the 1<sup>st</sup> and 3<sup>rd</sup> principal strains down the central axis. Thus, it can be concluded that this two order variation in thickness of the layer of shell elements has a negligible impact on the results gained by these experiments. Hence a layer thickness of 0.0001 mm was used in subsequent analyses.

#### 4.3.4 Linear vs Non-Linear Material Properties

It is well-known that biological materials frequently exhibit non-linear biomechanical properties, as discussed in Chapter 3, hence the sensitivity of the results to that non-linearity also needs to be investigated to determine whether that it is significant within the range of strains considered in this study. The non-linear and linear properties of the silicones were calculated from the tensile testing carried out in Chapter 3. Hence, in this section discusses and compares the results of the same, standard boundary and loading conditions with both linear and non-linear material properties. Figure 31 presents the resulting 1<sup>st</sup> and 3<sup>rd</sup> principal strains along the central axis for the two conditions.

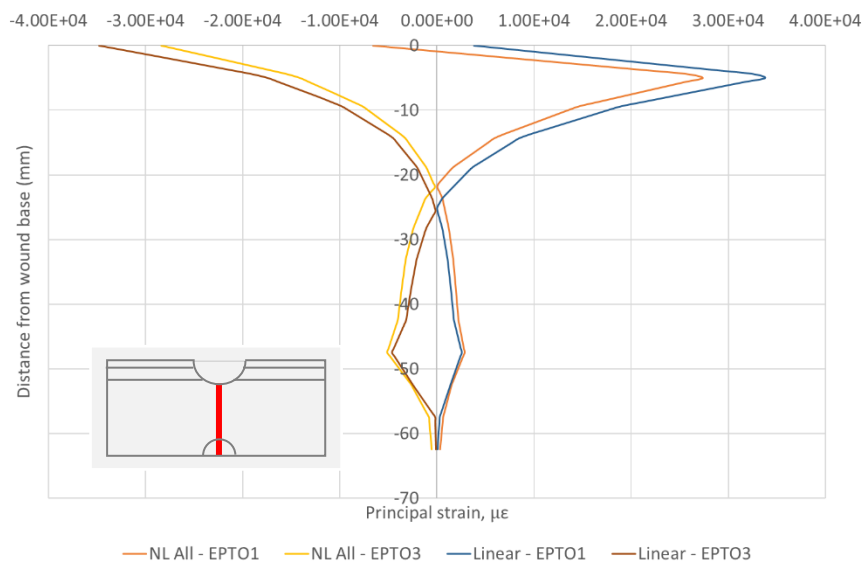


**Figure 31** 1<sup>st</sup> and 3<sup>rd</sup> principal strain plotted along a vertical path from the wound base shows that linear and non-linear material properties produce the same strain profile, but the non-linear stress values are less than those of the linear model.

It can be seen that whilst both linear and non-linear models follow the same pattern, there are some differences. Focussing on the 1<sup>st</sup> principal strain, it can be seen that the initial value for the non-linear model was significantly smaller than that of the linear model with a value of approximately  $-0.5 \times 10^4 \mu\epsilon$  in comparison to approximately  $0.5 \times 10^4 \mu\epsilon$ . From here, the non-linear model continued to be smaller than the linear model throughout, with both models reaching peak tensile strain at the same depth, approximately 5mm below the wound base. The non-linear model then reached equiaxial strain at approximately 2mm closer to the wound base than the linear model. From here, both models closely follow the same path with the non-linear model producing slightly higher strains than the linear model. A similar pattern can be seen with EPTO3.

Figure 32 shows the difference in vertical displacement for the linear and non-linear models. There is a clear difference in the magnitude of vertical displacement. Both datasets run

nearly parallel to each other throughout the muscle layer before converging at the bone. The main variance between the models is the displacement at the wound base. For non-linear models, this is approximately 0.1mm less than that of the linear model. In addition, the non-linear model first experiences compression at a shallower depth to the linear model, approximately 6mm below the wound base compared to 10mm for the linear model. This is not the only difference experienced by the model. The maximum compressive displacement is also much greater for the non-linear model at 0.13mm, compared to 0.08mm for the linear model.

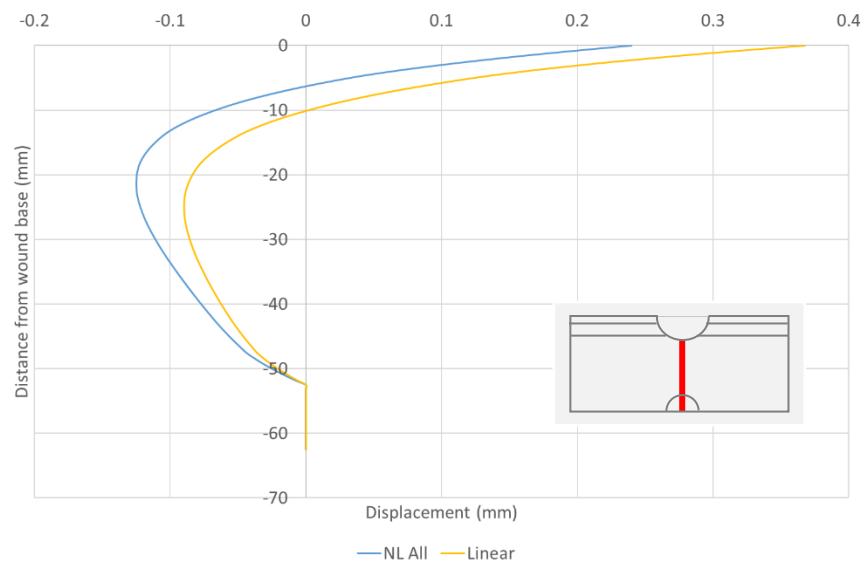


**Figure 32** Vertical displacement along a centrally plotted path in the y-direction shows that the non-linear model experiences greater displacement than the model with linear material properties.

The distribution of 1<sup>st</sup> and 3<sup>rd</sup> principal strain down the wound face is presented in Figure 33. It can be seen that there is little difference in the linear and non-linear 3<sup>rd</sup> principal strain around the wound. The most notable difference in this figure is the initial 1<sup>st</sup> principal stress peak, which is 25% larger than the non-linear value.

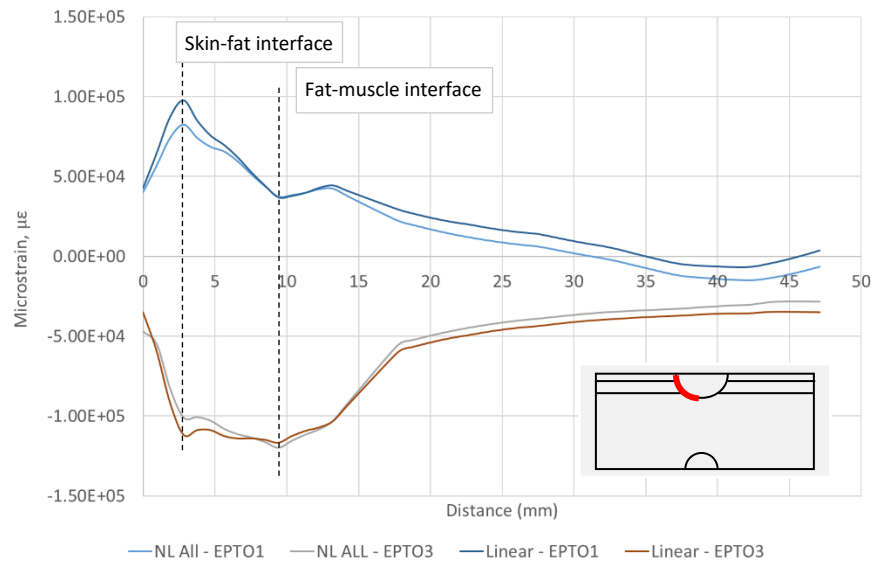


**Figure 33** The distribution of 1<sup>st</sup> and 3<sup>rd</sup> principal strains down the wound face follows a similar pattern for both the linear and non-linear model. The key difference is the magnitude of the 1<sup>st</sup> principal strain through the skin layer where the linear value is larger than that of the non-linear model.

The distribution of horizontal displacement down the wound face can be seen in Figure 34. As with previous models, the horizontal displacement down the wound face is greater in the linear model than the non-linear model. This is a common theme throughout the figures in this section. The initial peak displacement for the linear model has a value of approximately -0.7mm whereas the equivalent point for the model with non-linear material properties is approximately -1.1mm. After this initial variation, the displacements follow a similar pattern. The maximum compression occurs at approximately 7mm around the wound face, which lies within the fat layer.

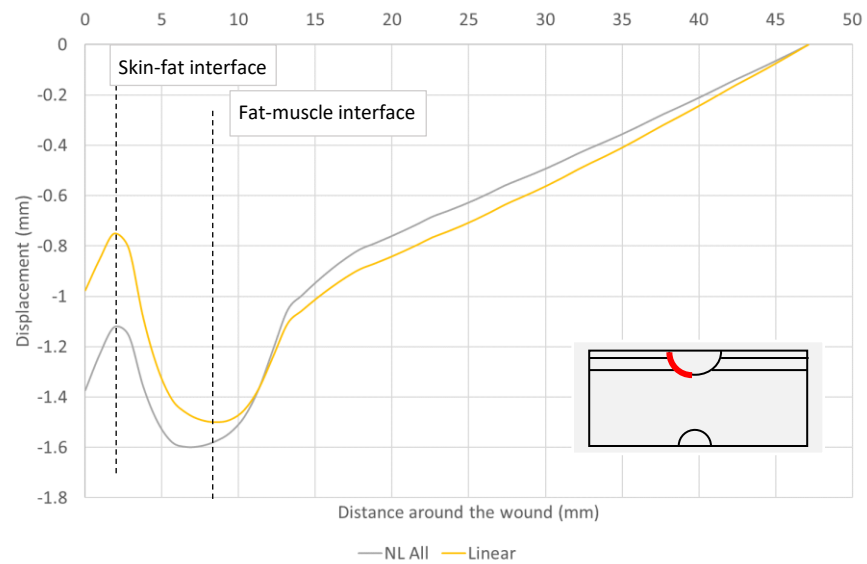


**Figure 34** The horizontal displacement down the wound face models with both linear and non-linear material properties. Both models follow the same pattern with a greater displacement being experienced by the non-linear model through the skin and fat layers, and the linear model through the muscle layer.

From Figure 31 to Figure 34, it can be seen that, whilst there is some variation in the results predicted from changing the material properties to non-linear values, for this particular model and loading conditions, this variation is minimal and does not significantly affect the distribution of the stresses and displacement in the model. Therefore, it is considered reasonable to continue with linear material properties from this point forward, since it allows a faster solution of the models and does not introduce potential unexpected effects due to uncertainties in the degree of non-linearity of the different materials.

### 4.3.5 Initial Model Testing – Varying Dimensions

In this section, the impact of varying tissue thickness, and bone and wound radii is examined. Three thicknesses of each material are investigated, as well as three different radii for the bone and wound profile. In these models, the parameter under investigation while the rest of the model's dimensions are held constant, as summarised in Table 4.

#### 4.3.5.1 Varying Skin Depth

In Figure 35, the impact of varying the thickness of the skin layer between 1.5 and 3.5mm is presented. When focussing on 1<sup>st</sup> principal strain, the initial value, at the base of the wound, is approximately  $-1.1 \times 10^4 \mu\epsilon$  for skin with a thickness of 1.5mm. This is significantly less than both the models with 2.5mm and 3.5mm skin thicknesses. Up to a depth of approximately 1.5mm for the model with 1.5mm skin depth, the muscle experiences a compressive strain in all three directions for all three skin thicknesses. At roughly 5mm below the wound base, a peak value of tensile strain is achieved. This value is approximately the same for all three models. The models reach equiaxial strain between 22mm and 28mm below the wound base. From here, the model experiences tensile strain once more, before returning to equiaxial strain at approximately 58mm below the wound bed.

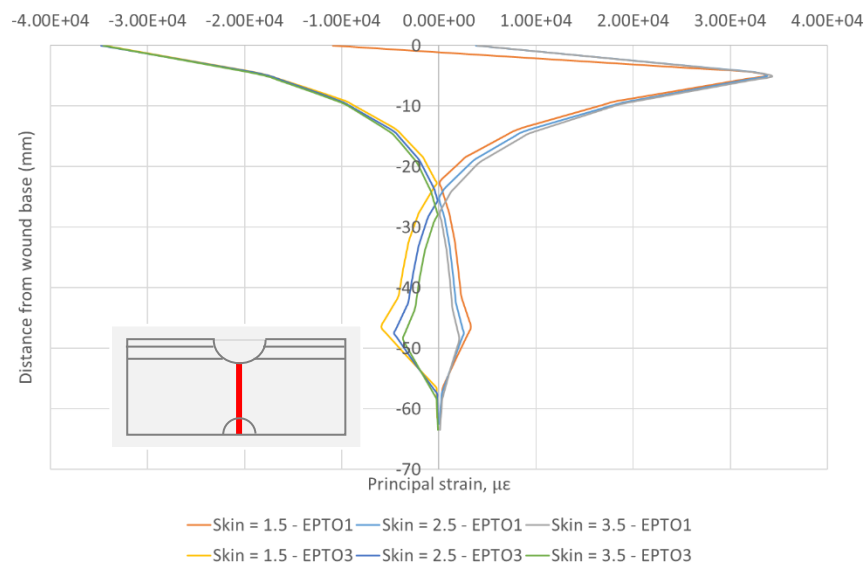


**Figure 35** 1<sup>st</sup> and 3<sup>rd</sup> principal strains along a centrally plotted path for different skin thicknesses. It can be seen that the results follow the same pattern, but with the magnitude of the tensile strains decreasing and compressive strains increasing as thickness decreases.

The vertical displacement along the central axis for models with varying wound thicknesses is shown in Figure 36. Again the results follow a similar profile to each other until

approximately 48mm below the wound base when the models converge. In general, the greater the thickness of the skin layer, the greater the value of displacement in the vertical direction.

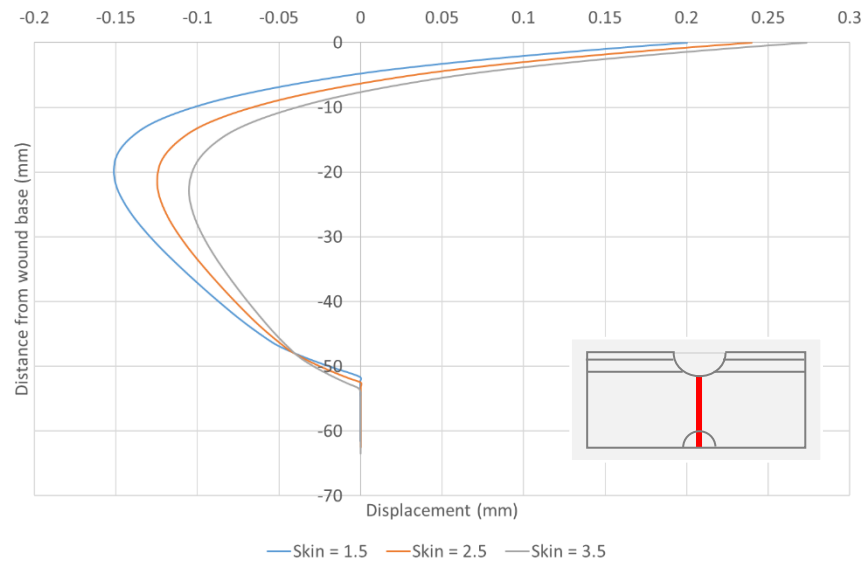


**Figure 36** A graph showing the vertical displacement along the central y-axis. The greater the thickness of the skin layer, the lower the magnitude of deformation.

In addition to plotting the principal strains down the vertical axis, the stresses around half of the wound were recorded. The 1<sup>st</sup> and 3<sup>rd</sup> principal strains recorded around the wound circumference are shown in Figure 37.

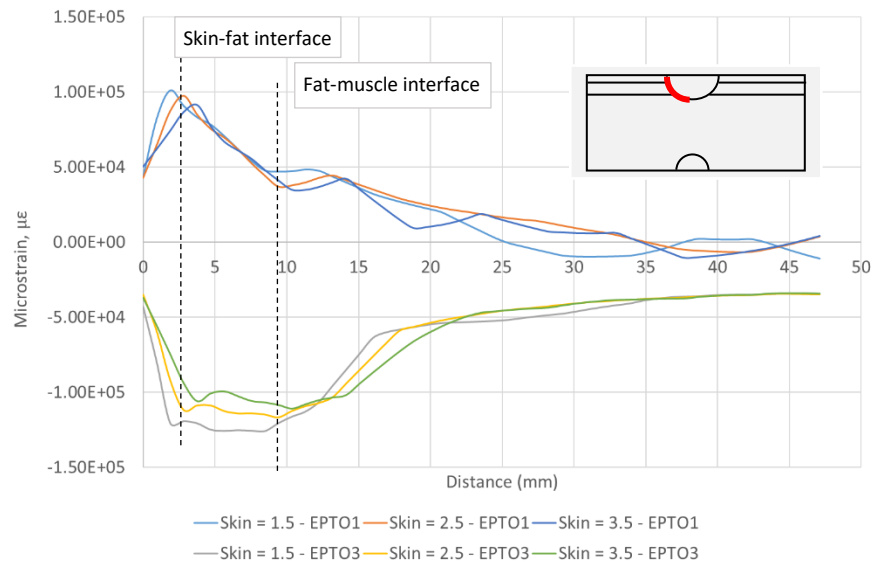


**Figure 37** Plot of the 1<sup>st</sup> and 3<sup>rd</sup> principal strains down the wound face when the skin thickness is varied. A similar pattern is followed throughout the graphs with the main differences being a higher value of 1<sup>st</sup> principal strain for the 1.5mm skin thickness model at the skin-fat interface.

Initially, the value of 1<sup>st</sup> principal strain for all three models is approximately equal, however the first difference becomes apparent at the skin-fat interface. At this point, the peak tensile strain is greatest for the 1.5mm skin model. From here, the models gradually decrease with various undulations until all three models experience negative tensile strain from approximately 35mm around the wound face. For the model with a 1.5mm skin thickness, negative tensile strain occurs much sooner, at approximately 25mm around the wound face. From here, this model experiences a period of positive tensile strain before returning to negative tensile strain at approximately 44mm around the wound face.

When looking at 3<sup>rd</sup> principal strain, it can be seen that the greatest strain is experienced by the 1.5mm skin model until approximately 12.5mm around the wound face when the 1.5mm skin thickness model has the lowest compressive strain, and the 3.5mm skin thickness model has the highest compressive strain. From approximately 20mm around the wound face, the models converge and little difference in compressive strain is visible between them.

The displacement around the wound diameter is shown in Figure 38. Initially, as the skin thickness increases, the displacement decreases, as expected. This continues until the model reaches the subcutaneous fat-muscle interface. At this point, the models experience a sudden reduction in the magnitude of displacement, after which the displacement decreases linearly to the centre line.

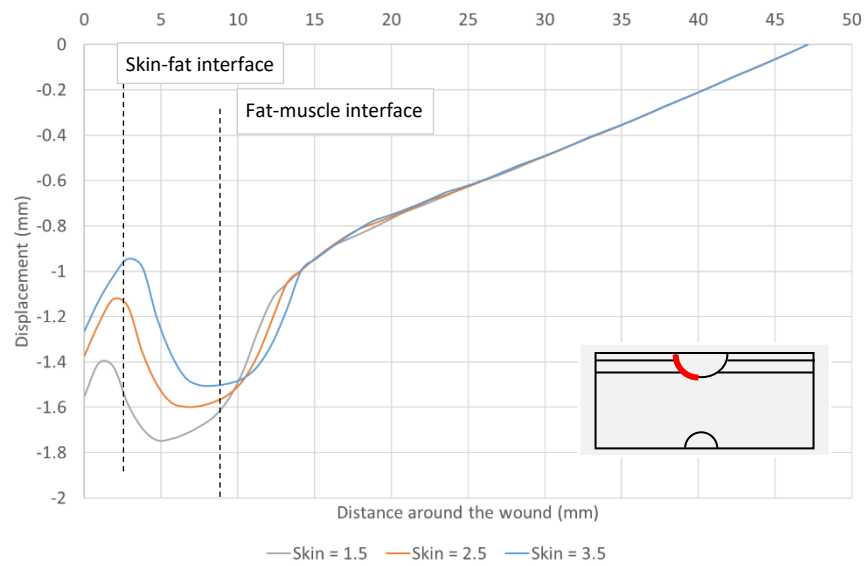
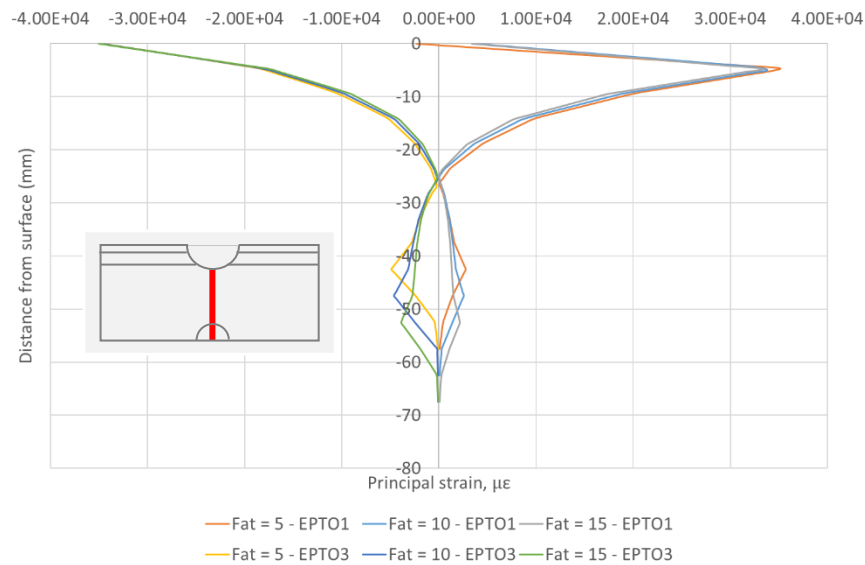


**Figure 38** Variation of the horizontal displacement around the wound circumference when skin thickness is varied. Prior to reaching the muscle layer, the pattern of the greater the skin thickness, the smaller the magnitude is observed.

From this point, the models run concurrently.

#### 4.3.5.2 Varying Subcutaneous Fatty Tissue Depths

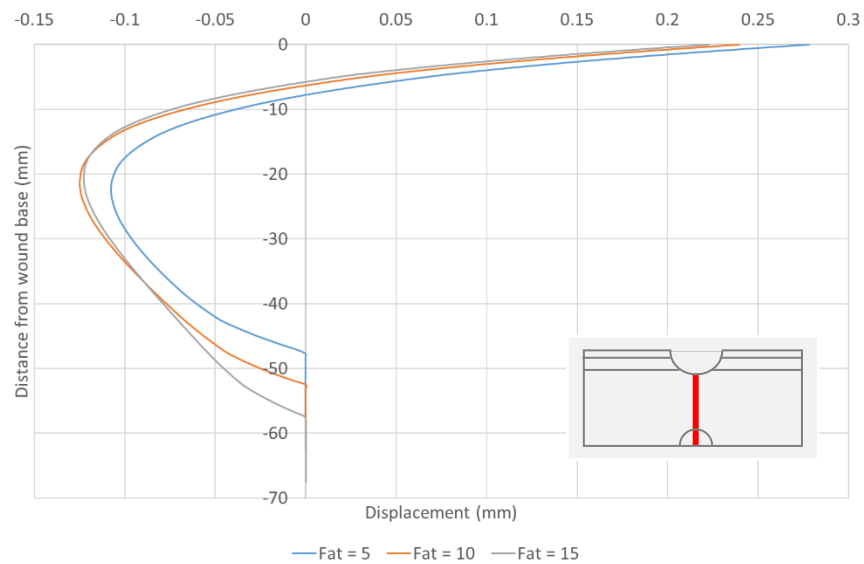
Figure 39 shows the variation of 1<sup>st</sup> and 3<sup>rd</sup> principal stresses for different thicknesses (5, 10 and 15mm) of subcutaneous fatty tissue.



**Figure 39** 1<sup>st</sup> and 3<sup>rd</sup> principal strain along a central path, with varying subcutaneous fatty tissue thickness. There is minimal variation in the stresses along the majority of the plots. Where variation occurs, the thinner fatty tissue models have higher 1<sup>st</sup> principal strain than the models with thicker layers of subcutaneous fat.

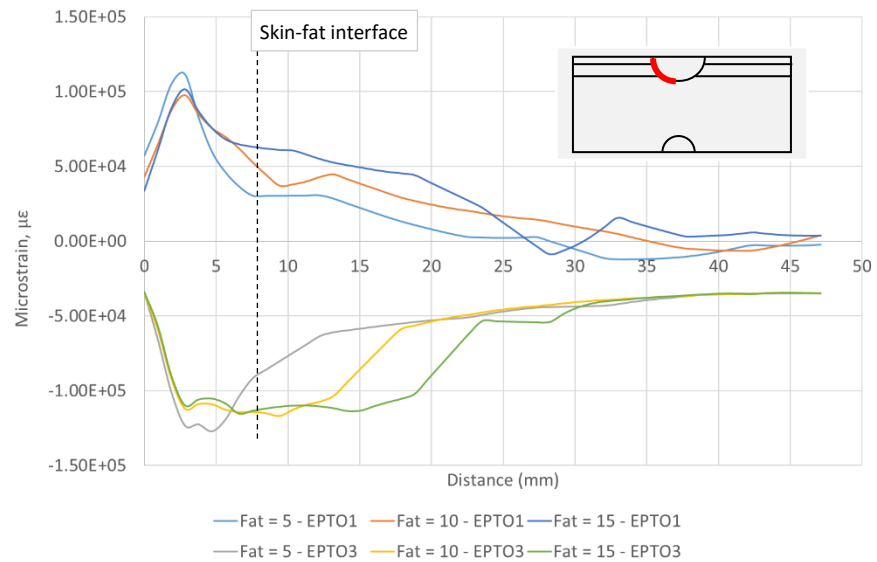
The 1<sup>st</sup> and 3<sup>rd</sup> principal strains for varying subcutaneous fatty tissue thickness, follow a similar pattern to those produced varying skin in Figure 38. The models follow a very similar pattern and run concurrently showing little difference. The primary change occurs in the muscle layer at the base due to the depth of the fat influencing the depth of the muscle. When looking specifically at the 3<sup>rd</sup> principal strain, initially, the values of 3<sup>rd</sup> principal stress for all three thicknesses of subcutaneous fat are homogenous, with the three models running with very little variation throughout.

Figure 40 presents the vertical displacement through the y-axis. What is particularly apparent when looking at this graph is that throughout the path plot, the displacement for the models with 10mm and 15mm subcutaneous fat is almost the same apart from at the muscle-bone intersection. In comparison, the model with a subcutaneous fat thickness of 5mm, persistently runs with an increased displacement in the tensile direction than the remainder of the models.



**Figure 40** A graph showing the vertical displacement along the central y-axis when the thickness of subcutaneous fatty tissue is varied. The plots for the 10mm and 15mm fat thickness run almost simultaneously, with little variation. In comparison, the 5mm fat model has a much smaller magnitude throughout

The distribution of 1<sup>st</sup> and 3<sup>rd</sup> principal strain around the wound circumference with varying subcutaneous fat depths is presented in Figure 41. It can be seen that the value of 1<sup>st</sup> principal strain at the wound bed reduces with increased fat thickness. Following the initial peak at the skin-fat interface, the greater tensile strains are experienced by the thicker fat layers. Apart from a minimum tensile strain experienced by the 15mm fat thickness model at approximately 28mm around the wound face, the models run approximately  $1.5 \times 10^4 \mu\epsilon$  apart for the majority of the path.



**Figure 41** The variation in 1<sup>st</sup> and 3<sup>rd</sup> principal strain around the wound circumference when the thickness of subcutaneous fatty tissue is changed. It can be seen that the thinner the fatty tissue layer, the greater the magnitude of tensile strain.

For compressive strain, it can be seen that the model with 5mm thickness of subcutaneous adipose tissue has a greater compressive strain at the skin-fat interface. From this point, 10mm and 15mm fat thickness models maintain a near constant compressive strain until the fat-muscle interface when the 3<sup>rd</sup> principal strain decreases. At approximately 20mm around the wound face, the models merge and the strain experienced is approximately the same.

The horizontal displacement around the wound circumference is presented in Figure 42.



**Figure 42** The distribution of horizontal displacement around the circumference of the wound when the thickness of subcutaneous fatty tissue is varied. The greater the fat thickness, the greater the displacement.

As with varying skin thicknesses, shown in Figure 38, it can be seen that initially, the greater the subcutaneous fatty tissue thickness, the smaller the displacement with the initial peak for the model with a thickness of 5mm being approximately -1.05mm, in comparison to approximately -1.19mm for the model with an initial thickness of 15mm. This occurs at the skin-fat interface, approximately 2.5mm around the wound circumference, from here, there is a maximum displacement through the fatty tissue, with the larger the fat thickness the greater the displacement. Once the path plot reaches the fat-muscle interface, the models have a simultaneous displacement until the middle of the vertical circumference when there is negligible displacement in the horizontal direction. These displacements are more significant than those of the varying skin thicknesses and show a clear compression of the fat layer.

#### 4.3.5.3 Varying Muscle Depth

Figure 43 presents the distribution of 1<sup>st</sup> and 3<sup>rd</sup> principal strain with varying muscle depths.

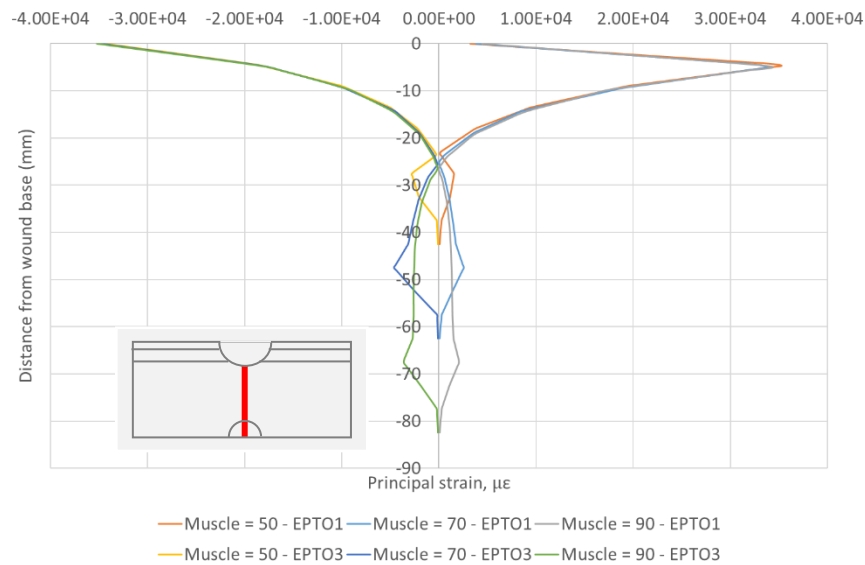


**Figure 43** A graph of 1<sup>st</sup> and 3<sup>rd</sup> principal strains throughout the model when the muscle thickness is varied. Prior to reaching the muscle layer, all models have the same strain. Following this, the smaller muscle thicknesses have a greater magnitude of compressive strain.

There is minimal difference in the 1<sup>st</sup> principal strain until the strain reaches the point of equilibrium. From this point, the 1<sup>st</sup> principal strain increases once more with the smaller model, 50mm muscle thickness, reaching a second peak tensile strain at 29mm below the wound base. In comparison, the 70mm and 90mm models achieve their second peak tensile strain at approximately -48mm and -68mm respectively. Following this, the models converge once more. This variation fits with the variation of the muscle depth and therefore the point in which the bone and base are reached. The main difference below this is the separation as each model reaches bone and subsequently the base of the model. This is important as it shows the depth of the model does not impact the strains experienced at the wound bed.

In comparison, the plot of 3<sup>rd</sup> principal strain shows there is great similarity in the values throughout the model, until approximately 20mm below the wound base. At this point, the graphs separate as the paths reach bone and subsequently reach the base of the model.

Figure 44 shows the vertical displacement (UY) along the central axis with varying muscle thickness.

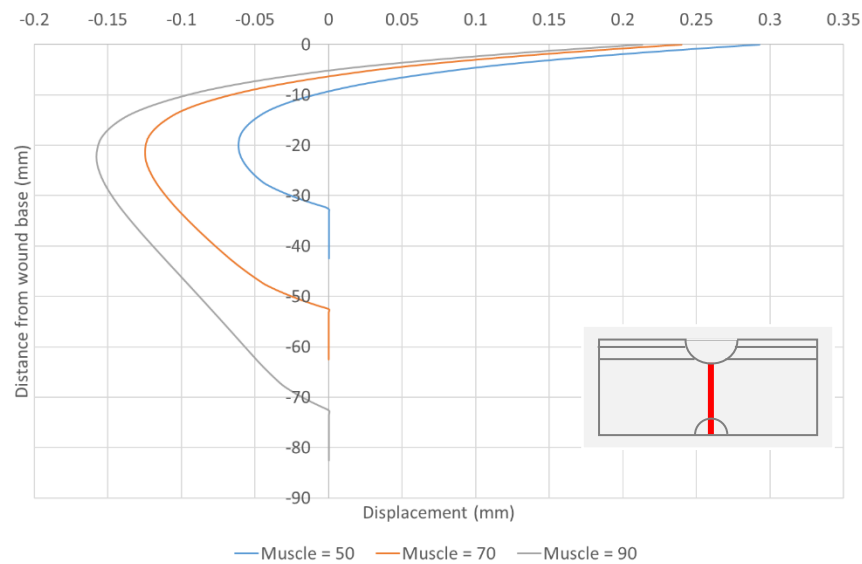


**Figure 44** The vertical displacement along the central y-axis for models with varying muscle thickness. The greater the muscle thickness, the greater the displacement in the y-direction.

The models initially all have a similar value of displacement. The 50mm model has an initial value of displacement approximately 0.3mm. This is in comparison to an initial value of displacement at the wound base for the models with muscle thicknesses of 70 and 90 mm being approximately 0.25 mm. The model is being brought up by negative pressure to a distance of approximately 6mm from the wound base for the 70mm and 90mm models. In contrast, the tensile zone for the 50mm model ranges from 0mm to 10mm below the wound base. A clear trend can be observed where an increase in muscle depth is associated with a greater compressive displacement. Once the paths reach the muscle-bone interface, they all return to a neutral displacement which continues until the path reaches the model base. It can be seen that there is a significant difference in displacement experienced through the muscle layer when the depth is varied.

The distribution of 1<sup>st</sup> and 3<sup>rd</sup> principal strain around the wound circumference is shown in Figure 45. There is little difference between the values of 1<sup>st</sup> principal strain for the models between 0mm and approximately 10mm. This is roughly between the model surface and the fat-muscle interface. At this point the models separate minimally and produce an extremely small difference in the stress values. The path plot results continue to run concurrently until they reach the base of the wound when there are some deviations.

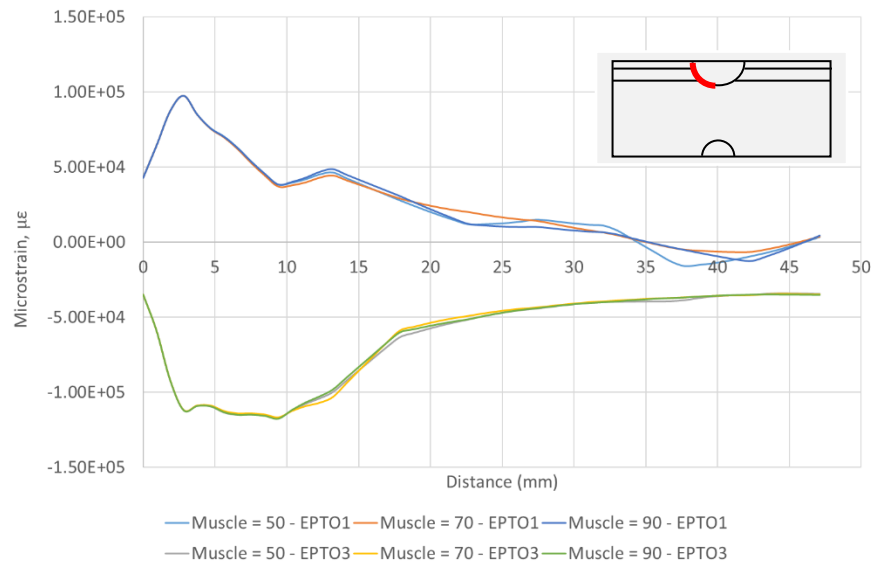


**Figure 45** 1<sup>st</sup> and 3<sup>rd</sup> principal strain around the wound circumference when the muscle thickness is varied. Prior to the muscle layer, there is no variation in the strain values. The variation throughout is minimal. No clear pattern of variation is visible, however all models run closely.

A similar pattern is followed for 3<sup>rd</sup> principal strain. There is no variation between the models for the stress values around the wound, until the fat-muscle interface is met. At this point there is minimal difference and the models primarily run concurrently.

#### 4.3.5.4 Varying Bone Diameter

The central distribution of 1<sup>st</sup> and 3<sup>rd</sup> principal strain when the bone diameter is varied can be seen in Figure 46.

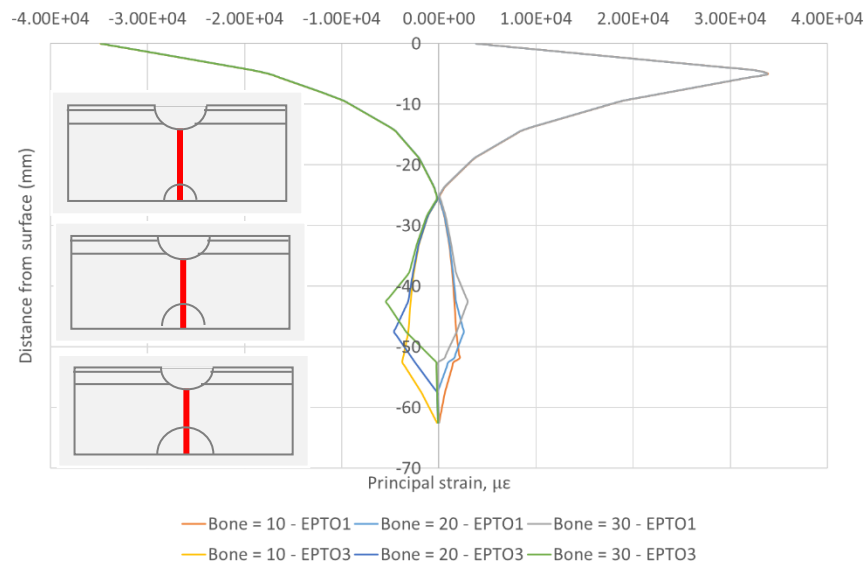


**Figure 46** The distribution of 1<sup>st</sup> and 3<sup>rd</sup> principal strain through the central Y-axis when the diameter of bone is varied. There is no variation through the soft tissue layers. The only obvious variation is the depth of the bone-muscle interface.

It is shown that the peak tensile strain and the equiaxial strain were the same for all three bone diameters. In fact, the 1<sup>st</sup> and 3<sup>rd</sup> principal strains with varying bone diameters did not change until the muscle-bone interface. Currently, it seems that the variability in the 3<sup>rd</sup> principal strain is predominantly associated with the distance between the muscle insertion point and the bone. The rationale for the discrepancy in bone strains observed in the 1<sup>st</sup> principal strain is not as easily understood. It appeared that the smaller the bone diameter, the larger the value of 1<sup>st</sup> principal strain. The value for bone with a diameter of 10mm was significantly bigger than the bones with diameters of 20mm and 30mm.

In Figure 47, the vertical displacement along the y-axis can be seen for models with varying bone diameters.

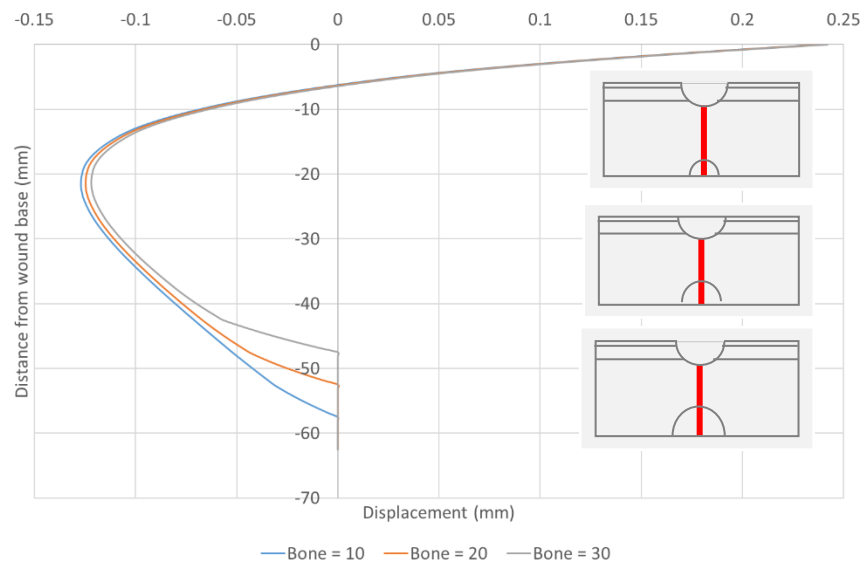


**Figure 47** The distribution of vertical displacement through the central y-axis. There is minimal variation throughout, although the smallest bone diameter has a slightly higher displacement than the larger bone diameters.

Initially the vertical displacement along the central Y-axis is the same for all variations of the model. Once the model reaches approximately -15mm below the wound base, there is a small separation between the models of approximately 0.01mm. The path plot results then run parallel to each other until the muscle-bone junction at which point the results separate and have a neutral displacement.

Figure 48 shows the 1<sup>st</sup> and 3<sup>rd</sup> principal strains around the circumference of the wound with varying bone diameters. From this figure, there is no variation between the models, with the plots running concurrently. It is noteworthy that in this graph, the path does not extend to the bone level, which is the variable being analysed.

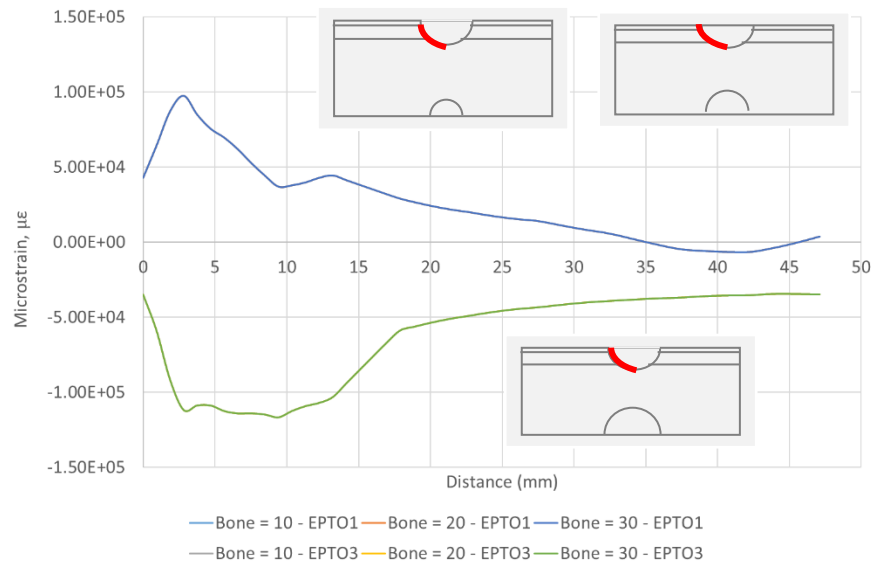


**Figure 48** 1<sup>st</sup> and 3<sup>rd</sup> principal strain around the wound circumference. There is no noticeable variation between the models.

#### 4.3.5.5 Varying Wound Diameter

The last study into wound geometry that was carried out in this initial testing stage of the model development investigated the effect of altering the diameter of the wound. Figure 49 shows the variation of 1<sup>st</sup> and 3<sup>rd</sup> principal strain through the central vertical axis.

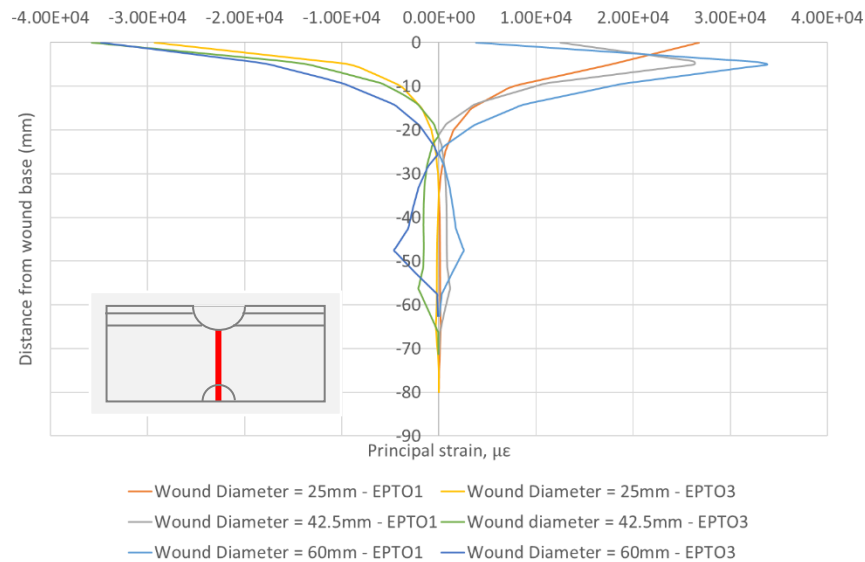


**Figure 49** The 1<sup>st</sup> and 3<sup>rd</sup> principal strains with varying wound diameters.

The 1<sup>st</sup> principal strain follows a similar shape as is observed in previous figures. It is of note that the initial strain experienced at the base of the wound is much greater for the model with the 25mm wound diameter and that this model does not experience a peak tensile strain at approximately 5mm below the wound surface unlike the 42.5mm and 60mm wound models. The model with a 60mm wound has the greatest tensile maximum, approximately  $1 \times 10^4$   $\mu\epsilon$  larger than that of the 42.5mm wound model at 5mm below the wound base. The model with the larger wound continues to experience greater tensile strain than the other models throughout the path.

The 3<sup>rd</sup> principal strain does not demonstrate as large variations between wound size as the tensile strain. It is seen that throughout the model, as with the tensile strain, the larger wound model experiences greater strain.

In Figure 50 the vertical displacement through the model can be seen. Throughout the figure, the greater wound diameters are observed to induce a greater displacement. In general, due to the variation in the distance from the base of the wound to the model base, the displacement graphs appear more elongated the greater the measured distance. The displacement for all models becomes neutral through the bone.

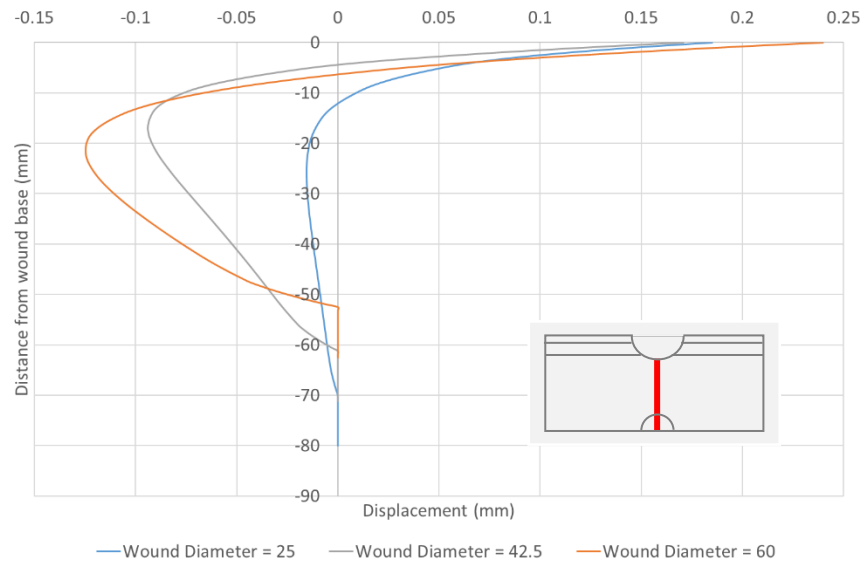


**Figure 50** The vertical displacement through the centre of the model when the wound diameter is varied. In general, the larger the wound, the greater the displacement.

The distribution of 1<sup>st</sup> and 3<sup>rd</sup> principal strain around the wound face can be seen in Figure 51.

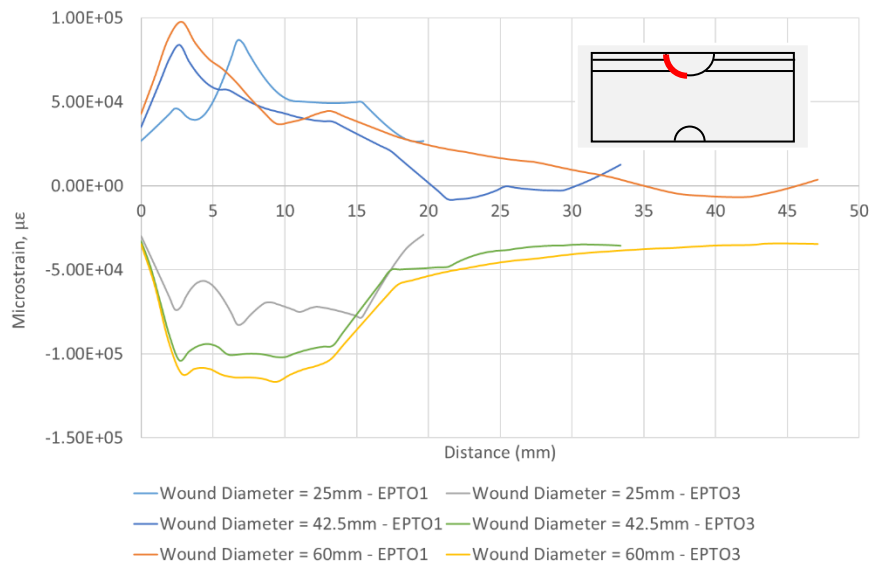


**Figure 51** 1<sup>st</sup> and 3<sup>rd</sup> principal strains around the wound for models with varying wound diameters. The wounds with larger diameters have a higher magnitude of stress than those with smaller diameters.

Figure 51 shows the distribution of the 1<sup>st</sup> and 3<sup>rd</sup> principal strains around the vertical wound diameter. It can be seen that, as with the central strains, the greatest 1<sup>st</sup> and 3<sup>rd</sup> principal strains are experienced by the model with the largest wound. Both the 60mm model and the

42.5mm model follow a similar pattern of both 1<sup>st</sup> and 3<sup>rd</sup> principal strains as each other. However, the 25mm model does not exhibit an initial peak at the skin-fat interface to the same extent as the other models. Instead, it experiences a second peak, approximately at the fat-muscle interface. From here, the pattern followed is approximately the same for all models.

The horizontal displacement around the vertical wound circumference for models with varying wound diameters can be seen in Figure 52.

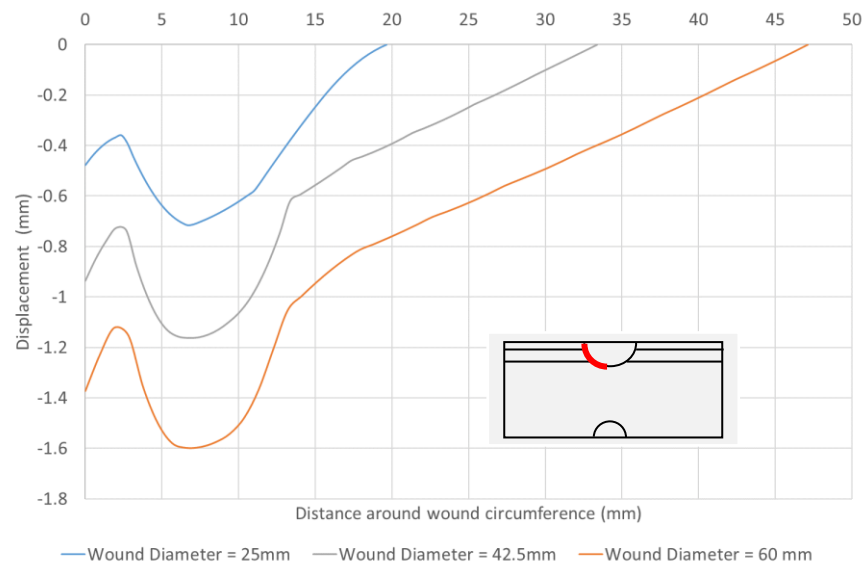


**Figure 52** A graph of horizontal displacement around the wound circumference. There is approximately 0.4mm difference between each model. The greater the wound diameter, the greater the displacement.

The horizontal displacement plots are an approximate translation of each other. There is a direct correlation between wound diameter and the displacement in the horizontal direction around the wound, the larger the wound diameter, the greater the displacement. In all models, a maximum compression appears through the fat layer indicating a greater displacement. This occurs at approximately -1.6mm for the 60mm model, -1.15mm for the 42.5mm model and -0.7mm for the 25mm model. This is a difference of approximately 0.4mm between the displacements of each model. The models run parallel to each other with this difference being constant.

### 4.3.6 Varying Pressure

In addition to the dimensional variation, the impact of the variation of pressure was investigated. Three values of pressure were used, 100mmHg (0.013 MPa), 150mmHg (0.0199984 MPa), and 200 mmHg (0.027 MPa). In Figure 53, the 1<sup>st</sup> and 3<sup>rd</sup> principal strain along a central axis are presented. It can be seen that the 3<sup>rd</sup> principal strain is almost a direct translation of itself. The larger the pressure, the larger the compressive strain with linear scaling occurring. These results are primarily included for clarity and ease of discussion as they are linearly scaled. All models converge to achieve equiaxial stress at approximately -22mm.

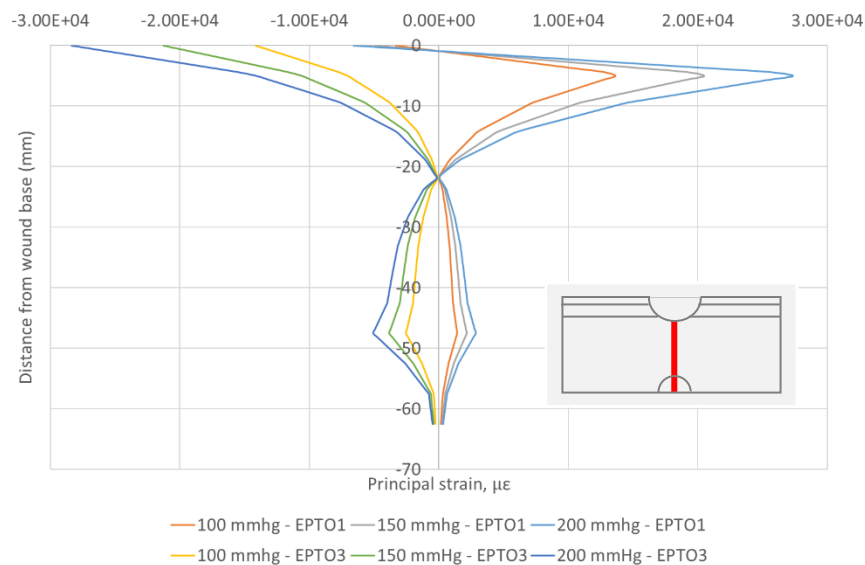


**Figure 53** 1<sup>st</sup> and 3<sup>rd</sup> principal stress from along a central path through the model. By changing the pressure, the stresses are scaled up or down. More pressure results in greater stress.

Figure 54 shows the deformation produced by varying the applied pressure on the wound. It can be seen that, the model is initially under tension prior to approximately 8mm below the wound surface. At this point, all three values of pressure have a value of 0mm displacement. Between approximately 8mm and 52mm below the wound base, a compressive displacement is recorded. Throughout the model, the general theme of the lower the applied pressure, the lower the value of displacement can be observed.

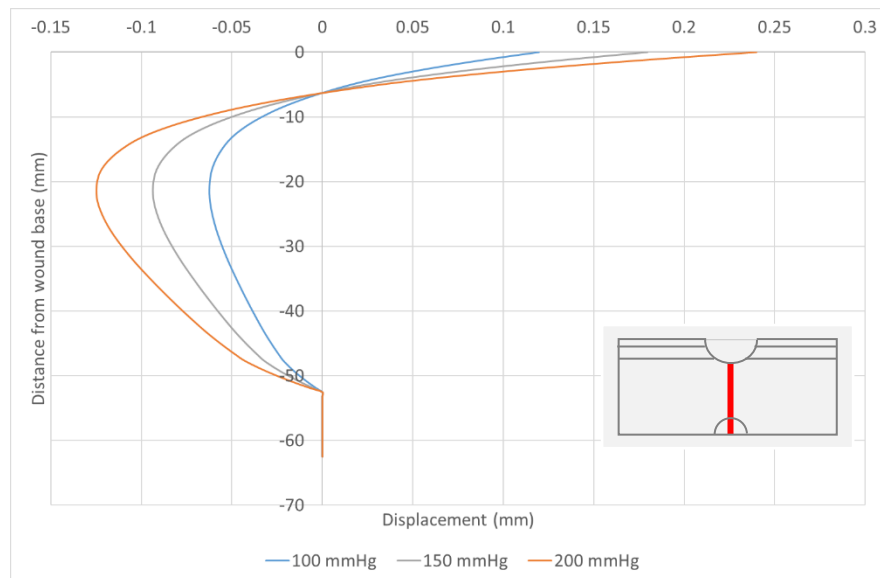


**Figure 54** The vertical displacement through the central axis when the pressure is varied. There is a scalar relationship with the higher pressure creating a greater displacement.

The 1<sup>st</sup> and 3<sup>rd</sup> principal strains around the vertical wound circumference can be seen in Figure 55. It is clear, when looking at 3<sup>rd</sup> principal strain, that varying the pressure causes a near direct translation of the graph. As with the graphs plotted of the central axis, the general trend of the smaller the value of pressure applied, the lower the value of compressive stress is followed.

This trend is also observed for the 1<sup>st</sup> principal strain. Prior to 5mm around the wound the model is in tension. For the remainder of the circumference, the model is in compression. Additionally, the observation that the initial peak of both 1<sup>st</sup> and 3<sup>rd</sup> principal strain corresponds with the skin-fat interface. Meanwhile the initial trough of both principal stresses roughly occurs at the fat-muscle interface.

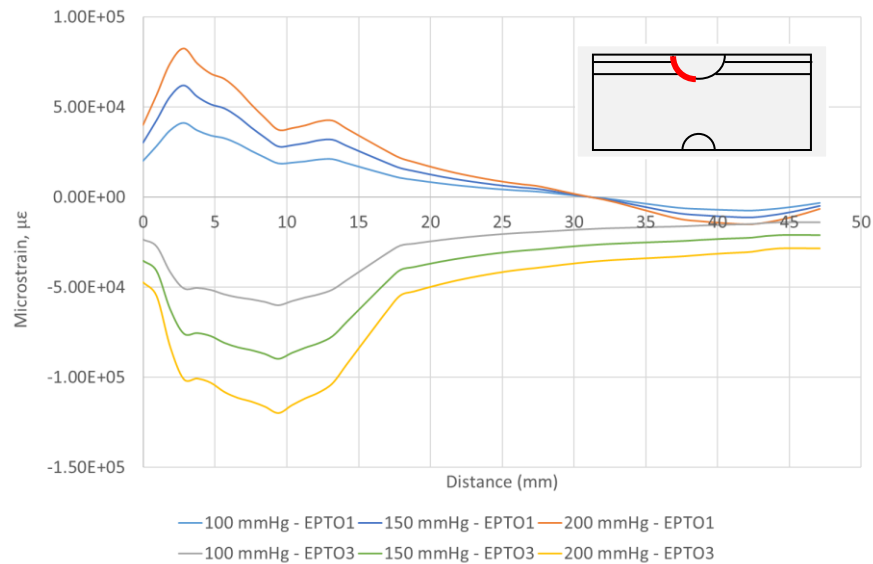
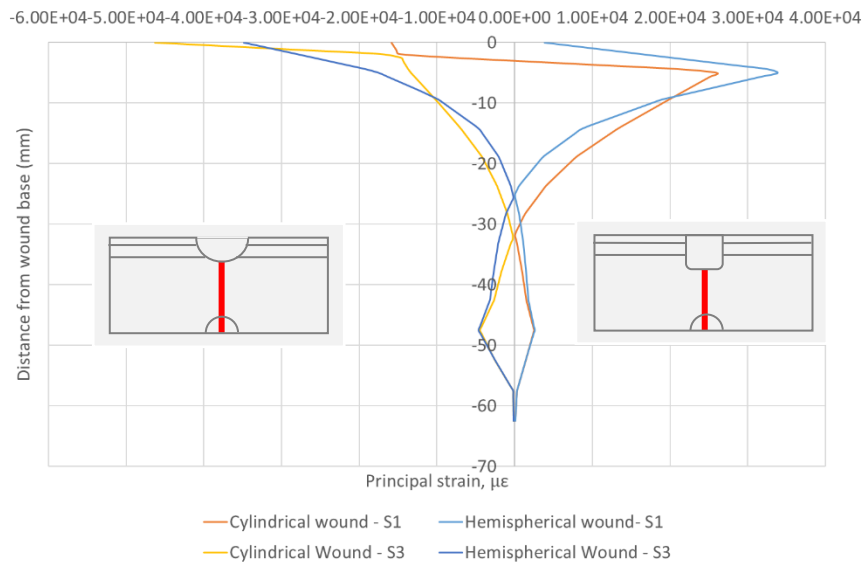


**Figure 55** The 1<sup>st</sup> and 3<sup>rd</sup> principal strain around the wound circumference. There is a direct relationship between the amount of applied pressure, and the quantity of strain produced. The greater the pressure, the greater the strain experienced by the surrounding tissue.

#### 4.3.7 Varying Wound Shape

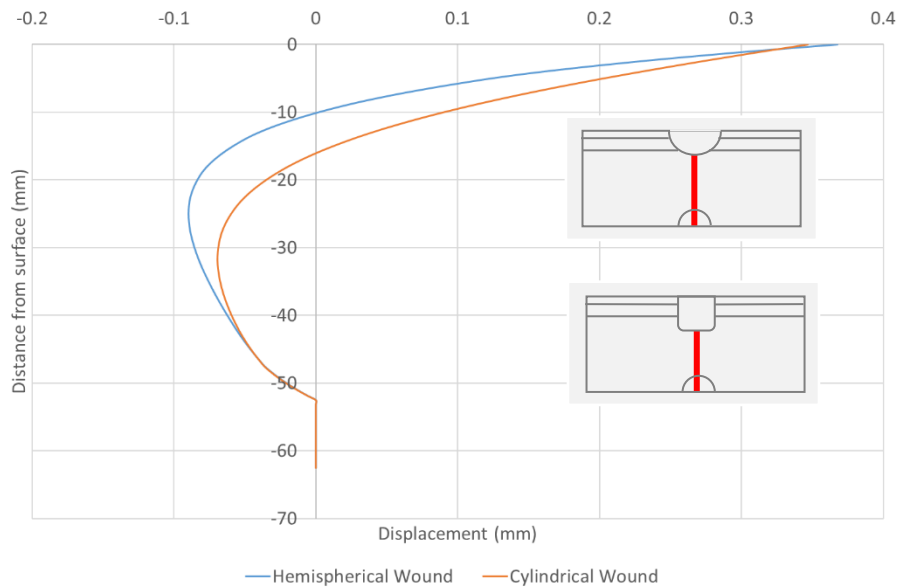
In addition to varying the properties of the hemispherical wound model, a model was developed where the wound had a filleted cylinder shape. This is particularly important as whilst arterial leg ulcers are typically smooth in shape, venous leg ulcers are shallower with ‘ragged’ edges (Endicott, 2019). The filleted cylindrical wound was developed with this in mind. Of particular interest is the impact of strain on the corners of the wound. This model had the same material properties and model dimensions as the hemispherical wound, with a 60mm wound diameter and a 60mm wound depth being the only variations.

Figure 56 shows the distribution of 1<sup>st</sup> and 3<sup>rd</sup> principal strain along a central vertical path. It can be seen that initial 1<sup>st</sup> and 3<sup>rd</sup> principal strains are much lower for the cylindrical model than the hemispherical wound model. From here, both models experience peak tensile strain at approximately the same depth. This peak is approximately 30% larger for the hemispherical wound than the cylindrical wound. From this point, the tensile strain decreases and the cylindrical wound experiences a greater tensile strain, with both models reaching equiaxial strain at different points, approximately 25mm below the wound surface for the hemispherical wound, and approximately 31mm below the wound surface for the cylindrical wound model. Following this point, both models experience the same strain from approximately 43mm below the wound surface to the base.



**Figure 56** Distribution of 1<sup>st</sup> and 3<sup>rd</sup> principal strains when varying the shape of the wound.

Figure 57 shows the vertical displacement experienced through the central path of the cylindrical and hemispherical wound. It can be seen that the initial displacement is similar for both wound models, however the displacement for the cylindrical wound model is more tensile throughout than the hemispherical wound model. At approximately 45mm below the wound base, the displacement for both models aligns. This continues through to the base of the model.



**Figure 57** Variation of vertical displacement through the central path of two models with hemispherical and cylindrical wounds.

As with previous models, the displacement and strain experienced around the wound face were also recorded and plotted. Figure 58 shows the 1<sup>st</sup> and 3<sup>rd</sup> principal strain around the wound face for a filleted cylindrical model and a with a hemispherical wound. It can be seen that the strain experienced by the hemispherical wound is smoother throughout the wound, experiencing two key peaks at approximately 2.5mm and 13mm along the wound face. In contrast, the strain experienced by the cylindrical wound was much more undulated in its distribution. The initial peak at 2.5mm around the wound edge experienced by the tensile strain is greater than that of the strain in the equivalent position on the hemispherical model. From

here, the strain decreases and plateaus for both models, with the tensile strain experienced by the hemispherical wound model continues to be approximately  $1 \times 10^4 \mu\epsilon$  lower than that experienced by the filleted cylindrical wound model. At approximately 15mm around the wound, the tensile strain experienced by the wound decreases rapidly, crossing into compressive strain at approximately 17.5mm. From here, this strain then increases to approximately  $-0.1 \times 10^4 \mu\epsilon$  at approximately 19mm along the wound face. The strain then decreases to reach a 1<sup>st</sup> principal strain minimum at approximately 23.5mm around the wound edge. This minimum has an approximate value of  $-3 \times 10^4 \mu\epsilon$ . From here, the strain increases gradually but remains at a value of approximately  $-2 \times 10^4 \mu\epsilon$  from 30mm around the wound until the end of the path.

Like the tensile strain, the compressive strain for the cylindrical wound model does not follow as smooth a path as the hemispherical wound model. It can be seen that the initial compressive strain is approximately equal for both models, and the models continue to experience similar strain until approximately 2.5mm around the wound face when the hemispherical model reaches a peak then stabilises until approximately 9.5mm. In contrast, the strain experienced by the cylindrical model continues to increase, reaching a peak of approximately  $-1.3 \times 10^5 \mu\epsilon$  at 12.5mm around the wound face. From here, the compressive strain decreases until it reaches approximately the same value as the hemispherical model at 15mm around the wound. The strain then increases to form a second peak at approximately 22mm around the wound face. This then decreases to approximately  $-0.5 \times 10^4 \mu\epsilon$  at 30mm around the wound. From here, the compressive strain increases once more experiencing  $-5.05 \times 10^4 \mu\epsilon$  between 35mm and 40mm around the wound, before decreasing slightly to approximately  $-4.95 \times 10^4 \mu\epsilon$  at the central point of the wound base.

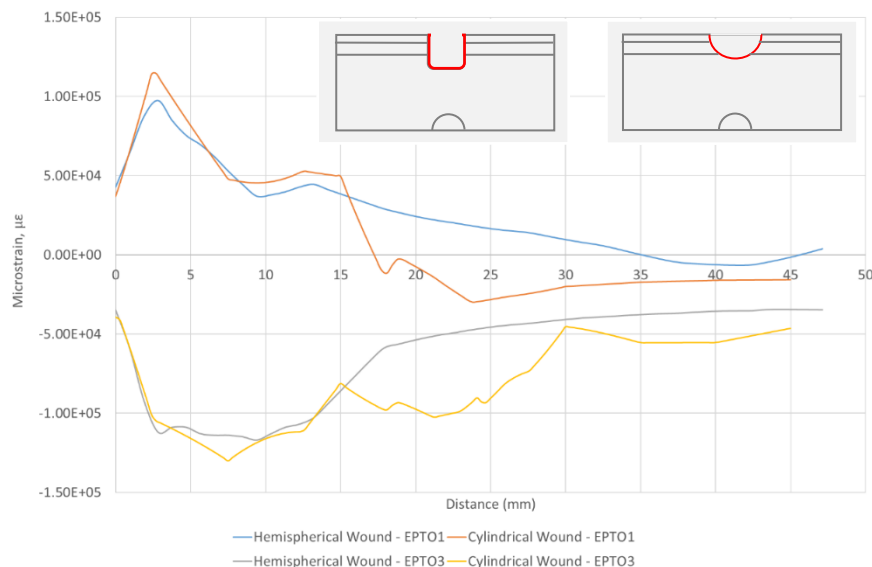


**Figure 58** 1st and 3rd principal strain around the wound face of a filleted cylindrical wound and a hemispherical wound

Figure 59 shows the horizontal displacement around the wound for the hemispherical and cylindrical wound models. It can be seen that in general the models follow the same pattern of displacement, with the cylindrical wound model experiencing greater negative displacement throughout until approximately 22mm around the wound model when the hemispherical wound model experiences the greater negative displacement for the remainder of the model. This phenomenon may be attributed to the differential pressure acting perpendicular to the surface of the wound. As a result, the cylindrical wound demonstrates increased displacement in the vertical direction along its base, while experiencing less vertical displacement along its sides.

Conversely, the hemispherical wound displays vertical displacement along its entire circumference.

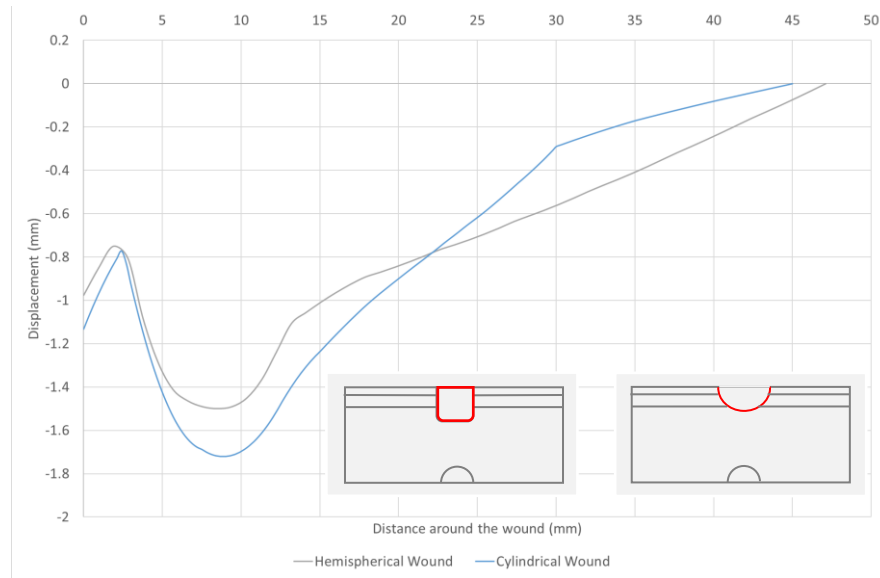


**Figure 59** Displacement around the wound experienced by the hemispherical and cylindrical wound models.

## 4.4 Discussion

This chapter investigated the impact of varying the parameters of the model during the development stage which had two purposes, the first to ensure that the properties and size of the model does not influence the results gained, and the second to investigate the impact of varying properties on the stress and strains experienced. In addition, this model is an *in silico* equivalent to an *in vitro* model discussed in Chapter 5.

When investigating the influence of the size of the wound model and the subsequent wound:model-side ratio, it was observed that the strain around the wound face for the models with a size of 300mm x 300mm and 240mm x 240mm ran concurrently with little variation in the strain experienced throughout the wound. In comparison, the model with dimensions of 180mm x 180mm had variations and additional peaks experienced at the fat-muscle interface. As this measurement influences the subsequent *in vitro* model, it was important to ensure the model is not made too large, thus wasting materials and potentially creating practical difficulties when transporting and using the model. Therefore, the model with the dimensions 240mm x 240mm was taken forward for further development. This ensured the smallest model dimensions that did not affect the results gained were utilised.

Whilst this model does provide an overview of the variations in strain and displacement experienced in a silicone wound model, there were some limitations in the development of this model. The primary limitation of this model was that silicone has non-linear material properties, which are difficult to emulate perfectly in a finite element model. The non-linear properties utilised in this model were calculated from tensile testing of silicones, discussed in Chapter 5. Whilst laboratory conditions for tensile testing were followed as closely as possible, it was found through this testing that the Young's modulus of materials are additionally influenced by time which was difficult to simulate in a finite element environment.

In addition, the influence of varying the depth of individual layers was investigated. It was observed that the greatest deformation occurred in the fat equivalent level. When the depth of this layer was increased, it was seen that the peak compressive strain remained constant throughout the layer, decreasing only once the path reached the fat-muscle interface. The variation in muscle and skin layer depths did not induce this magnitude of strain variation suggesting that the amount of subcutaneous adipose tissue has the greatest influence on the strain variation around the wound face. This did not translate to the strain through the central y-axis of the model, with little variation in strain being observed. No variation in layer depth was seen to induce a differentiation in strain through the central path of the model, suggesting that this is not the most influential factor in the strain through the depth of the tissue.

## Chapter 5 Design of a Physical Model

### 5.1 Introduction

Following the preliminary investigation of the *in silico* model discussed in Chapter 4, an *in vitro* model was created. This physical model had two key purposes; the primary purpose was to validate the *in silico* model, but in addition, it was developed as a potential testing platform for novel medical devices. The design, development and testing of the *in vitro* model is discussed in this chapter.

### 5.2 Model Requirements

As discussed in the review of literature in Chapter 2, there is currently no single animal model that has properties biomechanically similar to human tissue that can be used without major ethical considerations. This provides a lack of options for researchers developing novel medical devices that have a biomechanical mechanism of action on the wound and surrounding tissue. Therefore, it was important that the *in vitro* model discussed in this chapter was as biomechanically accurate as possible with the materials currently available.

This places several dimensional constraints on the model as it must match with those of the *in silico* model. As the *in silico* model has been designed to be highly parameterised, there is some flexibility in terms of altering the size of the model to fit other constraints. The dimensions of the model are crucial to ensuring an accurate stress-strain distribution is observable throughout the model.

During the development and preliminary testing of the *in silico* model, it was found that the model should have a wound:model-side ratio of 1:4 or greater, otherwise the boundaries of the model would have an impact on the deformation of the model and resultant stress and strain values when a negative pressure was applied. Therefore, the *in vitro* model must follow this as a minimum. However, a larger model may be more adaptable when testing novel medical devices.

As biological tissues have hyper elastic properties, the material used for *in vitro* model should have similar properties. Silicone rubbers are potentially suitable materials. They are available as two liquid parts that are then mixed and set, as discussed in Chapter 3, and hence can be moulded to any shape required. In this investigation, the use of 3D printing was investigated because it allowed any size and shape of wound model to be produced. However, the UltiMaker 2+ Extended 3D printer (UltiMaker, 2015) initially made available for this research had a base plate of 190mm x 190mm, allowing a maximum model dimension of typically 175mm

x 175mm. To ensure that the model has a minimum wound to edge ratio of 1:4, the hemispherical wound was therefore designed to have a diameter of 60mm.

In addition to the overall model dimensions, the layer thicknesses and materials selected are important. The selected silicones and model dimensions can be found in Table 3. Upon initial testing, it was found that, due to the Young's modulus of the material used for the layer representing skin being higher than that of skin itself, the skin layer thickness was reduced by 1mm to a thickness of 1.5mm.

In order to track the model deformation, thin metal fibres with a maximum length of 5mm were added to each layer of the model. These fibres were placed at 45° around the wound circumference to allow easy visualisation and comparison of the deformation experienced by the wound model when subjected to NPWT or other mechanical wound treatments. Additional metal fibres were placed in one corner of the model to aid orientation.

### 5.3 Mould Development

The model and its corresponding mould went through a multistage process of development. Initially, the model was created as a single layer to test the use of PLA and 3D printing as a method of mould production. Following this, the mould was further developed to allow the production of a layered model. In the second iteration of the mould, a modular design was followed. This allowed for interchangeable modules and therefore easy personalisation should a different layer thickness be required. By casting layers individually, the single layer modules allow the silicone to be levelled, producing the most accurate model in terms of thickness size. The model was produced upside down with the skin being the first layer applied. As this was the thinnest layer it was able to be applied at the correct thickness without being influenced by the previous layers. In addition, different wound and mould geometries could be easily created due to the modular design.

Upon printing the model, it was found that printing at the maximum plate size for the UltiMaker 3D printers caused warping due to an uneven distribution of heat across the plate. Therefore, the model was scaled down further, keeping the same wound to edge ratio, allowing easier printing. In addition, when the skin layer was reduced in thickness and combined with the base plate to reduce warping, the UltiMaker printers were unable to print the shape out of PLA, and thus the model was subsequently printed using ABS material.

### 5.4 Final Design

The final design of the mould was a modular multilayer design seen in Figure 60. The modular design allows for ease of variation of layer depths. To create the model, first the 'Food Grade'

silicone was mixed and cast in the base layer to represent the skin. Thin wires are then cut into lengths of approximately 5mm. These wires are then applied in a 'cross' shape at 45° intervals around the wound to allow the deformation of the wound and surrounding silicone to be tracked in a microCT scanner when subjected to negative pressure. The mould for the fat layer is then applied and the silicone is then left to set for 24 hours. The same process is then followed for the fat and muscle layers.

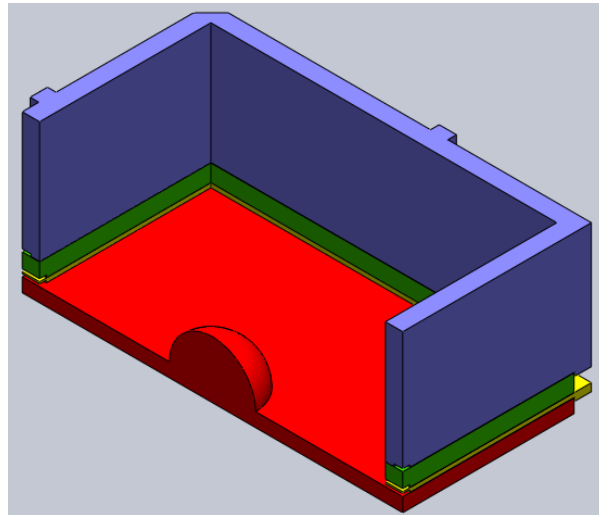


**Figure 60** Cross sectional isometric view of the mould used to cast the *in vitro* model. It can be seen that an interlocking modular design was used to allow adjustment for further model development.

## 5.5 Testing the Model

In order to ensure the preliminary *in silico* model was behaving in a way that was to be expected, the basic *in vitro* model created from silicone was subjected to negative pressure whilst being observed with microCT. To do this, once the model was cast, it was placed in an X-Tek HMX 160 micro-CT scanner (X-Tek Systems Ltd, Tring, Herts., UK). A set of TIF images centred on the hole of the model were produced, which were subsequently loaded into AVIZO (ThermoFisher Scientific, USA) to produce a 3D reconstruction of the model.

Once a 3D computerised construction of the model was created, AVIZO's segmentation tools were utilised to better understand the deformation of the wound. When the model was initially loaded into the software, the images produced were underexposed, with a relatively narrow pixel histogram that was shifted to the left. To counteract this, and to allow a clearer depiction of the wound shape, the image was normalised, and histogram equalisation was performed. This allowed a greater level of contrast between the wound and the surrounding silicone. It also allowed the layers to become more visible. The wires were depicted by a bright white lines and dots as metal is denser than silicone or foam and thus shows up more brightly on CT. From this, the wound was segmented manually by highlighting the wound on each layer

with the segmentation tool. The wires were segmented separately in the same fashion to allow the loaded and unloaded models to be orientated the same plane to allow direct comparison of the wound deformation. This allows a more accurate representation of deformation.

RenaSYS is a NPWT system developed by Smith & Nephew and used to apply negative pressure to patients in healthcare settings across the world. The original system was used for this project, which is typically used in hospital settings on immobile patients due to its size. A negative pressure of 200mmhg was applied, as this was the maximum pressure setting on the machine and therefore it was thought that, as the displacement shown in the *in silico* testing was small, applying the greatest possible negative pressure would be most likely to demonstrate a visible displacement in the wound.

A 30PPI polyurethane foam produced by Smith & Nephew PLC was inserted in the wound of the model, as it would when NPWT is being applied to a patient. The model was scanned both with and without negative pressure applied to allow the direct comparison of model deformation. In order to scan the model whilst subjected to negative pressure, an airtight seal was created between the RenaSYS machine and the wound model. Due to the non-adhesive properties of silicone, investigation was required to determine the most effective way to complete this. It was found that a combination of latex glue and clear self-adhesive vinyl was used. The glue provided a surface the vinyl could adhere to. To stabilise the airtight seal, the edges of the vinyl was further sealed to the silicone model using a cloth-backed waterproof adhesive tape. This layer of latex, vinyl and cloth-backed waterproof adhesive tape was represented in the *in silico* model by a layer of shell elements on the surface of the skin layer. This is seen in Figure 61.



**Figure 61** Attachment of NPWT device to the surface of the *in vitro* model.

To undertake the scan under negative pressure, the model was placed on the scanning table and attached to the RenaSYS EZ machine. A clamp stand was used to elevate the negative pressure tubing, reducing the likelihood of tangling during the rotation of the model and subsequently giving a clearer image. From this, TIF image files were produced and segmented using the same process as described for the unloaded model.

### 5.5.1 Results

The image below (Figure 62) shows the shape of the wound in the *in vitro* model without negative pressure applied. It can be seen that the segmentation occurred manually on a layer-by-layer basis as the segmented portion has a stepped appearance. This was due to the low contrast between the foam wound filler and the model in the microCT images creating difficulties in the automatic segmentation process. This process reduced the accuracy of the segmentation process.

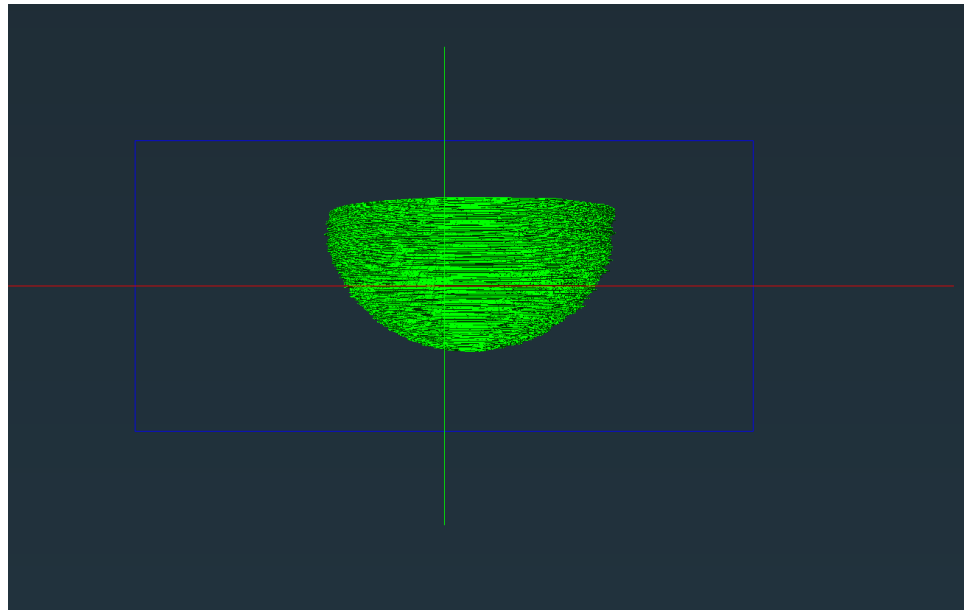


**Figure 62** Segmentation of wound from a microCT scan of the *in vitro* wound model without loading

Figure 63 shows the results of a microCT scan of the model whilst subjected to negative pressure of 200mmhg. When comparing these images, little visible difference in displacement is seen. Due to the difficulties with segmentation, conclusions are unable to be drawn regarding the impact of the application of NPWT on the model as it is unable to be confidently determined whether variations between the pressurised and non-pressurised scans are due to the negative pressure being applied or due to the induced error in the segmentation process. When comparing the central CT images, no visible difference between the models was seen.

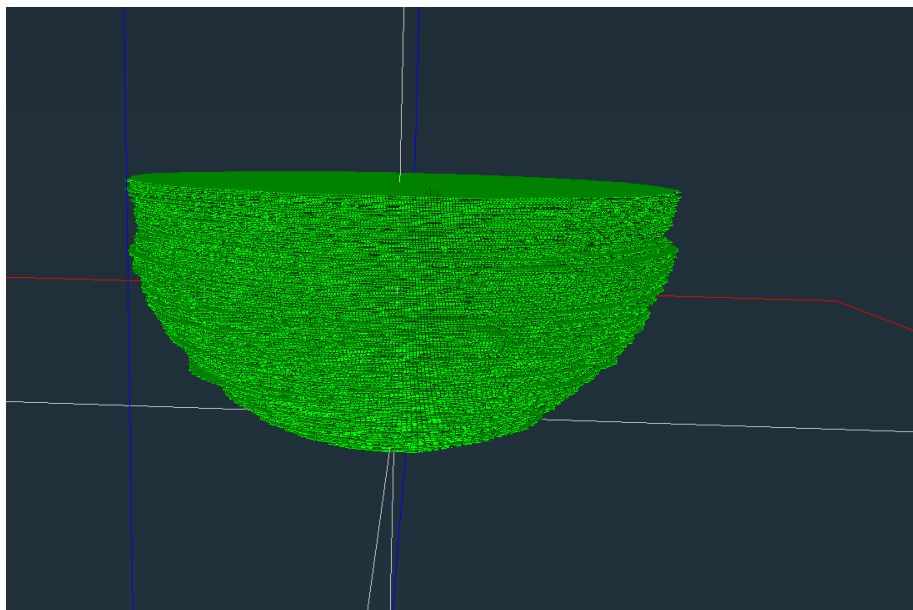


**Figure 63** Segmented hole from a microCT scan of the *in vitro* wound model whilst subjected to NPWT at a pressure of 200mmhg.

Unfortunately, the Coronavirus pandemic prevented further investigation of this due to lack of access to laboratory facilities and the microCT scanner.

## Chapter 6 Biologically Representative Wound Model

### 6.1 Introduction

Following the development and validation of the *in silico* model using the method discussed in the previous chapter, the material properties of the parameterised model were adapted to fit with biological material properties. This chapter details the development of a biologically representative wound model, from the selection of biologically representative material properties to the preliminary finite element modelling. Whilst tissue properties are discussed in previous chapters, they are vital to the development of the model and therefore are detailed in this chapter.

### 6.2 Selection of Material Properties

Following the development and validation of the *in silico* model described in Chapter 4, the material properties of the parameterised model were adapted to align more closely with biological material properties. As discussed in Chapter 4, biomechanical properties of biological tissues are highly variable and influenced by a number of factors, including age, race, physical health and lifestyle choices. This variability presents difficulties when it comes to providing definitive values for Young's modulus, leading it to ordinarily be presented as a range of values. In addition, the method of testing can influence the values given, as well as the location samples are taken from on a cadaver. This is particularly apparent with skin samples the skin tension varies throughout the body. There are thirty-six topographical maps of skin tension defining these invisible lines, examples include Kraissl lines and Kanavel lines, each defined in a different way. These topographical maps are often used by surgeons as a guide for elective incisions, to minimise scarring (Wilhelmi et al., 1999). The maps of skin tension preferred by both surgeons and researchers appear to be Langers lines and relaxed skin tension lines (RSTL). Academics investigating the biomechanical properties of skin often refer to their samples as being either taken perpendicular or parallel to these lines. Unfortunately, this variation in skin tension was unable to be accurately replicated in the models developed as part of this project due to the model requirements.

This wide variation in biomechanical properties presents obvious difficulties when designing a biologically representative *in silico* model. In order to decide which values of Young's modulus to use for skin, subcutaneous fatty tissue, and muscle for this project, a further review of the literature was carried out. In total, 30 sets of material property data were considered, and a stress-strain graph was plotted for each biological material up to a maximum strain of  $\epsilon = 0.3$

which was determined to be approximately the maximum strain a wound is subjected to during NPWT in preliminary testing. The results for each material are discussed in the following sections.

### 6.2.1 Skin

The Young's modulus of skin is highly variable, and measured values can vary by a factor of up to 3000 (Diridollou et al., 2000). This presents a particular challenge when choosing a single value of Young's modulus for the *in silico* model. An indication of that very wide range of values is shown in Figure 64 Stress-strain plots for skin from a review of literature, showing a large range of Young's modulus values. A range of factors were considered when selecting the biomechanical properties for the skin and the first step in this process was to plot all the values for stress against strain found in literature onto a graph, and to remove the extreme outliers. The result of this can be seen in Figure 64 below.

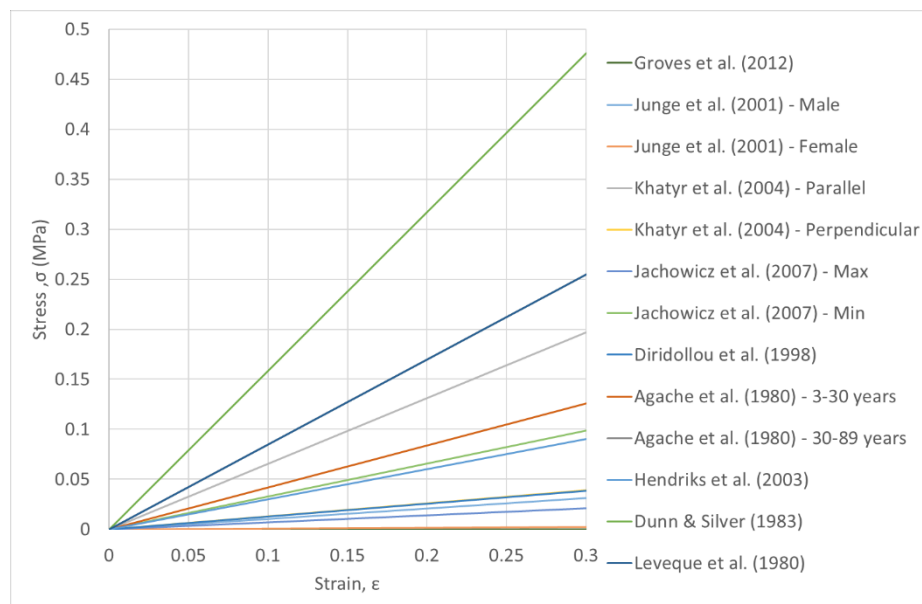


**Figure 64** Stress-strain plots for skin from a review of literature, showing a large range of Young's modulus values.

Thirteen datasets are plotted on the graph, with a range of approximately 0.45 MPa at  $\epsilon = 0.3$ . Coincidentally, the values reported by Leveque et al. (1980) and Agache et al. (1980) lie close to this median value, both of which investigated the impact of aging on the elasticity of the skin, finding that its Young's modulus increases during the aging process. While leg ulceration, particularly venous leg ulceration, can occur at any age, the condition is approximately 13 times more prevalent in those over 80 years of age, hence selection of this value seems appropriate (Nelson & Adderley, 2016). Both Leveque et al. (1980) and Agache et al. (1980) reported a Young's modulus of approximately 850 KPa.

## 6.2.2 Subcutaneous Fatty Tissue

Occasionally considered part of the skin layer, the Hypodermis or Subcutaneous Fatty Tissue has biomechanical properties that are not only highly variable but produce many challenges in their measurements. Its globular formation causes measuring the Young's modulus to be particularly challenging. This has resulted in a distinct paucity of literature discussing this particular biomechanical property. One area which appears to have been heavily focused on is the biomechanics of breast tissue, with the Young's modulus of subcutaneous adipose tissue being calculated largely as a byproduct of calculating the biomechanical properties of other tissues. As with skin, the Young's moduli of subcutaneous fatty tissue have been plotted with a maximum strain of 0.3 on a graph. This graph can be seen in Figure 65. It is widely accepted that the biomechanical properties of subcutaneous tissue is highly influenced by not only the sex and health of an individual, but the location in the body of the samples.

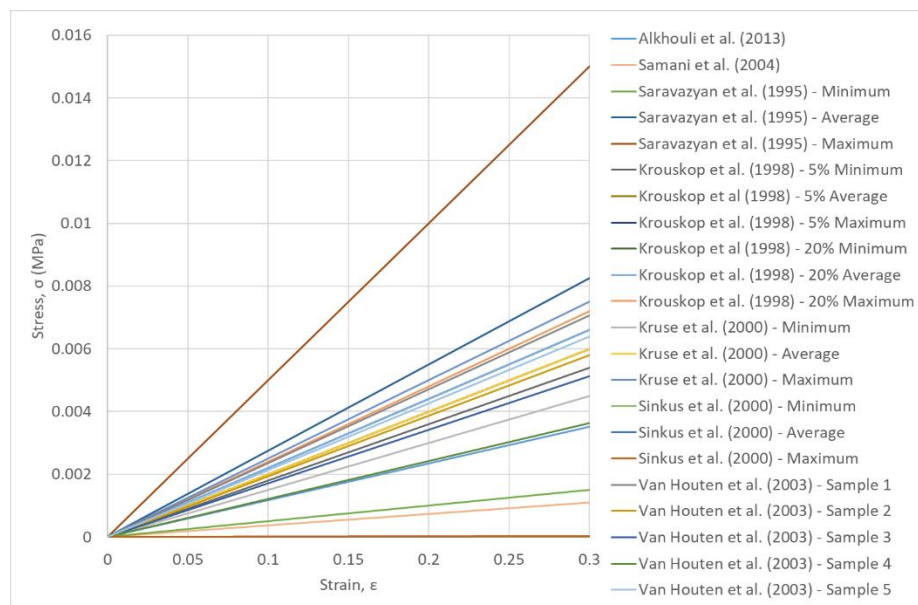


**Figure 65** A stress-strain analysis of the biomechanical properties of subcutaneous adipose tissue gained from reviewing literature.

Calvo-Gallego et al. (2018) compared the viscoelastic properties of human abdominal subcutaneous adipose tissue with that located in the breast. It was found that breast tissue “could be regarded as a unique tissue from a mechanical point of view” with significant differences between abdominal tissue and breast tissue found. Whilst the data collected from breast adipose tissue shown on the graph in Figure 65 is useful with regards to ensuring data representing adipose tissue from other areas of the body are of the same order of magnitude.

Alkhoul et al. (2013) investigated the biomechanical properties of human abdominal subcutaneous adipose tissue. It was found that the Young's modulus of abdominal subcutaneous adipose tissue was approximately 11.7 KPa. This is slightly lower than that of subcutaneous

adipose tissue located in the breast, however the fatty tissue found in the abdomen has very similar properties to that located in the lower leg and thus is the most suitable value for use in the biomechanical finite element model of the wound.

### 6.2.3 Muscle

Located below both the skin and subcutaneous adipose tissue is the final material layer in the *in silico* model, muscle. Many researchers have investigated the biomechanical properties of muscle, this project highlights those who have used human models as these are the most applicable. It is well known that muscle has anisotropic material properties with the Young's modulus in the direction following the muscle fibres is significantly higher than that in a transverse direction (Takaza et al., 2013). In addition to this, the Young's modulus of a contracted muscle is significantly higher than that of a relaxed muscle (Shinohara et al., 2010).

Following the same process as was followed for both skin and subcutaneous adipose tissue, and the values for Young's modulus found in literature were plotted on a stress-strain graph and clear outliers removed. The graph can be seen in Figure 66. When the average Young's modulus is calculated, it can be seen that Basford et al. (2002) has recorded a Young's modulus with a medial value. This value was measured using magnetic resonance elastography and taken from the medial gastrocnemius. This is of particular importance as ulceration typically occurs on the lower leg, in particular over this muscle. Therefore, the measured Young's modulus of 73.206 MPa was selected for use in the *in silico* model representing leg ulceration in the lower leg.

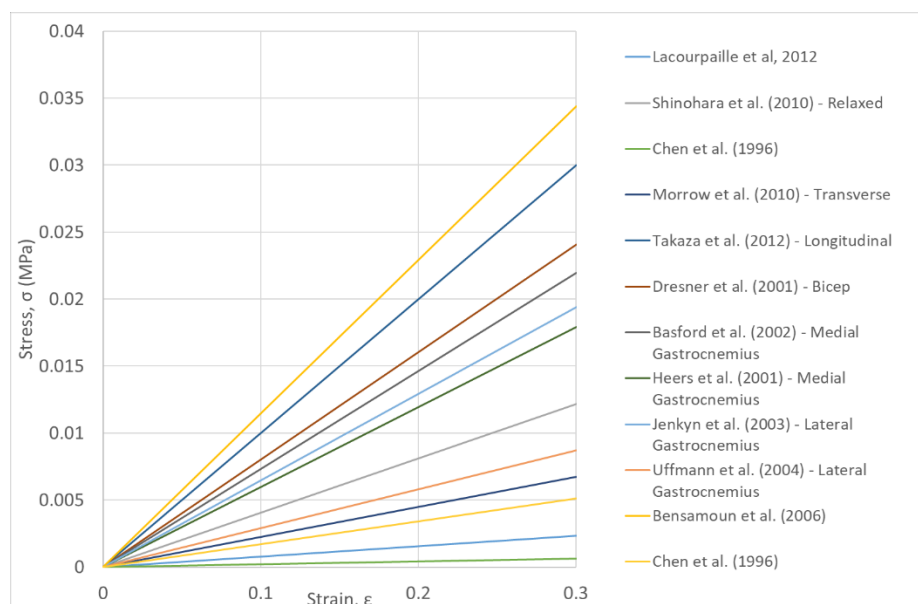


**Figure 66** A stress-strain analysis of skeletal muscle tissue with values gained from a review of literature.

### 6.3 Finite Element Analysis

Following selection of biological material properties, the properties were applied to the parameterised *in silico* model. This model was subsequently subjected to a uniform pressure of 200mmhg comparable to the pressure a wound is subjected to during NPWT. This enabled an accurate representation of the distribution of stress and strain throughout a chronic wound.

The model designed is identical to the parameterised model developed in Chapter 4, however the material properties align closely with those selected through a thorough review of literature and comparison of properties. The selected Young's moduli can be seen in Table 5 below.

**Table 5** Young's moduli of biological materials used in the biomechanically similar *in silico* model.

Biological Material	Young's Modulus (kPa)	Key Reference
Skin	850	Leveque et al. (1980) Agache et al. (1980)
Subcutaneous Fatty Tissue	11.7	Alkhoul et al. (2013)
Muscle	73.2	Basford et al. (2002)

As with previous models, the model with biological material properties had a hemispherical wound on the top surface, and a hemicylindrical bone shape at the base. In order to produce a detailed visualisation of the areas of particular interest, a path was plotted around the vertical wound circumference to allow a specific focus on the deformation of the wound itself. In addition, a path was plotted vertically from the central wound base to the base of the model to enable the dissipation of stress throughout the model as a whole to be observed. The results from these path plots were loaded into Microsoft Excel and are presented in graphical form below.

#### 6.3.1 Results

The distribution of 1<sup>st</sup> and 3<sup>rd</sup> principal strain along a central axis can be seen in Figure 67. Tensile strain is experienced between the wound base and for approximately 23mm along the path. It can be seen that the maximum tensile strain occurs at approximately 5mm. At this point, the 1<sup>st</sup> principal strain has a value of approximately  $5.9 \times 10^4 \mu\epsilon$ . Following this, the strain decreases, reaching equiaxial strain at approximately 23mm below the wound base. From this point the tensile strain increases once more, reaching a second peak at approximately 48mm below the wound base before decreasing once more to almost equiaxial strain through the bone.

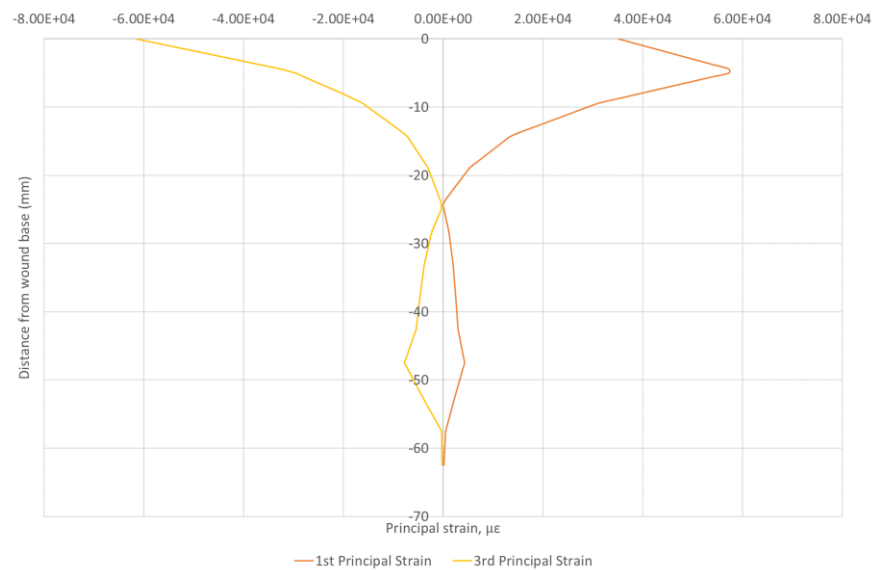


**Figure 67** A graph showing the displacement of the 1st and 3rd principal strain around the wound. There is an initial tensile peak at approximately 5mm below the wound base.

The 3<sup>rd</sup> principal strain follows a similar pattern to the tensile strain with equiaxial strain also reached at 23mm below the wound base. At the base of the wound, the compressive strain reached approximately  $-6.05 \times 10^4 \mu\epsilon$ . Unlike the tensile strain, from this point the strain decreases gradually towards equiaxial strain. From here, the compressive strain reflects the tensile strain.

In addition to investigating the distribution of 1<sup>st</sup> and 3<sup>rd</sup> principal strains along the vertical axis of the model, the displacement distribution is also of importance. Figure 68 shows that the greatest displacement occurs at the wound base. At this point, the model has a tensile displacement of approximately 0.61mm. From here, the displacement decreases at a steady rate, before reaching equilibrium at approximately 10mm below the wound base. The displacement becomes compressive following this point, and a maximum compressive displacement is achieved at approximately 23mm below the wound base. At this point, the displacement is approximately -0.15 mm. Following this, the compressive displacement begins to decrease at a slower rate than initially, before reaching negligible displacement at the muscle-bone interface. This negligible displacement remains constant throughout the bone until the base of the model is reached.

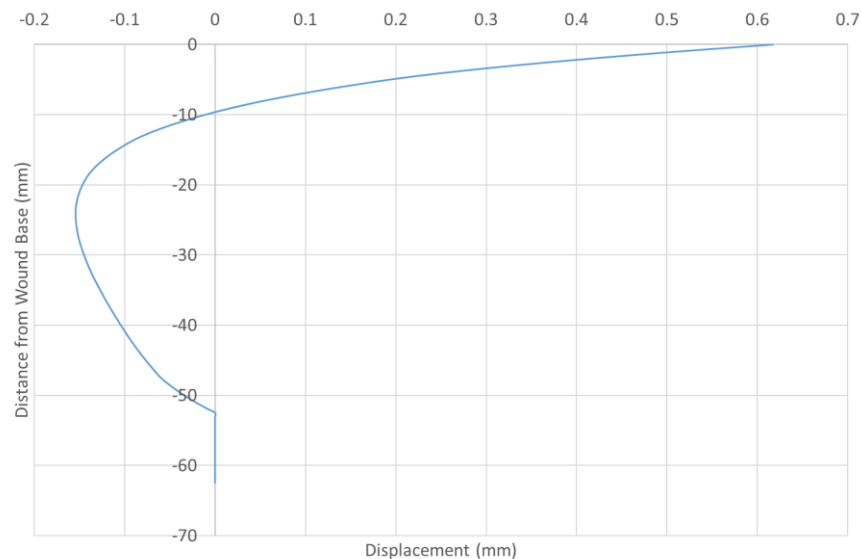


**Figure 68** Displacement through a central path for a macroscopic model with biomechanically similar properties to biological tissues

In addition to the path plotted along the central vertical axis, as with the models in Chapter 4, a path was plotted around the vertical wound face. This path was plotted between the surface and the wound base with the assumption that the strain is mirrored along the other half of the circumference.

As with the central path plot, the 1<sup>st</sup> and 3<sup>rd</sup> principal strains were plotted along this path and can be seen in Figure 69 below. It can be seen that, at the surface of the model, the 1<sup>st</sup> principal strain has a value of approximately  $0.4 \times 10^4 \mu\epsilon$ . This then increases through the skin layer, reaching a peak tensile strain, of  $1.07 \times 10^5 \mu\epsilon$  at approximately 3mm along the wound circumference. This approximately corresponds to the skin-fat interface. Through the fat layer, the 1<sup>st</sup> principal strain decreases, reaching an approximate local minimum of  $9.91 \times 10^4 \mu\epsilon$ . From this point, the 1<sup>st</sup> principal strain increases once more, reaching  $5.5 \times 10^4 \mu\epsilon$  at the fat-muscle interface. From here, the tensile strain decreases, reaching a minimum of  $2.17 \times 10^4 \mu\epsilon$  at approximately 39mm around the wound. The strain continues at this value until approximately 42mm around the wound face when it begins to increase, reaching a local maximum at of  $3.52 \times 10^4 \mu\epsilon$  at the centre of the wound base.

Also seen in Figure 69 is the compressive strain. This follows a similar pattern to that of the 1<sup>st</sup> principal strain, with an initial peak of approximately  $-1.21 \times 10^5 \mu\epsilon$  occurring at the skin-fat interface. From here, the strain becomes more compressive, sustaining a compressive maximum of approximately  $-1.44 \times 10^5 \mu\epsilon$  through the subcutaneous fat layer. From here, the 3<sup>rd</sup> principal strain decreases, reaching a minimum of approximately  $-8.67 \times 10^4 \mu\epsilon$  at the fat-

muscle interface. The strain then decreases slowly to reach a local minimum of  $-6.11 \times 10^4 \mu\epsilon$  at the central point of the wound base.

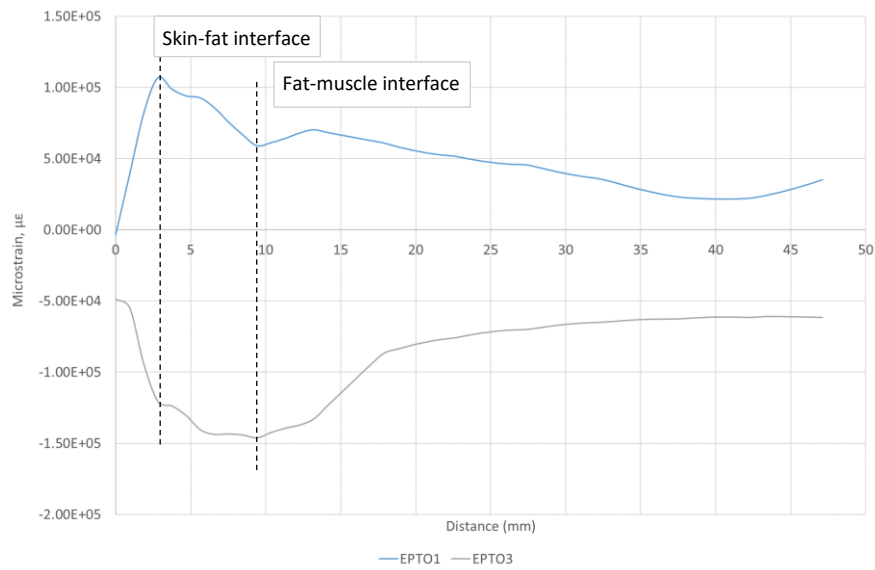


**Figure 69** A graph showing the distribution of tensile and compressive strain around a hemispherical wound face for a model with biomechanically similar properties.

In addition to studying the distribution of 1<sup>st</sup> and 3<sup>rd</sup> principal strain around the wound, the spread of horizontal displacement along the path was also shown in graphical form. This can be seen in Figure 70. The initial displacement at the surface has a value of approximately -1.45mm. From here, as with the 1<sup>st</sup> and 3<sup>rd</sup> principal stresses, a local maximum occurs as the skin-fat interface. At this point, the horizontal displacement is approximately -1.2mm. The horizontal displacement subsequently becomes more compressive, with a compressive maximum at approximately 9.4mm, just prior to the fat-muscle interface. Here, the displacement is approximately -2.15mm. Throughout the remainder of the path, the displacement becomes more tensile, eventually reaching a negligible displacement at the wound base.

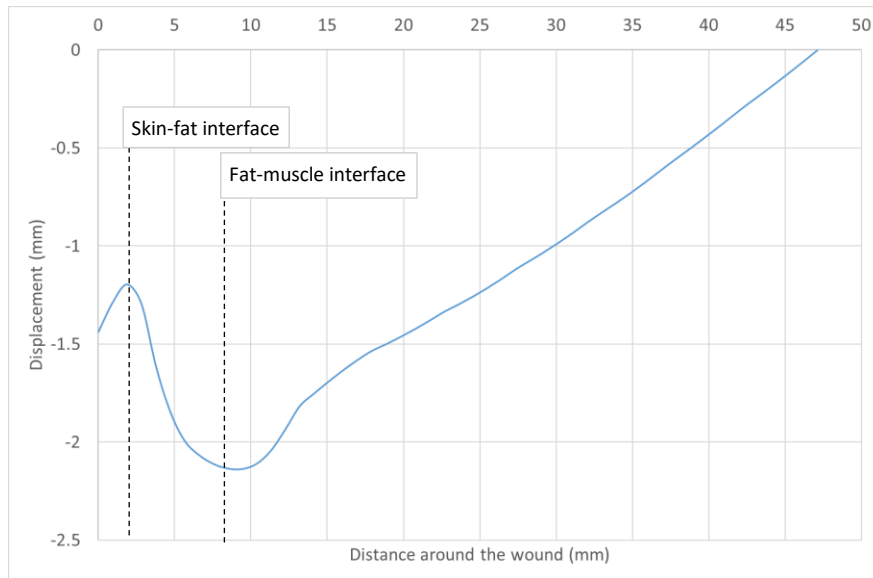


**Figure 70** Horizontal displacement (UX) experienced around the wound face of a model with biomechanically similar material properties.

The vertical displacement was also investigated. This can be seen in Figure 71 below. At first, there is a compressive displacement of the model, with a vertical compression of approximately 2.1mm on the surface of the model. The displacement then becomes less compressive at a relatively constant rate, eventually crossing into the tensile region at approximately 24mm around the wound. From here, the displacement continues to increase, with a maximum tensile displacement occurring at approximately 45mm around the wound, with a value of 0.62mm. This stays approximately constant until the path reaches the wound base at approximately 47mm around the wound.

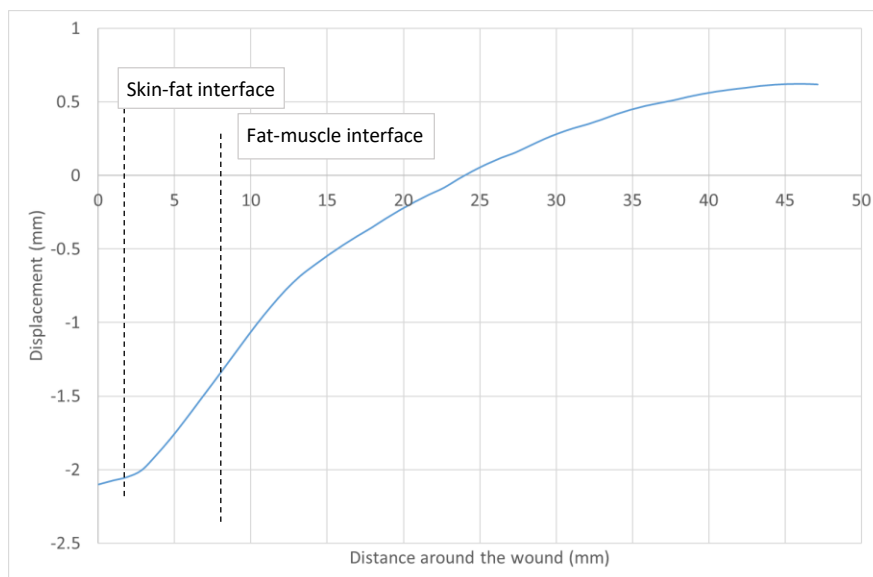


**Figure 71** Vertical displacement (UY) around the wound face for a biomechanically similar model.

## 6.4 Discussion

This chapter investigated the impact of negative pressure on the strains and displacement experienced by a macroscopic biomechanically similar wound model through the model depth and around the wound bed. The material properties and model thicknesses corresponded with those outlined in Table 5. The model had the same dimensional properties as the previous *in silico* models developed with the material properties of biomechanically similar silicones in Chapter 4.

The analysis reveals that there is a consistent distribution of strain around the wound bed and within the tissue directly beneath the wound, regardless of whether the model incorporates biological material properties or mechanical properties of biomechanically similar silicones. As a result, we can anticipate that the strain experienced by the wound will exhibit similar behaviours when biological material properties are applied.

It can be seen in Figure 69 that the wound experiences strain of approximately 11% at the skin-fat interface. When cells were subjected to strain of 10% in a study by Hicks et al. (2012) it was found that proteins and growth factors known to encourage wound healing and induce granulation tissue growth are expressed. This is highly suggestive of skin cells regenerating through the promotion of cell proliferation and therefore the wound healing process being induced at the levels of strains experienced by the wound during NPWT.

When looking at the strain experienced by the tissue underneath the wound, a peak of 5.8% was seen at approximately 5mm below the wound bed which suggests the effects of NPWT is not localised to the wound bed and effects the surrounding tissue. This suggests that stimulus for wound healing is provided on a larger scale. Whilst it is known that proteins and growth factors are expressed at 10% strain for fibroblast wound healing, osteoblasts have shown a response at lower levels to strains as low as 6% in a study by Tang et al. (2006). Whilst there is no equivalent study for fibroblasts at this stage, it is possible that the 5.8% strain may also induce regulatory factors for the wound healing process.

Chapter 4 demonstrated that variations in negative pressure applied to a wound directly impact strain levels in a predictable manner. Managing negative pressure levels can effectively reduce strain on the wound. By aligning with potential increases in fibroblast expression of key regulatory factors for healing at higher strain levels, it may be possible to customize negative pressure therapy to better suit the specific needs of individual patients with challenging wounds.

## Chapter 7 – Microscopic Computational Comparison of Wound

### Filler Materials

As discussed in previous chapters, the exact model of wound healing triggered by negative pressure wound therapy is currently unknown, this chapter investigates the magnitude, direction and quantity of macrodeformations induced by the wound treatment. The macrodeformations found using finite element modelling will then be compared to those found in literature to induce wound healing.

Macrodeformation is a widely theorised modulus of induction for the wound healing process. This level of deformation is caused by the collapse of pores and the centripetal forces exerted on the wound surface by the foam. This causes wound shrinkage, pulling the edges of the wound closer together (Huang et al., 2014). The subsequent wound contraction results in the overall wound size reducing (Hasan et al., 2015). NPWT traditionally utilises open cell polyurethane foam or a gauze as a wound filler during treatment. Applying negative pressure compresses this filler and leads to the development of microdeformations on the base of the wound. The term microdeformation describes the imprinting of the wound bed with the contours of the NPWT foam (Lalezari et al., 2017). Whilst this project does not focus on a cellular level, it is important to note that this microdeformation is associated with the expression of multiple proteins related to wound healing, including growth factors and collagen (Nie & Yue, 2016). In addition to the release of proteins associated with wound healing, the cell deformation that occurs during NPWT is associated with a number of other key wound repair mechanisms. The negative pressure applied has been shown to upregulate extracellular matrix production in human tissue.

## 7.1 Methodology

In order to understand the magnitude and distribution of micro stresses and strains created by the pressure induced by NPWT, a finite element model was designed.

### 7.1.1 Design of the model

In the previous chapter, the models developed looked at the stress-strain distribution and concentration on a macroscopic level. The aim of this model is to examine the variation in the stress-strain concentration with different wound fillers. This includes variations in the foam density and comparing the stress distribution under negative pressure wound therapy with a gauze wound filler. The stress-strain concentrations will then be compared to values found in literature, investigating whether the induction of micro stresses and strains in the wound bed induces granulation tissue growth and subsequently the wound healing process in chronic, hard-to-heal wounds. To do this, a parameterised finite element model was designed.

The model uses the results from the review of literature carried out in Chapter 6 to select the biomechanically relevant material properties. As the mechanical properties of interest are the micro-stresses and strains induced during the wound healing process by the interaction of the wound filler on the wound bed, the model developed in this chapter is a zoomed segment of the macroscopic model designed in previous chapters. Therefore, the biomechanical properties of the biological materials have remained unchanged. In addition to the mechanical properties, the Young's modulus of the wound filler was investigated and applied following a review of available literature. For the polyurethane foam strut, the Young's modulus was found to be approximately 91 kPa (Wondou et al., 2019). A similar process was conducted for the gauze, which was found to have a Young's modulus of 0.41 GPa (Mouro et al., 2021).

Following this the shape of the model was designed. The model was designed using a LOG file, a \*.txt document of instructions, telling the software what to build. This allows for full parameterisation and editing of the model. First, the material properties of the model were specified, followed by the parameters of the model. The parameterisation of the model includes the X, Y, and Z directions for each layer and the height of the strut. From here, the main model was built using a top down approach. To ensure accurate layers, the surface of the biological material was defined using key points. These key points were then copied to form a parallel surface below. The volumes were then defined by key points. In the foam model, this process was also used for the strut.

In addition to the parameterisation and automation of the model construction, the results output, once the appropriate properties were decided, was also automated. The results

that are of most use to this project are path plots along the X and Y axes, with 1<sup>st</sup> and 3<sup>rd</sup> principal stresses and strains and deformation plotted onto the paths. By automating the process, the path plots are guaranteed to be located in the same place for each model. It also increases the speed of post processing. This is important as it allows more flexibility for the future use of the model. The chance of user error is also reduced significantly by using an automated process.

The data produced by the finite element models take two different formats, each processed in a different way. The first, and most simple output in terms of analysis and post processing, is an image file in \*.jpg format. These images give an overall visual representation of the distribution of stress, strain or deformation in the model, highlighting any concentrations. Two main views of the model are saved. The first is an isometric view of the full model. This allows the surface to be viewed, and two of the four corners are visible. As the model has symmetry, these two corners in the printed image are satisfactory to allow any stress concentrations at the boundaries to be visible. In addition to this, a visual check is conducted prior to image printing, with the model rotated to ensure the symmetry of the model.

The second view of the model saved as a \*.jpg file is a cross sectional view. In this view, the model is cut along the x-axis, allowing an insight into the internal distribution of stress, strain and deformation. As with the isometric view, this image provides a way of checking for symmetry, whilst also providing information about where force concentrations occur.

Slightly more complicated in the data processing stage is the use of path plots. For the model discussed in this chapter, the paths are plotted along the X and Y axes. On both paths, the 1<sup>st</sup> and 3<sup>rd</sup> principal stresses and strains (S1, S3, EPTO1, EPTO3) are plotted, along with the deformation (UY, UX). The data is then saved to a file in the \*.txt format. From here, the data is exported into an Excel (\*.xlsx) spreadsheet and a set of line graphs depicting the variation in forces along the paths are produced. This allows a better understanding of the exact values of stress, strain or deformation at different depths.

## 7.2 Preliminary Testing – Mesh Convergence

In addition to dimensions influencing how the model reacts to applied strain, the size and arrangement of the mesh can also impact how it responds to applied strain. To ensure the results gained were not influenced by the meshing, a mesh convergence study was carried out. To do this, the mesh size was varied and graphs were plotted to observe when the results converged. Convergence studies were carried out for all models in this section.

### 7.2.1 Foam Strut Model

Shown in Figure 72 is a convergence study for the polyurethane strut model through the central path. It can be seen that all meshes give a similar displacement through the path, however the 0.05mm and 0.04mm meshes are converged.

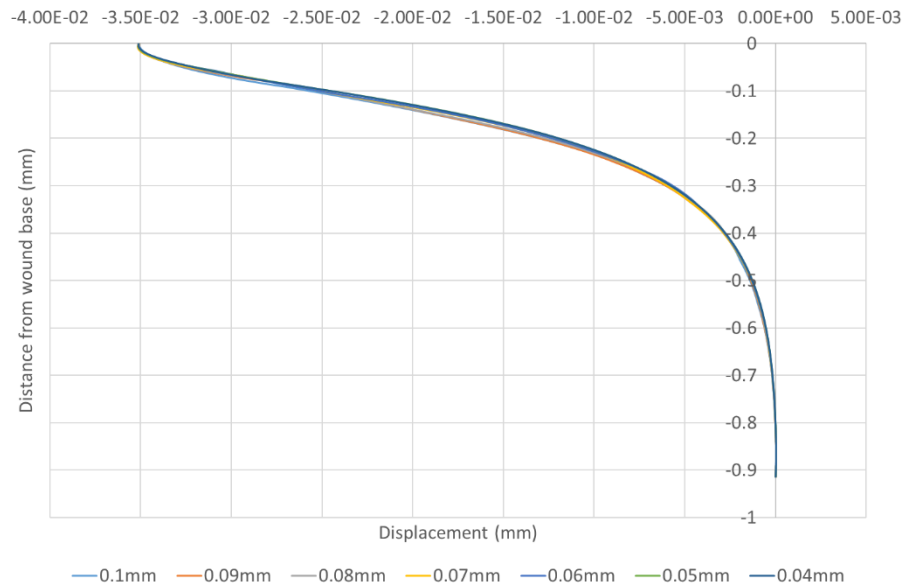


**Figure 72** Convergence study for foam strut model showing displacement through a central path.

The convergence along a horizontal path is displayed in Figure 73. It can be seen that, as with the displacement through the central path, there is little variation between the models. The models with 0.05mm and 0.04mm line edge size run on top of each other, thus demonstrating convergence. Therefore 0.05mm line edge size will be used to form the mesh.

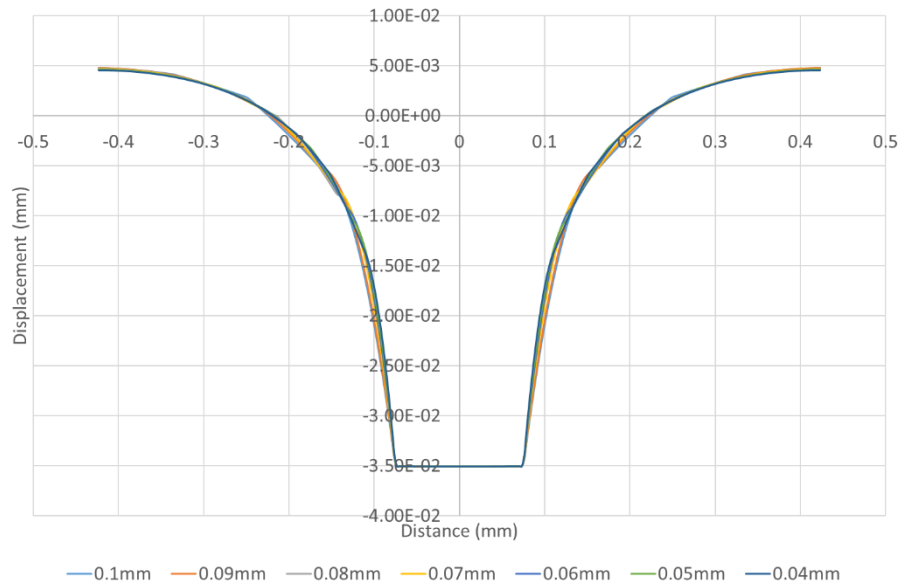


**Figure 73** Convergence study for foam strut model showing displacement along a horizontal path.

### 7.3 Preliminary Testing – Loading the Model

Following the basic design of the model, the next stage in the model development process was the loading of the model. It was important to maintain a biomechanically similar loading to that experienced by wounds under negative pressure, considering the fact that this model is a section of a larger scale model. The model was loaded incrementally, with each load added individually to ensure that the results are as expected. This helped to ensure an accurate loading of the model.

In addition to enabling the early detection of incorrect loading patterns, by loading the model incrementally, it allows investigation into the influence of each force a wound is subjected to when under NPWT. The first to be added was the pressure applied to the strut. This was applied in the form of a negative displacement in the y direction with a magnitude of  $-0.064$  (3 d.p.) x strut height. This was calculated by taking the displacement at the base of the wound on the previous model and applying scaling to ensure it fits the current model. A similar method was used to add the vertical displacement of the surrounding tissue. When investigating the impact of each aspect of the complex loading of the model, the horizontal path is most useful. It can be seen in Figure 74 that the displacement for the model with only strut loading applied, has primarily a local effect, with the area directly below the strut being pushed down to approximately  $-0.3 \mu\text{m}$ . The area immediately surrounding the strut is pulled down also, forming a curved shape at the corners.

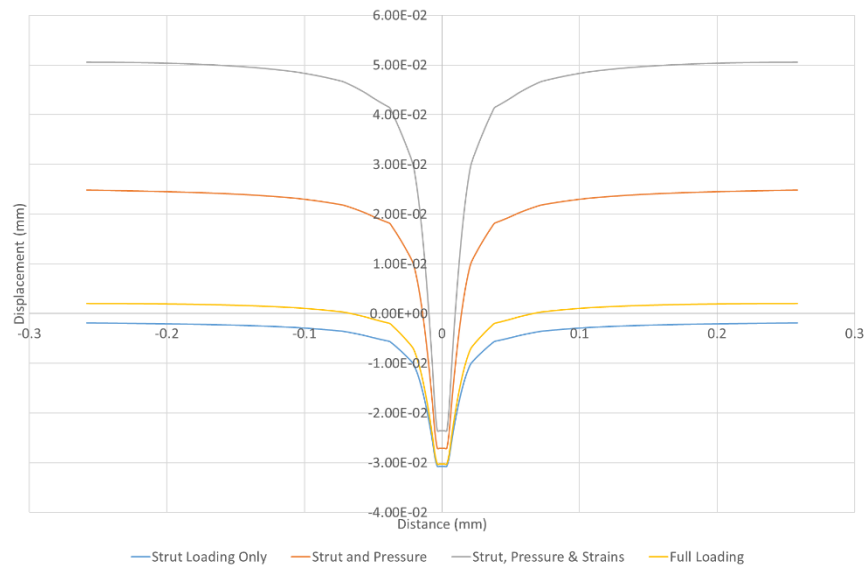


**Figure 74** The variation of displacement during incremental loading of a finite element model.

The next stage following the loading of the strut was the application of a negative pressure on the surface of the model. This is shown as a grey line in Figure 74. It can be seen that there is an increased displacement along the surface of the model, and that, in comparison with the strut only model, there is a much greater displacement from the surface to the base of the strut. When the strains calculated from the previous wound models are applied in addition, the surface displacement of the model increases to approximately  $0.5 \mu\text{m}$ . This is an increase of approximately  $0.53 \mu\text{m}$  from the strut only loading model. As a result of the increased surface displacement, the displacement under the strut is reduced. This is likely due to the finite ability of the material to stretch, and thus limit the strut displacement.

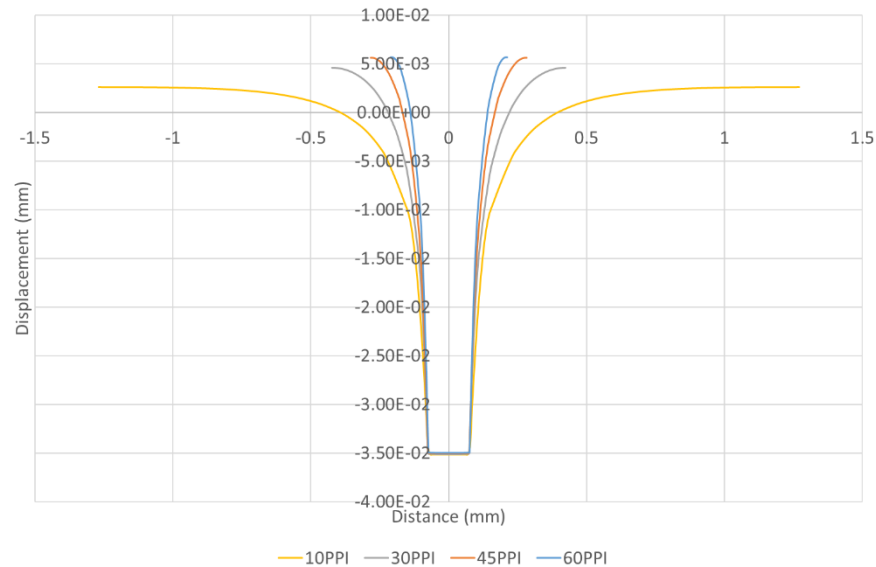
Following the surface displacement, the model was loaded with both the calculated strains and the strut loading. This is denoted by an orange line on the displacement-distance graph in Figure 74. It can be seen that the displacement directly under the strut is once again reduced in comparison to the pressure and strut loadings. The displacement is not as sharp as in previous loadings, with more displacement around the edges of the strut. This is because the surface of the model is affected by the applied surface strains calculated by previous models. In addition, the overall impact of the strut is much greater as the effect is no longer localised. This loading strategy is most representative of the real life impact of foam on the wound surface during negative pressure wound therapy and therefore is the loading strategy used in all future models in this chapter.

## 7.4 Varying Foam Density

Negative pressure wound therapy is applied with a range of polyurethane foams and gauzes. Smith and Nephew, one of the more prominent suppliers of NPWT devices and equipment, supply these foams come in varying densities, with 10 PPI, 30 PPI, 45 PPI and 60 PPI open-cell foams being available to healthcare staff for use. PPI stands for pores per inch, and whilst this is not a metric measurement, this is the standard classification of density in this domain and is therefore used in this project. The decision of which foam to use is a clinical one, however each foam has different benefits in terms of ingrowth and replacement frequency. The biomechanical impact of the choice of foam is not one that has been studied in depth, and there is a distinct lack of literature focussing on this particular issue. This section of the thesis aims to look at how the choice of filler medium for NPWT influences the biomechanical effect of the treatment on the wound bed.

In order to understand the impact of foam selection on the biomechanical forces the skin is subjected to during NPWT, the ANSYS model developed in the previous section was adapted, varying the space between each strut. A standard strut width of 0.15mm was used for all models to ensure any variation in stresses and strains was the result of the variation in pore size, and not as a result of variation in strut size. The standard strut width was used by Saxena et al. (2004) in their paper looking at the variation in micro deformations of the tissue between the struts. The distance between the struts have been calculated in accordance with the porosities of the foams.

Figure 75 below shows the deformation of the tissue around the strut. It can be seen that the distance between struts for a 10PPI foam is much greater than the deformation around the strut for the 30PPI and greater models. The general theme shown in this graph is that the greater the number of pores per inch, the smaller the deformation in the surrounding tissue. The peak deformation occurs on minimum and maximum of the distance across the wound, aligning with the midpoint between struts. This peak is greater the more porous foam has, although the variation between the 60PPI foam and the 10PPI foam is just  $2.7 \times 10^{-3}$ mm. From the graph, it can be seen that the deformation directly underneath the strut does not vary with porosity, remaining constant throughout the tests. This suggests that the maximum compression is approximately the same.



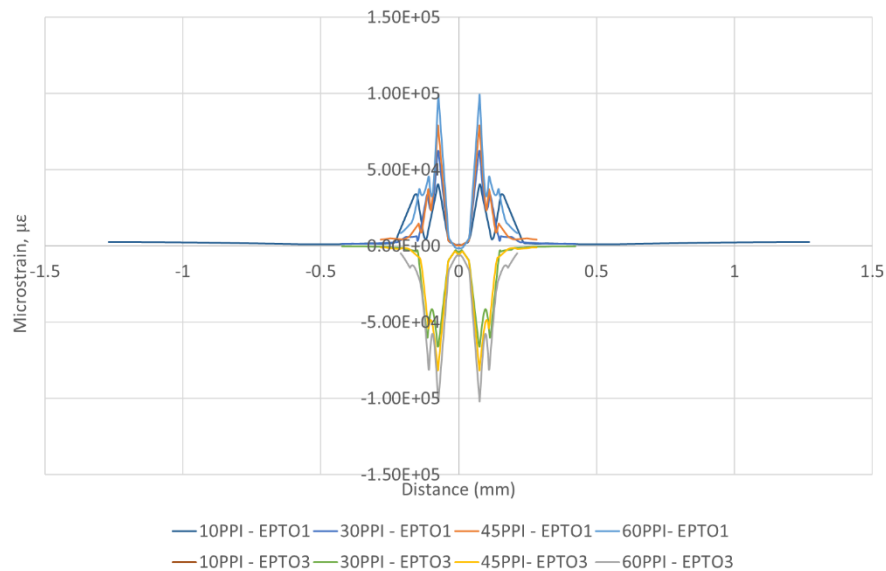
**Figure 75** A graph showing the variation of displacement with different porosities of polyurethane foam. The greater the porosity, the greater the deformation surrounding the foam strut.

Figure 76 shows the variation in 1<sup>st</sup> and 3<sup>rd</sup> principal strain with foam porosity. It confirms what is suggested by Figure 75 with regards to compressive strain. There is little variation in third principal strain directly under the strut, with the greatest variation occurring directly next to the strut at approximately  $\pm 0.05$ mm from the centre of the wound. The peak strain is greatest for the more porous foams. This is likely to be due to the pores being closer together, meaning there is less tissue between the struts to be displaced therefore placing the remaining tissue under more intense strain. It can be seen that the strain at the midpoint between the struts for each model, shown at the edge of each graph, is roughly the same, suggesting that the pore sizes do not influence the strain as much towards the centre of each pore. In addition to the peaks next to the strut there is an additional, smaller peak. For foams of lower porosity, this peak has greater magnitude. It could be hypothesised that this is due to there being more wound bed to deform, thus causing more compressive and tensile strains. In the foam with the lowest porosity, this peaks at 0.05mm and 0.15mm are approximately equal. In addition, it can be seen that the graph is symmetrical across the y-axis, which is to be expected as the model was reflected across this point. However, it validates the loading of the model and confirms that the model is loaded as expected.

In addition to the compressive strains, the 1<sup>st</sup> principal strain, also known as the tensile strain, is shown on this graph. Many of the same patterns can be seen in the tensile strain (EPT01) as the compressive strain, with it largely being a reflection in the x-axis. One key difference is that for the 10PPI model, the peak at approximately  $\pm 0.05$ mm from the centre of the strut is much smaller than that at approximately  $\pm 0.13$ mm. Apart from this, all porosities follow

approximately the same pattern with four peaks and a central trough before flattening as towards the edges of the model, which represents the centre point between the peaks.

Directly underneath the central point of the strut, it can be seen that both tensile and compressive strains are almost equal to zero. At this point, the least amount of compressive and tensile strain is experienced by the wound bed. It could be suggested that the edge of the struts have the biggest influence on the surface strains induced when negative pressure is applied.



**Figure 76** The variation of tensile and compressive strain with foam porosity on a strut model during negative pressure wound therapy. It can be seen that there is greater strain, both compressive and tensile, around the immediate edge of the foam struts, with more strain being experienced by the more porous foams.

In addition to the path plotted horizontally across the surface, measurements of stress, strain and displacement were taken vertically through the central axis of the model. This allows an understanding of the induction of microdeformation and strains through the model, directly under the wound strut.

Figure 77 shows the compressive and tensile strains through the wound model, to a depth of 0.9mm. It can be seen that the initial strain, directly underneath the strut is approximately 0mm for both compressive and tensile strains. This corresponds to the values found in Figure 76, thus validating the paths for the model as this is the intersection of the plotted paths. It can be seen that from the initial point, the tensile and compressive strains increase, reaching a maximum at approximately -0.07mm from the strut-wound intersection. Unlike the surface strains, the greatest internal strains, along the centre axis of the model, were found in the models with greater porosity. It can be seen that the maximum tensile microstrain experienced by the 60PPI model was approximately  $0.8 \times 10^5$ . In comparison, the maximum

tensile microstrain experienced by the 10PPI model was less than  $0.7 \times 10^5$ . A difference of this magnitude was also found in the compressive strain, with the maximum compressive strain experienced by the 60PPI model being approximately  $-1.8 \times 10^5$ , and the maximum compressive strain experienced by the 10PPI model being just less than  $-1.6 \times 10^5$ . Following this peak, there was a sudden reduction in strain, with each model getting approximately neutral strain between -0.22 and -0.3mm below the wound bed. From here, the strains crossed, with the tensile strain becoming negative, and the compressive strain becoming positive. It was found that the strain is approximately equal in this section for the models with 30-60PPI, however the strain is significantly less for the 10PPI model. From here, the models converge on the X axis, with no strain experienced from approximately 0.9mm below the wound bed. This depth of model was chosen as this is the point where there were no further strains on the central path during the preliminary model development stage.

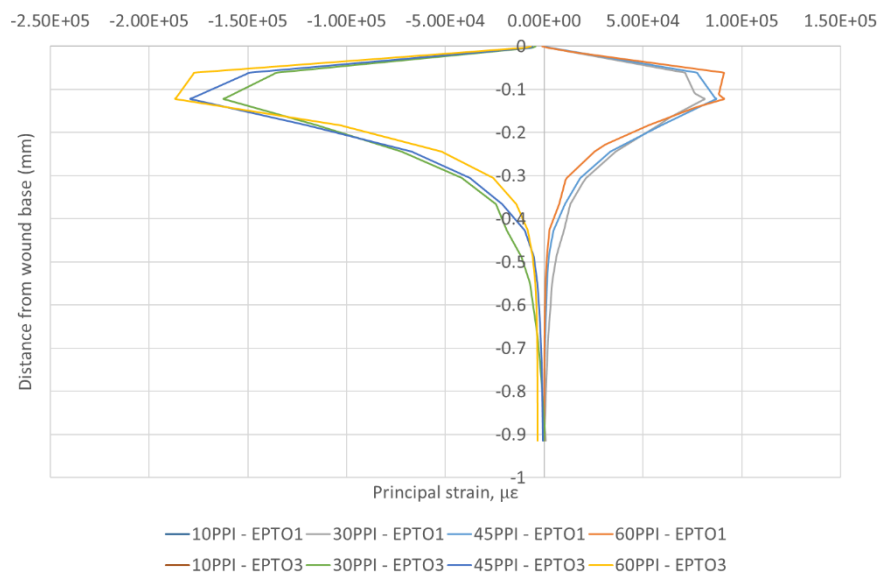


**Figure 77** Compressive and tensile strains experienced along a central vertical axis underneath the strut-wound interface for varying pores per inch foams.

In addition to the compressive and tensile strains, the displacement under the strut was of interest. This is shown in Figure 78. It can be seen that there is a negative displacement at the top of the model, corresponding with the model being compressed and moved downwards by the strut. The displacement decreases gradually for all porosities of foam, following the same curve. The displacement for the 10PPI model reaches neutral displacement at the base of the model more slowly than the other models. The models with a higher PPI value experience displacement at a reduced depth.

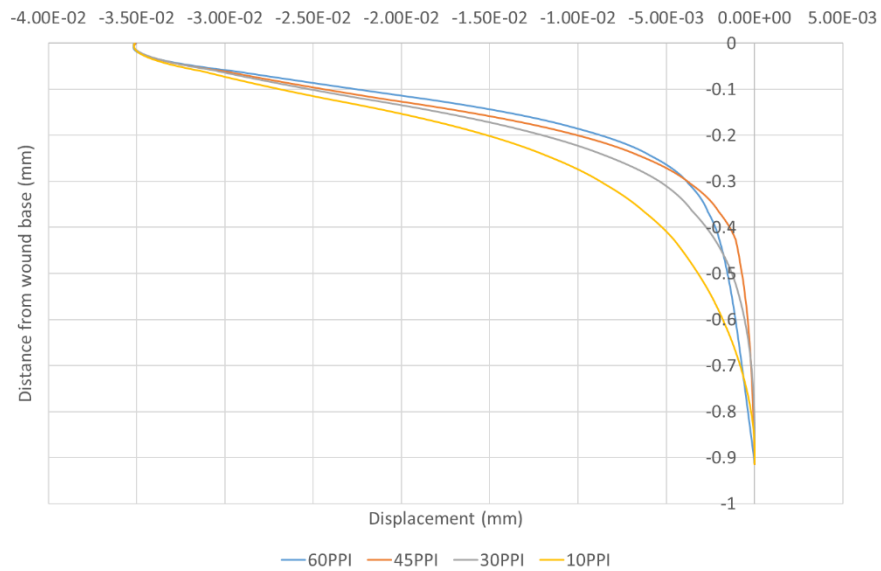


**Figure 78** Displacement experienced along a central vertical axis underneath the strut-wound interface for foams with varying porosities.

## 7.5 Gauze Model

In addition to foam wound filler, negative pressure wound therapy can also be performed using gauze as the wound filler medium. This is less common than the foam filler, however, is known to be less painful on removal. The second part of this chapter investigates the biomechanical impact of utilising gauze wound filler. This will then be compared with the biomechanical effects of foam wound filler and discussed in section 7.6 of this chapter.

### 7.5.1 Mechanical Properties of Gauze

Dating back to the Ancient Egyptians, gauze is one of the most commonly used items in wound care (Jones, 2006). Often believed to be a singular material, it is an umbrella term for a wide range of wound dressings, however these can be categorised in two primary groups, woven and non-woven. There are a variety of materials that can be used, including rayon and synthetic fibres, which are chosen due to their low adherence to the wound bed. However, for absorbent, woven, gauze, cotton yarn has been used for centuries. The exact material used for gauze based NPWT is not revealed in literature, however it is not unknown for clinical staff to use regular gauze materials, or materials that are impregnated with antiseptic materials. For the purpose of this biomechanical analysis of negative pressure wound therapy using a gauze wound filler, it will be assumed that the gauze used is a woven cotton gauze as this is one of the most common types of gauze used in healthcare settings.

It has been shown in literature that gauze wound fillers can be just as effective as foam wound fillers for the induction of wound healing in NPWT, but that a lower pressure can be used

if gauze is being used (Fraccalvieri et al., 2011a). Anesäter et al. (2011) found that, in a pig model, the mean wound bed pressure was comparable for both foam and gauze, with levels of  $103 \pm 2$  mmHg and  $104 \pm 2$  mmHg respectively. Gauze does have some drawbacks. Research has shown that gauze based NPWT can cause increased pain due to tissue ingrowth in comparison to open-cell polyurethane foam (Fraccalvieri et al., 2011).

### 7.5.2 Development of Gauze Model

In order to begin to understand the biomechanical impact of using gauze as a wound filler during negative pressure wound therapy, a finite element model was developed. For this model, assumptions were made with regards to the material and fibre organisation of the gauze. It was assumed that the gauze was made of organised cotton fibres as these are the most common gauzes available in a clinical environment, and for this model, it was assumed that any antibiotic impregnation had no impact on the mechanical properties of the fibre.

An image of the model can be seen in Figure 79 below. It can be seen that two materials are used, muscle and cotton fibres. Muscle has been chosen as the biological material, as it has been assumed, as with the previous model, that the wound has travelled through the skin and the subcutaneous fatty tissue and therefore the wound filler is interacting directly with muscle surface. As with the foam strut model, the biomechanical properties of muscle were selected from (Basford et al., 2002)'s study, with the Young's modulus being 0.073206 kPa.

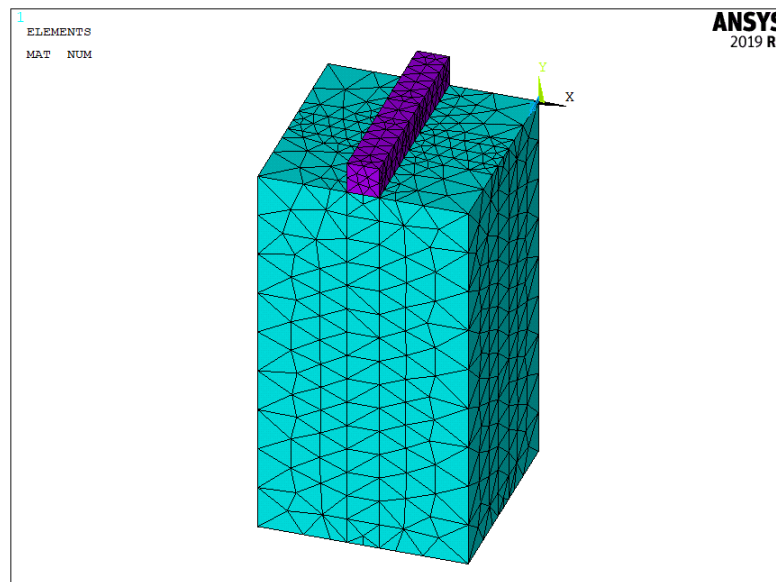
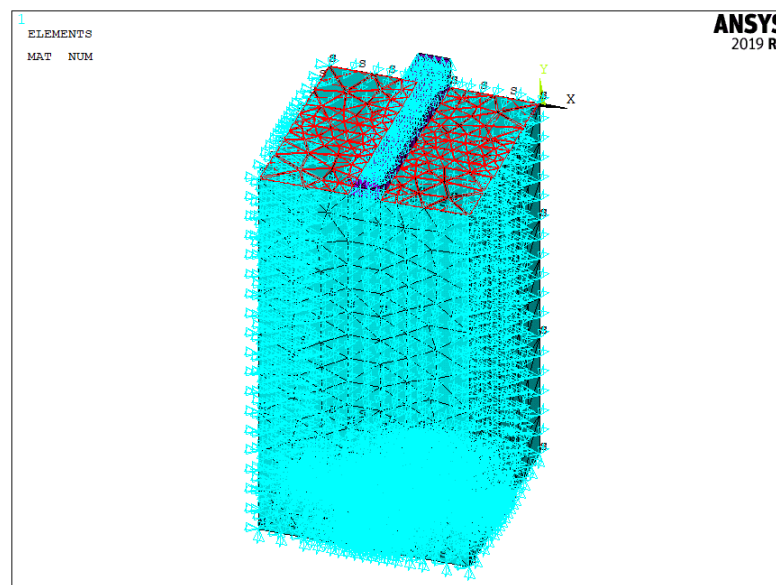


**Figure 79** Image of gauze model with arbitrary dimensions

As previously discussed, there is not a large amount of research into the mechanical properties of gauze or gauze's constituent materials. Therefore, a value of Young's modulus for cotton was chosen, specifically 0.41 GPa from Mouro et al.'s article. The fibres were arranged in

a similar way to woven gauze, with all fibres orientated in the same direction. As with the strut model, the gauze model was created in a fully parameterised fashion, with the material properties, and the dimensions of both the gauze and the muscle easily adjustable. This makes it much simpler to vary the properties of the model.

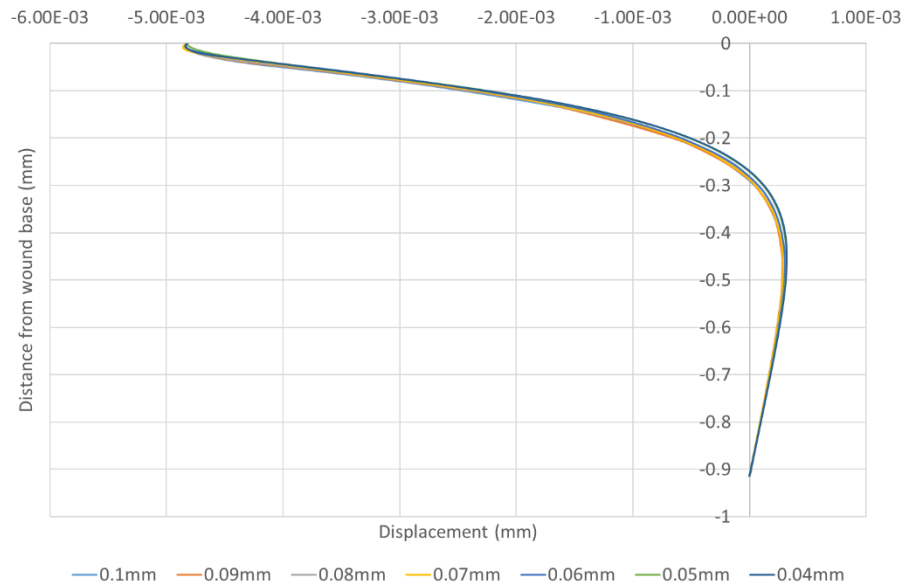
The model was built using an initial 16 key points to form the model's surface. A further 8 key points were constructed at a height of  $i$  to allow the gauze thread to be constructed. The 16 key points that form the surface of the model were selected and additional key points were generated from this pattern at a distance of  $-j$  (the muscle depth) from the model's surface. This parameterisation allows easy variation of the depth of the model being studied. The model was loaded in a similar fashion to the strut model developed earlier in the chapter. Strain values, which corresponds to the values found to be experienced by the whole wound model discussed in Chapter 6, were applied to the sides of the model. In addition, symmetry was applied to the vertical sides of the muscle aspect of the model, denoted by turquoise in Figure 80. This addition means that the model behaves as if it is part of a larger piece of tissue and repeats which means the strain experienced is more accurate. A displacement of  $-0.0643$  mm (3 s.f.) multiplied by the height of the thread was applied to the top surface of the thread, with an additional pressure of  $-0.00240$  kPa (3 s.f.) applied to the wound surface, demonstrating the negative pressure experienced by the wound during NPWT. To ensure the wound behaves like expected, the loading is gradually applied, with the strain and deformation plotted following each additional loading. The same process as with the strut model developed earlier in the chapter.



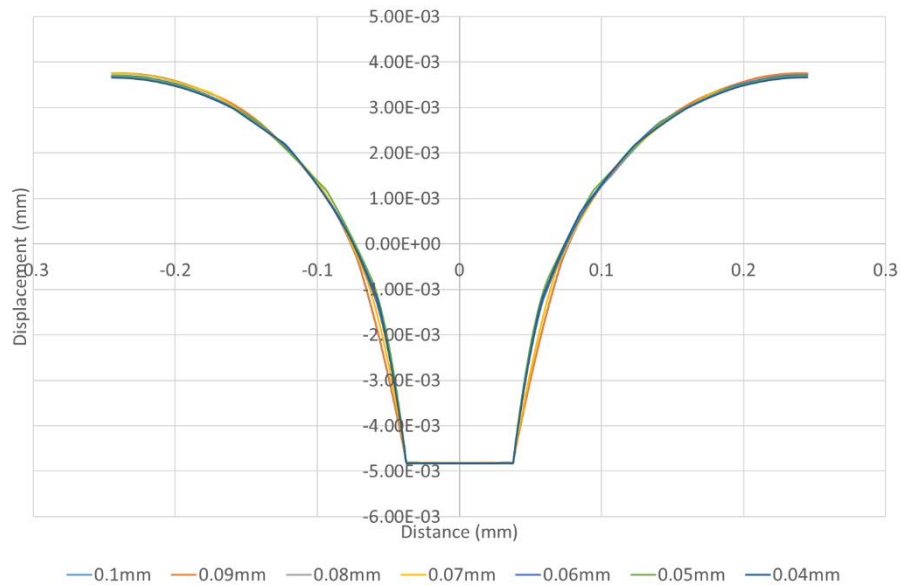
**Figure 80** Gauze model with arbitrary dimensions showing the applied loading conditions.

### 7.5.3 Mesh Convergence Study – Square Gauze Model

Figure 81 shows the convergence of displacement along a path plotted through the centre of the model. It can be seen that all line edge values provided similar results, however convergence was achieved by the 0.05mm and 0.04mm line edge size models. This can also be seen to be the case along the horizontal path, shown in Figure 82. Therefore, a line edge size of 0.05mm was used to mesh the square gauze model.

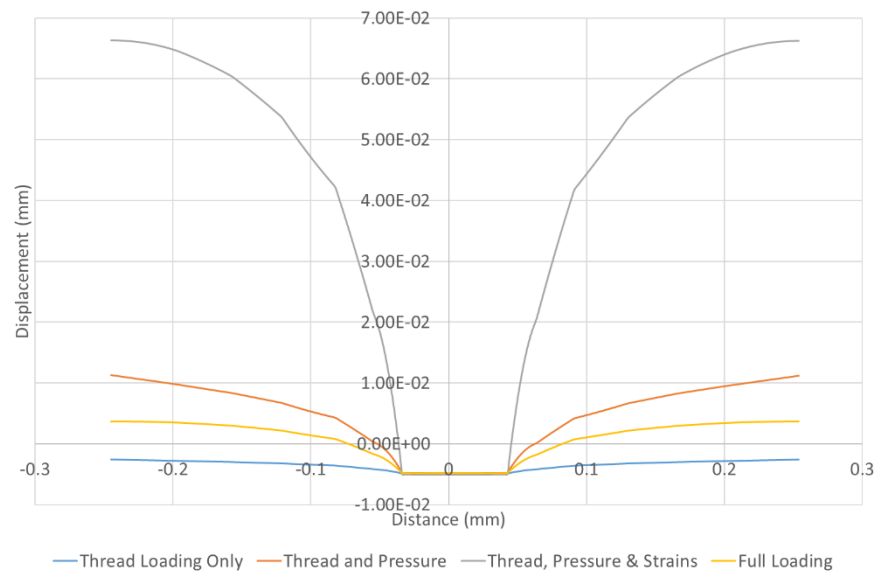


**Figure 81** Convergence study for square gauze model showing displacement through the model.



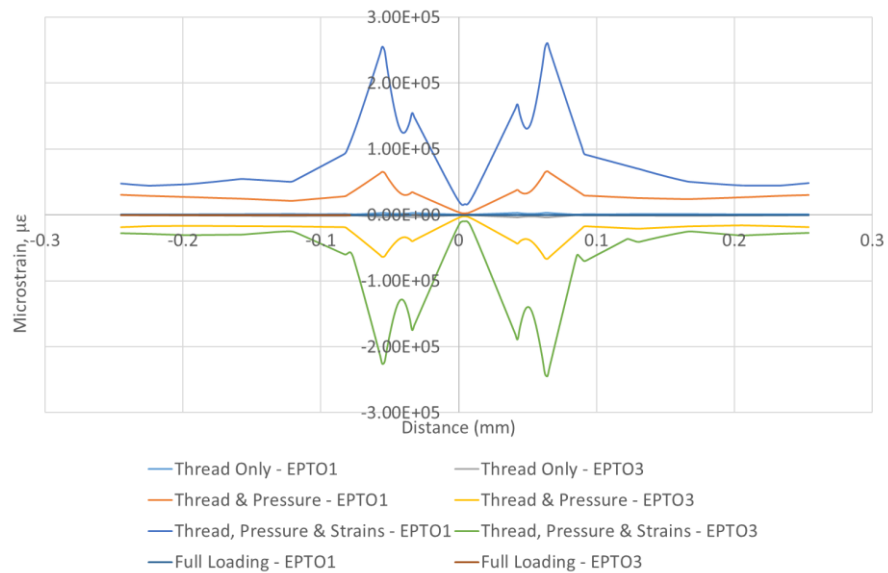
**Figure 82** Convergence study for a square gauze model showing displacement along a horizontal path.

Figure 83 shows the displacement experienced across the model along the surface X axis during gradual loading. This path goes through the central x-axis, taking it across the base of the thread. It can be seen that, when the displacement is applied to the thread, the surface of the model is displaced by approximately  $-0.2 \times 10^{-2}$ mm. The peak displacement in all loading conditions applies directly underneath the thread, with this displacement reducing by approximately  $0.3 \times 10^{-2}$ mm when each new loading condition is added. The width of this peak deformation is also reduced by approximately  $0.01 \times 10^{-1}$ mm. As this decreases, the maximum displacement of the tissue around the thread increased. The peak positive deformation occurred furthest from the central point on each side. When symmetry loading was added to the model, the displacement at the edges of the model decreased due to the influence of the next strut meaning that the tissue between the struts was unable to gain as much displacement at its peak.



**Figure 83** Vertical displacement experienced along the horizontal axis throughout the gradual loading of a square threaded gauze model.

In addition to comparing the displacement caused by the gradual loading of the model, the strains induced by the loading conditions were of particular interest. It can be seen in Figure 84 that the model has symmetrical strains. This was expected due to the loading and building method for this model. It can be seen that the peak tensile strain was experienced at approximately  $0.5 \times 10^{-3}$ mm either side of the central point. This aligns approximately with the corners of the thread edges. The maximum compressive strain occurs in the centre of the model, this corresponds with the minimum tensile strain. The strains correspond with the displacement, increasing as the loading increases. Whilst the peak tensile strains occur at the edges of the threads, a further tensile peak occurs at approximately  $\pm 0.5 \times 10^{-1}$ mm from the centre. This peak occurs on all models, with the highest tensile strain experienced here being approximately  $2.6 \times 10^5$ .



**Figure 84** 1st and 3rd principal strain variation along a horizontal path for a square threaded gauze model with gradual loading during model development.

In addition to the surface path, a path was plotted to allow an inspection of stress, strain and deformation along the central y-axis, located directly beneath the central point of the gauze thread. It can be seen in Figure 85 that a negative displacement occurred for all models at the thread-muscle interface. The thread only model experienced a slow decrease of displacement, reaching approximately 0mm at -0.9mm from the wound bed. The other model loading conditions induced a period of positive displacement. For the model with thread, pressure and strain loading conditions applied, the peak positive displacement was significantly higher than the other loading conditions. The peak positive displacement was approximately  $0.5 \times 10^{-3}$  for the model under full loading conditions.

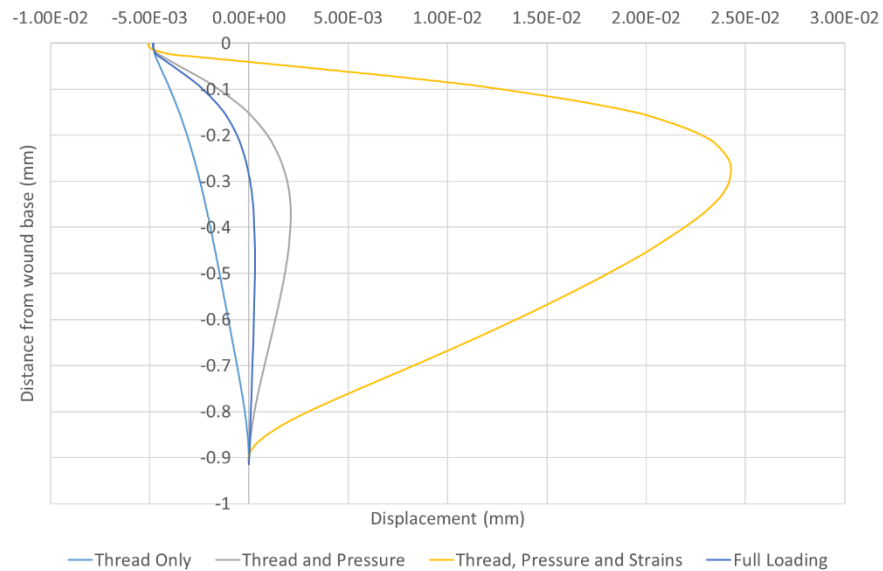


**Figure 85** Vertical displacement experienced by a square threaded gauze model during the gradual loading process.

As with the central displacement, the central strains experienced by the model with thread loading, surface strain, and applied strains were much greater than those experienced by the other models. For this model, the maximum tensile strain was experienced at approximately 0.025mm below the wound bed. This tensile strain is approximately  $2.25 \times 10^5$ . This can be observed in Figure 86. From here, the strain decreases to approximately  $2 \times 10^4$  at approximately 0.3mm below the wound bed. From here the model increases once more to approximately  $5.05 \times 10^4$  before reducing to approximately 0 at approximately 0.905mm below the wound surface. The compressive strain approximately mirrors the tensile strain in shape.

For the model with just the thread displacement applied, the strains experienced are significantly lower than those experienced by the model with almost full loading. Peak tensile strain is experienced approximately 0.05mm below the wound bed, with a microstrain of  $2.72 \times 10^{-3}$ . The compressive strain is approximately equivalent. From this point, the strain experienced is approximately 0 through the remainder of the central axis of the model.

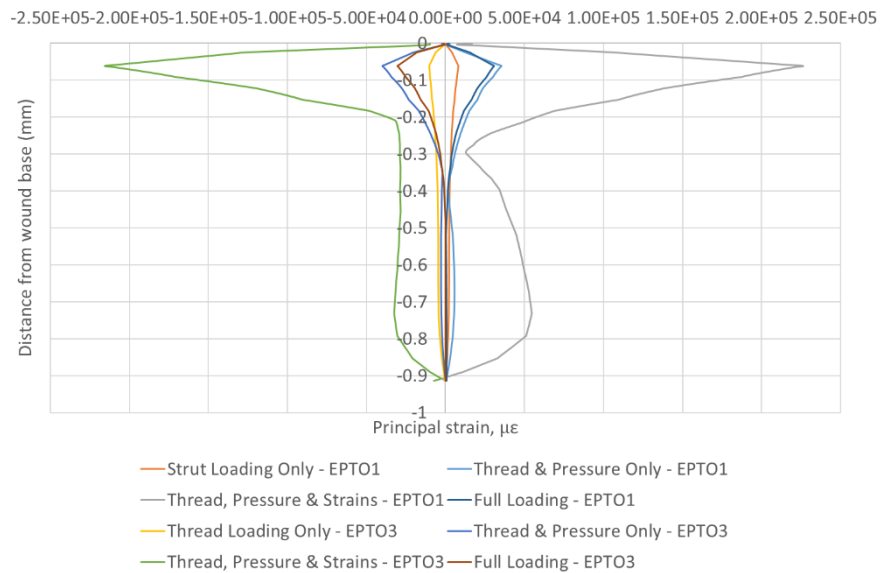


**Figure 86** 1st and 3rd principal strain through a central path for a square threaded gauze model with gradual loading

### 7.5.3.1 Development of Cylindrical Thread Model

In the initial gauze model, the threads were modelled with a square shape. This allowed the influence of the loading spread through the length of the model to be compared with a spot loading. However, the true shape and organisation of gauze can be better represented by a lattice of cylindrical threads. A cylindrical thread model was created using a different method to the square thread model due to the difficulties with meshing. This can be seen in Figure 87.

In order to create the cylindrical model, 4 key points were specified which were then replicated at a depth of  $-j$ . From this, 3 areas were created, and the working plane was offset by  $-D - E - F$  in the  $Z$  direction. From here, a cylinder with the diameter of  $I$  was created and the working plane was returned to the origin and a component was made from the cylinder called "Thread". This component was then unselected, and a component created from the remaining model called "Muscle". From here, the thread was subtracted from the muscle and the overlapping muscle was deleted. This deleted the 'Muscle' component and therefore the areas were reselected and renamed "Muscle2".

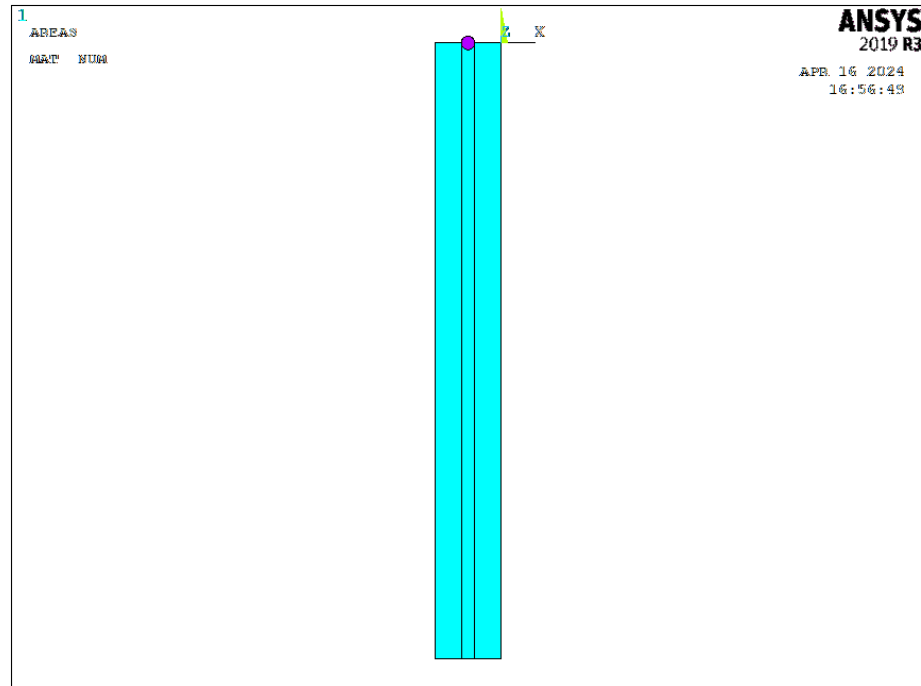


**Figure 87** Figure showing the construction of the cylindrical gauze model.

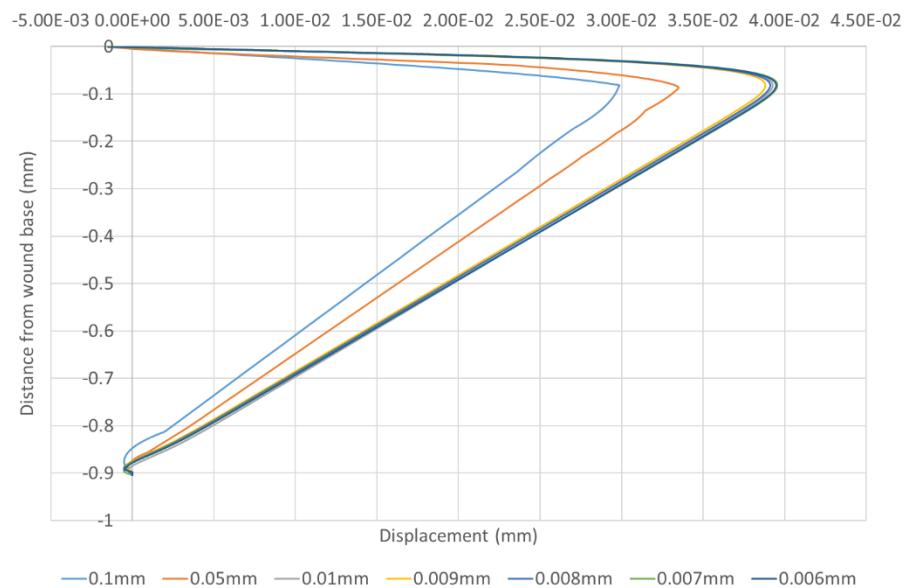
Once a 2D representation of the cylindrical thread model was created, it was meshed and run with appropriate loading to ensure the model was behaving in the expected way. Once it was established that it was reacting to loading appropriately, the model was re-loaded into the ANSYS software and selected. The VEXT command was then used to extend the areas in the Z direction by  $A + B + C$ . The cylindrical volume created from this extension was then selected and a further component called “Thread2” was created. This component was then unselected, and a component called “Muscle3” was created from the remaining volumes.

Following the creation of the 3D model, the model was meshed with different material properties applied to the muscle and thread components. The material properties were then coloured to provide a clear visual of what was each material. Once the model was meshed, loading could begin. The model was loaded in a gradual fashion, with the model initially loaded with only a displacement on the thread. From here a negative pressure was added to the surface of the surrounding tissue. A displacement calculated from the model in Chapter 6 was then added to the sides of the model, simulating the additional stress experienced on a macroscopic level by the surrounding tissue. Symmetrical loading was then applied to the same areas on the sides of the model to ensure the model behaves as part of a larger model, as the wound would in a clinical scenario. This symmetry restricts the movement of the sides of the model, reducing the muscles’ ability to be pulled in and up as a response to the pressure and strains that are applied. The base of the model is constrained in all directions as the surrounding tissue would be constricting this segment on a macroscopic scale.

Due to the cylindrical shape of the thread, to enable the model to run without interface errors, the thread was embedded into the wound tissue. This is different to the construction of the square shaped gauze model where the thread was sat on the surface of the muscle tissue. Therefore, the horizontal paths plotted for the cylindrical model were different to paths plotted for the square threads. Both horizontal paths were plotted through the base of the thread, however for the cylindrical model, this was at a distance of  $-0.5 * I$  below the wound bed, and for the square model, this was on the surface of the wound bed. Whilst gauze is generally made from a cotton fibre, the model was initially created with the same material properties as the polyurethane foam during the model testing stages.

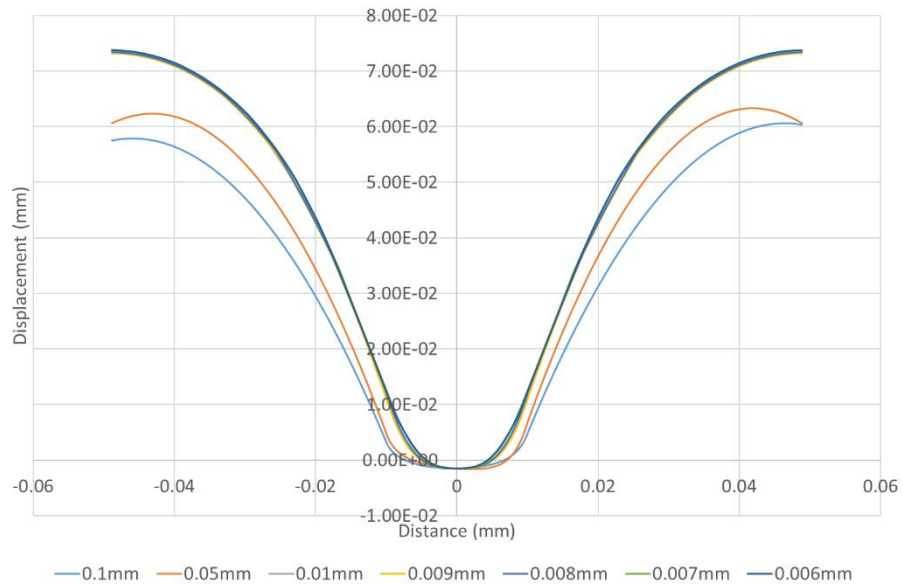
#### 7.5.4 Mesh Convergence Study – Cylindrical Gauze Model

Figure 88 shows the displacement of the model directly underneath the wound for the cylindrical wound model. It can be seen that there is a large amount of variation in the displacement. The variation reduces as the mesh becomes finer, with the meshes with line sizes of 0.007mm and 0.006mm converged.



**Figure 88** Convergence study for the cylindrical gauze model showing displacement through a central path.

It was important to check that the convergence along the horizontal path of the model agreed with the central path. Figure 89 presents the convergence of displacement through a horizontal path along the surface of the model. It can be seen that convergence occurs between the 0.007mm and 0.006mm meshes. As a result, a mesh with a line size of 0.006mm was used.



**Figure 89** Convergence study for the cylindrical gauze model showing displacement through a horizontal path.

As with the square shaped thread model, the cylindrical thread model was loaded gradually with each stage being solved and the data extracted. This data was then exported into an Excel spreadsheet to allow its presentation in graphical form, so the impact of each loading condition was able to be observed. Figure 90 shows the impact on each loading condition on the displacement experienced across the horizontal path, located at  $-0.5 * I$  below the wound surface. This path ran through the muscle-thread interface, as the thread was embedded to reduce mesh and geometry interface errors. It can be seen that for the gauze only loading condition, where apart from the constraint in all directions on the base of the model, the displacement of the model is negative throughout, with the lowest values directly underneath the thread. At the point furthest from the thread, approximately  $-0.25 \text{ mm}$  from the centre, the displacement is approximately  $-0.25 \times 10^{-2} \text{ mm}$ . This decreases gradually the closer to the central point that measurements are taken from. At the central point, the displacement is approximately  $-0.4 \times 10^{-2} \text{ mm}$ . The segment of the model in the positive x-direction is an exact reflection of the negative x-direction segment, with the displacement once again increasing to approximately  $-0.25 \times 10^{-2} \text{ mm}$  at  $0.25 \text{ mm}$  from the central point.

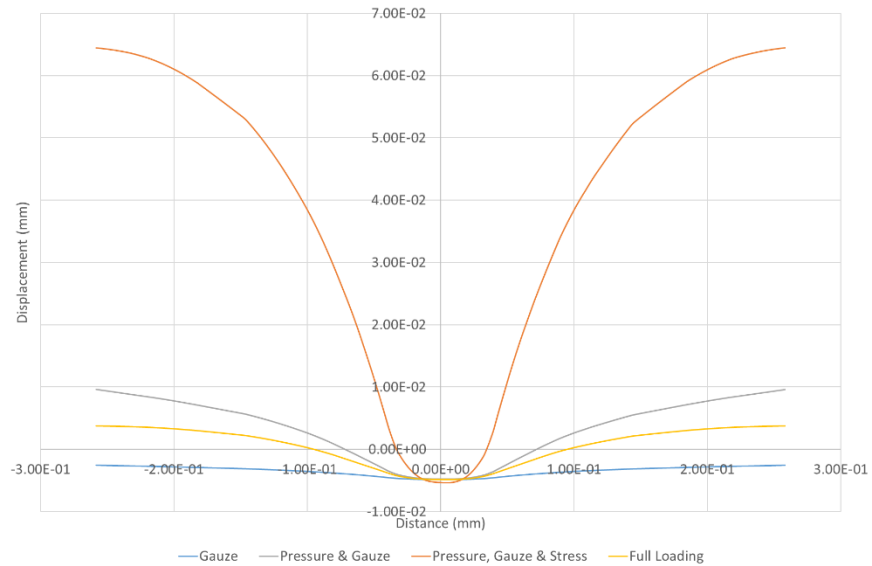


**Figure 90** Variation in displacement experienced a cylindrical thread gauze model during the gradual loading process.

When the negative pressure is added to the wound surface, there is a large increase to approximately  $0.99 \times 10^{-2}$  mm displacement of the edges of the model, with the central displacement remaining approximately the same as the thread only model. The orange line on the graph shows the displacement when strain is added to the sides of the model. The strain is created by a displacement added calculated from the strain experienced by the model on a macroscopic level in Chapter 6. This drastically increases the displacement experienced on the edges of the model to approximately  $6.45 \times 10^{-2}$  mm. This is approximately 6 x greater than the model with gauze and pressure loading. The displacement then decreases at a rate of approximately  $-0.067$  mm/mm until approximately  $-1.45 \times 10^{-2}$  mm when this increases to a rate of approximately  $-0.47$  mm/mm until approximately  $-0.3 \times 10^{-1}$  mm. The displacement graph then curves to reach a minimum displacement of  $-0.535 \times 10^{-2}$  mm at the central point, directly underneath the central point of the thread. As with the other loading conditions, the displacement in the positive x-direction is a near exact reflection of the displacement in the negative x-direction.

The full loading condition included the addition of symmetry on the sides of the model. This model behaves in a similar manner to the model with just pressure and thread displacement applied. The displacement on the edges of the model is approximately  $0.37 \times 10^{-2}$  mm which then decreases at a rate of approximately  $-0.013$  mm/mm until approximately  $-1.46 \times 10^{-1}$  mm from the central point of the model. From here the rate of displacement change increases to  $-0.086$  mm/mm until approximately  $-0.31 \times 10^{-1}$  mm from the central point when the displacement curves to a minimum of approximately  $-0.46 \times 10^{-2}$  mm. As with the other loading conditions, the displacement is equal in the positive and negative x-directions.

Figure 91 shows the compressive and tensile strains experienced by the model during the gradual loading process. The 'Thread Only' loading condition shows the least strain experienced by the model. From the edge of the model until approximately  $-1.17 \times 10^{-1}$  mm, both the compressive and tensile strains are almost unregistrable on the graph. From  $-1.17 \times 10^{-1}$  mm until approximately  $0.4 \times 10^{-1}$  mm from the centre, the strain increases, reaching a peak of approximately  $1.11 \times 10^4 \mu\epsilon$  before decreasing and reaching a minimum near  $0 \mu\epsilon$  in the centre of the thread. As with the displacement, the strain is then reflected in the y-axis for the second half of the model. The compressive strain follows the same pattern, reflected in the x-axis.

When the negative pressure was added to the surface of the model, the tensile strain at the edge of the model increased to  $3.62 \times 10^4$ . From here, the strain remains approximately constant until approximately  $-0.7 \times 10^{-1}$  mm from the centre when a peak of  $0.4 \times 10^5 \mu\epsilon$  occurs. From here, the tensile strain decreases to approximately  $3.8 \times 10^4 \mu\epsilon$  at approximately  $-0.62 \times 10^{-1}$  mm. A maximum tensile strain occurs at approximately  $-0.41 \times 10^{-1}$  mm from the central point, with a strain of approximately  $5.2 \times 10^4 \mu\epsilon$ . The strain then decreases, reaching a minimum of approximately  $7 \times 10^3 \mu\epsilon$  at the central point. This is then mirrored for the positive x-direction. The compressive strain follows the same pattern, reflected in the x-axis.

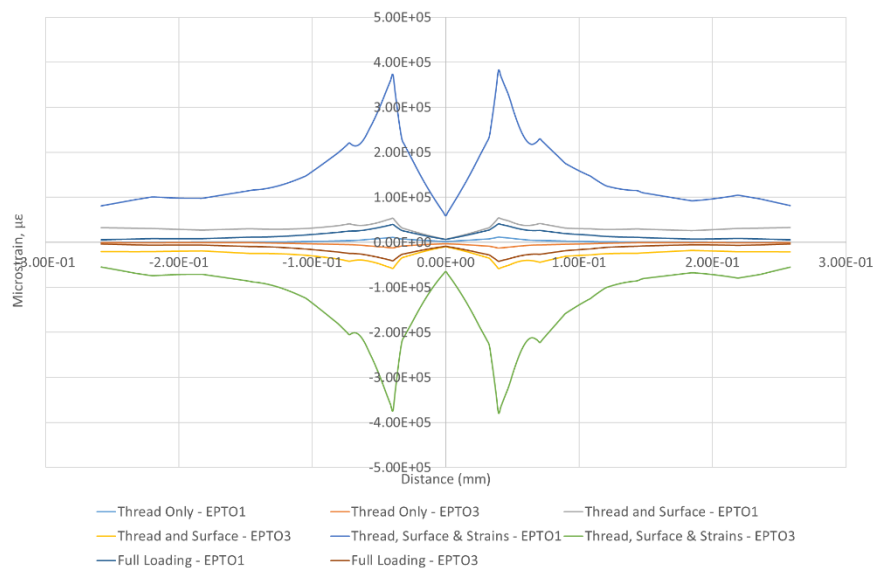


**Figure 91** Compressive and tensile strains through a central path during the gradual loading of a cylindrical thread model.

When the macroscopic strain is applied, both the tensile and compressive strains are significantly greater than previous models. The same pattern as previous models were followed with an initial peak followed by a maximum before reaching a minimum in the centre of the thread which is then reflected in the y-axis. The tensile strain at the edge of the model is  $0.816 \times 10^5$  which then increases to  $2.2 \times 10^5 \mu\epsilon$  at  $-0.072 \times 10^{-1}$  mm from the central point. The

maximum tensile strain is reached at approximately  $-0.4 \times 10^{-2}$  mm from the centre, with a value of  $3.72 \times 10^5 \mu\epsilon$ . This then decreases as the central point is reached, first to  $2.27 \times 10^5 \mu\epsilon$  at  $-0.372 \times 10^{-1}$  mm from the centre, then to the minimum of  $0.586 \times 10^5 \mu\epsilon$  at the centre. The compressive strain follows the same pattern, reflected in the x-axis.

The final model shown on the graph in Figure 91 is the model with full loading. This model is shown by navy and burgundy. The tensile strain at the edge of the model is approximately  $0.055 \times 10^5 \mu\epsilon$  which then increases to  $0.415 \times 10^5 \mu\epsilon$  at approximately  $0.4 \times 10^{-1}$  mm. A minimum of  $0.0644 \times 10^5 \mu\epsilon$  is then reached at the central point. This is reflected in the y-axis for the positive x-direction of the model. As with previous loading conditions, the compressive strain follows the same pattern of maximum and minimum points as the tensile strain.

In addition to the impact of each loading condition on the horizontal path directly underneath the wound-thread interface, the impact of the loading conditions on the depth of the model was of interest. Figure 92 shows the displacement experienced by the wound model directly under the central point of the strut. As with the corresponding horizontal model seen in Figure 90, it can be seen that the initial displacement for the thread only, thread and surface and full loading models are the same at approximately  $-4.82 \times 10^{-3}$  mm, whereas the model with thread, pressure and strains applied has a greater initial displacement of  $-5.35 \times 10^{-3}$  mm. From here, the displacement for all models decreases, moving towards neutral. The model with thread, pressure and strain loading reaches the y-axis first, with a neutral displacement occurring at approximately  $-0.6 \times 10^{-1}$  mm below the wound-thread interface. The thread and surface loading model is the next to reach a point of neutral displacement, with this occurring at approximately  $-1.9 \times 10^{-1}$  mm below the thread-wound interface. The royal blue coloured line denotes the displacement under the central point of the model in full loading conditions. This model reaches the point of no displacement at approximately  $-3 \times 10^{-1}$  mm. For the three loading conditions mentioned above, the model then experiences a period of positive displacement and a peak displacement. The peak displacement is greatest for the model with thread, pressure and strain loading, occurring at approximately  $-2.77 \times 10^{-1}$  mm with a value of  $2.43 \times 10^{-2}$  mm. From this point, the displacement decreases, reaching neutral displacement once again at approximately  $-8.9 \times 10^{-1}$  mm. For the model with thread and pressure loading, the peak displacement occurs at approximately  $4 \times 10^{-1}$  mm below the thread-wound interface. This has a value of approximately  $1.68 \times 10^{-3}$  mm. The model with full loading has a much smaller positive displacement than the previous two loading conditions, with a peak displacement of approximately  $2.38 \times 10^{-4}$  mm at  $5 \times 10^{-1}$  mm.

The model with only the thread loaded follows a different path to the other loading conditions. This model does not reach a neutral displacement until approximately  $-8.9 \times 10^{-1}$  mm below the wound surface. The displacement decreases at a steady rate of approximately 191 mm/mm. There is no positive phase or peak displacement for this graph, unlike the other loading conditions.

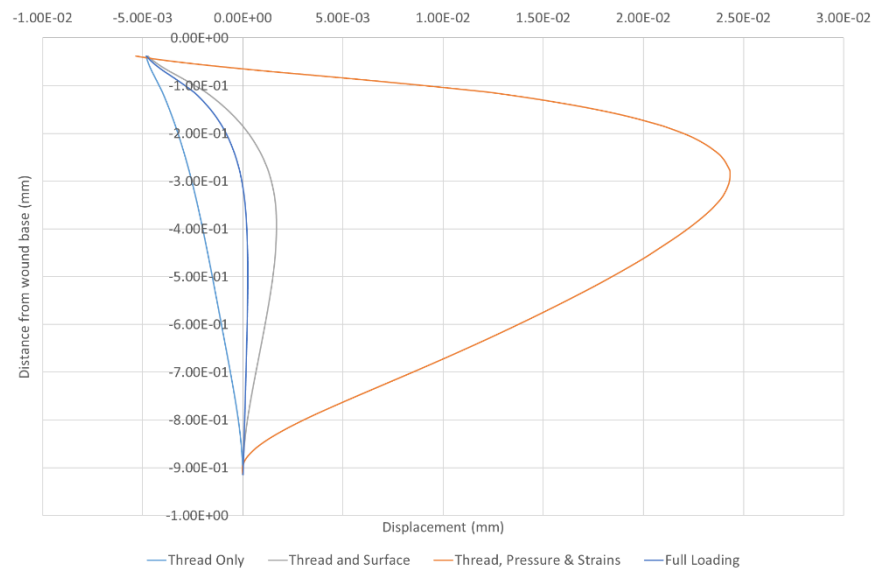


**Figure 92** 1st and 3rd principal strains through the vertical (Y-axis) path underneath the cylindrical gauze during gradual loading.

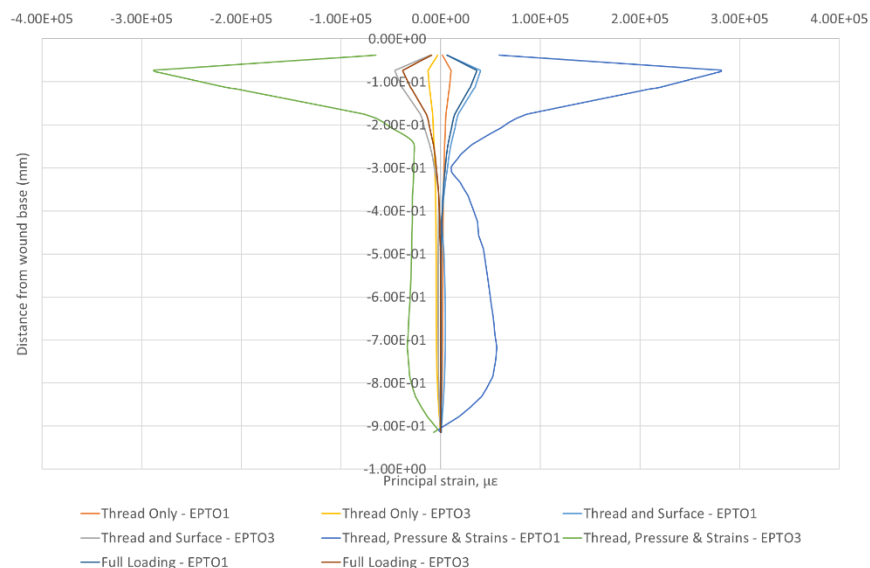
In addition to the displacement, as with the other models, the 1<sup>st</sup> and 3<sup>rd</sup> principal strains were investigated. It can be seen that the strain follows a similar pattern for all models, however the strain experienced by the thread, pressure and strains loading condition is much greater than the strain experienced by the other loading conditions. This corresponds with a greater displacement also. In general, the 1<sup>st</sup> and 3<sup>rd</sup> principal strains are reflections of each other. This is less the case for the thread, pressure and strains loading than it is for the other loading conditions.

All loading conditions experience a peak strain at approximately 0.9 mm below the wound surface. For the model with the thread only loading condition, this strain was the smallest, with the tensile strain having a value of  $1.05 \times 10^4 \mu\epsilon$ . From here, the strain tends towards  $0 \mu\epsilon$ . A similar pattern is seen in the thread and pressure model and the model with full loading conditions. The model under full loading conditions has a peak tensile strain of  $3.6 \times 10^4 \mu\epsilon$ , and the model with just thread and pressure loading conditions has a peak tensile strain of  $3.97 \times 10^4 \mu\epsilon$ . Whilst this is greater than the 30% strain expected, the model has linear material properties

that align with those presented by literature on the mechanical properties of muscle. These models then tend to no strain the further the strain travels below the wound surface.

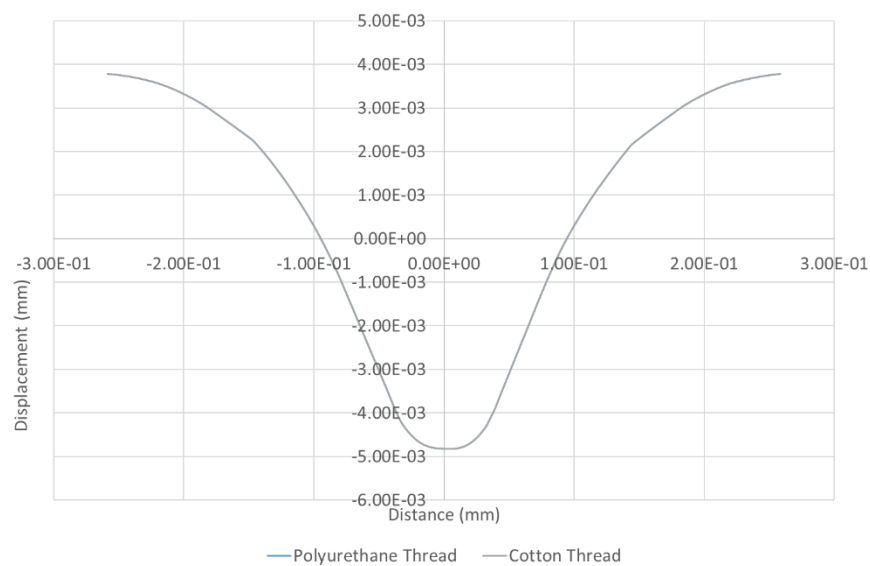
The main difference between the models described above and the model with thread, pressure and strain loading condition is the scale of strain experienced. The tensile strain at the thread-wound interface is  $5.86 \times 10^4 \mu\epsilon$  which then increases at a rate of  $-6.36 \times 10^6 \mu\epsilon / \text{mm}$  to  $2.82 \times 10^5 \mu\epsilon$ , reaching this point at  $-7.26 \times 10^{-2} \text{mm}$  below the wound surface. From here, the tensile strain decreases at approximately the same rate that the strain increased initially to approximately  $8.65 \times 10^4 \mu\epsilon$  at  $-1.75 \times 10^{-1} \text{mm}$ . The tensile strain then decreases at a slower rate to reach a minimum of  $1.07 \times 10^4 \mu\epsilon$  at approximately  $-3 \times 10^{-1} \text{mm}$  below the wound bed. From here, the tensile strain once again increases reaching a final local maximum of  $5.64 \times 10^4$  at approximately  $-7.2 \times 10^{-1} \text{mm}$  below the wound surface. From here the tensile strain reduces to reach  $0 \mu\epsilon$  at approximately  $-9 \times 10^{-1} \text{mm}$  below the surface.

The compressive strain follows approximately the same pattern as the tensile strain, also reaching a maximum before reducing to a minimum. The main difference between the pattern of the tensile and compressive strain for the model with thread, pressure, and strain loading is that once a local minimum has been reached at approximately  $-2.3 \times 10^{-1} \text{mm}$  below the surface, the strain remains constant until approximately  $-8 \times 10^{-1} \text{mm}$  below the wound surface where it reduces to approximately 0 strain at  $-9 \times 10^{-1} \text{mm}$ . A small increase is then seen between  $-9 \times 10^{-1} \text{mm}$  and  $-9.1 \times 10^{-1} \text{mm}$ .

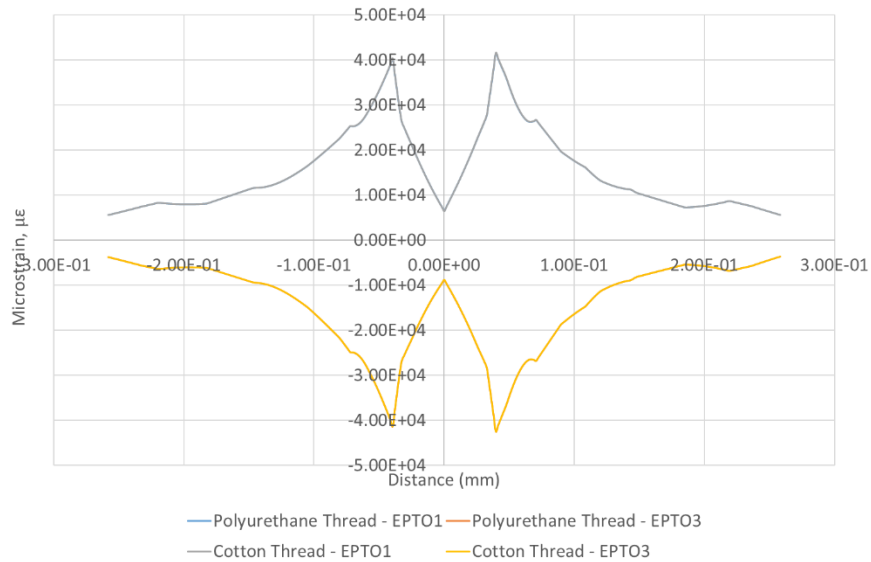


**Figure 93** 1st and 3rd principal strains through a vertical central path for the gradual loading of a gauze model with cylindrical threads.

Gauze is defined by the Cambridge Dictionary as “a very thin, light cloth, used to make clothing, to cover cuts and to separate solids from liquids, etc.” (Cambridge Dictionary, 2023). The previous models have been created using the same material properties as the polyurethane foam, however, in order to improve the accuracy of the replication of the clinical scenario, an additional model has been created with the material properties of cotton. This model has a Young’s modulus of  $4.1 \times 10^5$  kPa which has been taken from (Mouro et al., 2021)’s study. The Poisson’s ratio remains the same at 0.3. It can be seen in Figure 94 that there is no difference in the displacement along the horizontal path between the model with polyurethane material properties and cotton material properties. With there being no difference in displacement, there is also no difference in compressive and tensile strains, shown in Figure 95.

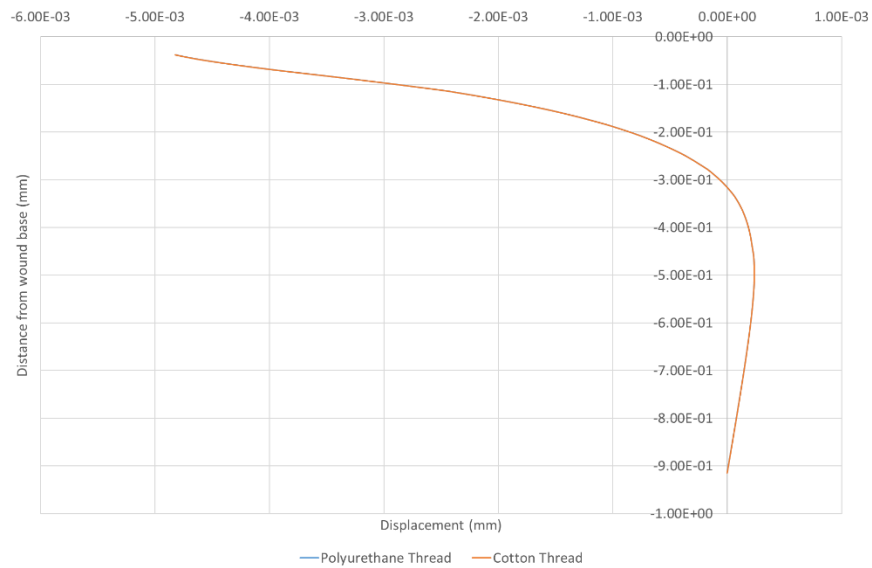


**Figure 94** Variation in displacement for a cylindrical gauze model with polyurethane thread material properties in comparison with cotton thread material properties through a horizontal path.



**Figure 95** Variation in 1st and 3rd principal strains for a cylindrical gauze model with polyurethane thread material properties vs cotton thread material properties.

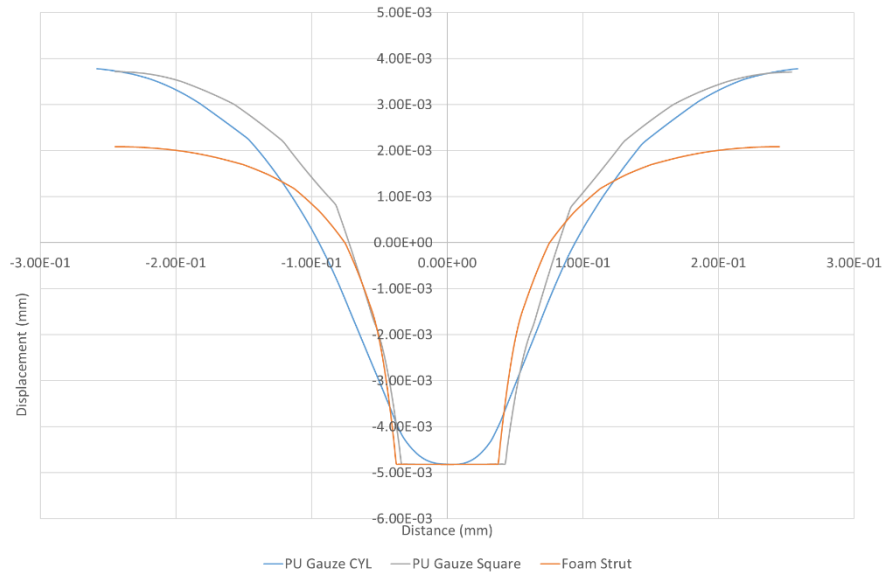
Figure 96 shows the displacement of the y-axis directly underneath the central point of the thread for the cotton and polyurethane gauze. It can be seen that, as with the horizontal path, there is no variation in displacement between the two material types. Therefore, it can be reasonably expected that there is no variation in strain experienced by the models.



**Figure 96** Variation of vertical displacement through a central vertical path for cylindrical thread models with polyurethane and cotton material properties

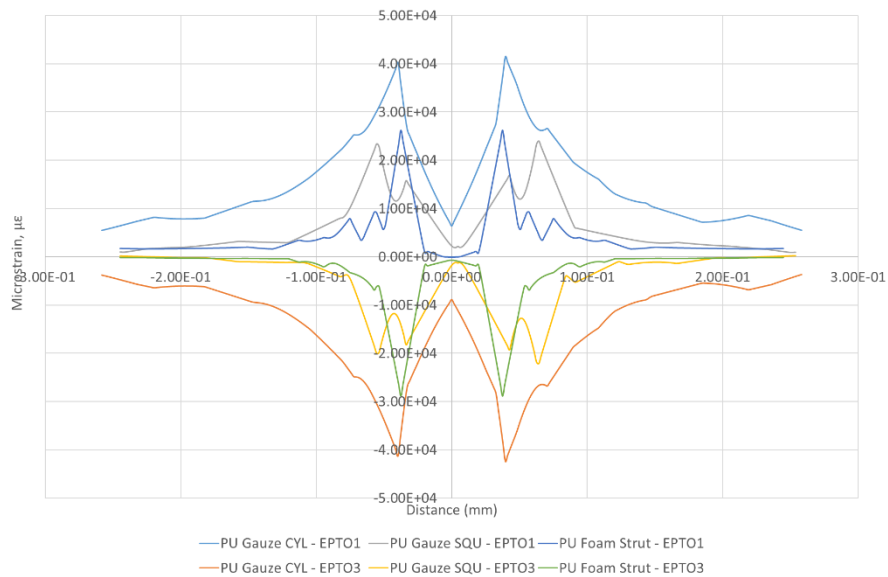
Figure 97 shows the impact of the different shaped threads and struts has on the vertical displacement along a horizontal path running directly underneath the wound filler. For this selection of models, the height of the strut was reduced to be equal to the height of the thread. This is because the applied displacement is scaled with the height of the strut/thread as a larger strut would experience greater displacement under negative pressure. It can be seen that the

displacement for the square gauze and the foam strut are similar, with the only difference being the peak displacement at the edge of the model being greater for the gauze model than the foam model. The key difference between the models is that the displacement has a curved shape for the cylindrical gauze whereas both the square gauze and foam strut have corners of approximately 90°.



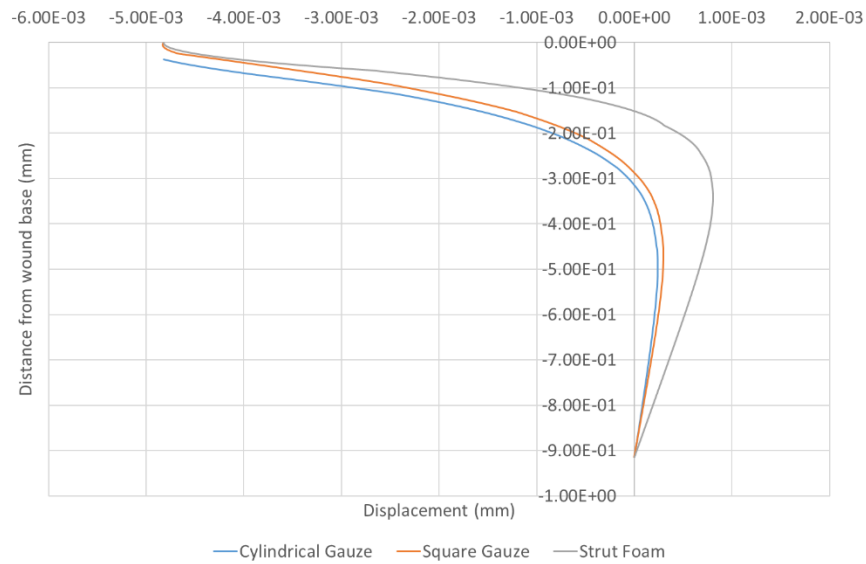
**Figure 97** Comparison of the displacement experienced by microscopic models simulating gauze and foam with polyurethane material properties and equal loading.

Figure 98 shows the strain along a horizontal path for models with varying shapes of thread and strut. It can be seen that the gauze thread with a cylindrical cross sectional area has a much greater peak compressive and tensile strain than the other shaped models, reaching a peak of approximately  $4 \times 10^4 \mu\epsilon$  at two points. The strain experienced at the central point of the cylindrical gauze model is greater than that experienced by the foam strut and square gauze models. The peak strain of the foam strut model is the next greatest, however the peak occurs directly on the point corresponding with the corners of the strut. This is unlike the square gauze model which has two peaks, an initial peak at the corner of the thread, and a greater peak at approximately  $\pm 0.7\text{mm}$  from the centre. The compressive strain follows the same variations as the tensile strain in the negative direction.



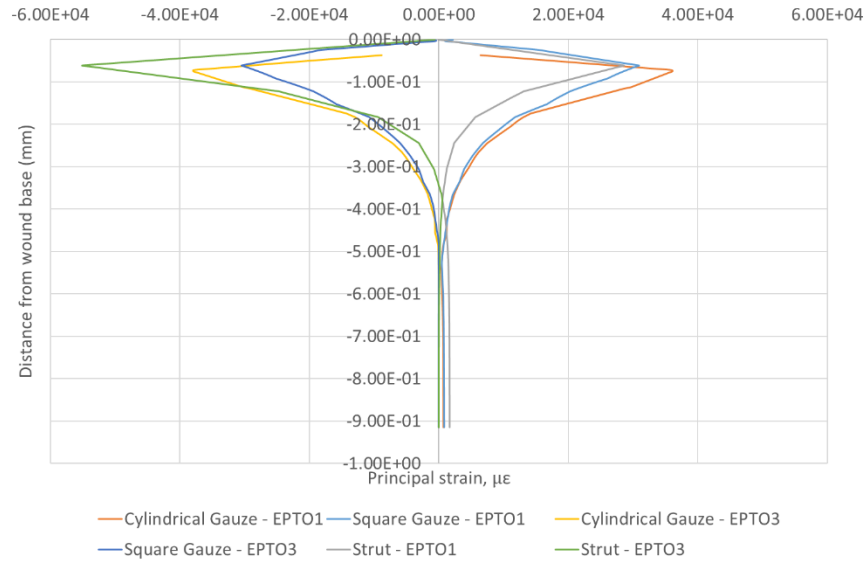
**Figure 98** Variation of 1st and 3rd principal strain through a horizontal path for models simulating gauze and foam with polyurethane material properties and equal loading.

Like previous models, the central displacement and strain is also of interest. Figure 99 displays this in graphical form. It can be seen that the displacement experienced takes a similar approach for all three models. The displacement directly underneath the wound-thread/strut interface was the same for all models with a value of approximately  $-4.8 \times 10^{-3}$ mm. As the path progresses, the negative displacement decreases, with the displacement of the model representing foam struts being the first to reach the position of neutral displacement at approximately  $-1.5 \times 10^{-1}$ mm below the wound surface. The square gauze is the next to experience neutral displacement, reaching this position at approximately  $-2.9 \times 10^{-1}$ mm, closely followed by the cylindrical gauze at approximately  $-3.1 \times 10^{-1}$ mm. From here, all three models experience a period of positive displacement, with the greatest peak positive displacement being experienced by the strut model. All models then converge to reach neutral displacement once more at the base of the model.



**Figure 99** Displacement through a central vertical axis for models simulating polyurethane foam and gauze with varying thread shapes.

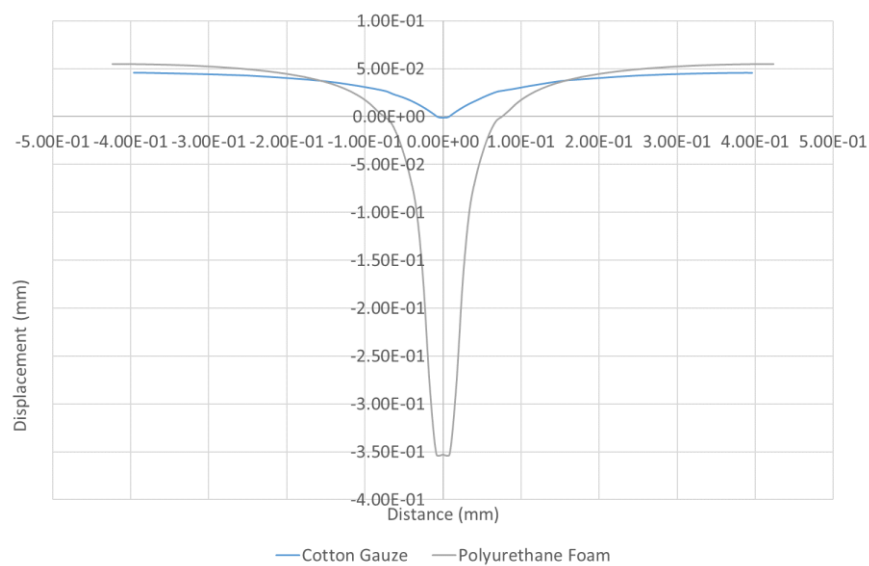
As with previous models, the central 1<sup>st</sup> and 3<sup>rd</sup> principal strains were also of interest. It can be seen in Figure 100 that whilst the strains for all three models all follow the same pattern, the square gauze once again creates a greater strain than either the circular or strut models. The strut model reaches a minimum strain earlier than the gauze models.



**Figure 100** 1st and 3rd principal strains through a central path for varying polyurethane gauze thread and foam strut shapes with equivalent loading.

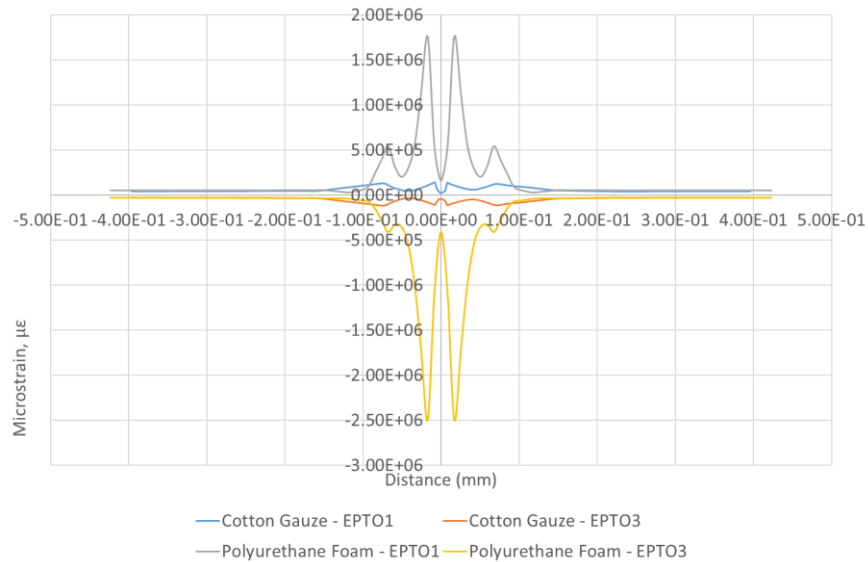
The final graphs compare the cylindrical model and the strut model under normal loading conditions. Both models were compared at 30PPI, using values found in literature to define the dimensions of the models. The cylindrical gauze model had cotton material properties applied, whilst the strut model had polyurethane material properties. The difference in strains experienced in these scenarios are of particular interest.

The displacement along the horizontal axis of these models can be seen in Figure 101. Gauze threads are much thinner and shorter in height than the polyurethane foam struts and as such, due to the scaling of the displacement, the displacement applied to the thread is smaller. Therefore, the peak displacement in the negative plane is significantly smaller, with a value of approximately  $1.03 \times 10^{-3}$  mm at the central point of the thread. The peak negative displacement in the strut model is approximately  $-3.44 \times 10^{-2}$  mm. The thread is significantly thinner in width than the strut, causing the negative displacement to occur in a narrower area. The difference in peak positive displacement between the models is much less pronounced than the peak negative displacement. This is seen at the edge of the model. In addition, the same difference in shape that was observed in Figure 97 is seen.



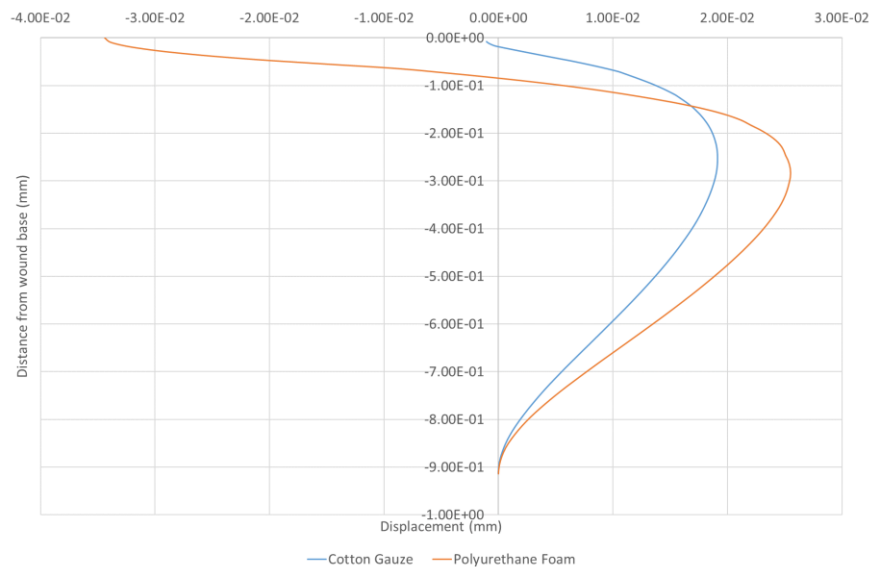
**Figure 101** Vertical displacement through a horizontal path for cotton gauze thread and polyurethane foam on a microscopic level.

The compressive and tensile strain along the horizontal axis can be seen in Figure 102. It can be seen that the strain experienced by the wound when the polyurethane foam was applied was much greater than the strain induced by the cotton gauze. In addition, whereas the foam strut induces strain primarily around the edges of the strut, the foam gauze also induces strain along its path.



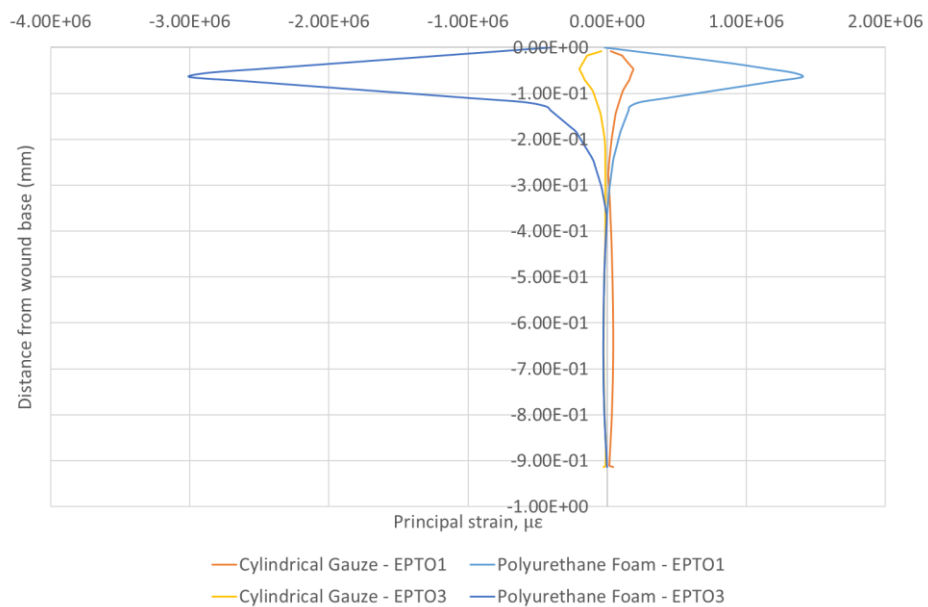
**Figure 102** Variation of tensile and compressive strain along a horizontal path for models of polyurethane foam and cotton gauze on a microscopic level.

Figure 103 shows the displacement on the central path for the cotton gauze and polyurethane foam. As shown on the horizontal graph in Figure 101, the initial displacement is greatest for the polyurethane foam. This displacement then moves towards positive displacement, crossing from negative to positive at approximately  $-0.9 \times 10^{-1}$  mm. This occurs at a much shallower depth for the cylindrical gauze model, with neutral displacement occurring at approximately  $-0.1 \times 10^{-1}$  mm. A peak positive displacement for the cotton gauze model occurs at approximately  $-2.5 \times 10^{-1}$  mm, with a peak of approximately  $1.9 \times 10^{-2}$  mm. This is compared to a peak of approximately  $2.5 \times 10^{-2}$  mm displacement at  $-3 \times 10^{-1}$  mm for the foam model.



**Figure 103** Variation of vertical displacement through a central path for microscopic models of cotton gauze and polyurethane foam.

The final graph, Figure 104, shows the induced tensile and compressive strains for cotton gauze and foam. As with the displacement, the compressive and tensile strains occur at a shallower point for the cotton gauze. In addition, the tensile strain has a peak of approximately  $2.8 \times 10^5 \mu\epsilon$  and continues to be greater throughout the depth of the model, remaining at approximately  $0.5 \times 10^5 \mu\epsilon$ . In contrast, the peak strains experienced by the polyurethane foam are greater with a peak of approximately  $2.8 \times 10^5 \mu\epsilon$  occurring at  $\sim -0.5 \times 10^{-1} \text{mm}$  below the wound surface. From here, the strain decreases, tending towards  $0 \mu\epsilon$ , reaching this value at approximately  $-3.0 \times 10^{-1} \text{mm}$ . From here, the strain remains at approximately  $0 \mu\epsilon$  throughout the remainder of the model.



**Figure 104** Variation of 1st and 3rd principal strain for models of gauze and foam through a central path on a microscopic level

## 7.6 Discussion

Research into the effect of mechanical strain on dermal cell proliferation has established that fibroblast and epithelial cell production increases when strain is applied. This chapter investigated the effect of the wound substrate on the strains experienced by the model on a microscopic level. The impact of varying the porosity of the foam was also investigated as a variety of different foams are available for negative pressure wound therapy.

### 7.6.1 Impact of Foam

It was seen in Figure 75 that, whilst the peak displacement remains the same for all struts, the wider impact of this strut varies. The strain was greatest for the models with the least pores per inch. These models have the largest space between each strut, thus allowing more movement of the wound tissue. This movement creates strains and thus the greater the

movement, the greater the strain experienced by the tissue. Whilst many studies have looked at the impact of mechanical strain on the expression of growth factors for granulation tissue growth, these focus mainly on establishing whether growth factor expression can be induced at a strain of 0.1. There is room in literature for a study on growth factor expression where the applied mechanical strain is increased gradually to find whether varying the strain has an impact on the quantity of growth factor expressed, and the minimum strain the cell must experience to induce this growth factor expression. The compressive strain of all models reached the value of  $0.1\epsilon$  known to induce wound healing.

In addition, when studying the strain experienced through the muscle the point of  $0.1\epsilon$  is experienced in both the tensile and compressive strains. This value is reached early in the path, at approximately 0.01mm below the strut-wound interface. Therefore, it is reasonable to assume that this also increases the rate of granulation tissue growth on the wound.

### 7.6.2 Influence of Gauze as a Wound Filler

In addition to investigating the effect of various porosities of foam, the impact of gauze as a wound filler was studied. There were two key stages to this investigation. The first stage modelled the gauze threads as if it was an elongated horizontal strut, with a square cross section. A more realistic model was then created with the gauze threads having a cylindrical cross section. When comparing these two models, it was found that the gauze model with cylindrical threads had a less dramatic difference in peak strain through the centre of the model, with the strain producing a rough semi-circular pattern. In addition, the tensile and compressive strains were experienced throughout the model, not reaching  $0\epsilon$  at the centre of the base of the cylindrical gauze, unlike both the square gauze and the strut models under the same loading conditions.

Of particular interest are the values of strain the model experiences when loaded with realistic conditions. The gauze model reaches a maximum strain of approximately 0.05, half of the value proven in literature to influence the wound healing process. However, gauze is used as a wound filler material for NPWT, suggesting that this material has some positive effect on the wound healing process. Therefore, it could be implied that applying a 5% strain to cells could also induce granulation tissue growth, whether through the expression of growth factors, or through other unknown means.

## Chapter 8 Discussion

### 8.1 Project Summary

This project took a multifactorial approach to the investigation of negative pressure wound therapy and the development of biomechanically similar models for the testing of novel medical devices. One of the key aims was to develop a model to allow greater understanding the distribution of strain throughout a wound during negative pressure wound therapy.

The first stage in the project was the development of a physical wound model. This *in vitro* model was developed using SolidWorks (Dassault Systèmes, 2020) computer-aided design application to create a multilayer mould, with each layer corresponding to a layer in the structure of the body, either skin, subcutaneous adipose tissue, or muscle. Literature was then used to determine the thickness of each of these layers.

A review of literature was conducted to establish the values of Young's modulus for the biological tissues being modelled. Skin was considered to be the epidermis and dermis combined, whilst 'fat' was subcutaneous adipose tissue, and 'muscle' referred to skeletal muscle. Biological tissues are highly influenced by external factors, meaning that the stiffness of these tissues is almost unique to individuals (Held et al., 2015). In addition to this variation, these tissues have non-linear material properties and whilst this is acknowledged by researchers, published material investigating the mechanical properties of these tissues generally provide a range of values.

To ensure the *in vitro* model was biomechanically similar to tissue, samples of silicone were tested to ASTM D412, an American standard for the testing of vulcanised rubber and thermoplastic elastomers under tension. A review by Dąbrowska et al. (2016) investigated the impact of different materials for the modelling of skin. It was found that silicone based models were durable and had long term stability, both qualities that are required when building a model for the testing of novel medical devices, particularly for repeat testing. It was however acknowledged that the material properties of silicone can alter over time for some silicones, and this led to the silicone samples being tensile tested at 1, 7 and 28 days post casting. Independent 2-tailed t-tests were carried out to determine whether there was a statistically significant change in material properties over time for varying strain for each silicone tested. It was found that the majority of silicones experienced statistically significant variation in Young's modulus over 28 days. This variation was found to be less significant for lower strain values, particularly up to 5% strain. As the strain experienced by the finite element model discussed in Chapter 4 was generally no higher than 10%.

To determine the most biomechanically similar silicone and therefore the most appropriate silicone to build the *in vitro* model from, the Young's moduli from the silicones were plotted alongside the Young's moduli for biological tissues found in literature. From here, it was observed that the Food Grade Silicone had the most similar Young's modulus to the skin, Silskin 10 2:1 ratio was most similar to the subcutaneous adipose tissue, and Silskin 10 1:1 ratio was most similar to muscle. Many assumptions were made in the process selecting these materials and it is acknowledged that this is not a perfect representation of the biological tissues being modelled, however the materials behave in a similar manner.

Following the material selection, a mould for the casting of an *in vitro* model was designed using Solidworks (Dassault Systèmes, 2020) computer-aided design and computer-aided engineering application and printed with polylactic acid (PLA) using fused deposition modelling (FDM). The mould for casting the model was created in a modular fashion, to allow variation in model and layer thickness if required at a later stage. The mould was inverted and cast one layer at a time with each selected silicone, starting with the skin and finishing with the muscle equivalent layer. Each silicone was cast according to manufacturer's instructions with the exception of the fat layer where the silicone was cast with a base: catalyst ratio of 1:2. The purpose of this was to further reduce the Young's modulus as fat is a particularly difficult substance to simulate as it has a gelatinous consistency less able to be emulated with silicone. In each layer of silicone, steel thread clippings under 10mm in length was added. This ensured the model could be oriented correctly during CT scanning.

Following the casting of the *in vitro* model, the impact of negative pressure wound therapy was studied. The first stage of this process was to understand the position of the model position prior to negative pressure being applied. To do this, the model was scanned using a MicroCT machine producing a set of .Tif images and location data. From here, this information was loaded into AVIZO data visualisation and analysis software, and the wound of the model and the steel threads were segmented from the rest of the model. The model was then scanned whilst subjected to negative pressure. In order to do this, a RenaSYS Negative Pressure Wound Therapy System was connected to the model. Due to silicone's anti-adhesive properties, difficulties were presented when securing the negative pressure device to the model as the seal must be airtight to enable a vacuum to be formed. It was discovered through experimentation that cloth backed waterproof adhesive tape was the most effective method for ensuring an airtight seal. One key limitation of this method is the Young's modulus of cloth backed waterproof adhesive is higher than that of the adhesive layer that is attached to the RenaSYS NPWT tubing. The same protocol of testing and image analysis was then followed to investigate the impact of the negative pressure on the deformation of the model.

In order to gain a greater and more specific understanding of the strain distribution throughout both the wound surface and depth during negative pressure wound therapy, finite element modelling was used. Multiple models were created, first investigating the strains and displacement experienced on a macroscopic level, modelling the wound as a whole, then on a microscopic level, looking at the impact of individual struts and threads on the displacement of the wound and strains experienced. The models were fully parameterised to allow for adjustments to be made as necessary to adapt to the needs of novel medical devices.

The material properties of the *in silico* model were then altered to become biological material properties, as discussed in Chapter 6. From here, the strains and displacement around the wound face of the model and along a central path were investigated. It was found that the peak tensile strain was experienced approximately 5mm below the wound base. This peak strain had a value of approximately 5.9%. Strain around the wound face was greater, with the skin-fat interface reaching a value of approximately 10.1% tensile strain. The fat layer experienced compressive strain of approximately 14.9%.

From here, a further modelling was carried out to investigate the impact of the wound filler material on the strains experienced at a microscopic level. The models developed in Chapter 7 represented cotton gauze with a cylindrical thread, and polyurethane foam struts. These models investigated the displacement in the first 0.91mm below the wound surface, specifically visualising approximately the top 9 layers of skeletal muscle cells (Alberts et al., 2002). The gauze and foam models were compared to investigate the impact of each wound filler on the distribution of strain and displacement on the muscle cells.

Limited research has been conducted on the dissipation of strains in chronic wounds undergoing negative pressure wound therapy. However the research that has been carried out primarily used a single layer model, often representing the impact of negative pressure wound therapy on the skin, this is not representative of real life, with skin not being present on the unhealed chronic wounds NPWT is applied to.

This chapter discusses each stage of the project and draws comparisons with the strains experienced and those in literature found to induce growth factor production and subsequent granulation tissue development and growth.

## 8.2 Macroscopic Impact of NPWT

In order to investigate the impact of NPWT on a macroscopic level, an *in silico* model was developed. This model was created with two wound shapes, a hemispherical wound and a

filleted cylindrical wound shape. The parameterised properties of these models were adjusted to study the impact of varying model dimensions, such as tissue depth, wound size, and applied pressure. Three paths were plotted on this model when solved, one through the central y-axis, one around the edge of the wound, and one through the surface x-axis. This allowed a comprehensive overview of the impact of the applied loading conditions on the wound and the surrounding tissue.

The macroscopic model consisted of three individual layers, each representing a layer of biological tissue, skin, subcutaneous adipose tissue, or skeletal muscle. This is unique to this project as previous investigations into the distribution of strain during negative pressure wound therapy have utilised single material models, using the material properties of a single elastomer rather than biological tissues to simulate the impact of negative pressure on the material.

This model had X and Z dimensions of 240mm x 240mm. This was determined through initial testing to be the most suitable dimensions, ensuring that the model was of appropriate size for efficient problem-solving, while also minimizing any potential impact on tissue strain. The model was initially tested with a hemispherical wound with a diameter of 60mm at a central point of 0,0,0.

The depth of each layer was based on values found in literature. As the thickness of biological tissues vary greatly between individuals and throughout areas of the body, assumptions were made to gain absolute values. Table 1 on page 46 contains the values of Young's modulus and thicknesses for biological tissues found during a review of literature. There was a distinct lack of literature surrounding tissue thickness, particularly using human data likely due to ethical challenges surrounding human research and difficulties in measuring tissue thickness *in vivo*.

The review of tissue properties found that skin typically has a thickness between 2.284mm and 6.0524mm (Oltulu et al., 2018). Wu et al. (2007) found the thickness of skin on a pig paw was  $2.5 \pm 0.6$  mm which corresponded to the results of *ex vivo* testing by Annaidh et al. (2012) that found the skin on a human back has a thickness of  $2.56 \pm 0.39$ mm. Therefore the skin was modelled with a thickness of 2.5mm.

The macroscopic model was initially developed with material properties that matched the silicone properties for the equivalent *in vitro* model. The purpose of this was to compare the response of the *in silico* model with the *in vitro* model under microCT for validation. However, due to the microscopic displacement experienced during NPWT and the inherent error in the detection of displacement due to the low contrast between materials in the microCT image. A

similar technique was utilised by Wilkes et al. (2009b) to validate their study on 3D strain measurement in soft tissue during NPWT. Wilkes et al. (2009a) also found poor definition between materials under  $\mu$ CT.

It was anticipated that the radio-opacity of silicone would be comparable to that of polyurethane foam. The insertion of metal into the model was expected to serve as a distinct marker for tracking displacement, something that had not been done by Wilkes et al. (2009a). However, the lack of displacement in the markers and the minimal displacement overall meant that, as with the model by Wilkes et al. (2009a), the displacement was unable to be validated using this method. Due to the coronavirus pandemic, this was unable to be investigated further due to the lack of access to laboratory and microCT facilities for an extended period.

To counteract this in future work, radiopaque nanoparticles could be mixed with the silicones being tested, to provide a clear image of the model under CT. This would be unlikely to impact the mechanical properties of the silicone being tested greatly and is likely to be acceptable for this role.

Of particular interest was the strain around the wound face. This allowed a visualisation of how the tensile strain was distributed at the tissue interfaces. The peak tensile strain was found to occur at the skin-fat interface with a value of approximately 10.5%. At the fat-muscle interface, the strain was observed to be approximately 5.5%.

When looking at the strains along a vertical path plotted through the model directly under the central point of the wound, a peak tensile strain of approximately 5.9% at approximately 5mm below the wound base. The compressive strain at the base of the wound was found to be approximately 6.05%.

This model is a simplified representation of a chronic wound and therefore there are multiple assumptions made in its development. The first is the model utilised isotropic material properties. It is known that this is not the case with many biological tissues: muscle in particular is known for being anisotropic. In addition, the model has a perfectly hemispherical wound. Whilst many ulcers have a hemispherical shape due to the pitting effect, the walls are unlikely to be clearly defined due to the nature of wound development. A further limitation was that the model did not take into account density and thus the weight of the biological materials. Therefore all materials were measured with the same density.

When fibroblasts are subjected to a mechanical strain from the extracellular matrix, the proteins required to build the extracellular matrix are formed (Hakkinen et al., 2011). When this

strain relaxes, the protein expression reduces, and proteolytic enzymes are expressed. The effects of different strain magnitudes of osteoblasts was studied by Tang et al. (2006). It was found that some of the key regulatory factors in cell regeneration increased with increasing strain, up to 102.77% increase of osteoprotegerin was found when cells were subjected to an 18% strain. This was also shown at lower strain levels as well. When cells are subjected to a 10% strain, it is documented in literature that growth factor expression occurs (Hicks et al., 2012). This growth factor expression has been shown to induce granulation tissue growth, a key part in the healing process of chronic wounds.

That this value has been reached at the skin-fat interface is highly suggestive of skin cells regenerating to begin the wound healing process. While this model has not been validated through physical modelling, the validity is supported by the fact that the strain experienced is within the same order of magnitude to that experienced by the models developed by Saxena et al. (2004) and Wilkes et al. (2009b).

Through this model, it has been discovered that, whilst the main area of influence of negative pressure wound therapy was surrounding the wound, the effect of the applied strain extends into the depth of tissue below. Therefore, it is likely that growth factor expression does not just occur in the immediate area, but also the surrounding tissue, providing a stimulus for wound healing on a larger scale.

With further work applying this to specific cell types, it may be possible in the future to use this knowledge to provide NPWT personalised to individuals and the type of wound they have. In addition, there is the potential for NPWT to be used to influence the healing of wounds that have not yet broken the surface of the skin.

### 8.3 Microscopic Impact of NPWT

Following the development of macroscopic model, a model demonstrating the impact of wound filler material on the strains induced by negative pressure wound therapy was created. This model allowed an investigation into polyurethane foam and cotton gauze through three-dimensional representations of individual threads and struts. The modelling was influenced by the modelling carried out by Saxena et al. (2004) which investigated the impact of micromechanical forces on wound healing using a two-dimensional finite element model and subsequent simulation of negative pressure wound therapy. This primitive model found that the deformations experienced were similar to the *in vitro* strain levels known to promote granulation tissue proliferation.

The novel three-dimensional aspect of the microscopic models created in this thesis allowed the impact of surrounding tissue and pressure applied over an area to be considered and took a significant step in understanding the strains experienced throughout the wound. Both microscopic models were created simulating the base of the wound found in the macroscopic model. Therefore the biological tissue modelled in this wound was muscle and the tissue had the same mechanical material properties as the muscle layer in the macroscopic model. Preliminary testing was carried out varying the depth of tissue to determine the most efficient depth for the model where the model did not take an extended period of time to solve, nor did the depth influence the results gained. This was determined to be 0.944mm, which is approximately the top 9 layers of muscle cells (Alberts et al., 2002).

### 8.3.1 Foam Model

The first model to be created represented a foam strut. A review of literature found that the Young's modulus of polyurethane foam was 91 kPa, and the Poisson's ratio was assumed to be 0.3 (Wondu et al., 2019). This foam comes in a variety of densities, measured in "pores per inch" or PPI. The most common porosities were modelled on a microscopic level in this thesis; the master model was created with the dimensions of 30PPI foam.

To understand the distribution of the strain experienced by the model, two paths were plotted. The first was horizontally along the x-axis, and the second was vertically, down the central y-axis. This was designed to give an overview of both the surface strain and the distribution of strain through the model. The foam struts were observed to induce a high level of strain directly underneath the corners, with the highest tensile strain being experienced by the model of 60PPI foam. This had a value of 35% strain, much greater than the strain shown to be experienced at a macroscopic level. This lack of detection is due to the scale of the microscopic model being much smaller and therefore the excess strain being undetected by the initial path as the points were not of a sufficient resolution to detect microscopic details.

The strut model assumed that all struts were cuboidal in nature, however this is known to not be the case. Electron microscopy has shown that struts are not regular in shape or size and do not form a perfect square (Milleret et al., 2009). Therefore this model is significantly simplified.

As mentioned when discussing the macroscopic model, the strain value shown in literature to have an influence on wound healing was 10%. All porosity of foam was shown to induce strain greater than 10% in the area directly underneath the strut. For all foam porosities other than the 10PPI foam, it was observed that the peak strain was approximately 32% and

occurred roughly 0.8mm below the wound base. For the 10PPI foam, the tensile strain achieved was significantly lower at approximately 19%.

The distribution of strain surrounding the struts demonstrated peak surface strain under the corners of the strut, and peak strain approximately 0.1mm below the wound surface. A similar pattern was demonstrated by Saxena et al. (2004) in their 2 dimensional representation of negative pressure wound therapy. Saxena et al. (2004) compared their model to wound biopsy specimens subjected to NPWT. These wound biopsy specimens were found to experience similar displacement to the model developed by Saxena et al. (2004) and therefore it is reasonable to assume similar strains. Of particular note was the displacement directly under the struts in the biopsy specimen was found to be similar to that of the two dimensional model developed by Saxena et al. (2004) and subsequently similar to that modelled by the foam strut model in this thesis. The implications of this is that the foam strut model in this thesis is validated through the direct comparison to the model and wound biopsies in Saxena et al. (2004)'s paper.

By understanding the influence of varying the porosity of foam on the strain distribution directly underneath the strut and on the surrounding tissue, there is scope for this to be taken into consideration when selecting foam to be used in clinical treatments in the future. This could provide better patient outcomes and less time under treatment for individuals.

### 8.3.2 Gauze Model

Despite polyurethane foam being the gold standard wound filler recommended by manufacturers of negative pressure wound therapy devices, gauze is also used as an alternative wound filler. This situation presents advantages and drawbacks. Gauze is a cost-effective and widely accessible wound filler compared to polyurethane foam; however, foam is believed to be more efficacious in promoting wound healing. To gain an understanding of the influence on wound filler on the strains induced by negative pressure wound therapy, a microscopic gauze model was developed in addition to the foam strut model discussed previously.

The structure of the gauze model was similar to that of the foam strut model, with a single thread of gauze directly interacting with a layer of muscle. This muscle had the same Young's modulus, 91 kPa, as the muscle layer of other models in this thesis. The gauze thread model was initially developed with a cuboidal thread which demonstrated a similar strain pattern to the foam strut model. However this is not a realistic representation of the shape of cotton thread, and a further model was developed with a cylindrical thread.

The model was loaded in a similar manner to the polyurethane strut model, with the negative pressure applied to the surface of the biological tissue, and strain calculated from the

macroscopic model applied to the sides of the model. In addition, displacement was applied to the top of the thread. The loading conditions for the square based thread model was similar to that of the cylindrical strain model and can be seen in Figure 79.

It was found that the peak strain could be found at approximately 0.09 mm below the thread. This strain was approximately 2.8%. When looking at the strain around the thread, two peaks of approximately 4.01% strain were observed where the thread started to interact with the wound surface. From here, the strain reduced to approximately 0.9% at the central point under the wound.

The thread was laid across the surface of the muscle in the z-direction and inset into the muscle layer by the depth of the radius to minimise contact errors when solving the model. A particular challenge arises during finite element analysis when considering the placement of threads, with an assumption that their placement had minimal impact on the distribution of induced strain. Further assumptions were made regarding the fibre organisation of the gauze. It was assumed that the gauze was made of perfectly cylindrical cotton fibres, which were spaced at regular intervals and placed flat on the wound. Whilst these were reasonable assumptions for a basic model to understand the influence of shape and strain application on the distribution of strain. Cotton gauzes are one of the most commonly available gauzes in clinical environments. It was also assumed that the gauze was not impregnated with antibiotics or silver, affecting the mechanical properties of the fibre.

There are currently no published studies investigating the influence of cotton gauze on wounds during negative pressure wound therapy on a microscopic level. Unlike the polyurethane foam strut model, the cylindrical cotton gauze model did not display strains of greater than 10% suggesting wound healing is unlikely to be as effectively induced by this wound filler material. The strain was observed in all areas surrounding the model with the lowest strain found directly underneath the central point of the interaction between the wound bed and the cotton gauze thread. The influence of this is not known as literature has not investigated the impact of induced strain lower than 10% on growth factor expression, however it is possible that some granulation tissue growth is still induced by this strain.

A study by Wilkes et al. (2009a) found that reticulated open-cell polyurethane foam produced higher levels of tissue microdeformation when subjected to subatmospheric pressure than a gauze dressing. This agrees with what was observed in the models outlined in this study, thus providing validation for this study.

These findings may offer a potential pathway for enhancing the effectiveness of negative pressure wound therapy treatments for patients. It provides a scientific rationale to support the recommendation of open-cell polyurethane foam as a wound filler for patients with difficult-to-heal wounds, encouraging clinical staff to consider this option in their treatment protocols more frequently. Additionally, in cases where a gentler approach is needed, gauze may be a suitable alternative. This research contributes valuable insights into the impact of wound filler materials on wound healing in the context of negative pressure wound therapy.

This study on the impact of wound filler material on induced strains offers valuable insight into the role of wound filler materials in enhancing the effectiveness of negative pressure wound therapy. Given the complexity of the human body, the models used in this study were intentionally simplified for clarity and focus. The research conducted in this thesis lays a solid foundation for future experimental in vitro and in vivo studies. The model developed in this thesis can be expanded upon for more detailed investigations into the biomechanical aspects of negative pressure wound therapy. This will facilitate continued progress and refinement of this treatment approach for patients with challenging wound healing needs.

## Chapter 9 Conclusions

This project has developed *in silico* and *in vitro* models for the testing of novel medical devices and for greater understanding of the strains induced during negative pressure wound therapy. Unlike previous *in silico* models for the investigation of NPWT found in literature, the models developed in this project took into consideration the material properties of the three layers of biological tissue generally impacted by wounds, skin, subcutaneous adipose tissue, and muscle. The strains experienced were investigated in three dimensions on a microscopic and macroscopic level, both on the wound bed, and throughout the tissue directly underneath.

The model was initially developed with material properties that corresponded to the silicones that had been selected through tensile testing in Chapter 3 as being mechanically similar to the biological materials that were being modelled. Biological tissues typically have a large range in stiffness due to the way they are highly influenced by external factors such as gender, race, age and health. The range of material properties for skin, subcutaneous adipose tissue, and muscle can be seen in Section 6.2. It was found that the strains induced in the model on both a microscopic and macroscopic level correspond with the strain levels known to induce protein and growth factor expression that regulate the wound healing process. In addition, it was found that when the pressure was varied, the strain experienced by the model increased and decreased linearly. Therefore, as literature has shown that greater strain levels can increase the quantity of hormones and proteins released, the wound healing process can potentially be upregulated and downregulated as appropriate by varying the pressure applied to the wound.

In addition to the development of *in silico* models, an *in vitro* model was developed with biomechanically similar silicones. The first stage in this development was the design and manufacture of the mould. The mould was designed to ensure the model was adaptable as possible. It was initially planned that there would be multiple iterations of the *in vitro* model, varying layer thickness and wound depth, however this was prevented when laboratory access was restricted due to the coronavirus lockdowns experienced in 2020. Therefore, *in silico* models were further developed prior to the investigation of the deformation of the *in vitro* model. Further development of this *in vitro* model would allow for greater flexibility when testing novel medical devices.

### 9.1 Future Work

This project has built the foundations for the future development of more complex models, taking into consideration the anisotropy of skin and muscle, and the gelatinous composition of subcutaneous adipose tissue. In addition, wounds are not typically dry in nature and generally experience exudate in response to inflammation and injury. Therefore, to make the physical

model more adaptable to different treatment types, a physical wound that could simulate exudate, and an *in silico* model that could investigate the fluid dynamics of exudate removal, could be beneficial. Further development of the *in vitro* model may include the addition of pressure tappings throughout to measure the pressure experienced through the wound when NPWT and other wound treatments with a mechanical influence are applied.

## Reference list

Abdullahi, A., Amini-Nik, S. & Jeschke, M.G. (2014) Animal Models in Burn Research. *Cellular and Molecular Life Sciences : CMLS*, 71(17), 3241–3255. Available online: <https://doi.org/10.1007/s00018-014-1612-5>.

Agache, P.G., Monneur, C., Leveque, J.L. & De Rigal, J. (1980) Mechanical properties and Young's modulus of human skin in vivo. *Archives of Dermatological Research*, 269(3), 221–232. Available online: <https://doi.org/10.1007/BF00406415>.

Alavi, A., Sibbald, R.G., Phillips, T.J., Miller, O.F., Margolis, D.J., Marston, W., Woo, K., Romanelli, M. & Kirsner, R.S. (2016) What's new: Management of venous leg ulcers: Approach to venous leg ulcers. *Journal of the American Academy of Dermatology*, 74(4), 627–640; quiz 641–642. Available online: <https://doi.org/10.1016/j.jaad.2014.10.048>.

Alberts, B., Johnson, A., Lewis, J., Raff, M., Roberts, K. & Walter, P. (2002) Genesis, Modulation, and Regeneration of Skeletal Muscle. In *Molecular Biology of the Cell. 4th Edition*. Garland Science. Available online: <https://www.ncbi.nlm.nih.gov/books/NBK26853/> [Accessed 25/07/2023].

Alkhouli, N., Mansfield, J., Green, E., Bell, J., Knight, B., Liversedge, N., Tham, J.C., Welbourn, R., Shore, A.C., Kos, K. & Winlove, C.P. (2013) The mechanical properties of human adipose tissues and their relationships to the structure and composition of the extracellular matrix. *American Journal of Physiology-Endocrinology and Metabolism*, 305(12), E1427–E1435. Available online: <https://doi.org/10.1152/ajpendo.00111.2013>.

Alpaslan, G., Nakajima, T. & Takano, Y. (1997) Extracellular alkaline phosphatase activity as a possible marker for wound healing: a preliminary report. *Journal of Oral and Maxillofacial Surgery: Official Journal of the American Association of Oral and Maxillofacial Surgeons*, 55(1), 56–62; discussion 62-63. Available online: [https://doi.org/10.1016/s0278-2391\(97\)90447-x](https://doi.org/10.1016/s0278-2391(97)90447-x).

Anderson, I. (2006) Wound Essentials 1: Aetiology, assessment & management of leg ulcers - Wounds UK. *Wound Essentials*, 1, 20–37.

Anesäter, E., Borgquist, O., Hedström, E., Waga, J., Ingemansson, R. & Malmsjö, M. (2011) The influence of different sizes and types of wound fillers on wound contraction and tissue pressure during negative pressure wound therapy. *International Wound Journal*, 8(4), 336–342. Available online: <https://doi.org/10.1111/j.1742-481X.2011.00790.x>.

- Annaidh, A.N., Bruyere, K., Destrade, M., Gilchrist, M.D. & Ottenio, M. (2012) Characterising the Anisotropic Mechanical Properties of Excised Human Skin. *Journal of the Mechanical Behavior of Biomedical Materials*, 5(1), 139–148. Available online: <https://doi.org/10.1016/j.jmbbm.2011.08.016>.
- Ansell, D.M., Holden, K.A. & Hardman, M.J. (2012) Animal models of wound repair: Are they cutting it?. *Experimental Dermatology*, 21(8), 581–585. Available online: <https://doi.org/10.1111/j.1600-0625.2012.01540.x>.
- Avram, A.S., Avram, M.M. & James, W.D. (2005) Subcutaneous fat in normal and diseased states: 2. Anatomy and physiology of white and brown adipose tissue. *Journal of the American Academy of Dermatology*, 53(4), 671–683. Available online: <https://doi.org/10.1016/j.jaad.2005.05.015>.
- Basford, J.R., Jenkyn, T.R., An, K.-N., Ehman, R.L., Heers, G. & Kaufman, K.R. (2002) Evaluation of healthy and diseased muscle with magnetic resonance elastography. *Archives of Physical Medicine and Rehabilitation*, 83(11), 1530–1536. Available online: <https://doi.org/10.1053/apmr.2002.35472>.
- Benítez, J.M. & Montáns, F.J. (2017) The mechanical behavior of skin: Structures and models for the finite element analysis. *Computers & Structures*, 190, 75–107. Available online: <https://doi.org/10.1016/j.compstruc.2017.05.003>.
- Böl, M., Kruse, R., Ehret, A.E., Leichsenring, K. & Siebert, T. (2012) Compressive properties of passive skeletal muscle—The impact of precise sample geometry on parameter identification in inverse finite element analysis. *Journal of Biomechanics*, 45(15), 2673–2679. Available online: <https://doi.org/10.1016/j.jbiomech.2012.08.023>.
- Buganza Tepole, A., Gosain, A.K. & Kuhl, E. (2012) Stretching skin: The physiological limit and beyond. *International Journal of Non-Linear Mechanics*, 47(8), 938–949. Available online: <https://doi.org/10.1016/j.ijnonlinmec.2011.07.006>.
- Calvo, B., Ramírez, A., Alonso, A., Grasa, J., Soteras, F., Osta, R. & Muñoz, M.J. (2010) Passive nonlinear elastic behaviour of skeletal muscle: Experimental results and model formulation. *Journal of Biomechanics*, 43(2), 318–325. Available online: <https://doi.org/10.1016/j.jbiomech.2009.08.032>.
- Calvo-Gallego, J.L., Domínguez, J., Gómez Cía, T., Gómez Ciriza, G. & Martínez-Reina, J. (2018) Comparison of different constitutive models to characterize the viscoelastic properties of human

abdominal adipose tissue. A pilot study. *Journal of the Mechanical Behavior of Biomedical Materials*, 80, 293–302. Available online: <https://doi.org/10.1016/j.jmbbm.2018.02.013>.

Cambridge Dictionary (2023) *Gauze*. Available online: <https://dictionary.cambridge.org/dictionary/english/gauze> [Accessed 25/07/2023].

Comley, K. & Fleck, N.A. (2010) A micromechanical model for the Young's modulus of adipose tissue. *International Journal of Solids and Structures*, 47(21), 2982–2990. Available online: <https://doi.org/10.1016/j.ijsolstr.2010.07.001>.

Corr, D.T. & Hart, D.A. (2013) Biomechanics of Scar Tissue and Uninjured Skin. *Advances in Wound Care*, 2(2), 37–43. Available online: <https://doi.org/10.1089/wound.2011.0321>.

Cukjati, D., Reberšek, S., Karba, R. & Miklavčič, D. (2000) Modelling of chronic wound healing dynamics. *Medical & Biological Engineering & Computing*, 38(3), 339–347. Available online: <https://doi.org/10.1007/BF02347056>.

Dąbrowska, A., Rotaru, G.M., Spano, F., Affolter, Ch., Fortunato, G., Lehmann, S., Derler, S., Spencer, N.D. & Rossi, R.M. (2017) A water-responsive, gelatine-based human skin model. *Tribology International*, 113, 316–322. Available online: <https://doi.org/10.1016/j.triboint.2017.01.027>.

Dąbrowska, A.K., Rotaru, G.-M., Derler, S., Spano, F., Camenzind, M., Annaheim, S., Stämpfli, R., Schmid, M. & Rossi, R.M. (2016) Materials used to simulate physical properties of human skin. *Skin Research and Technology*, 22(1), 3–14. Available online: <https://doi.org/10.1111/srt.12235>.

Diabetes UK (2019) *Number of people with diabetes reaches 4.7 million Diabetes UK*. Available online: [https://www.diabetes.org.uk/about\\_us/news/new-stats-people-living-with-diabetes](https://www.diabetes.org.uk/about_us/news/new-stats-people-living-with-diabetes) [Accessed 25/07/2023].

Diridollou, S., Patat, F., Gens, F., Vaillant, L., Black, D., Lagarde, J.M., Gall, Y. & Berson, M. (2000) In vivo model of the mechanical properties of the human skin under suction. *Skin Research and Technology*, 6(4), 214–221. Available online: <https://doi.org/10.1034/j.1600-0846.2000.006004214.x>.

Edwards, C. & Marks, R. (1995) Evaluation of biomechanical properties of human skin. *Clinics in Dermatology*, 13(4), 375–380. Available online: [https://doi.org/10.1016/0738-081X\(95\)00078-T](https://doi.org/10.1016/0738-081X(95)00078-T).

Endicott, M. (2019) *Arterial vs venous ulcers: What's the difference?* Medline. Available online: <https://www.medline.com/strategies/skin-health/distinguish-venous-ulcer-arterial-wound/> [Accessed 25/07/2023].

Etufugh, C.N. & Phillips, T.J. (2007) Venous ulcers. *Clinics in Dermatology*, 25(1), 121–130. Available online: <https://doi.org/10.1016/j.clindermatol.2006.09.004>.

Fang, R.C. & Mustoe, T.A. (2008) Animal models of wound healing: utility in transgenic mice. *Journal of Biomaterials Science, Polymer Edition*, 19(8), 989–1005. Available online: <https://doi.org/10.1163/156856208784909327>.

Fenwick, N., Griffin, G. & Gauthier, C. (2009) Animal Welfare Bien-être des animaux. *ANIMAL WELFARE*, 50, 8.

Fraccalvieri, M., Zingarelli, E., Ruka, E., Antoniotti, U., Coda, R., Sarno, A., Bocchiotti, M.A. & Bruschi, S. (2011) Negative pressure wound therapy using gauze and foam: histological, immunohistochemical and ultrasonography morphological analysis of the granulation tissue and scar tissue. Preliminary report of a clinical study. *International Wound Journal*, 8(4), 355–364. Available online: <https://doi.org/10.1111/j.1742-481X.2011.00798.x>.

Frykberg, R.G. & Banks, J. (2015) Challenges in the Treatment of Chronic Wounds. *Advances in Wound Care*, 4(9), 560–582. Available online: <https://doi.org/10.1089/wound.2015.0635>.

Gallagher, A.J., Ní Annaidh, A., Bruyère, K. & Al, E. (2012) Dynamic Tensile Properties of Human Skin. *2012 IRCOBI Conference Proceedings* [Preprint]. Available online: <http://hdl.handle.net/10197/4772> [Accessed 25/07/2023].

van Gent, W., Wilschut, E. & Wittens, C. (2010) Management of venous ulcer disease. *BMJ (Clinical Research Ed.)*, 341, c6045. Available online: <https://doi.org/10.1136/bmj.c6045>.

Geris, L., Schugart, R. & Van Oosterwyck, H. (2010) *In silico* design of treatment strategies in wound healing and bone fracture healing. *Philosophical Transactions of the Royal Society A: Mathematical, Physical and Engineering Sciences*, 368(1920), 2683–2706. Available online: <https://doi.org/10.1098/rsta.2010.0056>.

Geris, L., Vander Sloten, J. & Van Oosterwyck, H. (2009) *In silico* biology of bone modelling and remodelling: regeneration. *Philosophical Transactions of the Royal Society A: Mathematical, Physical and Engineering Sciences*, 367(1895), 2031–2053. Available online: <https://doi.org/10.1098/rsta.2008.0293>.

- Glozman, T. & Azhari, H. (2010) A Method for Characterization of Tissue Elastic Properties Combining Ultrasonic Computed Tomography With Elastography. *Journal of Ultrasound in Medicine*, 29(3), 387–398. Available online: <https://doi.org/10.7863/jum.2010.29.3.387>.
- Gould, J. (2018) Superpowered Skin. *Nature*, 536, S84–S85.
- Grey, J.E., Harding, K.G. & Enoch, S. (2006) Venous and arterial leg ulcers. *BMJ : British Medical Journal*, 332(7537), 347–350.
- Griffin, M., Premakumar, Y., Seifalian, A., Butler, P.E. & Szarko, M. (2016) Biomechanical Characterization of Human Soft Tissues Using Indentation and Tensile Testing. *Journal of Visualized Experiments*, (118), 54872. Available online: <https://doi.org/10.3791/54872>.
- Guest, J.F., Vowden, K. & Vowden, P. (2017) The health economic burden that acute and chronic wounds impose on an average clinical commissioning group/health board in the UK. *Journal of Wound Care*, 26(6), 292–303. Available online: <https://doi.org/10.12968/jowc.2017.26.6.292>.
- Guo, S. & DiPietro, L.A. (2010) Factors Affecting Wound Healing. *Journal of Dental Research*, 89(3), 219–229. Available online: <https://doi.org/10.1177/0022034509359125>.
- Hakkinen, K.M., Harunaga, J.S., Doyle, A.D. & Yamada, K.M. (2011) Direct comparisons of the morphology, migration, cell adhesions, and actin cytoskeleton of fibroblasts in four different three-dimensional extracellular matrices. *Tissue Engineering. Part A*, 17(5–6), 713–724. Available online: <https://doi.org/10.1089/ten.TEA.2010.0273>.
- Hasan, M.Y., Teo, R. & Nather, A. (2015) Negative-pressure wound therapy for management of diabetic foot wounds: a review of the mechanism of action, clinical applications, and recent developments. *Diabetic Foot & Ankle*, 6(1), 27618. Available online: <https://doi.org/10.3402/dfa.v6.27618>.
- Held, M., Rothenberger, J., Tolzmann, D., Petersen, W., Schaller, H.-E. & Rahmanian-Schwarz, A. (2015) Alteration of Biomechanical Properties of Skin During the Course of Healing of Partial-thickness Wounds. *Wounds: A Compendium of Clinical Research and Practice*, 27(5), 123–128.
- Hendriks, F.M., Brokken, D., van Eemeren, J.T.W.M., Oomens, C.W.J., Baaijens, F.P.T. & Horsten, J.B.A.M. (2003) A numerical-experimental method to characterize the non-linear mechanical behaviour of human skin. *Skin Research and Technology*, 9(3), 274–283. Available online: <https://doi.org/10.1034/j.1600-0846.2003.00019.x>.

- Hicks, M.R., Cao, T.V., Campbell, D.H. & Standley, P.R. (2012) Mechanical strain applied to human fibroblasts differentially regulates skeletal myoblast differentiation. *Journal of Applied Physiology*, 113(3), 465–472. Available online: <https://doi.org/10.1152/jappphysiol.01545.2011>.
- Hill, A.V. (1938) The heat of shortening and the dynamic constants of muscle. *Proceedings of Royal Society of London.*, 126(843). Available online: <https://doi.org/10.1098/rspb.1938.0050>.
- Hinds, S., Bian, W., Dennis, R.G. & Bursac, N. (2011) The role of extracellular matrix composition in structure and function of bioengineered skeletal muscle. *Biomaterials*, 32(14), 3575–3583. Available online: <https://doi.org/10.1016/j.biomaterials.2011.01.062>.
- Huang, C., Leavitt, T., Bayer, L.R. & Orgill, D.P. (2014) Effect of negative pressure wound therapy on wound healing. *Current Problems in Surgery*, 51(7), 301–331. Available online: <https://doi.org/10.1067/j.cpsurg.2014.04.001>.
- Ishida, Y., Kanehisa, H., Carroll, J.F., Pollock, M.L., Graves, J.E. & Ganzarella, L. (1997) Distribution of subcutaneous fat and muscle thicknesses in young and middle-aged women., 9.
- Jachowicz, J., McMullen, R. & Prettypaul, D. (2007) Indentometric analysis of in vivo skin and comparison with artificial skin models. *Skin Research and Technology*, 13(3), 299–309. Available online: <https://doi.org/10.1111/j.1600-0846.2007.00229.x>.
- Jones, V.J. (2006) The use of gauze: will it ever change?. *International Wound Journal*, 3(2), 79–88. Available online: <https://doi.org/10.1111/j.1742-4801.2006.00215.x>.
- Khatyr, F., Imberdis, C., Vescovo, P., Varchon, D. & Lagarde, J.-M. (2004) Model of the viscoelastic behaviour of skin in vivo and study of anisotropy. *Skin Research and Technology*, 10(2), 96–103. Available online: <https://doi.org/10.1111/j.1600-0846.2004.00057.x>.
- Lacourpaille, L., Hug, F., Bouillard, K., Hogrel, J.-Y. & Nordez, A. (2012) Supersonic shear imaging provides a reliable measurement of resting muscle shear elastic modulus. *Physiological Measurement*, 33(3), N19–N28. Available online: <https://doi.org/10.1088/0967-3334/33/3/N19>.
- Lalezari, S., Lee, C.J., Borovikova, A.A., Banyard, D.A., Paydar, K.Z., Wirth, G.A. & Widgerow, A.D. (2017) Deconstructing negative pressure wound therapy: Deconstructing NPWT. *International Wound Journal*, 14(4), 649–657. Available online: <https://doi.org/10.1111/iwj.12658>.
- Lapeer, R.J., Gasson, P.D. & Karri, V. (2010) Simulating plastic surgery: From human skin tensile tests, through hyperelastic finite element models to real-time haptics. *Progress in Biophysics*

and *Molecular Biology*, 103(2–3), 208–216. Available online: <https://doi.org/10.1016/j.pbiomolbio.2010.09.013>.

Larrabee, W.F. (1986) A finite element model of skin deformation. I. Biomechanics of skin and soft tissue: A review. *The Laryngoscope*, 96(4), 399–405. Available online: <https://doi.org/10.1288/00005537-198604000-00012>.

Leveque, J.L., de Rigal, J., Agache, P.G. & Monneur, C. (1980) Influence of ageing on the in vivo extensibility of human skin at a low stress. *Archives of Dermatological Research*, 269(2), 127–135. Available online: <https://doi.org/10.1007/BF00406532>.

Lindblad, W.J. (2008) Considerations for selecting the correct animal model for dermal wound-healing studies. *Journal of Biomaterials Science, Polymer Edition*, 19(8), 1087–1096. Available online: <https://doi.org/10.1163/156856208784909390>.

Linder-Ganz, E., Shabshin, N., Itzchak, Y. & Gefen, A. (2007) Assessment of mechanical conditions in sub-dermal tissues during sitting: a combined experimental-MRI and finite element approach. *Journal of Biomechanics*, 40(7), 1443–1454. Available online: <https://doi.org/10.1016/j.jbiomech.2006.06.020>.

Machado, M.J.C., Watson, M.G., Devlin, A.H., Chaplain, M.A.J., McDougall, S.R. & Mitchell, C.A. (2011) Dynamics of Angiogenesis During Wound Healing: A Coupled In Vivo and In Silico Study: Dynamics of Angiogenesis During Wound Healing. *Microcirculation*, 18(3), 183–197. Available online: <https://doi.org/10.1111/j.1549-8719.2010.00076.x>.

Marieb, E. & Keller, S. (2021) *Essentials of Human Anatomy & Physiology, Global Edition*. 13th Edition. Pearson. Available online: <https://www.pearson.com/en-gb/subject-catalog/p/essentials-of-human-anatomy--physiology-global-edition/P200000006208?view=educator> [Accessed 25/07/2023].

Marola, S., Ferrarese, A., Solej, M., Enrico, S., Nano, M. & Martino, V. (2016) Management of venous ulcers: State of the art. *International Journal of Surgery*, 33, S132–S134. Available online: <https://doi.org/10.1016/j.ijssu.2016.06.015>.

Martin, P. (1997) Wound Healing--Aiming for Perfect Skin Regeneration. *Science*, 276(5309), 75–81. Available online: <https://doi.org/10.1126/science.276.5309.75>.

Milleret, V., Bittermann, A.G., Mayer, D. & Hall, H. (2009) Analysis of Effective Interconnectivity of DegraPol-foams Designed for Negative Pressure Wound Therapy. *Materials*, 2(1), 292–306. Available online: <https://doi.org/10.3390/ma2010292>.

Morrow, D.A., Haut Donahue, T.L., Odegard, G.M. & Kaufman, K.R. (2010) Transversely isotropic tensile material properties of skeletal muscle tissue. *Journal of the Mechanical Behavior of Biomedical Materials*, 3(1), 124–129. Available online: <https://doi.org/10.1016/j.jmbbm.2009.03.004>.

Mouro, C., Dunne, C. & Gouveia, I. (2021) Designing New Antibacterial Wound Dressings: Development of a Dual Layer Cotton Material Coated with Poly(Vinyl Alcohol)\_Chitosan Nanofibers Incorporating Agrimonia eupatoria L. Extract. *Molecules*, 26(83).

Nachman, M. & Franklin, S.E. (2016) Artificial Skin Model simulating dry and moist in vivo human skin friction and deformation behaviour. *Tribology International*, 97, 431–439. Available online: <https://doi.org/10.1016/j.triboint.2016.01.043>.

Nelson, E.A. & Adderley, U. (2016) Venous leg ulcers., 36.

NHS Confederation (2021) *What were clinical commissioning groups? | NHS Confederation*. Available online: <https://www.nhsconfed.org/articles/what-are-clinical-commissioning-groups> [Accessed 25/07/2023].

Nie, B. & Yue, B. (2016) Biological effects and clinical application of negative pressure wound therapy: a review. *Journal of Wound Care*, 25(11), 617–626. Available online: <https://doi.org/10.12968/jowc.2016.25.11.617>.

Nussbaum, S.R., Carter, M.J., Fife, C.E., DaVanzo, J., Haught, R., Nusgart, M. & Cartwright, D. (2018) An Economic Evaluation of the Impact, Cost, and Medicare Policy Implications of Chronic Nonhealing Wounds. *Value in Health*, 21(1), 27–32. Available online: <https://doi.org/10.1016/j.jval.2017.07.007>.

Oltulu, P., Ince, B., Kokbudak, N., Findik, S. & Kilinc, F. (2018) Measurement of epidermis, dermis, and total skin thicknesses from six different body regions with a new ethical histometric technique. *Turkish Journal of Plastic Surgery*, 26(2), 56. Available online: [https://doi.org/10.4103/tjps.TJPS\\_2\\_17](https://doi.org/10.4103/tjps.TJPS_2_17).

Ottenio, M., Tran, D., Ní Annaidh, A., Gilchrist, M.D. & Bruyère, K. (2015) Strain rate and anisotropy effects on the tensile failure characteristics of human skin. *Journal of the Mechanical Behavior of Biomedical Materials*, 41, 241–250. Available online: <https://doi.org/10.1016/j.jmbbm.2014.10.006>.

Pereira, C.T. & Herndon, D.N. (2005) The Pharmacologic Modulation of the Hypermetabolic Response to Burns. *Advances in Surgery*, 39, 245–261. Available online: <https://doi.org/10.1016/j.yasu.2005.05.005>.

Perez, R. & Davis, S.C. (2008) Relevance of animal models for wound healing. *Wounds*, 20(1), 3–8.

Phillips, C.J., Humphreys, I., Thayer, D., Elmessary, M., Collins, H., Roberts, C., Naik, G. & Harding, K. (2020) Cost of managing patients with venous leg ulcers. *International Wound Journal*, 17(4), 1074–1082. Available online: <https://doi.org/10.1111/iwj.13366>.

Russell, W.M.S. & Burch, R.L. (1960) The Principles of Humane Experimental Technique. *Medical Journal of Australia*, 1(13), 500–500. Available online: <https://doi.org/10.5694/j.1326-5377.1960.tb73127.x>.

Saxena, V., Hwang, C.-W., Huang, S., Eichbaum, Q., Ingber, D. & Orgill, D.P. (2004) Vacuum-Assisted Closure: Microdeformations of Wounds and Cell Proliferation. *Plastic and Reconstructive Surgery*, 1086–1096. Available online: <https://doi.org/10.1097/01.PRS.0000135330.51408.97>.

Seaton, M., Hocking, A. & Gibran, N.S. (2015) Porcine Models of Cutaneous Wound Healing. *ILAR Journal*, 56(1), 127–138. Available online: <https://doi.org/10.1093/ilar/ilv016>.

Shinohara, M., Sabra, K., Gennisson, J.-L., Fink, M. & Tanter, M. (2010) Real-time visualization of muscle stiffness distribution with ultrasound shear wave imaging during muscle contraction. *Muscle & Nerve*, 42(3), 438–441. Available online: <https://doi.org/10.1002/mus.21723>.

Takaza, M., Moerman, K.M., Gindre, J., Lyons, G. & Simms, C.K. (2013) The anisotropic mechanical behaviour of passive skeletal muscle tissue subjected to large tensile strain. *Journal of the Mechanical Behavior of Biomedical Materials*, 17, 209–220. Available online: <https://doi.org/10.1016/j.jmbbm.2012.09.001>.

Takei, T., Rivas-Gotz, C., Delling, C.A., Koo, J.T., Mills, I., McCarthy, T.L., Centrella, M. & Sumpio, B.E. (1997) Effect of strain on human keratinocytes in vitro. *Journal of Cellular Physiology*, 173(1), 64–72. Available online: [https://doi.org/10.1002/\(SICI\)1097-4652\(199710\)173:1<64::AID-JCP8>3.0.CO;2-H](https://doi.org/10.1002/(SICI)1097-4652(199710)173:1<64::AID-JCP8>3.0.CO;2-H).

Tang, L., Lin, Z. & Li, Y. (2006) Effects of different magnitudes of mechanical strain on Osteoblasts in vitro. *Biochemical and Biophysical Research Communications*, 344(1), 122–128. Available online: <https://doi.org/10.1016/j.bbrc.2006.03.123>.

Thompson, G. (2008) An overview of negative pressure wound therapy (NPWT). *British Journal of Community Nursing*, 13(Sup3), S23–S30. Available online: <https://doi.org/10.12968/bjcn.2008.13.Sup3.29469>.

Trøstrup, H., Thomsen, K., Calum, H., Hoiby, N. & Moser, C. (2016) Animal models of chronic wound care: the application of biofilms in clinical research. *Chronic Wound Care Management and Research*, Volume 3, 123–132. Available online: <https://doi.org/10.2147/CWCMR.S84361>.

Ud-Din, S. & Bayat, A. (2017) Non-animal models of wound healing in cutaneous repair: In silico, in vitro, ex vivo, and in vivo models of wounds and scars in human skin: Models of wound repair in human skin. *Wound Repair and Regeneration*, 25(2), 164–176. Available online: <https://doi.org/10.1111/wrr.12513>.

Van Ee, C.A., Chasse, A.L. & Myers, B.S. (2000) Quantifying Skeletal Muscle Properties in Cadaveric Test Specimens: Effects of Mechanical Loading, Postmortem Time, and Freezer Storage. *Journal of Biomechanical Engineering*, 122(1), 9–14. Available online: <https://doi.org/10.1115/1.429621>.

Vermolen, F.J. & Adam, J.A. (2007) A Finite Element Model for Epidermal Wound Healing. In Shi, Y., van Albada, G.D., Dongarra, J., & Sloot, P.M.A. (eds) *Computational Science – ICCS 2007*. Berlin, Heidelberg: Springer Berlin Heidelberg, 70–77. Available online: [https://doi.org/10.1007/978-3-540-72584-8\\_10](https://doi.org/10.1007/978-3-540-72584-8_10).

Vermolen, F.J. & Javierre, E. (2010) Computer simulations from a finite-element model for wound contraction and closure. *Journal of Tissue Viability*, 19(2), 43–53. Available online: <https://doi.org/10.1016/j.jtv.2009.11.003>.

Vignos, P.J. & Lefkowitz, M. (1959) A biochemical study of certain skeletal muscle constituents in human progressive muscular dystrophy. *The Journal of Clinical Investigation*, 38(6), 873–881. Available online: <https://doi.org/10.1172/JCI103869>.

Wang, S. & Larin, K.V. (2015) Optical coherence elastography for tissue characterization: a review. *Journal of Biophotonics*, 8(4), 279–302. Available online: <https://doi.org/10.1002/jbio.201400108>.

Webb, L.X. & Pape, H.-C. (2008) Current Thought Regarding the Mechanism of Action of Negative Pressure Wound Therapy With Reticulated Open Cell Foam. *Journal of Orthopaedic Trauma*, 22, S135–S137. Available online: <https://doi.org/10.1097/BOT.0b013e31818956ce>.

Wheatley, B.B., Morrow, D.A., Odegard, G.M., Kaufman, K.R. & Haut Donahue, T.L. (2016) Skeletal muscle tensile strain dependence: Hyperviscoelastic nonlinearity. *Journal of the Mechanical Behavior of Biomedical Materials*, 53, 445–454. Available online: <https://doi.org/10.1016/j.jmbbm.2015.08.041>.

Wilhelmi, B.J., Blackwell, S.J. & Phillips, L.G. (1999) Langer's Lines: To Use or Not to Use. *Plastic and Reconstructive Surgery*, 104(1), 208.

Wilkes, R., Zhao, Y., Cunningham, K., Kieswetter, K. & Haridas, B. (2009a) 3D strain measurement in soft tissue: Demonstration of a novel inverse finite element model algorithm on MicroCT images of a tissue phantom exposed to negative pressure wound therapy. *Journal of the Mechanical Behavior of Biomedical Materials*, 2(3), 272–287. Available online: <https://doi.org/10.1016/j.jmbbm.2008.10.006>.

Wilkes, R., Zhao, Y., Kieswetter, K. & Haridas, B. (2009b) Effects of Dressing Type on 3D Tissue Microdeformations During Negative Pressure Wound Therapy: A Computational Study. *Journal of Biomechanical Engineering*, 131(3), 031012. Available online: <https://doi.org/10.1115/1.2947358>.

Wondu, E., Lule, Z. & Kim, J. (2019) Thermal Conductivity and Mechanical Properties of Thermoplastic Polyurethane-/Silane-Modified Al<sub>2</sub>O<sub>3</sub> Composite Fabricated via Melt Compounding. *Polymers*, 11(7), 1103–1115.

Wu, J.Z., Cutlip, R.G., Andrew, M.E. & Dong, R.G. (2007) Simultaneous determination of the nonlinear-elastic properties of skin and subcutaneous tissue in unconfined compression tests. *Skin Research and Technology*, 13(1), 34–42. Available online: <https://doi.org/10.1111/j.1600-0846.2007.00182.x>.

Yang, L., Witten, T.M. & Pidaparti, R.M. (2013) A biomechanical model of wound contraction and scar formation. *Journal of Theoretical Biology*, 332, 228–248. Available online: <https://doi.org/10.1016/j.jtbi.2013.03.013>.

Zahouani, H., Pailler-Mattei, C., Sohm, B., Vargiolu, R., Cenizo, V. & Debret, R. (2009) Characterization of the mechanical properties of a dermal equivalent compared with human skin *in vivo* by indentation and static friction tests. *Skin Research and Technology*, 15(1), 68–76. Available online: <https://doi.org/10.1111/j.1600-0846.2008.00329.x>.

Zhang, Y.-G., Yang, Z., Zhang, H., Wang, C., Liu, M., Guo, X. & Xu, P. (2010) Effect of negative pressure on human bone marrow mesenchymal stem cells in vitro. *Connective Tissue Research*, 51(1), 14–21. Available online: <https://doi.org/10.3109/03008200902855891>.

Zhu, J., Yu, A., Qi, B., Li, Z. & Hu, X. (2014) Effects of Negative Pressure Wound Therapy on Mesenchymal Stem Cells Proliferation and Osteogenic Differentiation in a Fibrin Matrix. *PLoS ONE*, 9(9), e107339. Available online: <https://doi.org/10.1371/journal.pone.0107339>.

## Appendix 1 – Engineering Drawing of ASTM D412 Moulds

Insert your appendixes here. Additional chapters can be added using the *Heading back matter* style. You can also delete out these placeholder chapters if there are too many.

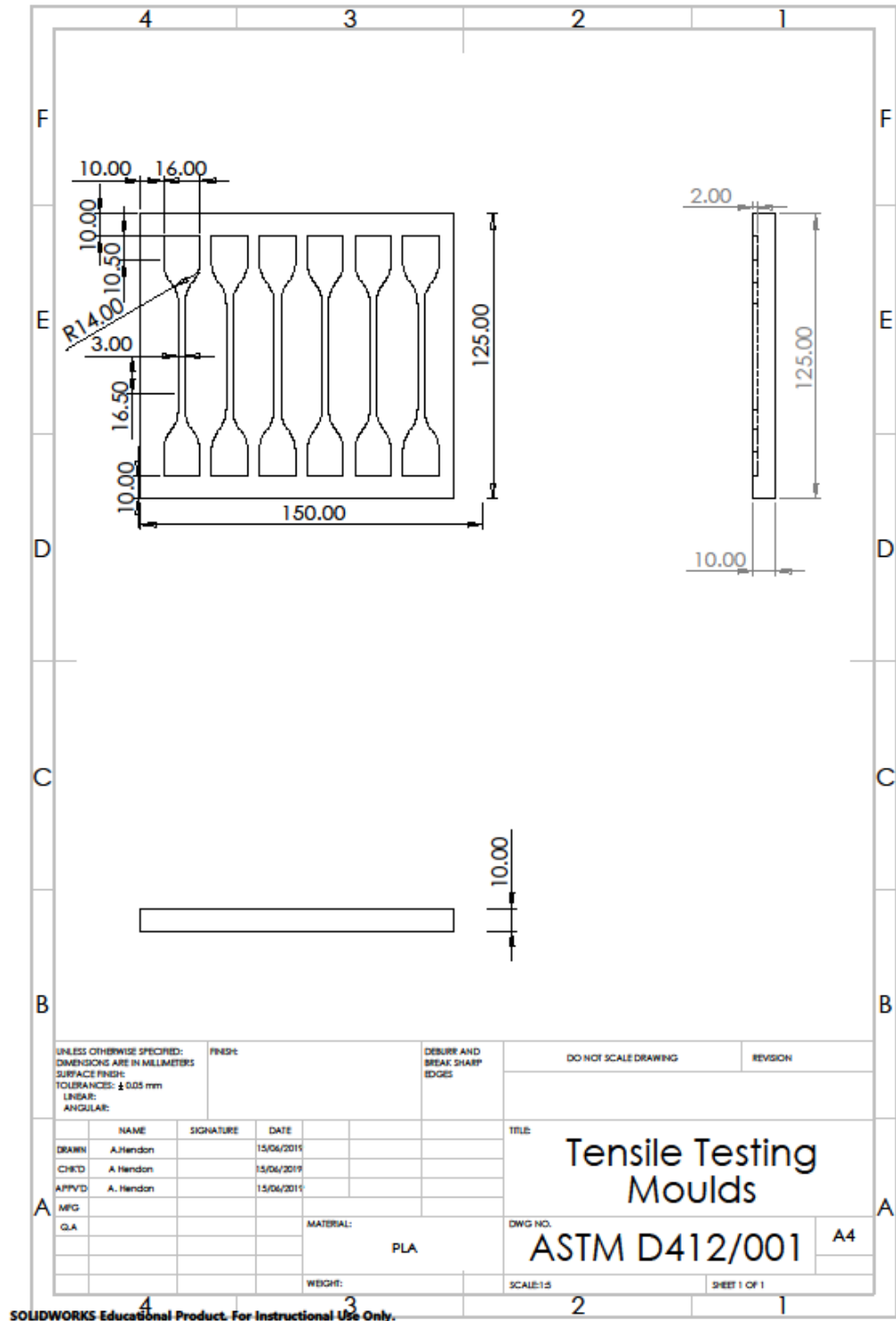


Figure 105 Engineering drawing of ASTM D412 compliant "dog-bone" moulds used in the tensile testing of silicones.

## Appendix 2 – Engineering Drawings of *In Vitro* Model Mould

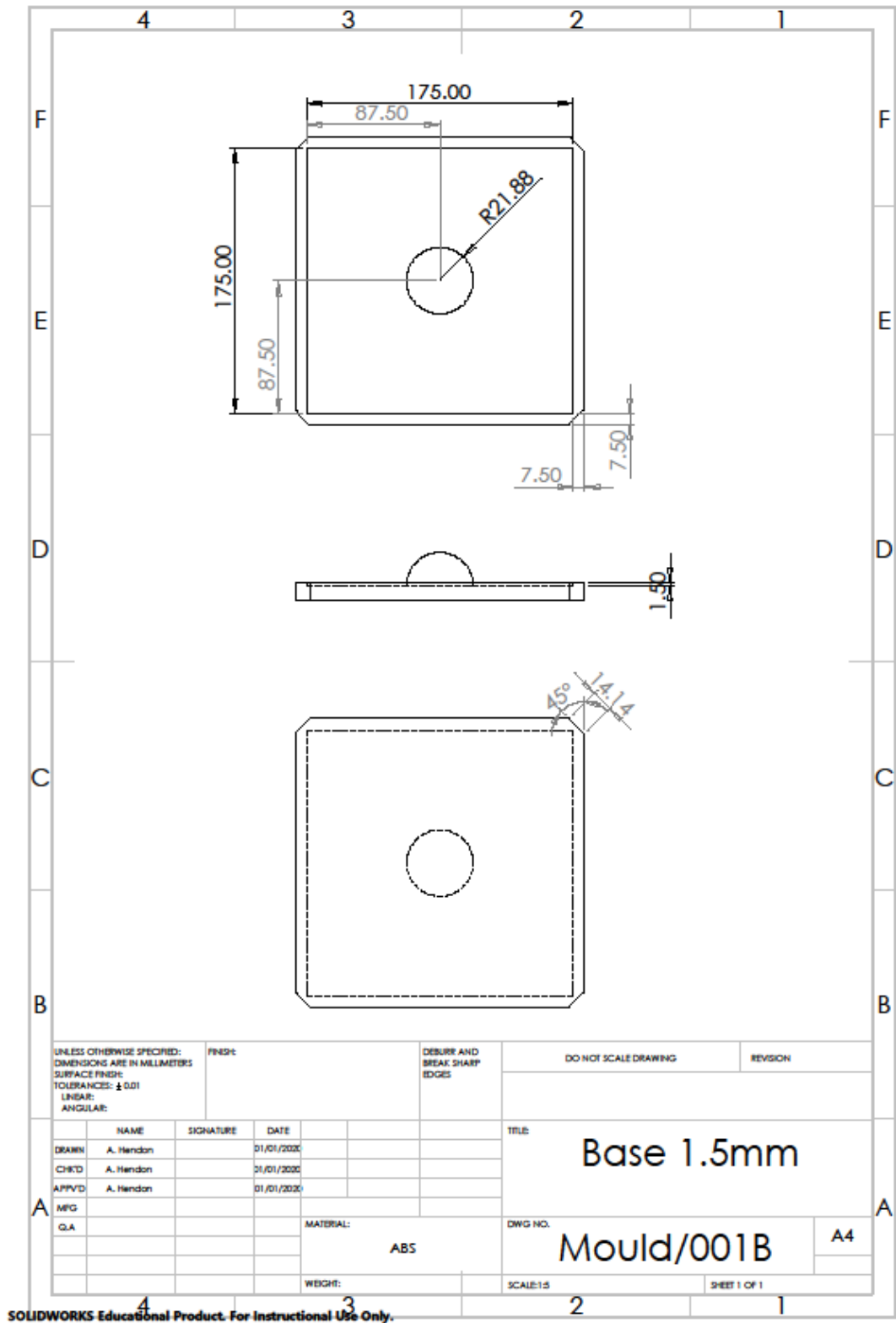


Figure 106 Engineering drawing of the base of the *in vitro* model mould.

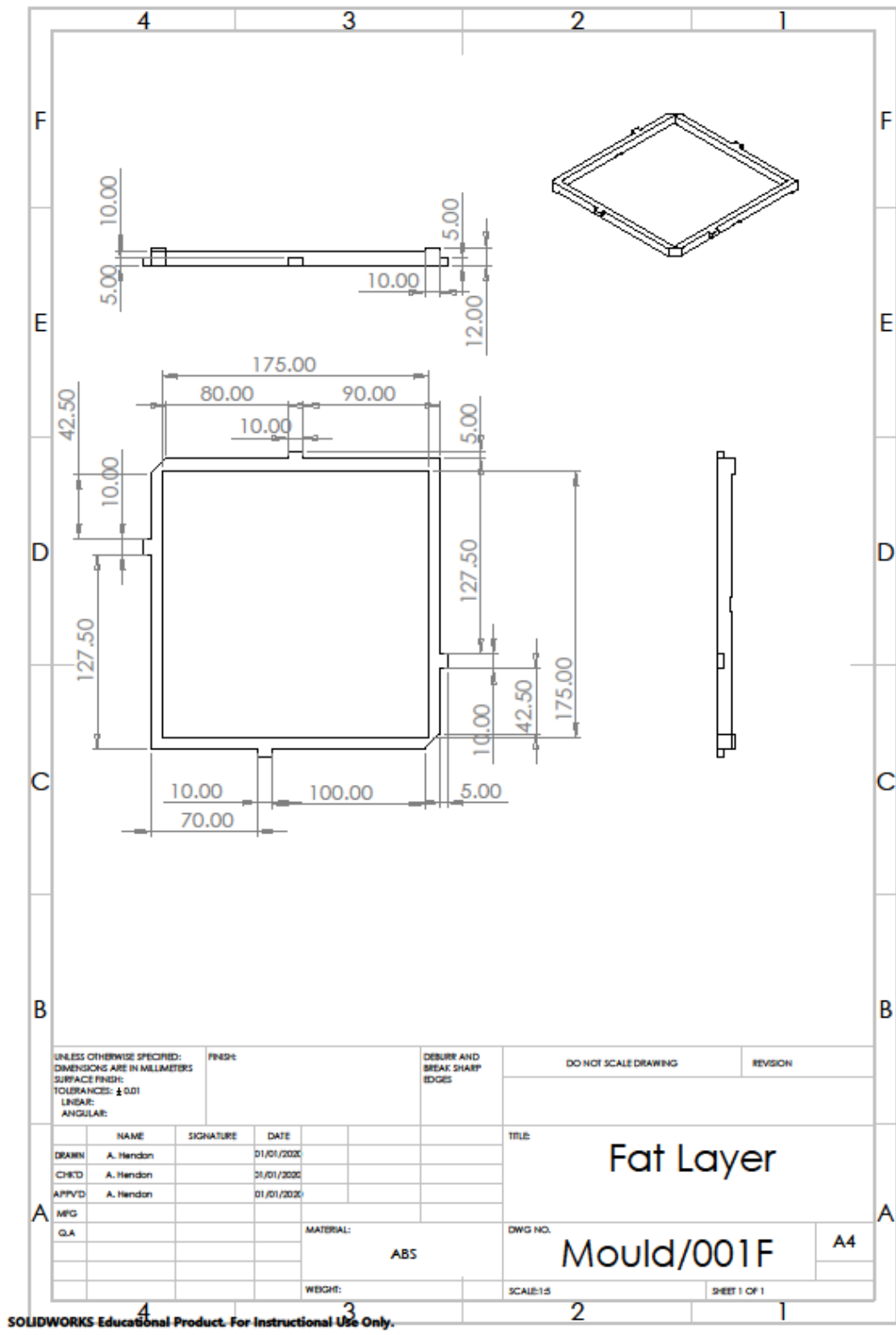


Figure 107 Engineering drawing of the muscle layer of the in vitro model mould.

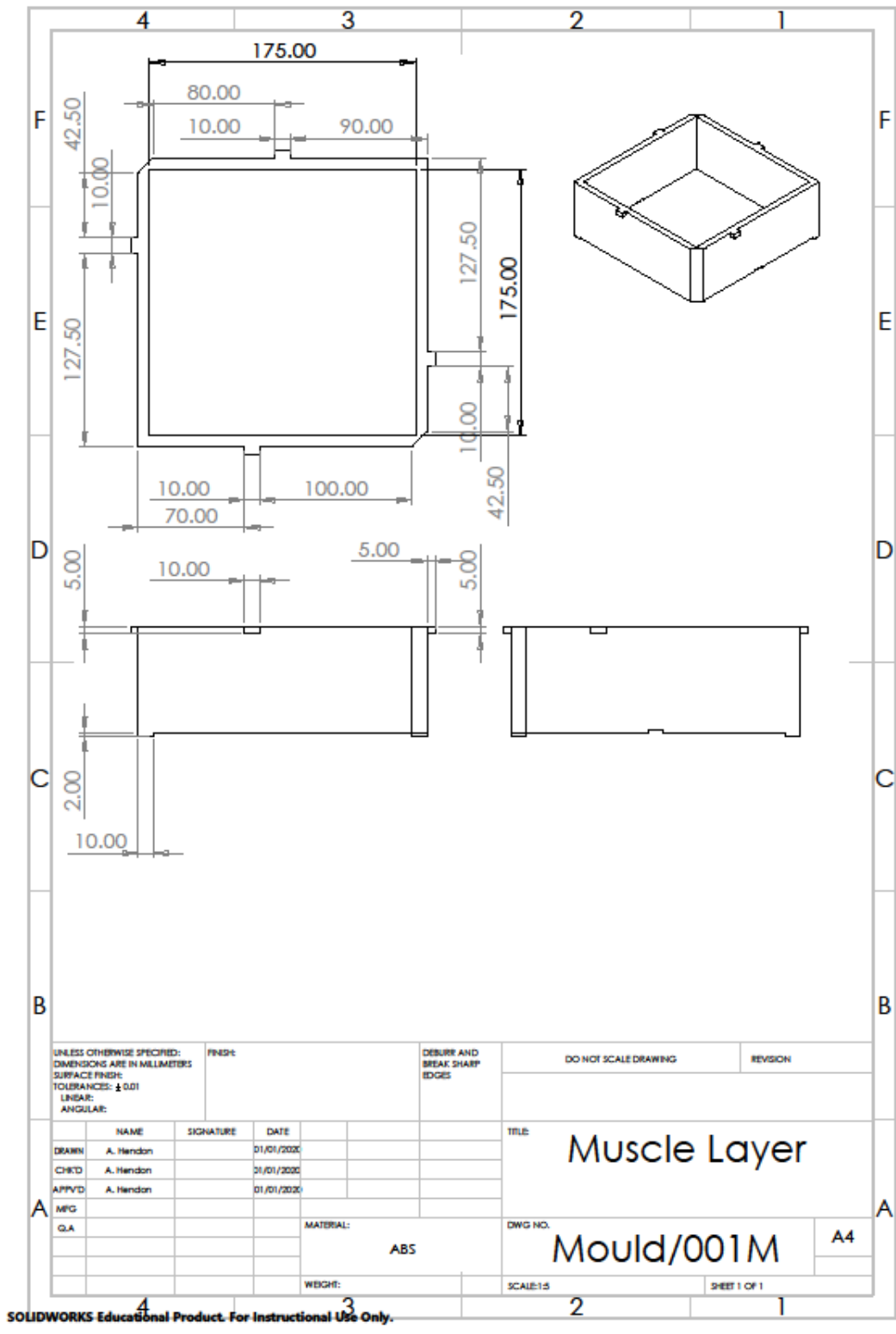
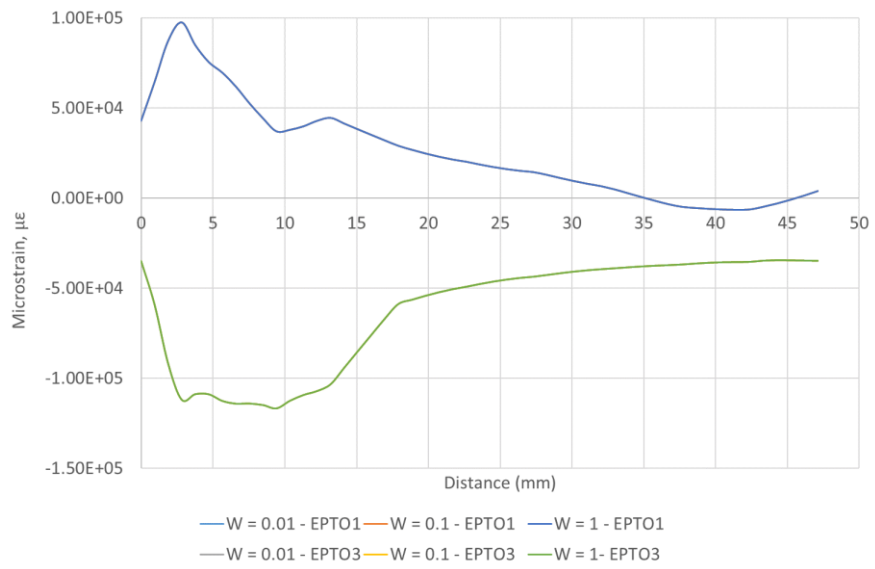


Figure 108 Engineering drawing of the muscle layer of the in vitro model mould.

## Appendix 3 – Surface Shell Element Thickness Variation Graph



**Figure 109** Variation of strain around the wound face when the surface shell element thickness is varied. It can be seen that there is no variation in strains experienced.

## Appendix 4 – Macroscopic *In Silico* Model Log File

/CLEAR

/START

/PREP7

mp,EX,1,0.85 ! YM SKIN - AGACHE (30-89)

MP,PRXY, 1,0.3

mp,EX,2,0.0117 ! YM FAT - ALKHOULI

MP,PRXY, 2,0.49

mp,EX,3,0.073206 ! YM MUSCLE - BASFORD

MP,PRXY, 3,0.49

mp,EX,4,14100 ! YM Tibia bone (Keller et al.,  
1990) 14100MPa = 14.1GPa

MP,PRXY, 4,0.3

MP,EX,5, 0.1 ! foam 100kPa

MP,PRXY, 5,0.3 ! changed as well

MP,EX,6,0.24 ! film 240kPa

MP,PRXY, 6,0.3 ! changed as well

! PARAMETERS 300 X 300

h=80 ! POSITIVE X

i=40 ! CENTRAL X

j=80 ! NEGATIVE X

```

l=80                ! POSITIVE Z
m=40                ! CENTRAL Z
n=80                ! NEGATIVE Z

a=2.5              ! a = SKIN
b=10               ! b = SUBCUTANEOUS FATTY TISSUE
c=60               ! c = MUSCLE
d=20               ! d = BASE LAYER (BONE)
r=30               ! RADIUS OF WOUND

o=10
p=l+2*m+n

f=0.1
W=0.1              ! Surface shell thickness
u=0.01             ! Wound shell thickness

ET,1,SOLID187      ! ELEMENT TYPE SOLID187
ET,2,SHELL281
KEYOPT,2,1,1

k,1,-h-i,0,-m-n   ! DEFINE KEYPOINTS
k,2,-i,0,-m-n
k,3,0,0,-m-n
k,4,i,0,-m-n
k,5,i+j,0,-m-n
k,6,-h-i,0,-m
k,7,-i,0,-m
k,8,0,0,-m

```

k,9,i,0,-m  
k,10,i+j,0,-m  
k,11,-h-i,0,0  
k,12,-i,0,0  
k,13,0,0,0  
k,14,i,0,0  
k,15,i+j,0,0  
k,16,-h-i,0,m  
k,17,-i,0,m  
k,18,0,0,m  
k,19,i,0,m  
k,20,i+j,0,m  
k,21,-h-i,0,m+L  
k,22,-i,0,m+L  
k,23,0,0,m+L  
k,24,i,0,m+L  
k,25,i+j,0,m+L

kgen,2,1,25,1,, -a,,100                   ! COPY KEYPOINTS  
kgen,2,101,125,1,, -b,,100  
kgen,2,201,225,1,, -c,,100  
kgen,2,301,325,1,, -d,,100

V,1,2,7,6,101,102,107,106   ! DEFINE VOLUMES  
V,2,3,8,7,102,103,108,107  
V,3,4,9,8,103,104,109,108  
V,4,5,10,9,104,105,110,109  
V,10,9,14,15,110,109,114,115  
V,8,9,14,13,108,109,114,113  
V,7,8,13,12,107,108,113,112  
V,6,7,12,11,106,107,112,111  
v,11,12,17,16,111,112,117,116

v, 12, 13, 18, 17, 112, 113, 118, 117  
v, 13, 14, 19, 18, 113, 114, 119, 118  
v, 14, 15, 20, 19, 114, 115, 120, 119  
v, 16, 17, 22, 21, 116, 117, 122, 121  
v, 17, 18, 23, 22, 117, 118, 123, 122  
v, 18, 19, 24, 23, 118, 119, 124, 123  
v, 19, 20, 25, 24, 119, 120, 125, 124

v, 101, 102, 107, 106, 201, 202, 207, 206  
v, 102, 103, 108, 107, 202, 203, 208, 207  
v, 103, 104, 109, 108, 203, 204, 209, 208  
v, 104, 105, 110, 109, 204, 205, 210, 209  
v, 110, 109, 114, 115, 210, 209, 214, 215  
v, 108, 109, 114, 113, 208, 209, 214, 213  
v, 107, 108, 113, 112, 207, 208, 213, 212  
v, 106, 107, 112, 111, 206, 207, 212, 211  
v, 111, 112, 117, 116, 211, 212, 217, 216  
v, 112, 113, 118, 117, 212, 213, 218, 217  
v, 113, 114, 119, 118, 213, 214, 219, 218  
v, 114, 115, 120, 119, 214, 215, 220, 219  
v, 116, 117, 122, 121, 216, 217, 222, 221  
v, 117, 118, 123, 122, 217, 218, 223, 222  
v, 118, 119, 124, 123, 218, 219, 224, 223  
v, 119, 120, 125, 124, 219, 220, 225, 224

v, 201, 202, 207, 206, 301, 302, 307, 306  
v, 202, 203, 208, 207, 302, 303, 308, 307  
v, 203, 204, 209, 208, 303, 304, 309, 308  
v, 204, 205, 210, 209, 304, 305, 310, 309  
v, 210, 209, 214, 215, 310, 309, 314, 315  
v, 208, 209, 214, 213, 308, 309, 314, 313  
v, 207, 208, 213, 212, 307, 308, 313, 312

v,206,207,212,211,306,307,312,311  
v,211,212,217,216,311,312,317,316  
v,212,213,218,217,312,313,318,317  
v,213,214,219,218,313,314,319,318  
v,214,215,220,219,314,315,320,319  
v,216,217,222,221,316,317,322,321  
v,217,218,223,222,317,318,323,322  
v,218,219,224,223,318,319,324,323  
v,219,220,225,224,319,320,325,324  
  
v,301,302,307,306,401,402,407,406  
v,302,303,308,307,402,403,408,407  
v,303,304,309,308,403,404,409,408  
v,304,305,310,309,404,405,410,409  
v,310,309,314,315,410,409,414,415  
v,308,309,314,313,408,409,414,413  
v,307,308,313,312,407,408,413,412  
v,306,307,312,311,406,407,412,411  
v,311,312,317,316,411,412,417,416  
v,312,313,318,317,412,413,418,417  
v,313,314,319,318,413,414,419,418  
v,314,315,320,319,414,415,420,419  
v,316,317,322,321,416,417,422,421  
v,317,318,323,322,417,418,423,422  
v,318,319,324,323,418,419,424,423  
v,319,320,325,324,419,420,425,424

SPHERE,R,,0,-180

VSEL,S,LOC,X,0,0

VSEL,R,LOC,Y,0,-R

CM,WOUND,VOLU

ALLSEL,ALL

CMSEL,U,WOUND,VOLU

CM,CMP1,VOLU ! CREATE A COMPONENT,  
CALLED CMP1, FROM THE REST OF THE VOLUMES

ALLSEL,ALL ! SELECT EVERYTHING AGAIN

VSBV,CMP1,WOUND,,DELETE,KEEP ! USE VSBV TO SUBTRACT 65 FROM  
ALL VOLUMES IN THE COMPONENT CMP1

ALLSEL,ALL

CM,CMP2,VOLU

ALLSEL,ALL

WPOFF,0,-A-B-C-D,-L-M ! OFFSET WORKPLANE TO BOTTOM OF  
MODEL

CYL4,0,0,0,,0,180,P ! CREATE CYLINDER WITH  
RADIUS 0

VSEL,S,LOC,Y,-A-B-C-D,-A-B-C-D+O

VSEL,R,LOC,X,0,0

CM,BONE,VOLU

VSBV,CMP1,BONE,,,

WPOFF,0,0,N

VSBW,ALL

WPOFF,0,0,M

VSBW,ALL

WPOFF,0,0,M

VSBW,ALL

WPOFF,0,0,-M

WPROTA,0,0,90

VSBW,ALL

CM,BONE,VOLU

```

WPROTA,0,0,-90
WPOFF,0,A+B+C+D,0

ALLSEL,ALL

VSEL,S,LOC,X,0,0
VSEL,R,LOC,Y,0,-R
VSBW,ALL,,,

WPOFF,0,-A,0           ! OFFSET WORKPLANE
BY -A

WPROTA,0,90,0         ! ROTATE AROUND Y BY
90 DEGREES

VSBW,ALL,,,

WPROTA,0,-90,0       ! RESET WORKPLANE
ROTATION

WPOFF,0,-B,0         ! OFFSET WORKPLANE
BY -B

WPROTA,0,90,0         ! ROTATE AROUND Y BY
90 DEGREES

VSBW,ALL,,,         ! CUT PLANE

CM,WOUND,VOLU

WPROTA,0,-90,0
WPOFF,0,A+B,0
ALLSEL,ALL

NUMMRG,ALL,,,,

ALLSEL,ALL

VSEL,S,LOC,X,-i,i     ! SELECT CENTRAL VOLUMES
VSEL,R,LOC,Z,-m,m     !
CMSEL,U,BONE,VOLU     ! UNSELECT THE BONE

```

```

ASLV,S                                ! SELECT ASSOCIATED
AREAS

LSLA,S                                ! SELECT ASSOCIATED
LINES

LESIZE,ALL,5, , , , , , ,1          ! SET LINE ELEMENT SIZE =
0.25

LSEL,INVE                             ! SELECT THE INVERSE
OF THE LINES

LESIZE,ALL,7, , , , , , ,1          ! SET LINE ELEMENT SIZE =
0.5

ALLSEL,ALL                             ! SELECT EVERYTHING
AGAIN

NUMMRG,ALL, , , ,LOW                 ! MERGES MATERIAL PROPS AS
WELL

ALLSEL,ALL                             ! SELECT EVERYTHING

MAT,4

CMSEL,S,BONE,VOLU

TYPE,1

VMESH,ALL

MAT,3                                ! MATERIAL 3
(SUBCUTANEOUS FATTY TISSUE)

VSEL,S,LOC,Y,-A-B,-A-B-C-D           ! SELECT VOLUMES (2ND
LAYER FROM TOP)

CMSEL,U,BONE,VOLU

CMSEL,U,WOUND,VOLU

CM,MUSCLE,VOLU

TYPE,1                                ! DEFINES THESE
VOLUMES AS A COMPONENT CALLED MUSCLE

VMESH,ALL                             ! MESH ALL

```

```

MAT,2                                ! MATERIAL 2
(MUSCLE)

VSEL,S,LOC,Y,-A,-A-B                ! SELECT VOLUMES (2ND
LAYER FROM BOTTOM)

CMSEL,U,WOUND,VOLU

CM,FAT,VOLU                          ! DEFINES THESE
VOLUMES AS A COMPONENT CALLED FAT

TYPE,1

VMESH,ALL                             ! MESH LAYER

MAT,1                                ! MATERIAL 1 (BONE)
VSEL,S,LOC,Y,0,-A                  ! SELECT VOLUMES
(TOP LAYER)

CMSEL,U,WOUND,VOLU

CM,SKIN,VOLU                         ! DEFINES THESE
VOLUMES AS A COMPONENT CALLED SKIN

TYPE,1

VMESH,ALL                             ! MESH LAYER

MAT,5

CMSEL,S,WOUND,VOLU

TYPE,1

VMESH,ALL

MAT,6

ASEL,S,LOC,Y,0,0

CM,FILM,AREA

TYPE,2

SECTYPE,1,SHELL                      ! section ID number =1
Type = SHELL

SECDATA,W,6,0,5                      ! shell thickness = 0.1
material property = 6                ignore the other terms

AMESH,ALL

```

```

/PNUM,MAT,1                                ! COLOUR EACH
MATERIAL DIFFERENTLY

/NUMBER,1                                    ! REMOVE NUMBERING

/VIEW,1,1,2,3

EPLO                                         ! PLOT ELEMENTS

ALLSEL,ALL

NUMMRG,MAT,,,,LOW

ASEL,S,LOC,Y,-a-b-c-d,-a-b-c-d
ASEL,A,LOC,X,-h-i,-h-i
ASEL,A,LOC,X,i+j,i+j
ASEL,A,LOC,Z,-m-n,-m-n
ASEL,A,LOC,Z,l+m,l+m

DA,ALL,SYMM,,

ALLSEL,ALL

EPLO

vsel,s,loc,x,0,0
vsel,r,loc,y,-r,0
aslv,s
asel,u,loc,y,0,0
ASEL,U,LOC,Y,-A,-A
ASEL,U,LOC,Y,-A-B,-A-B
ASEL,U,LOC,Z,0,0

CM,WOUNDLINER,AREA                          ! NEW

MAT,6

TYPE,2

```

```

SECTYPE,1,SHELL                                ! section ID number =1
Type = SHELL

SECDATA,u,6,0,5                                ! shell thickness = 0.0001
material property = 6      ignore the other terms

AMESH,ALL                                       ! create shells over
inside of wound

esla,s                                          ! select shell
elements

SFE,ALL,1,PRES,, -0.0266645                    ! apply pressure load on
shell elements

ALLSEL,ALL

vsel,s,loc,x,0,0
vsel,r,loc,y,-r,0
aslv,s
asel,r,loc,y,0,0

esla,s                                          ! select shell
elements on top of wound

SFE,ALL,1,PRES,, -0.0266645                    ! apply pressure load on
shell elements

ALLSEL,ALL

NUMMRG,ALL                                     ! NEW

/SOL
/STATUS,SOLU
SOLVE
FINISH

/POST1
/DSCALE
SET, LAST

```

## Appendix 5 – Macroscopic *In Silico* Model Post Processing File

```
! POSTPROCESSING

/POST1

/DSCALE

SET, LAST

/EDGE, 1, 0, 45

/REPLOT

/RGB, INDEX, 100, 100, 100, 0

/RGB, INDEX, 80, 80, 80, 13

/RGB, INDEX, 60, 60, 60, 14

/RGB, INDEX, 0, 0, 0, 15

/PLOPTS, LEG1, 1

/PLOPTS, LEG2, 0

/PLOPTS, LEG3, 1

/PLOPTS, FRAME, 0

/PLOPTS, TITLE, 0

/PLOPTS, MINM, 0

/PLOPTS, FILE, 0

/PLOPTS, SPNO, 0

/PLOPTS, WINS, 1

/PLOPTS, WP, 0

/PLOPTS, DATE, 0

/TRIAD, OFF

/REPLOT

allsel, all

PLNSOL, S, 1, 0, 1.0

!/CONT, 1, 9, -0.6, , 0.4
```

```

/REPLOT
/IMAGE,SAVE,STRESS 1,BMP

PLNSOL,S,2,0,1.0
!/CONT,1,9,-0.647075,,0.32825
/REPLOT
/IMAGE,SAVE,STRESS 2,BMP

PLNSOL,S,3,0,1.0
!/CONT,1,9,-1.60212,,0.076
/replot
/IMAGE,SAVE,STRESS 3,BMP

PLNSOL,EPTO,1,0,1.0
!/CONT,1,9,0,,0.960e-06
/REPLOT
/IMAGE,SAVE,STRAIN 1,BMP

PLNSOL,EPTO,2,0,1.0
!/CONT,1,9,-1.11e-07, ,0.32e-07
/REPLOT
/IMAGE,SAVE,STRAIN 2,BMP

PLNSOL,EPTO,3,0,1.0
!/CONT,1,9,-0.373e-05,,0.400e-06
/REPLOT
/IMAGE,SAVE,STRAIN 3,BMP

```

```

csys,1
cylindrical coordinate system

```

```
! change to global
```

```

path,WOUND,2,2,50
2 outputs here (s1 and s3)

```

```
! 2 points defining path and
```

```

ppath,1,,r,0,0                                ! top of wound
ppath,2,,0,-r,0

pdef,S1,s,1
pdef,S3,s,3
PDEF,SEQV,S,EQV
pdef,USUM,u,sum
pdef,uy,u,y
pdef,ux,u,x
pdef,EPTO1,epto,1
PDEF,EPTO3,EPTO,3
PDEF,EPTOEQV,EPTO,EQV
PDEF,EPTOX,EPTO,X
PDEF,EPTOZ,EPTO,Z

/OUTPUT,WOUND STRAIN,TXT    ! switches output to a file
PATH,WOUND
PRPATH,YG,EPTO1,EPTO3,EPTOEQV,UY,EPTOX
/OUTPUT,TERM

/OUTPUT,WOUND STRESS,TXT    ! switches output to a file
PATH,WOUND
PRPATH,YG,S1,S3,SEQV,USUM,UX,EPTOZ
/OUTPUT,TERM

/OUTPUT,WOUND EPTOZ,TXT
PATH,WOUND
PRPATH,YG,EPTOZ
/OUTPUT,TERM

```

csys,0  
coordinate system

! back to Cartesian

PATH,CENTRAL,2,30,100

PPATH,1,,0,-r,0

PPATH,2,,0,-a-b-c-d,0

PDEF,,U,Y,AVG

PDEF,,S,1,AVG

PDEF,,S,2,AVG

PDEF,,S,3,AVG

PDEF,,S,EQV,AVG

PDEF,,EPTO,1,AVG

PDEF,,EPTO,2,AVG

PDEF,,EPTO,3,AVG

PDEF,,EPTO,EQV,AVG

PATH,HORIZ,2,30,100

ALLSEL,ALL

EPLO

/TYPE,1,7

/CPLANE,1

/SHADE,1,1

/HBC,1,0

/REPLOT

/GRAPHICS,FULL

/EDGE,1,0,45

/REPLOT

/VIEW,1,,,1

/ANG,1

/REP,FAST

allsel,all

ESEL,U,MAT,,5

/replot

PLNSOL,S,1,0,1.0

!/CONT,1,9,-0.2666,,0.28889

/REPLOT

/IMAGE,SAVE,CROSS SECT STRESS 1,BMP

PLNSOL,S,2,0,1.0

!/CONT,1,9,-0.430366,,0.111511

!/REPLOT

/IMAGE,SAVE,CROSS SECT STRESS 2,BMP

PLNSOL,S,3,0,1.0

!/CONT,1,9,-0.68,,0.01

```

/REPLOT
/IMAGE,SAVE,CROSS SECT STRESS 3,BMP

PLNSOL,EPTO,1,0,1.0
!/CONT,1,9,0,,0.335e-06
/REPLOT
/IMAGE,SAVE,CROSS SECT STRAIN 1,BMP

PLNSOL,EPTO,2,0,1.0
!/CONT,1,9,-0.284e-07,,0.23e-06
/REPLOT
/IMAGE,SAVE,CROSS SECT STRAIN 2,BMP

PLNSOL,EPTO,3,0,1.0
!/CONT,1,9,-0.212e-05,,0.120e-06
/REPLOT
/IMAGE,SAVE,CROSS SECT STRAIN 3,BMP

/OUTPUT,CENTRAL STRESS,TXT ! switches output to a file
PATH,CENTRAL
PRPATH,YG,S1,S2,S3,SEQV,USUM
/OUTPUT,TERM ! switches output back to the screen

/OUTPUT,CENTRAL STRAIN,TXT ! switches output to a file
PATH,CENTRAL
PRPATH,YG,EPTO1,EPTO2,EPTO3,EPTOEQV,UY
/OUTPUT,TERM ! switches output back to the screen

```

## Appendix 6 – Microscopic *In Silico* Foam Model Log File

/CLEAR

/START

/PREP7

! MATERIAL PROPERTIES

MP,EX,1,0.073206 ! YM MUSCLE - BASFORD

MP,PRXY,1,0.49

MP,EX,2,91 ! YM STRUT - WONDU ET AL., 2019

MP,prxy,2,0.3

! PARAMETERS - 60PPI

! X DIRECTION

A=0.348

B=0.15 ! X STRUT

C=0.348

! Z DIRECTION

D=0.348

E=0.15 ! Z STRUT

F=0.348

! Y DIRECTION

G=0.09144\*6 ! STRUT HEIGHT

H=0.09144\*10 ! MUSCLE DEPTH

ET,1,SOLID187

K,1,-0.5\*B-A,0,0.5\*E+D

K,2,-0.5\*B,0,0.5\*E+D

K,3,0,0,0.5\*E+D

K,4,-0.5\*B-A,0,0.5\*E

K,5,-0.5\*B,0,0.5\*E

K,6,0,0,0.5\*E

K,7,-0.5\*B-A,0,0

K,8,-0.5\*B,0,0

K,9,0,0,0

! STRUT

K,10,-0.5\*B,G,0

K,11,0,G,0

K,12,-0.5\*B,G,0.5\*E

K,13,0,G,0.5\*E

KGEN,2,1,9,1,, -H,,100

V,1,2,5,4,101,102,105,104

V,2,3,6,5,102,103,106,105

V,4,5,8,7,104,105,108,107

V,5,6,9,8,105,106,109,108

! STRUT

V,5,6,9,8,12,13,11,10

ALLSEL,ALL

VSEL,S,LOC,Y,0,G

CM,STRUT,VOLU

MAT,1

VSEL,ALL

CMSEL,U,STRUT,VOLU

TYPE,1

VMESH,ALL

ALLSEL,ALL

MAT,2

CMSEL,S,STRUT,VOLU

TYPE,1

VMESH,ALL

ALLSEL,ALL

VSYMM,X,ALL,,0,0

ALLSEL,ALL

VSYMM,Z,ALL,,0,0

ALLSEL,ALL

ALLSEL,ALL

/PNUM,MAT,1

/NUMBER,1

/VIEW,1,1,2,3

EPLO

ALLSEL,ALL

NUMMRG,MAT,,,,LOW

ASEL,S,LOC,Y,-H,-H

DA,ALL,UX,0

DA,ALL,UY,0

DA,ALL,UZ,0

ALLSEL,ALL

! ADDED STRAIN

ASEL,S,LOC,Y,0,-H

ASEL,R,LOC,X,-0.5\*B-A,-0.5\*B-A

DA,ALL,UX,0.027371\*(B+A+C)\*0.5

DA,ALL,SYMM

ALLSEL,ALL

ASEL,S,LOC,Y,0,-H

ASEL,R,LOC,X,0.5\*B+C,0.5\*B+C

DA,ALL,UX,-0.027371\*(B+A+C)\*0.5

DA,ALL,SYMM

ALLSEL,ALL

ASEL,S,LOC,Y,0,-H

ASEL,R,LOC,Z,-0.5\*E-D,-0.5\*E-D

DA,ALL,UZ,0.028059\*(D+E+f)\*0.5

DA,ALL,SYMM

ALLSEL,ALL

ASEL,S,LOC,Y,0,-H

ASEL,R,LOC,Z,0.5\*E+F,0.5\*E+F

DA,ALL,UZ,-0.028059\*(D+E+f)\*0.5

DA,ALL,SYMM

ALLSEL,ALL

ASEL,S,LOC,Y,G,G ! SELECT TOP OF STRUT - matches excel file

! ASEL,S,LOC,Y,0,0

ASEL,R,LOC,Z,-0.5\*E,0.5\*E

ASEL,R,LOC,X,-0.5\*B,0.5\*B

DA,ALL,UY,-0.06433828571\*G

! SFA,ALL,1,PRES,0.0023998

ALLSEL,ALL

ASEL,S,LOC,Y,0,0 ! SELECT TOP OF MUSCLE LAYER - matches  
pressure & strut excel file

ASEL,R,LOC,Z,-0.5\*E,0.5\*E

ASEL,R,LOC,X,-0.5\*B,0.5\*B

ASEL,INVE

ASEL,R,LOC,Y,0,0

! DA,ALL,UY,0.36771

SFA,ALL,1,PRES,-0.0023998

ALLSEL,ALL

NUMMRG,ALL

/SOL

/STATUS,SOLU

SOLVE

FINISH

/POST1

/DSCALE

SET, LAST

## Appendix 7 – Microscopic *In Silico* Foam Model Post Processing Log File

```
! POSTPROCESSING

/POST1

/DSCALE

SET, LAST

/EDGE, 1, 0, 45

/REPLOT

/RGB, INDEX, 100, 100, 100, 0

/RGB, INDEX, 80, 80, 80, 13

/RGB, INDEX, 60, 60, 60, 14

/RGB, INDEX, 0, 0, 0, 15

/PLOPTS, LEG1, 1

/PLOPTS, LEG2, 0

/PLOPTS, LEG3, 1

/PLOPTS, FRAME, 0

/PLOPTS, TITLE, 0

/PLOPTS, MINM, 0

/PLOPTS, FILE, 0

/PLOPTS, SPNO, 0

/PLOPTS, WINS, 1

/PLOPTS, WP, 0

/PLOPTS, DATE, 0

/TRIAD, OFF

/REPLOT

allsel, all

PLNSOL, S, 1, 0, 1.0
```

```

!/CONT,1,9,-0.6,,0.4
/REPLOT
/IMAGE,SAVE,STRESS 1,BMP

PLNSOL,S,2,0,1.0
!/CONT,1,9,-0.647075,,0.32825
/REPLOT
/IMAGE,SAVE,STRESS 2,BMP

PLNSOL,S,3,0,1.0
!/CONT,1,9,-1.60212,,0.076
/replot
/IMAGE,SAVE,STRESS 3,BMP

PLNSOL,EPTO,1,0,1.0
!/CONT,1,9,0,,0.960e-06
/REPLOT
/IMAGE,SAVE,STRAIN 1,BMP

PLNSOL,EPTO,2,0,1.0
!/CONT,1,9,-1.11e-07,,0.32e-07
/REPLOT
/IMAGE,SAVE,STRAIN 2,BMP

PLNSOL,EPTO,3,0,1.0
!/CONT,1,9,-0.373e-05,,0.400e-06
/REPLOT
/IMAGE,SAVE,STRAIN 3,BMP

!Path through centre

PATH,CENTRAL,2,30,300

```

PPATH,1,,0,0,0

PPATH,2,,0,-H,0

PDEF,,U,Y,AVG

PDEF,,S,1,AVG

PDEF,,S,2,AVG

PDEF,,S,3,AVG

PDEF,,S,EQV,AVG

PDEF,,EPTO,1,AVG

PDEF,,EPTO,2,AVG

PDEF,,EPTO,3,AVG

PDEF,,EPTO,EQV,AVG

! PATH ACROSS SURFACE

PATH,HORIZONTAL,2,30,300

PPATH,1,,-0.5\*B-A,0

PPATH,2,,0.5\*B+C,0

PDEF,,U,Y,AVG

PDEF,,S,1,AVG

PDEF,,S,2,AVG

PDEF,,S,3,AVG

PDEF,,S,EQV,AVG

PDEF,,EPTO,1,AVG

PDEF,,EPTO,2,AVG

PDEF,,EPTO,3,AVG

PDEF,,EPTO,EQV,AVG

ALLSEL,ALL

EPLO

/TYPE,1,7

/CPLANE,1

/SHADE,1,1

/HBC,1,0

/REPLOT

/GRAPHICS,FULL

/EDGE,1,0,45

/REPLOT

/VIEW,1,,,1

/ANG,1

/REP,FAST

```
PLNSOL,S,1,0,1.0
!/CONT,1,9,-0.2666,,0.28889
/REPLOT
/IMAGE,SAVE,CROSS SECT STRESS 1,BMP
```

```
PLNSOL,S,2,0,1.0
!/CONT,1,9,-0.430366,,0.111511
!/REPLOT
/IMAGE,SAVE,CROSS SECT STRESS 2,BMP
```

```
PLNSOL,S,3,0,1.0
!/CONT,1,9,-0.68,,0.01
/REPLOT
/IMAGE,SAVE,CROSS SECT STRESS 3,BMP
```

```
PLNSOL,EPTO,1,0,1.0
!/CONT,1,9,0,,0.335e-06
/REPLOT
/IMAGE,SAVE,CROSS SECT STRAIN 1,BMP
```

```
PLNSOL,EPTO,2,0,1.0
!/CONT,1,9,-0.284e-07,,0.23e-06
/REPLOT
/IMAGE,SAVE,CROSS SECT STRAIN 2,BMP
```

```
PLNSOL,EPTO,3,0,1.0
!/CONT,1,9,-0.212e-05,,0.120e-06
/REPLOT
/IMAGE,SAVE,CROSS SECT STRAIN 3,BMP
```

```
/OUTPUT,CENTRAL STRESS,TXT ! switches output to a file
PATH,CENTRAL
```

PRPATH, YG, S1, S2, S3, SEQV, USUM

/OUTPUT, TERM ! switches output back to the screen

/OUTPUT, CENTRAL STRAIN, TXT ! switches output to a file

PATH, CENTRAL

PRPATH, YG, EPTO1, EPTO2, EPTO3, EPTOEQV, UY

/OUTPUT, TERM ! switches output back to the screen

/OUTPUT, HORIZ STRAIN, TXT

PATH, HORIZONTAL

PRPATH, YG, EPTO1, EPTO2, EPTO3, EPTOEQV, UY

/OUTPUT, TERM

/OUTPUT, HORIZ STRESS, TXT

PATH, HORIZONTAL

PRPATH, YG, S1, S2, S3, SEQV, USUM

/OUTPUT, TERM

## Appendix 8 – Microscopic *In Silico* Gauze Model Log File

! Circular Gauze Model 12.04.2023

/CLEAR

/START

/PREP7

! MATERIAL PROPERTIES

MP,EX,1,0.073206 ! YM MUSCLE - BASFORD

MP,PRXY,1,0.49

MP,EX,2,4.1\*10E5 ! YM STRUT - WONDU ET AL., 2019

MP,prxy,2,0.3

! PARAMETERS - ARBITRARY

! X DIRECTION

A=0.0388333

B=0.02

C=0.0388333

! Z DIRECTION

D=0.0388333

E=0.02

F=0.0388333

! Y DIRECTION

```

I=0.02          ! THREAD DIAMETER
J=0.09144*10    ! MUSCLE DEPTH

! ET,1,SOLID187

ET,1,PLANE183

K,1,-A-B-C,0,D+E+F
K,2,-B-C,0,D+E+F
K,3,-C,0,D+E+F
K,4,0,0,D+E+F

KGEN,2,1,4,1,, -J,,100

A,1,2,102,101
A,2,3,103,102
A,3,4,104,103

WPOFF,0,0,D+E+F

CYL4,-C-0.5*B,0,0.5*I,,0.5*I,,

WPOFF,0,0,-D-E-F

ALLSEL,ALL

ASEL,S,LOC,Y,-0.5*I,0.5*I

CM,THREAD,AREA

ALLSEL,ALL

```

CMSEL,U,THREAD,AREA

CM,MUSCLE,AREA

ALLSEL,ALL

ASBA,MUSCLE,THREAD,,DELETE,KEEP

ALLSEL,ALL

ASEL,S,LOC,Y,-0.5\*I,-J

CM,MUSCLE2,AREA

ALLSEL,ALL

LSLA,S

LESIZE,ALL,0.005,,,,,,,,1

MAT,2

CMSEL,S,THREAD,AREA

TYPE,1

AMESH,ALL

ALLSEL,ALL

MAT,1

CMSEL,S,MUSCLE2,AREA

TYPE,1

AMESH,ALL

/PNUM, MAT, 1

/NUMBER, 1

/VIEW, 1, 1, 2, 3

EPLO

ALLSEL, ALL

NUMMRG, MAT, , , , LOW

EEXTRUDE, PLANE, , , D+E+F, , , ,

NSEL, S, LOC, Y, 0, 0

SF, ALL, PRES, -0.0023998

ALLSEL, ALL

NSEL, S, LOC, X, 0, 0

! D, ALL, SYMM

D, ALL, UX, -0.027371\*2\*(B+A+C)\*0.5

ALLSEL, ALL

NSEL, S, LOC, X, -D-E-F, -D-E-F

! DL, ALL, , SYMM

D, ALL, UX, 0.027371\*2\*(B+A+C)\*0.5

ALLSEL, ALL

NSEL, S, LOC, Z, A+B+C, A+B+C

NSEL, R, LOC, Y, 0, -J

D,ALL,UZ,0.028059\*2\*(D+E+f)\*0.5

NSEL,S,LOC,Z,2\*A+2\*B+2\*C,2\*A+2\*B+2\*C

NSEL,R,LOC,Y,0,-J

D,ALL,UZ,-0.028059\*2\*(D+E+f)\*0.5

NSEL,S,LOC,Y,-J,-J

D,ALL,UX,0

D,ALL,UY,0

D,ALL,UZ,0

ALLSEL,ALL

NSEL,S,LOC,Y,0.5\*I,0.5\*I

D,ALL,UY,-0.06433828571\*I

ALLSEL,ALL

NUMMRG,ALL

/SOL

/STATUS,SOLU

SOLVE

FINISH

/POST1

/DSCALE

SET, LAST



## Appendix 9 – Microscopic *In Silico* Gauze Model Post Processing Log File

! POSTPROCESSING

/POST1

/DSCALE

SET, LAST

/EDGE, 1, 0, 45

/REPLOT

/RGB, INDEX, 100, 100, 100, 0

/RGB, INDEX, 80, 80, 80, 13

/RGB, INDEX, 60, 60, 60, 14

/RGB, INDEX, 0, 0, 0, 15

/PLOPTS, LEG1, 1

/PLOPTS, LEG2, 0

/PLOPTS, LEG3, 1

/PLOPTS, FRAME, 0

/PLOPTS, TITLE, 0

/PLOPTS, MINM, 0

/PLOPTS, FILE, 0

/PLOPTS, SPNO, 0

/PLOPTS, WINS, 1

/PLOPTS, WP, 0

/PLOPTS, DATE, 0

/TRIAD, OFF

/REPLOT

allsel, all

PLNSOL, S, 1, 0, 1.0

```

!/CONT,1,9,-0.6,,0.4
/REPLOT
/IMAGE,SAVE,STRESS 1,BMP

PLNSOL,S,2,0,1.0
!/CONT,1,9,-0.647075,,0.32825
/REPLOT
/IMAGE,SAVE,STRESS 2,BMP

PLNSOL,S,3,0,1.0
!/CONT,1,9,-1.60212,,0.076
/replot
/IMAGE,SAVE,STRESS 3,BMP

PLNSOL,EPTO,1,0,1.0
!/CONT,1,9,0,,0.960e-06
/REPLOT
/IMAGE,SAVE,STRAIN 1,BMP

PLNSOL,EPTO,2,0,1.0
!/CONT,1,9,-1.11e-07,,0.32e-07
/REPLOT
/IMAGE,SAVE,STRAIN 2,BMP

PLNSOL,EPTO,3,0,1.0
!/CONT,1,9,-0.373e-05,,0.400e-06
/REPLOT
/IMAGE,SAVE,STRAIN 3,BMP

!Path through centre

PATH,CENTRAL,2,30,300

```

PPATH,1,, -D-0.5\*E, -0.5\*I,2\*A+1.5\*B+C

PPATH,2,, -D-0.5\*E, -J,2\*A+1.5\*B+C

PDEF,,U,Y,AVG

PDEF,,S,1,AVG

PDEF,,S,2,AVG

PDEF,,S,3,AVG

PDEF,,S,EQV,AVG

PDEF,,EPTO,1,AVG

PDEF,,EPTO,2,AVG

PDEF,,EPTO,3,AVG

PDEF,,EPTO,EQV,AVG

! PATH ACROSS SURFACE

PATH,HORIZONTAL,2,30,300

PPATH,1,, -D-E-F, -0.5\*I,2\*A+1.5\*B+C

PPATH,2,,0, -0.5\*I,2\*A+1.5\*B+C

PDEF,,U,Y,AVG

PDEF,,S,1,AVG

PDEF,,S,2,AVG

PDEF,,S,3,AVG

PDEF,,S,EQV,AVG

PDEF,,EPTO,1,AVG

PDEF,,EPTO,2,AVG

PDEF,,EPTO,3,AVG

PDEF,,EPTO,EQV,AVG

ALLSEL,ALL

EPLO

/TYPE,1,7

/CPLANE,1

/SHADE,1,1

/HBC,1,0

/REPLOT

/GRAPHICS,FULL

/EDGE,1,0,45

/REPLOT

/VIEW,1,,,1

/ANG,1

/REP,FAST

PLNSOL,S,1,0,1.0

```

!/CONT,1,9,-0.2666,,0.28889
/REPLOT
/IMAGE,SAVE,CROSS SECT STRESS 1,BMP

PLNSOL,S,2,0,1.0
!/CONT,1,9,-0.430366,,0.111511
!/REPLOT
/IMAGE,SAVE,CROSS SECT STRESS 2,BMP

PLNSOL,S,3,0,1.0
!/CONT,1,9,-0.68,,0.01
/REPLOT
/IMAGE,SAVE,CROSS SECT STRESS 3,BMP

PLNSOL,EPTO,1,0,1.0
!/CONT,1,9,0,,0.335e-06
/REPLOT
/IMAGE,SAVE,CROSS SECT STRAIN 1,BMP

PLNSOL,EPTO,2,0,1.0
!/CONT,1,9,-0.284e-07,,0.23e-06
/REPLOT
/IMAGE,SAVE,CROSS SECT STRAIN 2,BMP

PLNSOL,EPTO,3,0,1.0
!/CONT,1,9,-0.212e-05,,0.120e-06
/REPLOT
/IMAGE,SAVE,CROSS SECT STRAIN 3,BMP

/OUTPUT,CENTRAL STRESS, TXT ! switches output to a file
PATH,CENTRAL
PRPATH,YG,S1,S2,S3,SEQV,USUM

```

```
/OUTPUT,TERM ! switches output back to the screen
```

```
/OUTPUT,CENTRAL STRAIN,TXT ! switches output to a file
```

```
PATH,CENTRAL
```

```
PRPATH,YG,EPTO1,EPTO2,EPTO3,EPTOEQV,UY
```

```
/OUTPUT,TERM ! switches output back to the screen
```

```
/OUTPUT,HORIZ STRAIN,TXT
```

```
PATH,HORIZONTAL
```

```
PRPATH,YG,EPTO1,EPTO2,EPTO3,EPTOEQV,UY
```

```
/OUTPUT,TERM
```

```
/OUTPUT,HORIZ STRESS,TXT
```

```
PATH,HORIZONTAL
```

```
PRPATH,YG,S1,S2,S3,SEQV,USUM
```

```
/OUTPUT,TERM
```